Optimalisatie van het hydrodynamische gedrag
van golfenergieconvertoren gebaseerd op golfoverslag:
experimentele studie van optimale geometrie
en kansverdeling van overslagvolumes

Optimization of the Hydrodynamic Performance
of Overtopping Wave Energy Converters:
Experimental Study of Optimal Geometry
and Probability Distribution of Overtopping Volumes

Lander Victor

Promotor: prof. dr. ir. P. Troch
Proefschrift ingediend tot het behalen van de graad van
Doctor in de Ingenieurswetenschappen: Bouwkunde

Vakgroep Civiele Techniek
Voorzitter: prof. dr. ir. J. De Rouck
Faculteit Ingenieurswetenschappen en Architectuur
Academiejaar 2011 - 2012

UNIVERSITEIT
GENT

ISBN 978-90-8578-478-4
NUR 956, 961
Wettelijk depot: D/2012/10.500/4

Universiteit Gent
Faculteit Ingenieurswetenschappen en Architectuur
Vakgroep Civiele Techniek
Afdeling Weg- en Waterbouwkunde

Supervisor:

Prof. dr. ir. P. Troch

Research institute:

Ghent University
Faculty of Engineering and Architecture

Department of Civil Engineering
Coastal Engineering Division
Technologiepark 904
B-9052 Zwijnaarde, Belgium

Tel.: +32-9-264.54.89
Fax.: +32-9-264.58.37

Research funded by a PhD grant of the Fund for Scientific Research – Flanders (FWO – Vlaanderen), Belgium.

Dankwoord
Acknowledgements

Opluchting! Dat is het overheersende gevoel na vier jaar hard werken aan mijn doctoraat. Dit boek beschrijft de resultaten van mijn onderzoek en vormt zo het sluitstuk van een intense periode. Ik wil deze gelegenheid dan ook aangrijpen om een aantal mensen te bedanken, wiens steun en bijdrage onontbeerlijk waren tijdens mijn doctoraatsperiode.

In eerste instantie wil ik graag mijn promotor, prof. Peter Troch, bedanken omdat hij me aanbood een doctoraat aan te vatten aan de Afdeling Weg- en Waterbouwkunde (AWW) van de Universiteit Gent. Ondanks mijn initiële twijfels tussen "industrie" en een doctoraat ben ik, nu alles achter de rug is, blij dat ik deze unieke kans heb gegrepen. Mijn promotor heeft hij me tijdens mijn doctoraat ook de gelegenheid gegeven mijn technische en niet-technische skills verder te ontwikkelen aan de hand van verschillende workshops, conferenties, een doctoraatsstage in Denemarken en mijn engagement in INORE. Zijn steun tijdens de intense laatste maanden van mijn doctoraat heb ik ook enorm geapprecieerd.

Tevens dank ik prof. Julien De Rouck en prof. Mia Loccufier voor de interessante gesprekken over mijn doctoraatsonderzoek. Heel specifiek wil ik ook dr. Jentsje van der Meer (Van der Meer Consulting B.V., Nederland) vermelden. Dankzij zijn expertise met betrekking tot golfoverslag van kustwaterbouwkundige structuren hebben onze discussies over mijn onderzoek me heel wat bijkomend inzicht verschaft. Onze samenwerking in het laatste anderhalf jaar van mijn doctoraat heeft een groot aandeel in de kwaliteit van dit werk.

In de eerste fase van mijn doctoraat heb ik vijf maanden doorgebracht aan het Department of Civil Engineering van Aalborg University in Denemarken om er experimentele proeven uit te voeren. Ik wil dan ook mijn dank betuigen aan enkele mensen van Aalborg. First, I would like to thank prof. Jens Peter Kofoed. His suggestions before and during the (analysis of the) experiments and his expertise on overtopping wave energy converters helped me to gain insight in the obtained results. Jens Peter, *tusen tak* for making time available for me (even when you actually didn't have any time) and for helping me out with all the small and bigger questions I had, not only during my stay in Aalborg but also afterwards! Second, some words of thanks go to prof. Peter Frigaard and dr. Lucia Margheritini. They gave me a warm welcome and stay in Aalborg, for which I am really grateful! Kurt, Jens and Nick,

technicians at Aalborg University, are also greatly acknowledged for their help and expertise during the construction of the test set-up. Finally, I would like to thank my roommates in Aalborg: Orlando, Ju and Moh. I really enjoyed our conversations about anything but work and our big dinners in the weekends!

Via mijn doctoraatsstudie was ik gedurende twee jaar bestuurslid van het International Network on Offshore Energy (INORE), een organisatie van en voor jonge onderzoekers die werken rond offshore hernieuwbare energie. Ik wil ook een woordje van dank richten aan mijn medebestuursleden. In particular, I would like to thank Sarah and Tom for the many joyful moments we shared when organizing the conferences and workshops and while discussing the future steps for INORE. I'll never forget them!

Mijn collega's (van AWW en Labo Hydraulica) verdienen ook een plaatsje in dit dankwoord: Amélie, Anny, Anke, Bart, Corneel, Dieter M. Dogan, Dries, Ellen, Etienne, Florent, Hans, Jan, Jesus, Jimmy, Johannes, Ken, Kevin, Koen, Lien D.B., Lien V., Liesbet, Leen B., Ludo, Philippe, Pieter D.W., Pieter M., Pieter R., Ronny, Sieglien, Tingqui, Tomas, Vicky, Vincent, Wim, Wouter en Yvan. De geanimeerde discussies over het al dan niet plaatsvinden van de opwarming van de aarde en de vele babbels over fietsen zullen me altijd bijblijven. Verder ook een dikke merci aan Dave, Herman, Sam en Tom voor hun technische assistentie bij het uitvoeren en verwerken van de experimentele proeven in Aalborg en Gent en voor hun hulp bij het optimaliseren van de proefopstelling. Jullie zijn echte kraks. In het bijzonder wil ik ook Charlotte, Griet, Hadewych en Leen D.V bedanken. Naast het feit dat jullie toffe collega's waren, hebben jullie me tevens geholpen in het doorgronden van de mogelijkheden en verplichtingen tijdens een doctoraat en waren jullie steeds geïnteresseerd in de voortgang van mijn werk. Some words of thanks also go to my colleague Giang for his hospitality when visiting him in Vietnam. Als laatste wil ik graag mijn vaste bureaugenoot Dieter V. bedanken. Gedurende de afgelopen vier jaar hebben we talloze discussies gehad en momenten van lachen (maar ook van vloeken) gedeeld die ik me steeds zal herinneren. Dieter, nog een laatste duwtje, het einde is in zicht!

Ik wil verder ook Jan, Ruth en Walid danken voor hun inzet tijdens hun Master thesis. De vele uren in de kelder van AWW hebben meer dan geloond en vormden een belangrijke input voor mijn doctoraatsonderzoek.

Natuurlijk wil ik ook graag een dankwoordje richten aan "min moaten". De weekendjes weg, de avonden op café, de skireis, het roeien, het componeren en musiceren met Bataclãn Drumband en Homelands, … mede dankzij jullie kon ik me tijdens mijn vrije momenten ook echt ontspannen. Super merci! Ik apprecieer jullie

warmte en vriendschap enorm. Dieter, bovendien bedankt voor het grondig nalezen van mijn manuscript.

Ik wil heel graag ook mijn mama en twee broers danken voor hun steun en hun niet aflatende interesse in de vorderingen van mijn onderzoek tijdens de afgelopen vier jaar. Muti, de positieve energie waarmee jij in het leven staat, heeft me geïnspireerd om te blijven doorgaan en de moed niet te laten zakken.

Last but not least wil ik het geschreven woord richten tot mijn vriendin. Stephanie, merci voor al je liefde en steun, dag in dag uit! Bedankt om er steeds te zijn voor mij, ook op de momenten dat ik niet het meest aangename gezelschap was. Ik ben zo blij dat we samen door het leven kunnen gaan! We hebben in de afgelopen jaren samen reeds vele toffe avonturen beleefd. Ik kijk heel erg uit naar het vervolg dat we hier samen zullen aan breien!

Gent, januari 2012
Lander Victor

Table of contents

List of Symbols

1 Symbols

a	[m³/m]	=	scale factor Weibull distribution individual overtopping volumes
a'	[-]	=	factor relating a to b: $a' = 1/\Gamma(1+1/b)$
a_H	[m]	=	scale factor Weibull distribution individual wave heights
A, B	[-]	=	coefficients in the dimensionless equation $q/\sqrt{g H_{m0}^3} = A\exp(B R_c / H_{m0})$
A'	[-]	=	$\ln(A)$
A_{Z1}, B_{Z1}	[-]	=	coefficients A and B in the zone Z1
A_{Z2}, B_{Z2}	[-]	=	coefficients A and B in the zone Z2
A_{Z3}, B_{Z3}	[-]	=	coefficients A and B in the zone Z3
A_{Z4}, B_{Z4}	[-]	=	coefficients A and B in the zone Z4
b	[-]	=	shape factor Weibull distribution individual overtopping volumes
b_H	[-]	=	shape factor Weibull distribution individual wave heights
b_{Owen}	[-]	=	coefficient in prediction formula of Owen (1980), Eq. (4.9)
B_{berm}	[m]	=	width of the berm of a sea defence structure
B_q	[m]	=	width for which the overtopped water is collected
B_t	[m]	=	width of the toe of a sea defence structure
$B_{Z2\ 0.2}$	[-]	=	coefficient B in the zone Z2 with $A_{Z2} = 0.2$
c	[m/s]	=	wave propagation velocity of a linear wave, defined by $c = L/T$
c_{deep}	[m/s]	=	wave propagation velocity of a linear wave in deep water, defined by $c_{deep} = gT/2\pi$
c_g	[m/s]	=	group velocity of linear wave, i.e. energy propagation velocity of a wave

$c_{g,deep}$	[m/s]	=	group velocity of linear wave in deep water, defined by $c_{g,deep} = c_{deep}/2$
C, D	[-]	=	coefficients of hyperbolic tangent function
CF	[-]	=	complexity factor of a test result of the CLASH database, possible values are 1,2,3 and 4
f_1, f_2, f		=	random functions
$f_{r,1}$	[-]	=	reduction factor for smaller relative crest freeboards applied to K_r, suggested by Van der Meer et al. (2005)
$f_{r,2}$	[-]	=	reduction factor for smaller relative crest freeboards applied to K_r, suggested by Zanuttigh and Van der Meer (2008)
f_R	[-]	=	random reduction factor applied to K_r
FO_j	[%]	=	frequency of occurrence of a particular characteristic sea state, defined by $FO_j = \sum_{l=1}^{N_T} FO_{j,l}$
$FO_{j,l}$	[%]	=	frequency of occurrence of a particular combination of wave height (j) and wave period (l) in a scatter diagram
g	[m/s^2]	=	acceleration due to gravity
h	[m]	=	generic water depth
h^*	[-]	=	impulsiveness parameter
h_t	[m]	=	water depth at the toe of the structure
h_{paddle}	[m]	=	water depth at the wave paddle
h_{deep}	[m]	=	water depth in deep water
H	[m]	=	wave height of a linear wave
$\tilde{H}$	[m]	=	stochastic variable individual wave heights
$H_{1/3}$	[m]	=	significant wave height at the toe of the structures defined as the average of the 1/3rd largest wave heights
H_{deep}	[m]	=	wave height of a linear wave in deep water
H_j	[m]	=	class representative of a class of characteristic wave heights in a scatter diagram, i.e. the characteristic wave height of a characteristic sea state
H_m	[m]	=	mean wave height of the incident waves at the toe of the structure
H_{m0}	[m]	=	spectral wave height of the incident waves at the toe of the structure
$\hat{H}_{m0}$	[m]	=	sea state averaged spectral wave height

$H_{m0,paddle}$	[m]	=	spectral wave height of the incident waves at the wave paddle
H_s	[m]	=	H_{m0} or $H_{1/3}$
$H_{s,j}$	[m]	=	class representative of a class of significant wave heights in a scatter diagram
k	[1/m]	=	wave number for a linear wave, defined by $k = 2\pi / L$
k_{deep}	[1/m]	=	wave number for a linear wave in deep water, defined by $k_{deep} = 2\pi / L_{deep}$
$k_{m-1,0,t}$	[1/m]	=	wave number at the toe of the structure, defined by $k_{m-1,0,t} = 2\pi / L_{m-1,0,t}$
$k_{m-1,0,paddle}$	[1/m]	=	wave number at the wave paddle, defined by $k_{m-1,0,paddle} = 2\pi / L_{m-1,0,paddle}$
K_d	[-]	=	Dissipation coefficient
K_r	[-]	=	reflection coefficient, ratio of incident and reflected wave height
$K_{r,overall}$	[-]	=	overall reflection coefficient, weighted over the characteristic sea states at a particular location by their frequencies of occurrence
K_{OT}	[-]	=	transmission coefficient due to wave overtopping only
K_S	[-]	=	shoaling coefficient, generic
$K_S(h,h_{deep})$	[-]	=	shoaling coefficient between water depths h and h_{deep}
$K_S(h_t,h_{deep})$	[-]	=	shoaling coefficient between water depths h_t and h_{deep}
$K_S(h_{paddle},h_{deep})$	[-]	=	shoaling coefficient between water depths h_{paddle} and h_{deep}
K_t	[-]	=	transmission coefficient
L	[m]	=	wave lenght of linear wave, defined by the dispersion relationship: $L = \left(gT^2 / 2\pi\right)\tanh\left(2\pi h / L\right)$
L_{deep}	[m]	=	wave lenght of linear wave in deep water, defined by $L_{deep} = gT^2 / 2\pi$
$L_{m-1,0}$	[m]	=	deep water wave length at the toe of the structure, defined by $L_{m-1,0} = gT_{m-1,0}^2 / 2\pi$
$L_{m-1,0,t}$	[m]	=	wave length at the toe of the structure, defined by $L_{m-1,0,t} = \left(gT_{m-1,0}^2 / 2\pi\right)\tanh\left(2\pi h_t / L_{m-1,0,t}\right)$

$L_{m-1,0,paddle}$	[m]	=	wave length at the toe of the structure, defined by $L_{m-1,0,paddle} = \left(gT_{m-1,0}^2 / 2\pi\right)\tanh\left(2\pi h_{paddle} / L_{m-1,0,paddle}\right)$
L_s	[m]	=	length of the slope of the OWEC
m_{-1}	[m²s]	=	first negative moment of the incident wave spectrum
m_0	[m²]	=	zeroth moment of the incident wave spectrum
M_{abs}	[kg]	=	real mass of water inside the reservoir
M_{diff}	[kg]	=	difference between absolute mass of water inside the reservoir at the start of the test and at the end of that test
M_i	[kg]	=	individual overtopping mass, defined by $M_i = V_i \rho B_q$
M_{rel}	[kg]	=	relative mass of water inside the reservoir, including the effect of the pump suspended inside the reservoir
M_{total}	[kg]	=	total absolute mass that enters the reservoir during T_0
N_{mass}	[-]	=	number of masses added to the reservoir when setting up the calibration curve for the reservoir
N_{ow}	[-]	=	number of overtopping waves during a test
N_{pump}	[-]	=	number of pumping events during a test
N_{res}	[-]	=	number of reservoirs of an OWEC
N_{SS}	[-]	=	number of sea states at a particular deployment site
N_{test}	[-]	=	number of tests in a particular subset of the UG10 dataset
N_T	[-]	=	number of wave periods for category of H_j in scatter diagram
N_w	[-]	=	number of incoming waves during a test
$P_{hydr,k,j}$	[kW/m]	=	hydraulic power for a particular reservoir of the OWEC (k) and a particular sea state (j)
$P_{hydr,overall}$	[kW/m]	=	overall hydraulic power, i.e. the sum of hydraulic power over all reservoirs and sea states
$P_{wave,j}$	[kW/m]	=	wave power for a particular sea state defined by $P_{wave,j} = \left(\rho g^2 / 64\pi\right) H_{m0,j}^2 T_{m-1,0,j}$
Pr	[-]	=	probability
P_H	[-]	=	exceedance probability of individual wave heights
P_{ow}	[-]	=	probability of overtopping, defined by $P_{ow} = N_{ow} / N_w$

P_{Ru}	[-]	=	exceedance probability of individual wave run-up heights
P_V	[-]	=	exceedance probability of individual overtopping volumes
q	[m³/s/m]	=	average overtopping rate
q_{max}	[m³/s/m]	=	maximum average overtopping expected for a number of tests
Q_0	[-]	=	coefficient in prediction formula of Owen (1980), Eq. (4.9)
Q_{pump}	[m³/s]	=	pump discharge
r	[-]	=	set-off coefficient Weibull distribution individual overtopping volumes
R_c	[m]	=	crest freeboard height, i.e. the vertical distance between the crest of the structure and the still water level
R_u	[m]	=	wave run-up height
$R_{u2\%}$	[m]	=	wave run-up height exceeded by 2% of the wave run-up heights
RF	[-]	=	reliability factor of a test result of the CLASH database, possible values are 1,2,3 and 4
$s_{m-1,0}$	[-]	=	wave steepness at the toe of the structure defined by $s_{m-1,0} = 2\pi H_{m0} / gT_{m-1,0}^2$
$\hat{s}_{m-1,0}$	[-]	=	sea state average wave steepness
s_m	[-]	=	wave steepness at the toe of the structure defined by $s_m = 2\pi H_s / gT_m^2$
s_p	[-]	=	wave steepness at the toe of the structure defined by $s_p = 2\pi H_s / gT_p^2$
T	[s]	=	wave period of linear wave
$T_{m-1,0}$	[s]	=	spectral incident wave period at the toe of the structure defined by $T_{m-1,0} = m_{-1} / m_0$
T_0	[s]	=	total duration of a test, minus the horizontal parts at the start and end of the test, i.e. the sum of all individual wave periods
T_i	[s]	=	wave period of individual wave in incoming wave train during a test
T_j	[s]	=	characteristic wave period of a characteristic sea state
T_l	[s]	=	characteristic wave period in a scatter diagram

T_m	[s]	=	mean zero-crossing wave period of the incident waves at the toe of the structure
T_p	[s]	=	peak incident wave period at the toe of the structure
$T_{p,i}$	[s]	=	peak wave period of a characteristic sea state
T_{pump}	[s]	=	duration of pumping (no cooling down)
v_d	[-]	=	vertical dimension of lower part of the slope of the AAU08 test set-up
v_u	[-]	=	vertical dimension of upper part of the slope of the AAU08 test set-up
$\overline{V}$	[m³/m]	=	mean individual overtopping volume
V_0	[m³/m]	=	sum of individual overtopping volume
V_i	[m³/m]	=	individual overtopping volume
V_{max}	[m³/m]	=	maximum individual overtopping volume
$V_{res,min}$	[m³]	=	minimum allowable volume of water in the reservoir
$V_{res,max}$	[m³]	=	maximum allowable volume of water in the reservoir
W	[kg]	=	average absolute mass of water transported during T_{pump}, no incoming waves during pumping
x_{hinge}	[m]	=	horizontal dimension of the slope of the OWEC at the seabed
$z_{p/2}$	[-]	=	percentile of the standard normal distribution exceeded by 100% - p/2 percent of the observations
α	[-]	=	characteristic slope angle of the structure in radians
$\alpha_\circ$	[°]	=	characteristic slope angle of the structure in degrees
$\eta_{hydr,j}$	[-]	=	hydraulic efficiency for a particular sea state for an OWEC with a single level reservoir, i.e. the proportion of the hydraulic power and the wave power
$\eta_{hydr,overall}$	[-]	=	overall hydraulic efficiency, i.e. the sum of hydraulic efficiency over all reservoirs and sea states
α_d	[-]	=	slope angle of the structure part below the berm compared to a horizontal
α_{incl}	[-]	=	Mean slope angle of the structure compared to a horizontal, including the width of the berm (CLASH database)
α_u	[-]	=	slope angle of the structure part above the berm compared to a horizontal
β	[°]	=	angle of wave attack

χ	[-]	=	coefficient relating P_{ow} to R_c / H_{m0} (Eq. 8.15)
φ	[-]	=	slope angle of the cumulative absolute mass in time
γ_b	[-]	=	reduction factor taking into account the effect of a berm, varying between 0 (full berm) and 1 (no berm)
γ_f	[-]	=	friction coefficient of a structures, varying between 0 (rough) and 1 (smooth)
γ_v	[-]	=	reduction factor taking into account the effect of a vertical wave wall, equal to 1 without wall
γ_β	[-]	=	reduction factor taking into account the effect of oblique wave attack, equal to 1 for normal wave attack
λ_{dr}	[-]	=	correction coefficient for the draft of the structure by Kofoed (2002)
λ_α	[-]	=	correction coefficient for the slope angle of the structure by Kofoed (2002)
λ_s	[-]	=	correction coefficient for small relative crest freeboards by Kofoed (2002)
μ	[ ]	=	mean of a stochastic variable
ρ	[kg/m³]	=	density of water (1000 kg/m³ for fresh water and 1025 kg/m³ for salt water)
σ	[ ]	=	standard deviation of a stochastic variable
ξ	[-]	=	breaker parameter at the toe of the structure for regular waves, defined by $\xi = \tan\alpha / \sqrt{2\pi H / (gT^2)}$
$\xi_{m-1,0}$	[-]	=	breaker parameter at the toe of the structure, defined by $\xi_{m-1,0} = \tan\alpha / \sqrt{s_{m-1,0}}$
ξ_p	[-]	=	breaker parameter at the toe of the structure, defined by $\xi_p = \tan\alpha / \sqrt{2\pi H_{m0} / (gT_p^2)}$

2 Subscripts

i	=	individual
j	=	(wave height of) sea state
k	=	reservoir
l	=	wave periods in scatter diagram
n	=	index N_{mass}
meas	=	measured
pred	=	predicted
opt	=	maximum hydraulic efficiency for relative crest freeboard, and maximum overtopping rate for slope angle
r	=	index running through the test results of a subset of the UG10 dataset
S&A	=	referring to Seelig and Ahrens (1981)
trad	=	traditional sea defence structures
Z&V	=	referring to Zanuttigh and Van der Meer (2008)

List of Acronyms

AAU08	=	test series carried out during this PhD-research at Aalborg University, Denmark
AWA	=	wave gauge used for active absorption system
CLASH	=	Crest Level Assessment of coastal Structures by full scale monitoring, neural network prediction and Hazard analysis on permissible wave overtopping
CLASH_SL	=	subset of the CLASH database applicable to steep low-crested slopes
DELOS	=	Environmental Design of Low Crested Coastal Defence Structures
JONSWAP	=	Joint North Sea Wave Project
OWEC	=	Overtopping Wave Energy Converter
SSG	=	Seawave Slot-Cone Generator
UG10	=	test series carried out during this PhD-research at Ghent University, Belgium
WD	=	Wave Dragon
WEC	=	Wave Energy Converter
WG	=	wave gauge
S1 to S5	=	scenario 1 to scenario 5

Nederlandse samenvatting – Summary in Dutch

De nadelen verbonden aan fossiele brandstoffen en kernenergie, in het bijzonder de beperkte voorraden en hun negatieve impact op het milieu, staan in schril contrast met de steeds stijgende vraag naar energie. Sinds de jaren '70 zoekt men wereldwijd naar alternatieven voor deze traditionele energiebronnen: de zogenaamde 'hernieuwbare energiebronnen'. De Europese Unie (EU) had in dit proces een voortrekkersrol, omdat het in grote mate afhankelijk is van politiek onstabiele regio's voor de invoer van de fossiele brandstoffen. Ambitieuze doelstellingen werden opgelegd aan elk van de lidstaten met betrekking tot het percentage van de nationale energieconsumptie dat dient afkomstig te zijn van hernieuwbare energiebronnen.

Eén van de pistes die bewandeld wordt in de zoektocht naar hernieuwbare energie is die van golfenergie, i.e. energie afkomstig uit windgolven. De oceanen vormen immers een onuitputbare bron van energie en bestrijken tevens ongeveer 3/4^{e} van het aardoppervlak. Verschillende concepten werden ontwikkeld voor het converteren van golfenergie naar elektriciteit, i.e. de golfenergieconvertoren (GECs). Enkele van deze concepten werden reeds als prototype gebouwd, de meeste bevinden zich echter nog in ontwerpfase. Geen enkel concept heeft tot dusver de fase van commercialisatie bereikt. Dit werd verhinderd door zowel technische als niet-technische barrières. Heel wat onderzoek is dus nog vereist om de GECs verder te optimaliseren.

Het hoofddoel van dit doctoraatsonderzoek is het optimaliseren van een bepaald type GEC, gebaseerd op golfoverslag (OGECs). Bij dit type lopen golven op op een talud dat in zee wordt geplaatst en slaan ze over in een reservoir, waar het water tijdelijk wordt gestockeerd op grotere hoogte dan het gemiddelde waterpeil. Vervolgens loopt het terug naar zee via openingen in de bodem van het reservoir waarin turbines werden geplaatst. Deze turbines wekken de elektriciteit op.

De huidige kennis omtrent OGECs is in grote mate beperkt tot complexe structuren. Een optimalisatie van OGECs vereist een **fundamentele studie van de relatie tussen de geometrie van de OGEC, de golfkarakteristieken en de hoeveelheid golfoverslag**, en dit voor OGECs met een eenvoudige geometrie. In dit doctoraatsonderzoek werd het overslaggedrag van **vaste** (niet-drijvende) **structuren met één reservoir** bestudeerd. Dit gedrag wordt volledig bepaald door de hellingshoek, vrijboord (verticale afstand tussen de kruin van de structuur en het gemiddelde waterpeil), karakteristieke golfhoogte en –periode.

Uit de literatuur blijkt dat het geproduceerde vermogen van OGECs kan stijgen indien de controlestrategie van de turbines wordt aangepast aan de grootte van de overslagvolumes. Kennis over de **kansverdeling van de individuele (golf per golf) overslagvolumes** draagt bij tot het opstellen van dergelijke controlestrategie. In dit doctoraatsonderzoek werd daarom tevens deze kansverdeling bestudeerd voor de OGECs met een eenvoudige geometrie.

Beide aspecten, met name het overslaggedrag en de kansverdeling van vaste structuren met één reservoir, werden bestudeerd door middel van een **experimentele studie**. Daartoe werd een testopstelling ontwikkeld die in staat is om grote overslagvolumes accuraat te meten. Het is de eerste keer dat dergelijke testopstelling werd toegepast. Deze opstelling is gebaseerd op de weegschaaltechniek, waarbij de overslagvolumes worden opgevangen in een reservoir en een weegschaal continu de massa van het reservoir en de waterinhoud registreert. De individuele overslagvolumes worden uit het weegschaalsignaal afgeleid.

Zowel structurele aanpassingen als een meer verfijnde data-analyse werden uitgevoerd t.o.v. de klassiek toegepaste weegschaaltechniek. Door de grote overslagvolumes die het reservoir vullen werd een pomp in het reservoir geplaatst die het water tijdens een proef terug naar de golfgoot transporteert. De vele pompbeurten vereisen een accurate compensatie voor de aanwezigheid van de pomp in het reservoir (callibratiecurve) en voor het pompen. De nauwkeurigheid van de meettechniek wordt dus bepaald door de accuraatheid van de callibratiecurve van het reservoir tussen twee pompbeurten, en door de nauwkeurigheid van het compenseren voor pompen tijdens een pompbeurt.

Testen met een breed bereik aan hellingshoek, relatieve vrijboord (verhouding van vrijboord tot karakteristieke golfhoogte) en golfsteilheid (verhouding van golfhoogte tot golflengte) werden uitgevoerd. Hierdoor zijn de experimentele resultaten niet enkel toepasbaar voor OGECs, maar meer algemeen voor steile laagkruinige hellingen. Voor elke experimentele proef werden het gemiddelde overslagdebiet, de reflectiecoëfficiënt en de individuele overslagvolumes bepaald. De testmatrix werd dusdanig opgebouwd dat de effecten van de hellingshoek, relatieve vrijboord en golfperiode (en hun interacties) op deze drie outputgegevens konden worden bestudeerd.

Eerst werd de **relatie tussen de geometrie, golfkarakteristieken en het gemiddeld overslagdebiet** onderzocht. Gemeten overslagdebieten werden daarbij vergeleken met overslagdebieten berekend door middel van courante voorspellingsmethodes uit de literatuur (empirische formules en een neuraal netwerk). Daaruit blijkt dat de hellingshoek en relatieve vrijboord de twee dominante parameters zijn voor het overslagdebiet van steile laagkruinige hellingen. Een toename in relatieve vrijboord veroorzaakt een daling van het gemiddelde

overslagdebiet, die minder scherp is voor kleinere relatieve vrijboorden. Daarnaast is er een relatief zwak effect van de hellingshoek voor minder steile hellingen – waarbij een maximum overslagdebiet wordt bereikt – en een significante daling in het gemiddeld overslagdebiet voor toenemende hellingshoek bij steile hellingen. Naarmate de relatieve vrijboord toeneemt, wordt ook het effect van de hellingshoek groter. Het effect van de golfperiode is relatief klein, maar uit zich in een afhankelijkheid van de optimale hellingshoek (die aanleiding geeft tot het maximale overslagdebiet) van de golfperiode. Uit de grafische vergelijking bleek dat geen van de beschikbare voorspellingsmethodes in staat is om al deze effecten nauwkeurig te voorspellen. Daarom werd een nieuwe set empirische formules afgeleid op basis van de experimentele resultaten. In vergelijking met het neuraal netwerk biedt dit het voordeel dat de formule fysisch inzicht verschaft in de effecten van de bepalende parameters en hun interacties. De betrouwbaarheid van deze nieuwe formules werd besproken. Aan de hand van enkele grafische voorbeelden werd de geldigheid van de formules aangetoond.

Ten tweede werd de **relatie tussen de geometrie, golfkarakteristieken en het reflectiegedrag van steile laagkruinige hellingen** bestudeerd. De reflectiecoëfficiënten werden bepaald door middel van drie golfhoogtemeters die net vóór de helling gepositioneerd waren. De reflectiecoëfficiënten bestreken een breed interval voor de uitgevoerde testen (0.3 tot iets kleiner dan 1.0). Beschikbare voorspellingsformules voor de reflectiecoëfficiënten maken een onderscheid tussen twee types structuren: zonder golfoverslag en met golfoverslag. De formules voor het eerste type structuren zijn enkel functie van de hellingshoek en golfkarakteristieken. Voor de structuren met golfoverslag wordt een reductiefactor toegepast die functie is van de relatieve vrijboord. Deze methodiek werd nog nooit eerder toegepast op niet-poreuze structuren met golfoverslag. De gemeten reflectiecoëfficiënten werden vergeleken met waarden voorspeld d.m.v. de beschikbare voorspellingsformules. Op basis van deze vergelijking werd een nieuwe voorspellingsformule samengesteld, bestaande uit een formule voor niet-poreuze structuren zonder golfoverslag en een reductiefactor (beide afkomstig uit de literatuur). Verder werd ook nog de link gelegd tussen de reflectiecoëfficiënt en het gemiddelde overslagdebiet aan de hand van de energiebalans.

De tot dan toe verworven kennis m.b.t. het gemiddelde overslagdebiet en de reflectiecoëfficiënt werden vervolgens toegepast voor het vinden van de **optimale geometrie en de bijhorende reflectiecoëfficiënt**. De optimale geometrie is gerelateerd aan de maximalisatie van de totale hydraulische efficiëntie, berekend als de verhouding van het totale hydraulisch vermogen tot het totale golfvermogen (totaal slaat hier op de som voor alle bepalende sets van golfkarakteristieken). Het hydraulisch vermogen voor zekere golfkarakteristieken is functie van het product van

het gemiddelde overslagdebiet (voorspeld d.m.v. de nieuw afgeleide empirische formules) en de vrijboord. Een maximalisatie van dit product werd mathematisch opgelegd, waaruit de voorwaarden voor de optimale hellingshoek en relatieve vrijboord volgden. Tevens werd de bijhorende reflectiecoëfficiënt K_r bepaald (K_r = 0.57). Het hanteren van deze geometrie voor elke bepalende set van golfkarakteristieken (adaptieve geometrie), i.e. de optimale geometrie, leidt tot maximale waarden voor het totaal hydraulisch vermogen en de totale hydraulische efficiëntie. Dit scenario is echter praktisch niet eenvoudig realiseerbaar. Daarom werden nog drie andere scenario's beschouwd, met ofwel een adaptieve hellingshoek, adaptieve vrijboord of een vaste geometrie. Een vijfde scenario realiseert een adaptieve vrijboord d.m.v. een draaipunt aan de bodem van de helling, waardoor een gecombineerd effect met de hellingshoek ontstaat. De totale hydraulische efficiëntie, het totale hydraulisch vermogen en de reflectiecoëfficiënt werden bepaald voor de vijf scenario's op drie hypothetische locaties. Daaruit bleek dat een adaptieve hellingshoek slechts een relatief klein effect heeft op het geleverd vermogen. Anderzijds leidt een adaptieve vrijboord tot een aanzienlijke toename in de totale hydraulische efficiëntie en het totaal hydraulisch vermogen in vergelijking met het scenario met de vaste geometrie. Het vijfde scenario (met draaipunt aan bodem van de helling) is het meest realistische scenario. T.o.v. een vaste geometrie geeft dit scenario een toename van 10% hydraulisch vermogen. De totale reflectiecoëfficiënt (bepaald door golfkarakteristieken met grootste voorkomingfrequenties) varieert tussen 0.57 en 0.80. De scenario's met minder geometrische vrijheidsgraden resulteren in grotere reflectiecoëfficiënten.

Als laatste onderdeel van dit doctoraatsonderzoek werd de **kansverdeling van de individuele overslagvolumes van steile laagkruinige hellingen** onderzocht. Voor kustverdedigingsstructuren volgen deze volumes typisch een Weibull verdeling met een vormfactor 0.75. Voor dijken met een negatieve vrijboord werd vastgesteld dat de vormfactor grotere waarden aanneemt (1.0 à 3.5). Op basis van de gemeten overslagvolumes voor steile laagkruinige hellingen werd aangetoond dat deze eveneens een Weibull verdeling volgen. Daarenboven blijkt de vormfactor in grote mate afhankelijk te zijn van de relatieve vrijboord en van de hellingshoek. Voor hogere vrijboorden werd de gemiddelde waarde van 0.75 bevestigd, terwijl vormfactoren tot 1.5 werden vastgesteld voor lagere vrijboorden (tussen die van kustverdedigingstructuren en dijken met een negatieve vrijboord). Een grotere waarde van de vormfactor gaat gepaard met kleinere waarden van de grootste volumes. Verder veroorzaakt een daling in hellingshoek een lineaire toename van de vormfactor. De kans op overslag, die een belangrijke rol speelt in de schaalfactor van de Weibull verdeling, is ook hoofdzakelijk afhankelijk van de relatieve vrijboord en de hellingshoek. Het effect van de relatieve vrijboord op de kans op overslag wordt beschreven door een Rayleigh verdeling van de relatieve vrijboord. Een stijging van

de hellingshoek veroorzaakt een daling van de kans op overslag, volgens een lineaire functie van de cotangens van de hellingshoek. Twee formules die de vormfactor en kans op overslag uitdrukken in functie van de hellinghoek en relatieve vrijboord zijn afgeleid. De verworven kennis m.b.t. de kansverdeling van de individuele overslagvolumes kan worden gebruikt voor de simulatie van overslagvolumes voor OGECs en voor kustverdedigingstructuren met een lage vrijboord in stormcondities.

English summary

The drawbacks of fossil fuels and nuclear power - in particular the limited resources and the negative effects for the environment - are in contrast to the increasing energy demand. Since the seventies, there is a global search for alternative sources of energy, i.e. the renewable energy sources. The European Union (EU) has played an important role in this process, since large part of its fossil fuels is imported from politically unstable regions. Ambitious targets were imposed by the EU to its members concerning the contribution of renewable energy sources to their national energy consumption.

Wave energy, i.e. energy from ocean waves, is a promising source of renewable energy. The oceans are a vast source of energy and cover approximately 3/4th of the global surface. Different concepts have been developed to convert the energy from the waves into electricity, i.e. the wave energy converters (WECs). A number of these concepts were built as a prototype, while most concepts are still in the design phase. So far, no concept has reached the commercialization phase. This has been prevented by both technical and non-technical barriers. Hence, additional research is required to further optimize the WECs.

The main goal of this PhD-research is to optimize a particular type of WEC, based on wave overtopping (OWECs). This type is based on waves running up a slope and overtopping into a reservoir. The water is stored temporary in the reservoir at a higher level than mean water level, before it flows back to the ocean through a set of turbines installed at the bottom of the reservoir. These turbines are responsible for generating the electricity.

The state-of-the-art knowledge on OWECs is mainly limited to concepts with a rather complex geometry. An optimization of OWECs requires a **fundamental study on the relationship between the geometry of the OWEC, the wave characteristics and the amount of wave overtopping**, for an OWEC with a simplified geometry. The overtopping behaviour of **fixed (non-floating) structures with a single level reservoir** is studied in this PhD-research. This behaviour is fully determined by the slope angle, freeboard (vertical distance between the crest of the structure and the mean water level), the characteristic wave height and wave period.

Previous studies on OWECs also conclude that the produced power of OWECs can be increased by adapting the control strategy of the turbines to the size of the overtopping volumes. Knowledge on the probability distribution of the individual (wave-by-wave) overtopping volumes contributes to formulating such control

strategy. Therefore, this probability distribution is studied in this PhD-research for OWECs with a simplified geometry.

Both aspects, i.e. the overtopping behaviour and the probability distribution of fixed structures with a single reservoir, are investigated based on an **experimental study**. A test set-up is developed that is able to measure large overtopping volumes accurately. This test set-up is applied for the first time here. It is based on the weigh cell technique: the overtopping volumes are collected in a reservoir positioned on top of a weigh cell that measures the mass of the reservoir and its water content continuously. The individual overtopping volumes are derived based on the weigh cell signal.

Both structural adaptations and a more detailed data analysis are applied to the traditional weigh cell technique. Due to the large overtopping volumes entering the reservoir, a pump is installed in the reservoir to transport water from the reservoir to the wave flume during a test. The large number of pumping events requires an accurate compensation for the presence of the pump inside the reservoir (calibration curve) and for pumping. The accuracy of the measurement technique is determined by the accuracy of the calibration curve of the reservoir (in between two pumping events) and by the accuracy of the compensation for pumping (during a pumping event).

Tests with broad ranges of slope angle, relative crest freeboard (ratio of crest freeboard and characteristic wave height) and wave steepness (ratio of wave height and wave length) are carried out. Hence, the test results are not only valid for OWECs, but more in general for steep low-crested slopes. The average overtopping rate, reflection coefficient and the individual overtopping volumes are determined for each experimental test. The test matrix is particularly designed to investigate the effects of the slope angle, relative crest freeboard and wave period (and their interactions) on those three output data.

First, the **relationship between the geometry, wave characteristics and the average overtopping rate** is investigated. Measured overtopping rates are compared with average overtopping rates predicted by commonly used prediction models from literature (empirical formulae and a neural network tool). It appears that the slope angle and relative crest freeboard are the dominating parameters for the average overtopping rate of steep low-crested slopes. An increase in the relative crest freeboard causes a decrease in the average overtopping rate, which is less explicit for smaller relative crest freeboards. Furthermore, the effect of the slope angle is relatively weak for milder slopes – although a maximum average overtopping rate is reached, while it is more explicit for steeper slopes: there is a significant decrease in average overtopping rate towards vertical walls. The effect of the slope angle is larger for larger relative crest freeboards. The effect of the wave period is relatively

small; it corresponds to a dependency of the optimal slope angle (resulting in the maximum average overtopping rate) on the wave period.

The comparison with the predicted average overtopping rates shows that none of the existing prediction models is able to predict all of these effects accurately. Therefore, a set of new prediction formulae is derived based on the experimental test results. Compared to the neural network, an empirical formula allows to gain physical insight in the effects of the governing parameters and their interactions based on its expression. The reliability of the set of new formulae is discussed. A number of graphical examples confirm the validity of the new formulae.

Secondly, the **relation between the geometry, wave characteristics and the reflective behaviour of steep low-crested slopes** is studied. The reflection coefficients are determined based on the signals of three wave gauges positioned in front of the slope. The reflection coefficients cover a broad range for the experiments (0.3 up to almost 1.0). Existing prediction formulae for the reflection coefficients exist for both structures without wave overtopping and structures with wave overtopping. The formulae for the first type of structures are only a function of the slope angle and the wave characteristics. A reduction factor, which is a function of the relative crest freeboard, is applied for the structures with overtopping. This methodology has not yet been applied to overtopped non-porous structures before.

The measured reflection coefficients are compared to values predicted by the existing prediction formulae. Based on this comparison, a new prediction formula is derived, composed of a formula for non-porous structures without wave overtopping and a reduction factor (both found in literature).

Furthermore, the relationship between the reflection coefficient and the average overtopping rate is also discussed, based on the energy balance equation.

The acquired knowledge on the average overtopping rate and the reflection coefficient is successively applied to find the **optimal geometry and the corresponding reflection coefficient**. The optimal geometry is determined by the maximisation of the overall hydraulic efficiency, i.e. the ratio of the overall hydraulic power and the overall wave power (overall means summed over all characteristic sea states). The hydraulic power for a specific sea state is a function of the product of the average overtopping rate (predicted by the set of new prediction formulae) and the crest freeboard. Expressing the maximisation of this product mathematically results in the conditions for the optimal slope angle and relative crest freeboard. The corresponding reflection coefficient K_r equals 0.57.

The maximal overall hydraulic power and efficiency are reached when applying this geometry for each characteristic sea state (geometry control), i.e. the optimal geometry. However, this scenario is not easily realizable. Therefore, three other scenarios are considered: applying only an adaptive slope angle, an adaptive crest

freeboard or a fixed geometry. A fifth scenario realizes the adaptive crest freeboard by using a hinge at the bottom of the slope, resulting in a combined effect with the slope angle.

The overall hydraulic efficiency, overall hydraulic power and reflection coefficient are determined for the five scenarios at three hypothetical deployment sites. Based on these simulations, the effect of an adaptive slope angle on the power output is relatively small. On the other hand, an adaptive crest freeboard considerably increases the overall hydraulic efficiency and power compared to the fixed geometry. The fifth scenario (hinge at the bottom of the slope) is the most realistic scenario. Compared to a fixed geometry, its overall hydraulic power is increased by approximately 10 %.

The overall reflection coefficient (which represents the sea states with the largest frequencies of occurrence) varies between 0.57 and 0.80. It increases when the geometry is more fixed.

The **probability distribution of the individual overtopping volumes of steep low-crested slopes** is investigated in the last part of this PhD-research. The individual overtopping volumes of sea defence structures typically follow a Weibull distribution with a shape factor of 0.75. On the other hand, dikes with a negative crest freeboard correspond to a larger shape factor (1.0 to 3.5).

Based on the measured overtopping volumes for the steep low-crested slopes, it appears that these volumes also follow a Weibull distribution. Furthermore, the shape factor is mainly dependent on the relative crest freeboard and the slope angle. An average shape factor of 0.75 is found for the larger relative crest freeboards, while shape factors up to 1.5 are identified for smaller relative crest freeboards (in between those of sea defence structures and dikes with a negative crest freeboard). A larger value of the shape factor corresponds to smaller values of the largest overtopping volumes. Furthermore, the shape factor linearly increases for a decreasing slope angle.

The probability of overtopping, which plays an important role for the scale factor of the Weibull distribution, is also mainly dependent on the relative crest freeboard and the slope angle. The effect of the relative crest freeboard is according to a Rayleigh distribution. An increase in slope angle decreases the probability of overtopping, expressed by a linear function of the cotangent of the slope angle.

Two formulae are derived which take into account the observed effects of the slope angle and relative crest freeboard on the shape factor and probability of overtopping.

The knowledge acquired on the probability distribution of the individual overtopping volumes can be used for simulating the overtopping volumes of OWECs and of sea defence structures with a small relative crest freeboard in severe storm conditions.

1

Problem statement

1.1 Framework

1.1.1 Introduction

The general framework for this PhD-research is the global search for competitive and reliable sources of renewable energy. Due to the limited availability of fossil fuels, the dependency of many countries on imports of fossil fuels from politically unstable countries, the negative effects of fossil fuels regarding climate change, the negative impact of nuclear waste and the rapidly increasing energy demand, research on renewable energy has gained importance worldwide since the late nineties. Accordingly, a large number of nations have set ambitious goals for the contributions of renewable energy sources to their energy production in the near future. Europe has played a world-leading role in the renewable energy policy from the early start. Recently, the European Commission endorsed the ambitious target to raise the share of renewable energies in the final energy consumption[1] of the 27 countries in the European Union from 8.5% in 2005 to 20 % by 2020 (COM 2007). In 2008, that share has been increased up to 10.3 % (EEP 2011). For the particular case of Belgium, the share of renewable energy in its final energy consumption has increased from 2.2 % in 2005 up to 3.3% in 2008, with a final goal of 13 % in 2020.

Among the renewable energy sources, hydropower, wind energy, biomass and solar power have been studied thoroughly and therefore have been exploited for a

[1] Final energy consumption = energy consumed by households, industry, services, agriculture and transport sector.

relatively long period of time. Hence, these sources significantly contribute to the increase in the share of renewable energy in the final energy consumption of the 27 countries of the European Union (EC 2011).

On the other hand, wave energy - i.e. energy extracted from ocean waves - is not yet economically competitive. However, its potential is comparable to those of hydropower and wind energy:

- the global wave power potential is estimated to be 2 TW, i.e. the same order of magnitude as the world's electricity consumption (Cruz 2008). The waves that reach the European coastlines contain a large amount of energy. The annual average deep water resource along the Atlantic and Mediterranean coasts of Europe is approximately 320 GW (Pontes et al. 1998);

- the energy density in waves is larger than it is in wind. As winds blow over the oceans, energy is transferred to the water and waves are generated. The wind energy is stored in the water near the free surface;

- waves travel over thousands of kilometres with a very limited loss of energy.

Extensive research is required, both fundamental and applied, to improve the performance and reliability of wave energy conversion techniques and thus the competitiveness of wave energy on the global energy market (Brooke 2003).

A wide variety of wave energy converters (abbreviated WECs), with development stages ranging from concept to prototypes at sea, has been identified (Waveplam 2009). This PhD-manuscript focuses on one particular type of WECs: overtopping wave energy converters (abbreviated OWECs). The following two sections 1.1.2 and 1.1.3 give more detailed information on the principle and the geometry of OWECs.

1.1.2 Principle of overtopping wave energy converters (OWECs)

The working principle of OWECs is based on waves running up a slope and overtopping into a reservoir, which is emptied into the ocean through a set of low-head turbines (Kofoed 2002). In terms of energy, OWECs convert kinetic and potential energy of the waves into potential energy (water storage in the reservoir), which is then converted into electricity by the low-head turbines.

In the past two decades, extensive research has been carried out in relation to two specific OWEC concepts: the Wave Dragon (abbreviated WD) which has been

developed in Denmark, and the Norwegian concept Seawave Slot-Cone Generator (abbreviated SSG).

The WD is a floating OWEC with a single reservoir and a double-curved ramp (Tedd and Kofoed 2009). Its floating level is regulated through air cells beneath the reservoir, in order to achieve optimal energy absorption for different wave characteristics. A concept sketch of the WD is shown in Fig. 1.1.

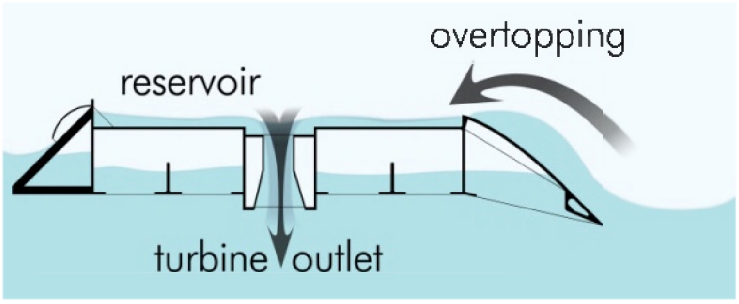

Fig. 1.1: Concept sketch of the Wave Dragon overtopping wave energy converter (Kofoed et al. 2000).

After a prove of concept and extensive small scale testing in the laboratory at the Department of Civil Engineering of Aalborg University (Denmark), a prototype with an installed power of 20 kW has been tested since 2003 in Nissum Bredning, an inland sea of Northern Denmark. Over 20.000 hours of data have been gathered for the prototype, resulting in an increased knowledge on the performance of the moorings and the hydro-turbines, the global performance in storms, the control of the WD, and the power production (Tedd 2007). A WD with an installed power of 7 MW is expected to be deployed in the Irish Sea near Pembrokeshire, Wales (UK) in the near future. The launch of this device has been postponed due to the recent financial crisis (Friis-Madsen 2011).

The SSG is a multi-level OWEC, which is primarily designed to be deployed in (non-floating) sea defence structures. The SSG achieves optimal energy absorption for different wave characteristics by using three reservoirs – one on top of the other (Fig. 1.2). This particular geometry allows the overtopped water to be collected on different levels for a broad range of waves: larger waves fill up all three reservoirs, while smaller waves overtop into the lowest reservoir. This results in a considerable

increase in efficiency. The average wave-to-wire efficiency[2] for the WD is expected to be 18 % (Tedd 2007), while this efficiency is expected to be 25 % to 35 % for the SSG (Margheritini et al. 2009a).

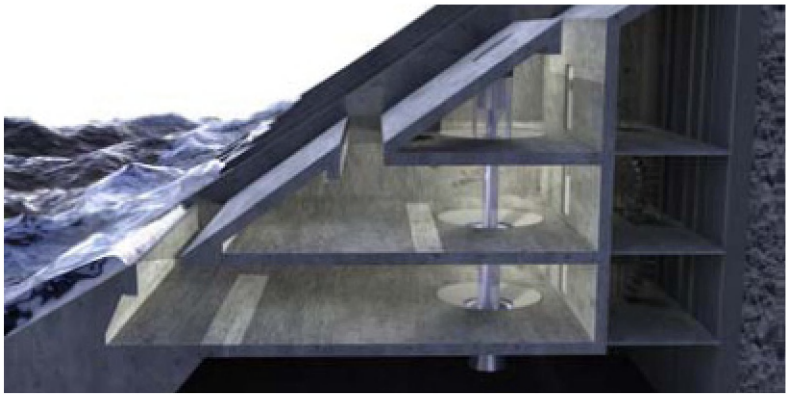

Fig. 1.2: Artist impression of the Seawave Slot-Cone Generator overtopping wave energy converter (Margheritini et al. 2009a).

The overtopping performance, structural response, reflection performance and efficiency of the SSG built in a sea defence structure have been studied to a large extent by Margheritini (2009). Plans for installing prototypes of the SSG are in progress for the outer harbour of the port of Hanstholm (Denmark) and for a jetty reconstruction project at the port of Garibaldi (Oregon, USA).

Wave energy converters built in sea defence structures tend to be more economically viable than offshore floating WECs (Graw 1996). Although offshore floating WECs are located in more energetic seas, leading to a larger energy production, their installation and maintenance costs are expected to be rather high. These costs are lower for WECs built in sea defence structures due to increased accessibility.

Furthermore, the crest level of many sea defence structures needs to be increased due to the rising global mean sea water level caused by global warming. According to the Intergovernmental Panel on Climate Change (IPCC), the global mean sea water level has increased with an average rate of about 3.1 mm per year from 1993 to 2003 and will continue to increase each year, associated with a change in wave

[2] Wave-to-wire efficiency = ratio of wave power and electric power output to the power grid.

climate (IPCC 2007). The required increase in crest level for many sea defence structures provides the opportunity to install WECs in sea defence structures with shared costs.

These arguments are in favour of the application of OWECs in a sea defence structure.

1.1.3 Geometry of OWECs

It is clear that the geometry of an OWEC has a major effect on the amount of wave energy that is captured, as illustrated by the variable floating level of the WD and the three-level geometry of the SSG.

The geometry of sea defence structures, such as mildly sloping dikes, vertical walls and rubble mound breakwaters, on the other hand is particularly suitable to limit wave overtopping. The slopes of smooth impermeable sea defence structures either dissipate a large amount of the wave energy by wave breaking on mildly sloping dikes or reflect a large part of that energy for vertical walls. Furthermore, sea defence structures typically feature high relative crest freeboards expressed as R_c / H_{m0}, where R_c is the freeboard (height) of the structure – i.e. the vertical distance between the crest of the structure and the still water level, and H_{m0} is the spectral estimate of the incoming significant wave height at the toe of the structure. An increased roughness or permeability, berms or vertical walls decrease the wave overtopping at mildly sloping dikes even more. Recurve walls introduce a similar effect for vertical walls. A rubble mound breakwater is a special case of a very rough and permeable mildly sloping dike.

The geometry of the slope profile of OWECs is designed to maximize the amount of water overtopping the crest of the slope. This amount is traditionally defined by the average overtopping rate per meter crest width q [m³/s/m]. Hence, a completely opposite way of thinking is required for the design of OWECs compared to sea defence structures. Based on the features of sea defence structures mentioned above, it is clear that OWECs should feature smooth impermeable slopes with slope angles α [-] in between those of mildly sloping dikes (for example $\cot\alpha = 6.0$) and vertical walls ($\cot\alpha = 0.0$) (Fig. 1.3).

Kofoed (2002) proposed a slope of 1:1.73 for floating OWECs located in the Danish North Sea featuring a single reservoir and a linear slope, shown in Fig. 1.3 for OWECs. A different slope, $\cot\alpha = 1.43$, is proposed for the three levels of the SSG (Margheritini et al. 2009a), also located in the Danish North Sea.

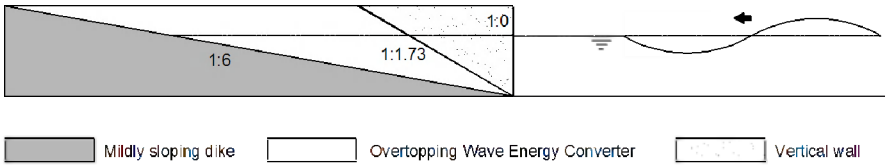

Fig. 1.3: Comparison between slope angles typical for sea defence structures and slope angles for OWECs.

The fact that OWECs feature steep slopes compared to mildly sloping dikes is also explained based on the type of wave breaking, which is determined by the slope angle of the structure α and the wave steepness (Battjes 1974). Both parameters are combined in the breaker parameter $\xi_{m-1,0}$ [-] (Eq. 1.1), which is also referred to as the surf similarity or Irribarren number in literature. The wave steepness $s_{m-1,0}$ [-] in Eq. (1.1) is defined as the ratio of the wave height H_{m0} and the deep water[3] wave length $L_{m-1,0} = gT_{m-1,0}^2 / 2\pi$ (Eq. 1.2), in which g [m/s²] is the acceleration due to gravity (9.81 m/s²) and $T_{m-1,0} = m_{-1} / m_0$ [s] is the spectral wave period at the toe of the structure (m_{-1} is the first negative moment of the spectrum, m_0 is the zeroth moment of the spectrum).

$$\xi_{m-1,0} = \frac{\tan\alpha}{\sqrt{s_{m-1,0}}} \tag{1.1}$$

$$s_{m-1,0} = \frac{2\pi H_{m0}}{g T_{m-1,0}^2} \tag{1.2}$$

According to EurOtop (2007), waves are considered to be breaking on slopes for $\xi_{m-1,0} < 2.0$ - 3.0, ranging from collapsing waves, over plunging waves to spilling waves for decreasing values of the breaker parameter (Fig. 1.4). On the other hand, waves are considered to be non-breaking (surging waves) for $\xi_{m-1,0} > 2.0$ - 3.0. Since wave breaking means energy loss for OWECs, the slopes of the structures should be

[3] Deep water: $h_{deep} / L_{m-1,0,j} > 0.5$ (Dean and Dalrymple 1991) (h_{deep} [m] is the water depth in deep water).

sufficiently steep for the condition $\xi_{m-1,0} > 2.0$ - 3.0 to be fulfilled. This justifies the choice for rather steep slopes of OWECs (e.g. for the WD and the SSG).

Note that the steepest waves may still break although the waves are categorized as non-breaking waves for a particular slope angle.

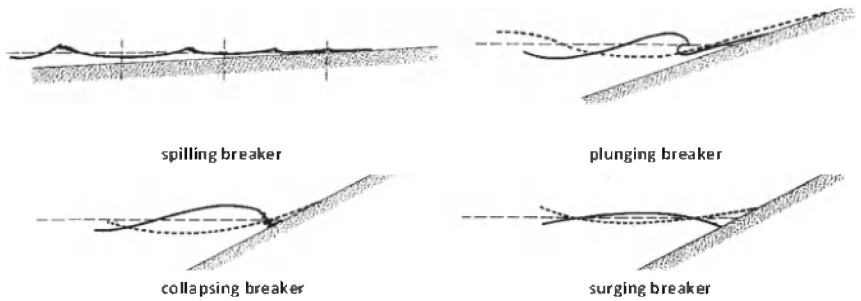

Fig. 1.4: Types of wave breaking (Battjes 1974).

A second important feature for OWECs is the relative crest freeboard R_c / H_{m0}. OWECs with a single reservoir typically feature a low relative crest freeboard, in order to allow large amounts of water to overtop the crest of the OWEC. More in general, the vertical position of the crest(s) of the reservoir(s) of an OWEC is determined based on the maximization of the overall hydraulic efficiency $\eta_{hydr,overall}$ [-], i.e. the ratio of the power of the water overtopping the crest(s) of the reservoir(s) (i.e. the hydraulic power) and the available wave power, summed over all reservoirs (number of reservoirs N_{res} [-]) and all sea states[4] (number of sea states N_{SS} [-]) occurring at the deployment site of the OWEC. The hydraulic power $P_{hydr,k,j}$ [kW/m] of the water overtopping a particular reservoir (indicated by the subscript *k*) with crest freeboard $R_{c,k}$ for a particular sea state (subscript *j*) is defined by:

$$P_{hydr,k,j} = \rho g \, q_{k,j} \, R_{c,k} \tag{1.3}$$

[4] A sea state refers to a particular wave condition with a characteristic wave height and a characteristic wave period.

where ρ [kg/m³] is the density of water (1025 kg/m³ for sea water and 1000 kg/m³ for fresh water in laboratory) and $q_{k,j}$ [m³/s/m] is the average overtopping rate per meter crest width for reservoir k and sea state j.

The expression for the wave power $P_{wave,j}$ [kW/m] for a particular sea state is given in Eq. (1.4), assuming deep water waves.

$$P_{wave,j} = \frac{\rho g^2}{64\pi} H_{m0,j}^2 T_{m-1,0,j} \tag{1.4}$$

Eq. (1.3) and Eq. (1.4) determine the expression for the overall hydraulic efficiency $\eta_{hydr,overall}$ (Eq. 1.5), taking into account the frequency of occurrence FO_j [%] for each sea state.

$$\eta_{hydr,overall} = \frac{\sum_{j=1}^{N_{SS}} \sum_{k=1}^{N_{RES}} \rho g \, q_{k,j} \, R_{c,k} \, FO_j}{\sum_{j=1}^{N_{SS}} \frac{\rho g^2}{64\pi} H_{m0,j}^2 \, T_{m-1,0,j} \, FO_j} \tag{1.5}$$

The crest freeboards of the three reservoirs of the SSG are determined by numerical simulations based on the expression for the vertical distribution of overtopping determined by Kofoed et al. (2002) and on Eq. (1.5).

As a result of the discussion given above (section 1.1.3), the typical basic geometry of OWECs is characterized by smooth impermeable steep low-crested slopes.

1.2 Objectives

This PhD-research aims at optimizing the performance of overtopping wave energy converters. The four main research objectives are outlined below:

1. *Detailed study of relationship between OWEC geometry, wave characteristics and wave overtopping*

As mentioned in section 1.1.3, Kofoed (2002) found an optimal slope of 1:1.73 and an optimal crest freeboard based on $R_{c,1}/h_t = 0.10$ for floating OWECs with a single

reservoir deployed in the Danish part of the North Sea. Those optimal values are based on a maximization of the overall hydraulic efficiency $\eta_{hydr,overall}$ for five sea states occurring at a particular location in the Danish North Sea (Point 3, Meyer 2002), which all correspond to a nearly constant wave steepness $s_{m-1,0} \approx 0.033$. Hence, it is unclear whether the optimal values of the slope and relative crest freeboard according to Kofoed (2002) also result in a maximum overall hydraulic efficiency for other deployment sites, with different values of the wave steepness (for each sea state).

In order to optimize the performance of OWECs for other deployment sites, a detailed study of their wave overtopping behaviour for different geometrical and wave characteristics is required. The first objective of this PhD-research is to obtain a relationship between wave overtopping, geometrical parameters and wave characteristics for OWECs.

2. *Detailed study of the relationship between OWEC geometry, wave characteristics and wave reflection*

The reflection of OWECs should be low for a number of reasons. First, when large part of the wave energy is reflected by the OWEC, less kinetic energy of the waves is converted into potential energy. Second, when a structure exhibits high reflection coefficients scour is induced at the toe of the structure, progressively decreasing the stability of the structure. Eventually, this may result in failure due to scour. Finally, when applied in outer harbour sea defence structures, the reflection coefficients of OWECs should be rather low, in order to allow ships to enter the harbour in all wave conditions.

A detailed study on the effects of the geometrical and wave characteristics on the reflection coefficient of OWECs is required. Hence the second objective of this PhD-research is to determine a relationship between wave reflection, geometrical parameters and wave characteristics for OWECs.

3. *Case study on "adaptive geometry" for OWECs*

Typically, the fixed geometry of an OWEC is determined by the maximization of the overall hydraulic efficiency (Eq. 1.5). A maximization of the hydraulic efficiency for each sea state requires an adaptation of the geometrical parameters to each sea state, i.e. the concept of an *adaptive geometry* control strategy. The third objective of this PhD-research is to investigate whether an adaptive geometry significantly increases the overall hydraulic efficiency and obtained hydraulic power compared to a fixed geometry. Furthermore, a study on the effect of an adaptive geometry on the reflection coefficient is required.

The knowledge acquired from the first two objectives can be used to carry out this feasibility study.

4. *Detailed study on the distribution of the wave-by-wave overtopping volumes for OWECs*

The design of the reservoir of an OWEC and the control strategy of its turbines are strongly determined by the amount of water overtopping its crest wave-by-wave. In theory, the reservoir should be filled up to its crest at all times to maintain the largest possible hydraulic head over the turbines. However, in practice spill of water out of the reservoir occurs, since the wave-by-wave overtopping volumes entering the reservoir are unknown (Tedd 2007). The fourth objective of this PhD-research is to improve the knowledge on the distribution of the wave-by-wave overtopping volumes per meter crest width V_i [m³/m] for OWECs, and to study the effects of the geometrical and wave characteristics on that distribution.

1.3 Structures under study

Both WD and SSG have a rather complex geometry and exhibit complex control strategies. Therefore, the objectives for this PhD-research (section 1.2) are not investigated specifically for these particular OWECs. Instead, OWECs with a more simplified design are considered, consisting of a single reservoir and a *simple slope profile*, installed in a sea defence structure due to the corresponding advantages mentioned in section 1.1.2. Consequently, an economically viable OWEC with a more easily predictable overtopping performance should be achieved.

The simple slope profile features a steep characteristic slope, situated in between mildly sloping dikes and vertical walls resulting in non-breaking waves, and a low relative crest freeboard R_c / H_{m0}, in accordance with section 1.1.3. According to EurOtop (2007), gentle slopes have roughly $\cot\alpha \geq 2.0$. This explains the requirements for the characteristic slopes of the structures studied in this PhD-research in Eq. (1.6).

$$0.0 < \cot\alpha \leq 2.0 \tag{1.6}$$

The requirement for non-breaking waves is given in Eq. (1.7). It is important to note that the relatively large values of the breaker parameter are assumed to be caused by the steep slope (Fig. 1.3), not by small values of the wave steepness related to heavy broken waves due to the limited water depth (Van Gent 2001). Accordingly, the structures considered in this PhD-research are located in relatively deep water.

The corresponding relative toe depth h_t / H_{m0} is assumed to be larger than 2.0 (Eq. 1.8) to avoid heavy depth-induced breaking.

$$\xi_{m-1,0} > 2.0 \text{ - } 3.0 \tag{1.7}$$

$$\frac{h_t}{H_{m0}} > 2.0 \tag{1.8}$$

Furthermore, low vertical structures feature a relative crest freeboard $0.0 < R_c / H_{m0} < 1.5$ (EurOtop 2007). This is also assumed for inclined structures. Larger values of R_c / H_{m0} are allowed for the structures in this PhD-research (Eq. 1.9) in order to overlap with existing knowledge on sea defence structures, which typically feature relatively large crest freeboards.

$$0.0 < \frac{R_c}{H_{m0}} \leq 2.0 \tag{1.9}$$

Further assumptions are:

- smooth and impermeable slope;
- no berms, vertical wave walls nor recurve walls;
- normal wave attack; and
- non-floating: slopes extend to the sea bottom.

The structures studied in this PhD-research, fulfilling the above-mentioned assumptions are referred to as *steep low-crested slopes* in this manuscript. The term *OWEC* has been omitted from this name, since the knowledge gathered in this PhD-research is not only applicable to OWECs, but to all structures fulfilling the assumptions above. A definition sketch of a steep low-crested slope is shown in Fig. 1.5.

The slope geometry of steep low-crested slopes is fully determined by the slope angle α, the crest freeboard R_c and the water depth h_t at the toe of the structure. These geometrical parameters are, combined with the spectral wave height H_{m0} and wave period $T_{m-1,0}$ at the toe of the structure, the determining parameters for the overtopping and reflective behaviour of the steep low-crested structures.

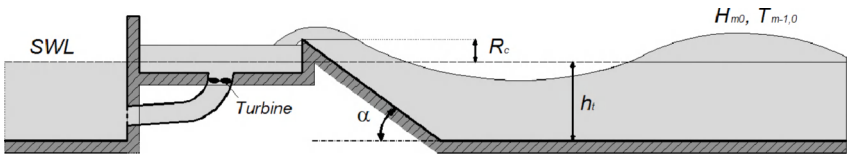

Fig. 1.5: Sketch of steep low-crested slopes studied in this PhD-research together with parameters which determine the overtopping behaviour (SWL stands for the Still Water Level).

1.4 Outline

The four objectives mentioned in section 1.2 are discussed in this PhD-manuscript for the steep low-crested slopes defined in section 1.3, based on a review of existing knowledge from literature and new test results of experimental tests carried out during this PhD-research.

This PhD-manuscript consists of five parts. The first part deals with the experimental tests (chapters 2 and 3). The development of the test set-up which is able to measure the large wave-by-wave overtopping volumes of steep low-crested slopes is described in chapter 2. The test conditions applied during the experimental tests are discussed in chapter 3. The remaining four parts each correspond to one of the objectives in section 1.2.

The second part of this manuscript elaborates on the effect of the geometrical and wave characteristics on the average overtopping rate (per meter crest width) of steep low-crested slopes. A literature review of the existing knowledge on the average overtopping rates applicable to steep low-crested slopes is given in chapter 4. In chapter 5, the average overtopping rates measured during the experimental tests are compared with their predictions from literature, and a new set of prediction formulae is proposed.

A similar approach is followed for the third part, in which the effects of the geometrical and wave characteristics on the reflection coefficient of steep low-crested slopes are discussed (chapter 6).

The knowledge acquired from the second and third part is applied in the fourth part (chapter 7) to determine the effects of an adaptive geometry on the overall

hydraulic efficiency, obtained power and reflection behaviour for a number of potential deployment sites.

The fifth part (chapter 8) deals with the study of the distribution of the wave-by-wave overtopping volumes for steep low-crested slopes. The characteristics of the distributions determined based on the wave-by-wave overtopping volumes measured during the experimental tests are compared with traditionally applied characteristics from literature. Eventually, new expressions for these characteristics are proposed.

Finally, chapter 9 contains the general conclusions and recommendations for further research.

2

Development of a test set-up to measure large wave-by-wave overtopping volumes

Experimental tests have been carried out to reach the objectives in section 1.2. Accordingly, a test set-up able to measure large average overtopping rates and both large and small wave-by-wave overtopping volumes accurately has been developed. The main goal of this chapter is to describe the development of this test set-up.

2.1 Traditional measurement set-ups

2.1.1 Overview

There are a number of different measurement techniques which enable a direct quantification of wave overtopping (e.g. Kortenhaus et al. 2004; Troch et al. 2004). Figure 2.1 gives an overview of the concepts of the three most widely applied techniques to measure wave overtopping in a wave flume and in prototype, i.e. the wave gauge technique (Fig. 2.1a), the pressure sensor technique (Fig. 2.1b) and the weigh cell technique (Fig. 2.1c).

The principle of these three techniques is identical: the overtopped water is collected over a specific crest width and runs down a chute into a reservoir where the amount of accumulated overtopped water is measured continuously during a test run. The idea behind this principle is that the output of the measurements consists of a gradually increasing curve of water elevation, pressure or mass as a function of time, which is the basis for determining the average overtopping rate q [m³/s/m] and wave-by-wave overtopping volumes V_i [m³/m]. This approach has been used for example by Franco et al. (1994) to derive average overtopping rates and wave-by-

wave overtopping volumes for vertical walls in relatively deep water, applying the weigh cell measurement technique.

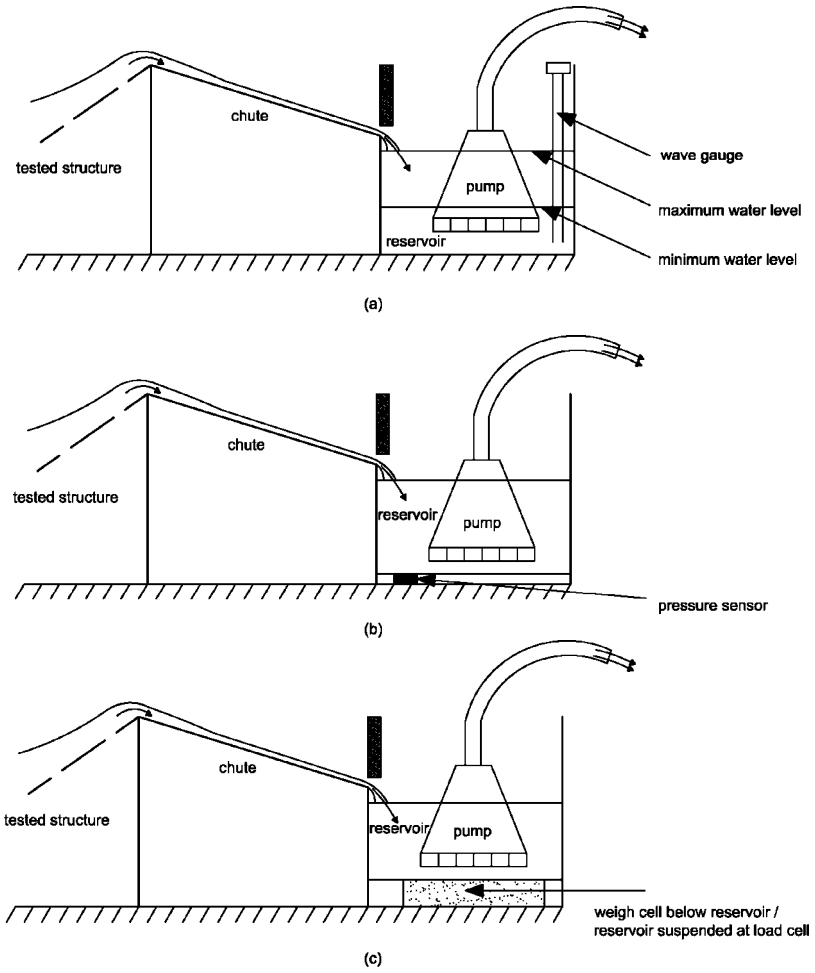

Figure 2.1: Concept sketches of most commonly used techniques to measure wave overtopping volumes in a wave flume and in prototype: (a) wave gauge technique, (b) pressure sensor technique, (c) weigh cell technique.

The difference between the overtopping measurement techniques (Fig. 2.1) is related to the type of measurement device that is used to determine the amount of accumulated overtopped water inside the reservoir:

- a (set of) wave gauge(s) suspended in the reservoir, measuring the water level inside the reservoir (Fig. 2.1a);
- a (set of) pressure sensor(s) positioned at the bottom of the reservoir measuring the pressure of the water column above the pressure sensor(s) (Fig. 2.1b); and
- a (multiple) weigh cell(s) positioned below or above (the reservoir is suspended at a load cell) the reservoir measuring the mass of the water inside the reservoir (Fig. 2.1c).

Wave gauges are established devices, used for measuring water surface elevations in laboratory. Consequently, wave gauges are commonly used to determine the water level inside the reservoir and accordingly to quantify wave overtopping (e.g. Kofoed 2002; Lykke Andersen and Burcharth 2009). An important disadvantage is the susceptibility of the output signal of a wave gauge to oscillations of the water level inside the reservoir. These oscillations are caused by the impact of the overtopping water when it enters the reservoir. The importance of these oscillations increases when the length of the chute decreases. By using a set of wave gauges, small oscillations can be eliminated by averaging the signals of these wave gauges.

The disadvantage of the wave gauge technique is also valid for a (set of) pressure sensor(s). In addition to these disadvantages, the installation of the pressure sensors at the bottom of the reservoir is practically less convenient. The pressure sensor technique is mainly used in prototype devices (e.g. Tedd and Kofoed 2009; Troch et al. 2004).

The output signal of a (set of multiple) weigh cell(s) is less susceptible to oscillations of the water inside the reservoir. Whereas a wave gauge and a pressure sensor both correspond to measurements in one particular point, the weigh cell measures the total amount of accumulated overtopped water inside the reservoir directly. This means that the output signal of the weigh cell is only affected by the average oscillations of the total volume of water inside the reservoir, i.e. a mechanical low-pass filtering is applied due to the set-up of the measurement device.

Apart from the advantage of being less susceptible to oscillations of water inside the reservoir, weighing systems are intrinsically more accurate than wave gauge techniques. Based on a number of examples, Van der Meer et al. (2005a) concluded that the accuracy of the average overtopping rate in small scale overtopping measurements is about 10^{-6} m³/s/m when based on water level changes, while it is about 10^{-8} m³/s/m when using the weigh cell technique. In prototype, assuming a

Froude length scale of 1:30, the accuracy is about 0.16 l/s/m for the less accurate technique, while it is about 0.0016 l/s/m for the most accurate technique. Knowing that the allowable overtopping rate of many sea defence structures is set to 1.0 l/s/m (EurOtop 2007), it is clear that the difference in measurement accuracy plays an important role in the design of those structures.

The weigh cell technique is used for example by Schüttrumpf (2001), Pullen et al. (2009) and Franco et al. (1994).

2.1.2 Application of traditional measurement set-ups to steep low-crested slopes

When applying the principle of the traditional measurement set-ups, described in section 2.1.1, to the steep low-crested slopes studied in this PhD-research, a number of aspects need to be taken into account:

- since the steep low-crested slopes are intended to maximize wave overtopping, large oscillations of the water mass inside the reservoir can be expected;

- a mix of large and small wave-by-wave overtopping volumes occurs for steep low-crested slopes. Consequently, the measurement technique should be able to measure both large and small overtopping volumes accurately.

These aspects are in favour of the weigh cell technique to determine the wave overtopping behaviour accurately for steep low-crested slopes. The weigh cell measurement technique is described in detail in section 2.2. Its ability to determine the wave-by-wave overtopping volumes accurately for steep low-crested slopes is discussed in detail in section 2.3.

The consequences of the transport of water, the procedure to determine the average overtopping rates and wave-by-wave overtopping volumes, and the design of the components, discussed in section 2.2 for the weigh cell measurement technique, are similarly applicable to the wave gauge technique and pressure sensor technique.

2.2 Weigh cell measurement technique

The concept of the weigh cell technique is shown in Fig. 2.1c for the configuration with a weigh cell positioned below the reservoir. This configuration is preferred to the configuration with a reservoir suspended from a load cell, since it is less susceptible to the impacts of larger volumes of water (which may cause resonance of

the suspended measurement set-up). The weigh cell should remain dry and therefore is usually positioned outside the wave flume. Accordingly, the test set-up traditionally has a long chute.

The design of the components of the weigh cell measurement technique is an iterative process; it is described in section 2.2.2. First, the consequences of the transport of water for the test set-up and for the output signals of the weigh cell are discussed in section 2.2.1.

2.2.1 Consequences of transport of water

For test runs with larger average overtopping rates, an unintentional decrease in water level occurs in the area of the wave flume seaward of the structure, which would eventually cause overtopping to stop. In order to compensate for this decrease, water needs to be transported to that area during the test run.

There are two approaches for this transport, depending on the ratio of the total volume of overtopped water over a test run compared to the volume of the reservoir and to the capacity of the weigh cell. When the total volume of overtopped water over a test run exceeds the volume of the reservoir or the capacity of the weigh cell, water is transported from the reservoir back to the flume by a pump which is suspended inside the reservoir (Fig. 2.1). The pump is triggered by the weigh cell and starts pumping when a specific maximum volume is reached. Furthermore, a minimum volume is set to avoid the pump from running dry. Examples of the water levels corresponding to the maximum and minimum volume are shown in Fig. 2.1a.

The second approach is used when the total volume of overtopped water over a test run is smaller than the total volume of the reservoir and it does not exceed the capacity of the weigh cell. In that case, water is pumped from a second independent reservoir to the flume. This situation only occurs when the average overtopping rate is very small for all tests in a test series. In general, this is not the case and a pump is suspended inside the reservoir.

The presence of the pump inside the reservoir has a double effect on the output signals of the weigh cell. First, the mass indicated by the weigh cell consists of the real mass of water inside the reservoir added up with the displacement of the submerged part of the pump. Therefore, it is referred to as the "relative" mass of water inside the reservoir M_{rel} [kg]. The mass of the reservoir is not part of M_{rel}, since the weigh cell is zeroed after the reservoir is put in place. A calibration curve should be set up between the real mass of water inside the reservoir and M_{rel}, due to the fact that one is only interested in the real accumulated mass of water inside the reservoir. Such calibration curve (Fig. 2.2) has been created for the AAU08 and

UG10 test series carried out during this PhD-research (see chapter 3). The derivation of the calibration curve for the UG10 test series is as follows. The relative mass of water inside the reservoir indicated by the weigh cell at the start of the calibration process was 38.000 kg. This value is chosen as the bottom value for the calibration, since it approximately corresponds to the minimum volume of water required inside the reservoir to avoid the pump from running dry. The weigh cell below the reservoir has an accuracy of 0.005 kg.

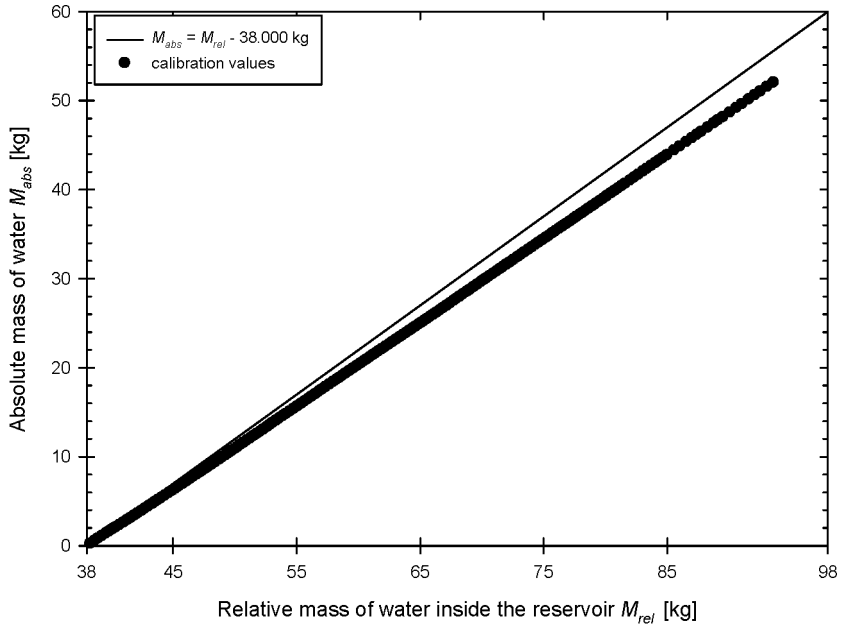

Figure 2.2: Calibration curve between real mass of water inside the reservoir and measurement by the weigh cell, UG10 test series.

By gradually adding known volumes of water (0.200 kg to 0.550 kg, accuracy of the weigh cell used for weighing the added volumes is 0.002 kg) to the reservoir, the relative mass of water inside the reservoir increases. This process is continued up to a relative mass of 94.000 kg, i.e. equal to the maximum capacity of the weigh cell (100.000 kg) minus the mass of the reservoir (6.000 kg). The horizontal axis in Fig. 2.2 contains the relative mass of water inside the reservoir, while the vertical

axis shows the total mass of water added to the reservoir starting from the relative mass of 38.000 kg. Since the total mass of water added to the reservoir is related to the real mass of water inside the reservoir, it is referred to as the *absolute mass of water* inside the reservoir M_{abs} [kg]. Note that this absolute mass is not the total real mass of water inside the reservoir, since it is still relative to the initial relative mass of 38.000 kg read from the weigh cell. However, this relative reference mass has no effect on the intended output of the test, i.e. the accumulated real mass of water inside the reservoir over a test run.

The following relationship was found between M_{rel} and M_{abs} for the calibration curve in Fig. 2.2:

$$M_{rel} = 1.075 M_{abs} + 38.000\,\text{kg} \tag{2.1a}$$

Equation (2.1) corresponds to a straight increasing line, indicating the displacement of the submerged part of the pump increases linearly with the absolute mass. The following example illustrates the importance of the use of Eq. (2.1a). When pumping between 70.000 kg and 40.000 kg, a decrease in M_{rel} of 30.000 kg is registered, while in reality only a decrease of 28.000 kg occurs. This corresponds to a 7.5 % overestimation of the pumped mass of water, i.e. a conservative approach. Hence, applying the calibration curve is particularly important when an accurate determination of the average overtopping rates and wave-by-wave overtopping volumes is required.

The reliability of Eq. (2.1a) is expressed by a *root mean square error* (*rmse*), defined as:

$$rmse = \sqrt{\frac{1}{N_{mass}} \sum_{n=1}^{N_{mass}} \left(M_{rel,meas,n} - M_{rel,pred,n} \right)^2} \tag{2.1b}$$

in which N_{mass} is the number of masses added to the reservoir when setting up the calibration curve. The rmse-value of the calibration curve for the UG10 test series equals 0.20. The 90% prediction interval of Eq. (2.1a) is bounded by:

$$\begin{cases} M_{rel,90\%,upper} = M_{rel,pred} + 1.645\, rmse \\ M_{rel,90\%,lower} = M_{rel,pred} - 1.645\, rmse \end{cases} \tag{2.1c}$$

For example, a mass of 22.360 kg ± 0.002 kg added to the reservoir corresponds to a measured relative mass $M_{rel,meas}$ of 62.205 kg ± 0.005 kg. The predicted relative

mass $M_{rel,pred}$ by Eq. (2.1a) is 62.037 kg. This shows that the accuracy of the weigh cell below the reservoir is not taken into account when using the prediction formula in Eq. (2.1a). The upper and lower boundaries of the 90% prediction interval are 62.366 kg and 61.708 kg respectively. Accordingly, the uncertainty concerning the measured values is overruled by the uncertainty of the predicted relative mass $M_{rel,pred}$.

The second consequence of the transport of water with the pump is related to the output signals of the weigh cell. Instead of the intended gradual increase in real mass (i.e. the cumulative curve), a decrease occurs in the signal each time the pump transports water to the flume. In order to achieve the cumulative curve, the weigh cell signal should be compensated for pumping. This process is discussed in detail in section 2.2.3.

2.2.2 Design of components of traditional weigh cell measurement technique

The design of the components of the weigh cell measurement technique (outlined below) is an iterative process, since these components are related to each other:

- expected average overtopping rates;
- dimensions of the reservoir;
- width of collection zone of overtopped water, i.e. the *overtopping width*;
- capacity of the weigh cell
- pump: discharge and duration of pumping
- allowable decrease of water level inside the wave flume

Based on the experiences with the test set-ups developed for this PhD-research, a method has been derived to achieve a first estimate of the characteristics of each of the above components. A stepwise description of this method is given below:

1. Predict the average overtopping rates based on prediction methods from literature for all planned tests and select the test which results in the largest average overtopping rate q_{max} [m³/s/m].

2. In order to be able to decrease the water level inside the reservoir, the pump discharge Q_{pump} [m³/s] should be larger than the largest average overtopping rate multiplied by the overtopping width B_q [m]:

$$q_{\max} B_q < Q_{pump} \tag{2.2}$$

Preferably, $q_{\max}$ is multiplied by a safety factor (see below), since the instantaneous overtopping rate during a test run can be larger than the average overtopping rate.

3. The horizontal dimensions of the reservoir are determined by (1) the dimensions of the pump, (2) the dimensions of the weigh cell, (3) the overtopping width, and (4) the width of the wave flume. Based on the horizontal dimensions of the reservoir and the height of the pump inlet, the minimum volume $V_{res,\min}$ [m³] that should be available in the reservoir for avoiding the pump from running dry is determined.

4. The maximum volume $V_{res,\max}$ [m³] is determined by (1) the allowable vertical dimensions of the reservoir (limited by the height of the collection zone, i.e. the inlet zone of the reservoir), (2) the allowable decrease of water inside the wave flume and (3) the capacity of the weigh cell.

5. The strategy for pumping is that the pump transports water during a fixed time period T_{pump} [s], starting from the moment the volume in the reservoir reaches $V_{res,\max}$. The period T_{pump} is defined as the duration of pumping between the maximum and minimum volume, assuming no water enters the reservoir during pumping:

$$Q_{pump} T_{pump} < V_{res,\max} - V_{res,\min} \tag{2.3}$$

The method outlined above results in an initial design of the components of the weigh cell measurement technique. Their design is an iterative procedure enhanced by the fact that a number of dynamic effects occur during the test related to $q_{\max}$:

- The instantaneous overtopping rate will be larger than the average overtopping rate. In that case, the water level inside the reservoir still increases during pumping. This unfavourable dynamic effect is solved by choosing a pump with a larger discharge compared to Eq. (2.2) (for example with $2 q B_q < Q_{pump}$), and by limiting $V_{res,\max}$ to allow a small temporary increase of the water level inside the reservoir during pumping for the largest instantaneous overtopping rates.

- The discharge of the pump Q_{pump} is not constant during pumping; there is a start up and cooling down period. The start up period is caused by the reaction time of the pump (0.4 s for the pump of the UG10 test series, chapter 3), and thus affects the value of $V_{res,\max}$. The cooling down period (2.0 s for the pump of the UG10 test series) corresponds to a further decrease of water level inside the reservoir due to the fact that the rotor of the pump takes a small period of time before it stands still. The variation in Q_{pump} during pumping should be taken into account in the left hand side of Eq. (2.3) when determining the duration of pumping T_{pump}.

- Overtopping occurs during pumping. Correspondingly, a larger amount of water is present in the reservoir after pumping compared to the case when no overtopping occurs during pumping. This means that the pump starts pumping within a smaller time period, resulting in a larger number of pumping events and an evenly larger number of pump compensations. In order to decrease this number, the duration of pumping may be increased. However, this intervention increases the risk for the pump to run dry when no overtopping occurs during pumping.

2.2.3 Determination of average overtopping rate by weigh cell measurement technique

The procedure to derive the average overtopping rate from the output signals of the weigh cell measurement technique is explained in this section based on an example of a small scale test of the UG10 test series with a relatively small amount of wave overtopping.

The variation of the relative mass of water inside the reservoir (expressed in kg) over the duration of the test run is shown in Fig. 2.3. Five pumping events occur. The pump turns during a fixed number of seconds and starts when a maximum relative mass of 70 kg is reached.

Based on the calibration curve between relative and absolute masses (Fig. 2.2), the variation in absolute mass over time is obtained (Fig. 2.4). This is the starting point to determine the average overtopping rate, which can be determined in four different ways.

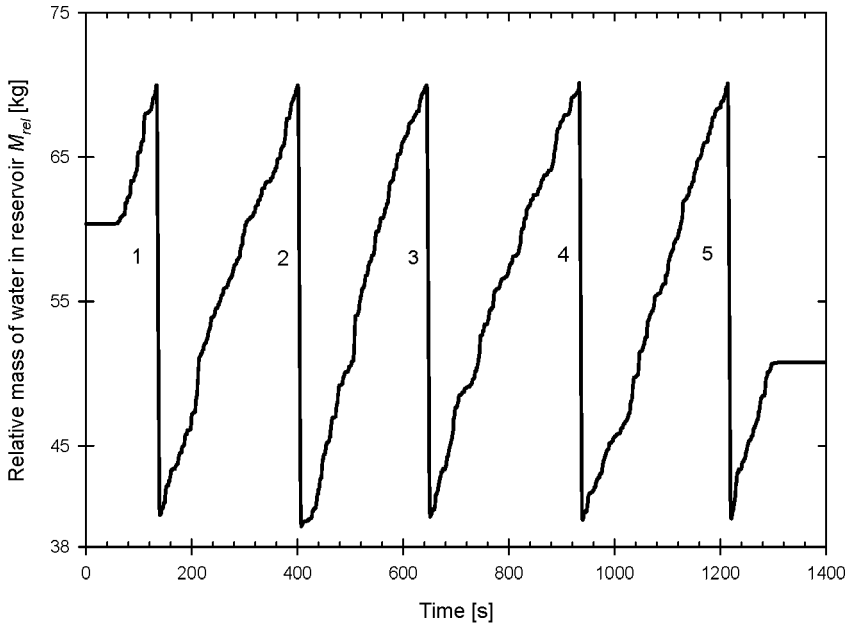

Figure 2.3: Variation in relative mass of water over time for a small scale test of the UG10 test series with a relatively small average overtopping rate.

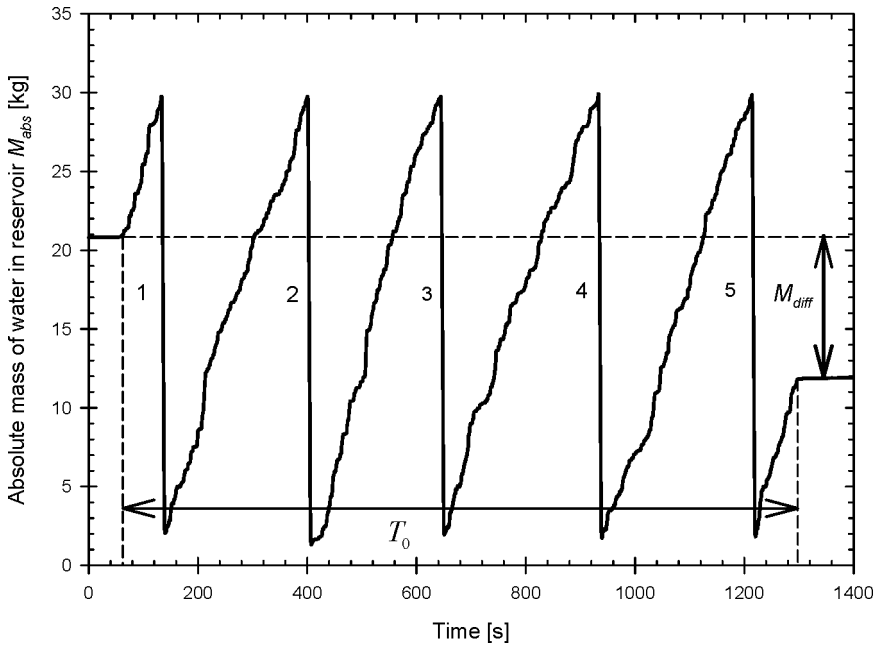

Figure 2.4: Variation in absolute mass of water over time for a small scale test with a relatively small average overtopping rate.

A first estimate of the average overtopping rate q is achieved based on the number of pumping events (N_{pump}) and the average absolute mass of water $W = \rho Q_{pump} T_{pump}$ [kg] transported during the fixed pump duration. The corresponding expression for the average overtopping rate q is:

$$q = \frac{\left(M_{diff} + N_{pump} W\right)}{\rho T_0 B_q} \tag{2.4}$$

The parameter M_{diff} [kg] is obtained by subtracting the mass of water in the reservoir at the end of the test run from the initial mass of water in the reservoir at the

start of the test run (Fig. 2.4). The terms in the denominator of the right hand side of Eq. (2.4) are added to obtain the dimension m³/s/m for q. The parameter T_0 [s] is the total duration of the test run, not including the parts at the start and end of the test run without wave overtopping (Fig. 2.4).

A second estimate of the average overtopping rate is achieved based on the curve of the cumulative mass in the reservoir over time (Fig. 2.7). This curve has been generated by compensating for pumping, which consists of the following steps:

1. Derivation of the characteristic pump curve (Fig. 2.5). A pump curve is achieved as the output of the weigh cell when pumping from the maximum volume $V_{\max}$ for the duration T_{pump} and allowing no water to enter the reservoir. This process is repeated at least five times. The pump curves exhibit a spreading around an average pump curve, i.e. the characteristic pump curve. The calibration curve (relative vs. absolute masses of water in the reservoir) is used in a next step to translate the vertical axis of the characteristic pump curve to absolute masses. The corresponding characteristic pump curve used for the UG10 test series is shown in Fig. 2.5 (spreading ± 0.090 kg). Despite the spreading on the pump curve, the pump is assumed to describe the characteristic pump curve for each pumping event during the test runs. Furthermore, tests carried out in the framework of the UG10 test series (chapter 3) show that the characteristic pump curve is not affected by both the impact of the overtopped water entering the reservoir, and the occurrence of overtopping during pumping.

2. A new curve is determined by subtracting the characteristic pump curve from the horizontal line corresponding to the absolute mass at the start of pumping (i.e. 30 kg for the UG10 test series, Fig. 2.5). This curve is referred to as the *conjugate characteristic pump curve*.

3. Based on the weigh cell signal in Fig. 2.3, the start positions for pumping are identified as the moments when the relative mass of water inside the reservoir exceeds 70 kg.

4. A curve is assembled by adding the conjugate characteristic pump curve at each of the start positions for pumping, with constant values in between. This results in the *curve of pumped mass* (Fig. 2.6).

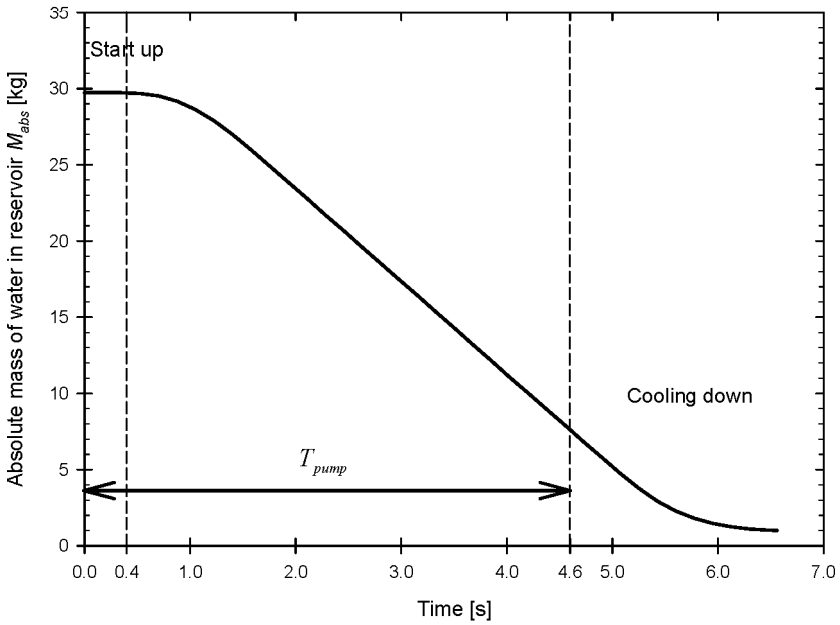

Figure 2.5: Characteristic pump curve for the UG10 test series. The start up period is 0.4 s, while the cooling down period is 2.0 s.

5. By adding the curve of pumped mass (Fig. 2.6) to the curve of absolute mass in the reservoir over time (Fig. 2.4), the cumulative curve is achieved (Fig. 2.7). This step finalizes the process of compensating for pumping.

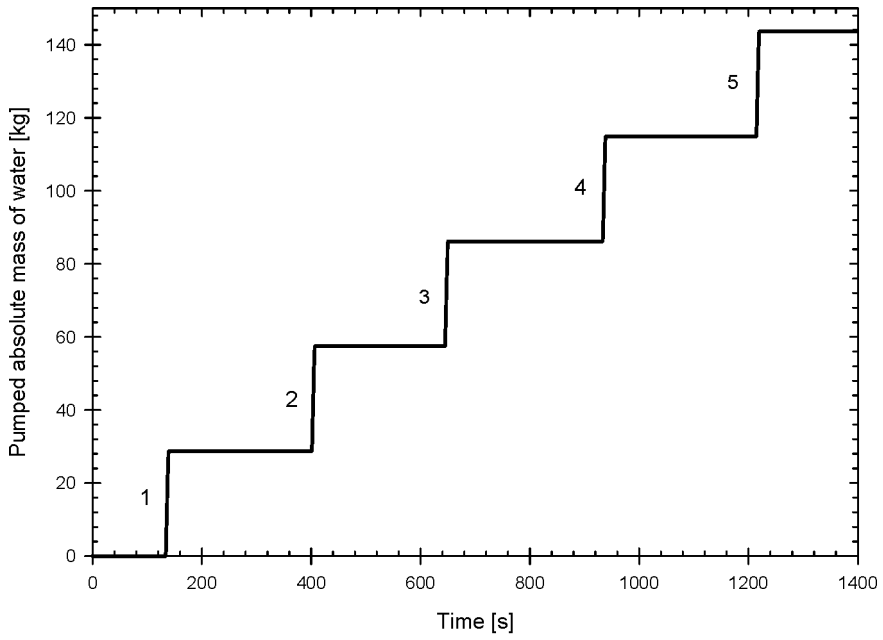

Figure 2.6: Curve of pumped mass over time for a small scale test with a relatively small average overtopping rate.

The average slope angle φ of the cumulative curve (Fig. 2.7) determines the average overtopping rate q :

$$q = \frac{\tan\varphi}{\rho B_q} \tag{2.5a}$$

$$= \frac{M_{total}}{\rho T_0 B_q} \tag{2.5b}$$

M_{total} [kg] is the difference in cumulative mass between the end and the start of the test run (Fig. 2.7).

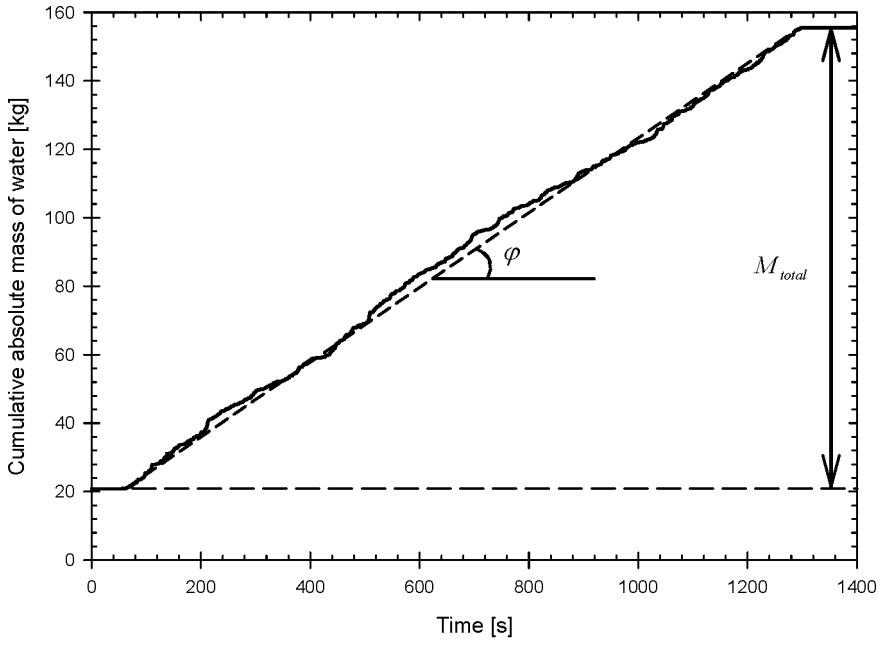

Figure 2.7: Cumulative absolute mass in reservoir over time for a small scale test with a relatively small average overtopping rate.

Determining the slope angle of the cumulative curve comes down to averaging the time-differentiated cumulative mass of water dq/dt [kg/s] in the reservoir over time. Hence, a third expression for the average overtopping rate q is:

$$q = \left(\frac{dq}{dt}\right)_{mean} \frac{1}{\rho B_q} \tag{2.6}$$

The time-differentiated cumulative mass of water in the reservoir over time is given in Fig. 2.8.

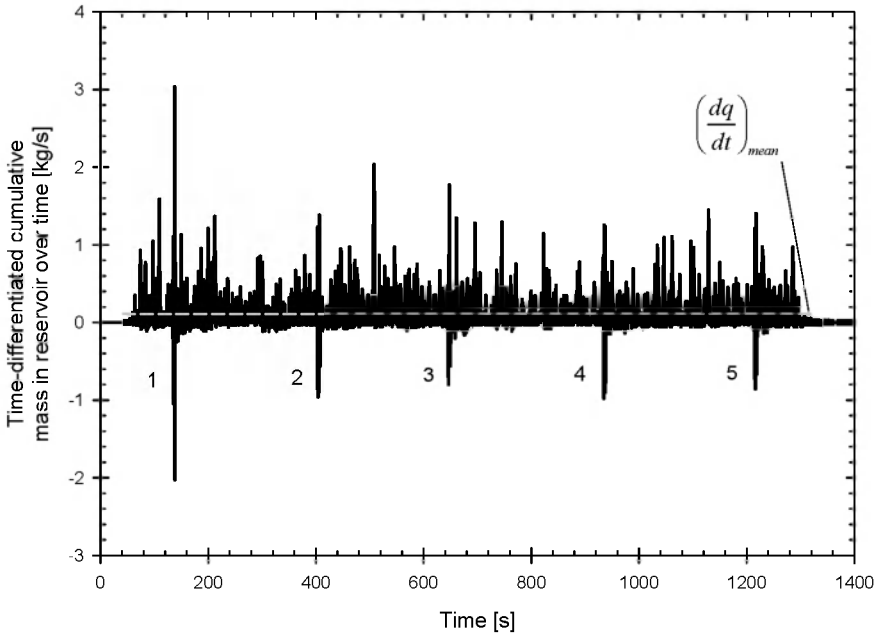

Figure 2.8: Time-differentiated cumulative mass in reservoir over time for a small scale test with a relatively small average overtopping rate.

The large negative peaks in Fig. 2.8 are caused by imperfect compensation for pumping, for example due to the spreading on the characteristic pump curve. When the characteristic pump curve is positioned below the real pump curve, descending sections occur in the cumulative curve in Fig. 2.7, resulting in the negative peaks in Fig. 2.8. The smaller negative peaks in Fig. 2.8 are caused by the impacts of the larger overtopping waves when they reach the reservoir. This impact results in a temporary overestimation of the overtopped mass. Hence, a negative peak occurs in

its derivative. The effect of the negative peaks on the average overtopping rate q is negligible. However, when applying the weigh cell measurement technique to determine wave-by-wave overtopping volumes (section 2.2.4), the negative peaks should be as little as possible, in order to maximize the accuracy of the derived volumes (during pumping).

2.2.4 Determination of wave-by-wave overtopping volumes by weigh cell measurement technique

The identification of the wave-by-wave overtopping volumes is based on the cumulative curve (Fig. 2.9).

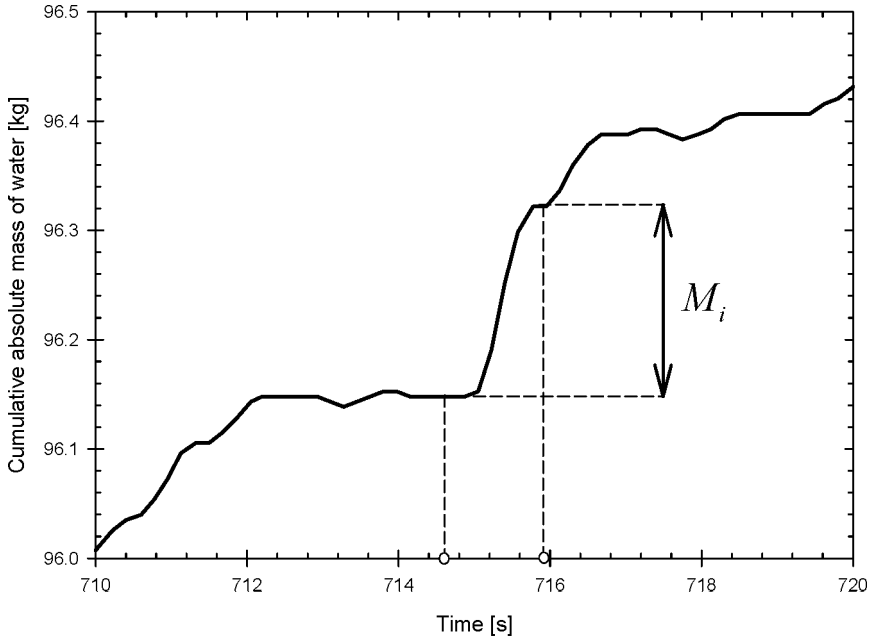

Figure 2.9: Detail of cumulative mass in reservoir over time for the small scale test with the sea defence structure – identification of wave-by-wave overtopping masses.

This technique was used for the first time by Franco et al. (1994) for the case of caisson breakwaters (vertical walls) and later for example by Pearson et al. (2002) (10:1 battered walls). It is based on the fact that each overtopping wave causes an abrupt increase in cumulative mass in the reservoir. Consequently, the differences in cumulative mass between two consequent horizontal sections of the cumulative curve correspond to the wave-by-wave overtopping masses M_i [kg] (Fig. 2.9). These masses are related to the wave-by-wave overtopping volumes V_i [m³/m] through division by ρB_q, i.e. $V_i = M_i / \rho B_q$.

Accordingly, there is a fourth expression for the average overtopping rate q, defined as the ratio of the sum of the wave-by-wave overtopping volumes V_i and the total duration of the test run T_0:

$$q = \frac{\sum V_i}{T_0} \tag{2.7}$$

It should be noted that this method is originally designed for deriving relatively small wave-by-wave overtopping volumes for tests with small average overtopping rates which do not require the installation of a pump inside the reservoir (Franco et al. 1994). Since large average overtopping rates and large wave-by-wave overtopping volumes are expected for the steep low-crested slopes considered in this PhD-research, the ability of the traditional weigh cell technique (described in section 2.2) to determine those rates and volumes should be investigated. This is the subject of the following section 2.3.

2.3 Ability of weigh cell measurement technique to determine overtopping behaviour of steep low-crested slopes

When large average overtopping rates occur, a pump with a large discharge Q_{pump} should be used, Eq. (2.2). Despite the large value of Q_{pump}, the number of pumping events N_{pump} is high due to the relatively limited dimensions of the reservoir. Accordingly, the number of negative peaks occurring in a figure similar to Fig. 2.8 is also high. This means that an accurate compensation for pumping is very important

for steep low-crested slopes in order to obtain a sufficient accuracy of the derived wave-by-wave overtopping volumes.

Traditionally the length of the chute is rather long for the configuration with the weigh cell positioned below the reservoir, since the weigh cell is installed outside the wave flume to keep the weigh cell dry. Due to the long chute, there is a significant time delay between the moment a wave overtops the structure and the moment the corresponding overtopped water mass is registered by the weigh cell. When two waves overtop the crest of the structure within a small time interval, the two corresponding water masses could merge along the length of the chute. Hence, an accurate measurement of the wave-by-wave overtopping volumes requires a short chute.

A proper identification of the wave-by-wave overtopping volumes based on the cumulative curve requires knowledge on the times when waves overtop the crest (dots on horizontal axis Fig. 2.9). This means that a measurement system should be installed at the crest of the slope able to identify those times, similar to Pullen et al. (2009) which improved the test set-up of Franco et al. (1994) using an overtopping detection system.

The following two sections describe the overtopping measurement systems of the two test set-ups that have been developed during this PhD-research to measure large wave-by-wave overtopping masses accurately for steep low-crested slopes. Both measurement systems are based on the weigh cell measurement technique (section 2.2), which has been adjusted to enable accurate determination of large wave-by-wave overtopping volumes.

A first test set-up has been installed in a wave flume at the Department of Civil Engineering at Aalborg University (Denmark), resulting in the AAU08 test series (section 2.4). A second test set-up has been installed in a wave flume at the Department of Civil Engineering at Ghent University (Belgium) resulting in the UG10 test series (section 2.5). The test set-up in section 2.5 is considered as an improved version of the test set-up in section 2.4, since it is able to measure the large individual overtopping volumes more accurately compared to the test set-up described in section 2.4.

2.4 Overtopping measurements for AAU08 test series

This section describes the adjustments to the weigh cell measurement technique for the AAU08 test series. A detailed description of the test conditions for the AAU08 test series is given in chapter 3.

Based on section 2.3, two requirements apply for the measurement set-up to determine the overtopping behaviour of steep low-crested slopes more accurately, i.e. the application of a short chute and an overtopping detection system.

A reduction of the length of the chute requires the weigh cell and reservoir to be positioned inside the wave flume. Correspondingly, both components are positioned directly behind the crest of the steep slope in a wooden box, referred to as the *dry area* (Fig. 2.10). Since the dry area is located inside the wave flume, the wooden box is heavily ballasted in order to withstand the large upward Archimedes forces of the surrounding water.

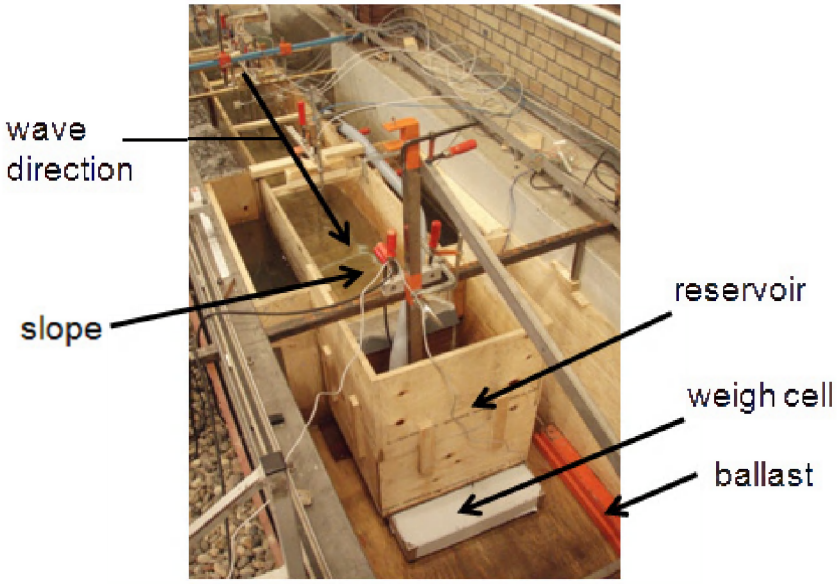

Figure 2.10: Back view of the AAU08 test set-up. The dry area with reservoir, weigh cell and ballast is clearly visible.

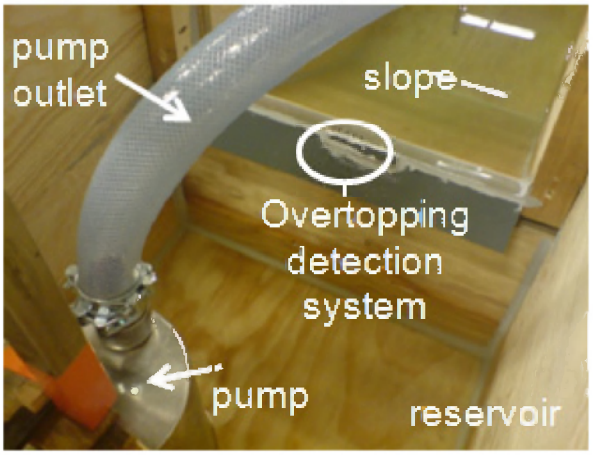

Figure 2.11: Inside view of the reservoir.

Furthermore, an overtopping detection system is installed at the crest of the tested slopes (Fig. 2.11), similar to (Pullen et al.(2009). The system consists of two vertical metal wires with a limited height that are connected to a power source (5 V). The working principle of the overtopping detection system is similar to that of a wave gauge: the voltage between the two wires changes when these are covered by water. Each overtopping wave causes a peak in the output signal of the overtopping detection system. This is explained by the movement of the overtopping tongue of an overtopping wave. That tongue reaches the crest of the structure and overtops into the reservoir. When the trough of the wave reaches the slope, the overtopping tongue withdraws until finally no water covers the two wires of the overtopping detection system.

Note that the two wires are installed in the centre of the wave flume width, at the crest of the slope. Pullen et al.(2009) detect wave-by-wave overtopping events using two parallel strips of metal tape run along the total structure crest width which act as a switch closed by the water. Due to the perpendicular wave attack of the structures in the wave flume of the AAU08 test series, the difference between both methods is expected to be negligible.

A typical output signal of the overtopping detection system of the AAU08 test set-up is shown in Fig. 2.12 (short-dashed line). The corresponding cumulative weigh cell signal is also displayed (solid line). The overtopping detection signal is

scaled for the purpose of visualization. Each peak of the overtopping detection system exceeding a specific threshold corresponds to a significant wave-by-wave overtopping volume. Due to the fact that the weigh cell and reservoir are positioned directly behind the crest of the slopes, the time delay between the peaks and the corresponding increase in the cumulative curve is reduced to a minimum (illustrated by the arrows in Fig. 2.12). This confirms the suitability of the overtopping detection system to derive the wave-by-wave overtopping volumes accurately. Accordingly, the procedure described in section 2.2.3 to find the cumulative curve is completed with the following steps to determine the wave-by-wave overtopping volumes:

6. Each peak of the output signal of the overtopping detection signal that exceeds a threshold determined based on the output of the overtopping detection system when dry, corresponds to a considerable increase in the cumulative average overtopping rate. Since the overtopping detection system is positioned at the crest of the slope, a delay occurs between the peaks and the corresponding increases in the cumulative curve. The cumulative mass corresponding to the horizontal sections preceding each of these increases, is linked to the corresponding peak of the overtopping detection signal (Fig. 2.12).

7. The wave-by-wave overtopping masses M_i are defined by the differences between the cumulative masses corresponding to the horizontal sections for two consecutive peaks of the overtopping detection signal (Fig. 2.9). The corresponding wave-by-wave overtopping volumes are calculated using the relationship $V_i = M_i / \rho B_q$.

Due to the high number of pumping events and the fact that wave-by-wave overtopping volumes occurring during pumping need to be determined accurately, an accurate compensation for pumping has to be applied. One of the corresponding measures is the generation of a binary signal during each test run (0 when the pump is not working and 1 during T_{pump}). At the start of the cooling down period, the data acquisition system verifies if the volume of water inside the reservoir is larger than $V_{res,\max}$ or not, and correspondingly decides if a new pumping event is required or not. When a new pumping event is started, the pump continues pumping. The occurrence of two consecutive pumping events is particularly important for larger average overtopping rates.

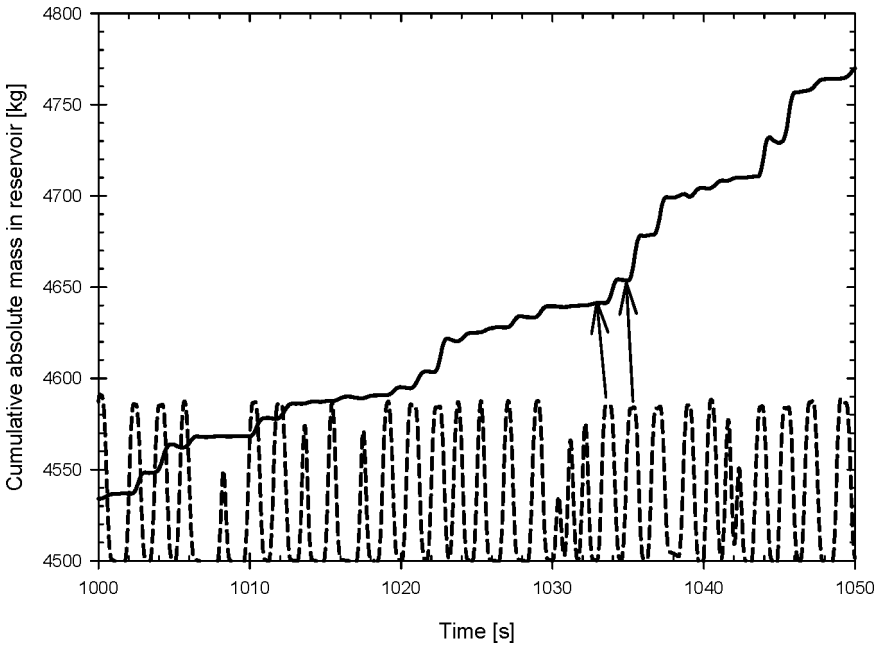

Figure 2.12: Typical example of output signal of overtopping detection system for AAU08 test set-up, with the corresponding cumulative weigh cell signal.

An accurate compensation for pumping was impeded for the AAU08 test series, since a pump without return valve was applied, allowing water in the outlet tube to run back to the reservoir after pumping. Furthermore, other "children's diseases" appeared while carrying out the tests and when analyzing the test results of the AAU08 test series:

- The dry area (containing the reservoir and weigh cell) is positioned across the total width of the wave flume, i.e. 1.2 m, to allow a person to enter and carry out adjustments to the overtopping measurement set-up (Fig. 2.13).

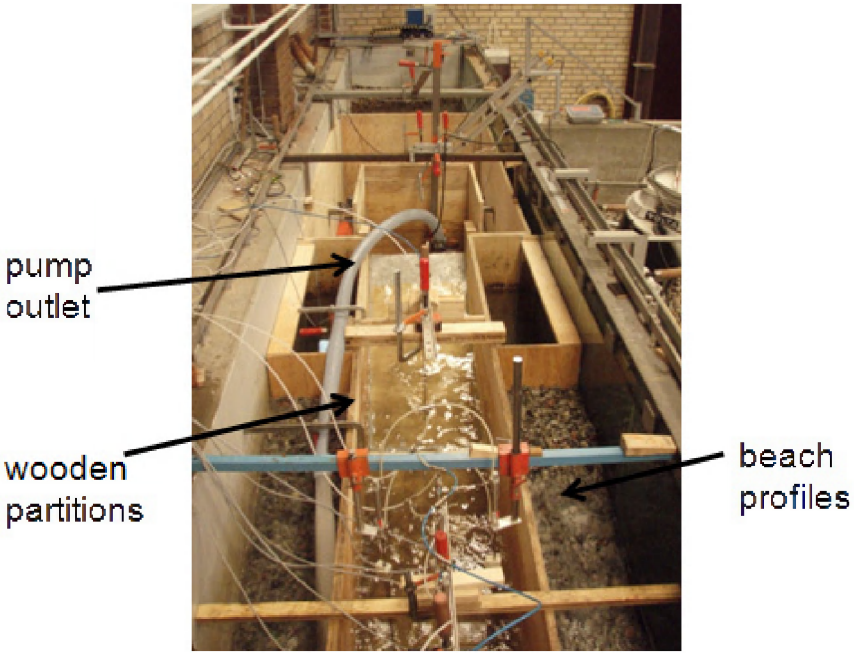

Figure 2.13: Top view of the AAU08 test set-up. The wave direction is upwards.

The overtopped water is collected over a crest width of only 0.5 m along the centre of the wave flume, in order to limit both the dimensions of the reservoir and the capacity of the weigh cell. Since the dry area had to be kept dry, wave overtopping outside the collection zone of the overtopped water was not allowed. In order to avoid wave overtopping, mild gravel beaches have been installed in front of the crest of the slope in the zones outside the collection zone of the overtopped water to induce wave breaking (Fig. 2.13). Consequently, the width of the tested structure is reduced to 0.5 m, equal to the width of the overtopping tray. Furthermore, wooden partitions are installed between the structure and the adjacent beach zones over approximately 1/3rd of the length of the wave flume in order to allow the installation of the beaches.

The resulting "slope" consists of three zones, with a highly reflective zone in the centre (the actual structure) and beach profiles at the sides of the structure with very little reflection. The differences in reflection coefficient between the structure and beach profiles affect the incoming waves and the performance of

the active wave absorption system, which is designed to reduce the rereflection of the reflected waves from the structure at the wave paddle.

- Since transport of water from the reservoir to the flume was impossible below the test set-up, the pump outlet was positioned in one of the beach profile sections (Fig. 2.13) in order not to disturb the incoming waves in the central section. The jet of the pump outlet also affects the incoming waves and the performance of the active wave absorption system.

- By positioning the reservoir directly behind the crest of the slope, large oscillations of the water level occur inside the reservoir. The output signal of the weigh cell is affected by those oscillations, which are enhanced by the large sampling frequency (40 Hz) of the weigh cell of the AAU08 test series.

Eventually, the active wave absorption system has not been activated during the AAU08 test series, since the obtained wave spectra in the central zone appeared to approach the intended wave spectra better without active absorption.

Despite the "children's diseases" of the AAU08 test set-up, their effects on the average overtopping rates q for the irregular wave tests are considered to be negligible. The corresponding test results are presented and discussed in chapter 5 of this PhD-manuscript. However, the "children's diseases" related to the pump and the oscillations inside the reservoir resulted in the derivation of unrealistic negative wave-by-wave overtopping volumes. Consequently, the wave-by-wave overtopping volumes determined for the AAU08 test series are not used for further analysis in this PhD-manuscript.

The size of the negative peaks in the curve of the time-differentiated cumulative mass in the reservoir over time is a measure for the quality of the determination of the wave-by-wave overtopping volumes. Larger negative peaks correspond to a less accurate compensation for pumping and to a larger impact of the waves when these enter the reservoir. Due to this impact the positive peaks will also be larger.

The time-differentiated cumulative mass in the reservoir over time is shown in Fig. 2.14 for a typical example of an irregular wave test carried out with the AAU08 test set-up. Negative peaks down to -10 kg/s and positive peaks up to 60 kg/s occur, indicating that the accuracy of the compensation for pumping and the measurement technique need to be improved in order to measure wave-by-wave overtopping volumes accurately. Therefore, a second improved test set-up has been designed, described in section 2.5.

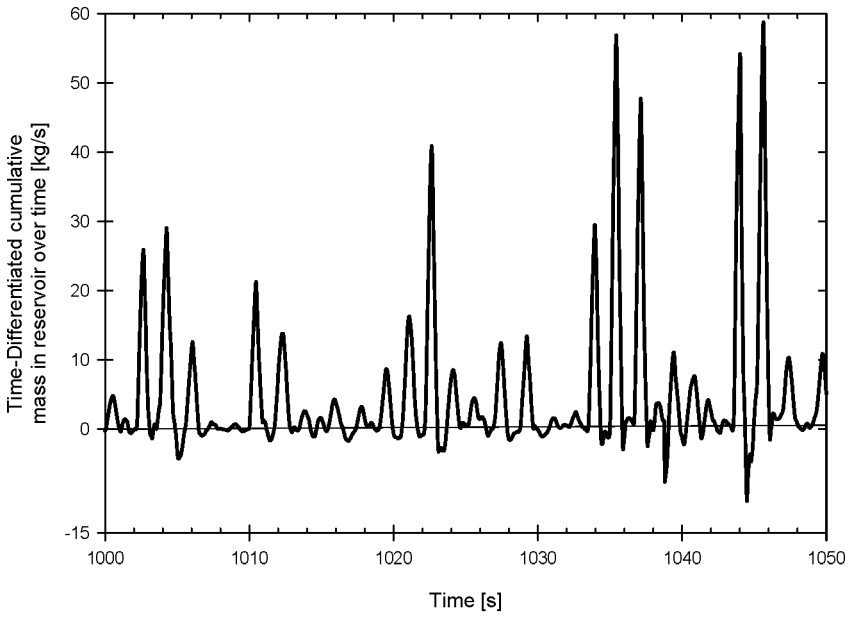

Figure 2.14: Time-differentiated cumulative mass in reservoir over time – AAU08 test set-up.

2.5 Overtopping measurements for UG10 test series

This section describes the adjustments to the AAU08 test set-up for the UG10 test series carried out at Ghent University, Belgium. A detailed description of the test conditions of the UG10 dataset is given in chapter 3. The following adjustments have been made to the AAU08 test set-up to solve its "children's diseases":

- A pump with return valve has been applied in the UG10 test series.

- The shape and width of the dry area have been altered in order to allow waves to overtop the structure over the whole width of the wave flume (Figs. 2.15, 2.16

and 2.17). Consequently, the installation of beach profiles is redundant. The rear side of the dry area is sufficiently wide and long to install the weigh cell and the reservoir (Fig. 2.16). The dry area is attached to the bottom of the wave flume. CAD-drawings of the UG10 and AAU08 test set-ups are given in Appendix A.

Figure 2.15: Front side of the dry area.

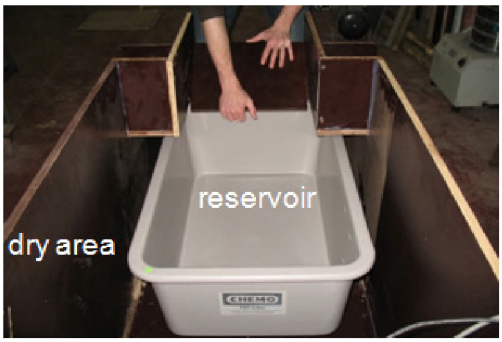

Figure 2.16: Rear side of the dry area.

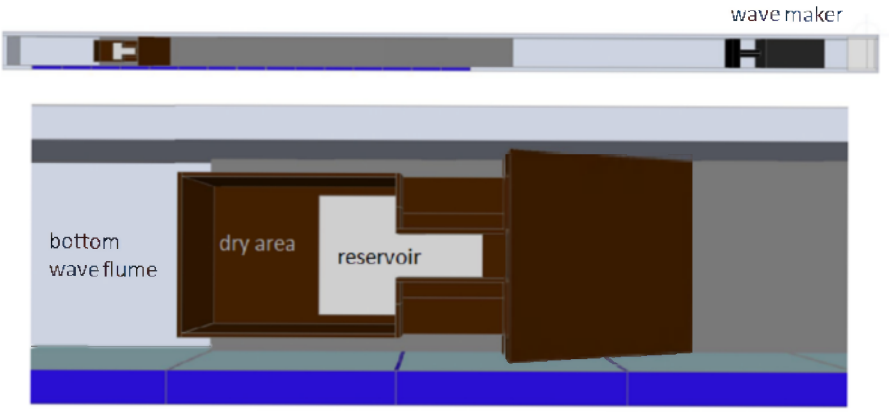

Figure 2.17: UG10 test set-up - top view.

- The structure is built on top of a hollow foreshore, which enables the water to be transported from the reservoir to the seaward side of the structure below the structure (indicated by *water current* in Fig. 2.18). The foreshore is not built to model a reduction in water depth or a specific beach profile.
  This measure further reduces the negative effects on the incoming waves and the active wave absorption system.

- The overtopping width is reduced to 0.2 m (the wave flume has a width of 1 m) and a smaller sampling frequency is applied for the weigh cell (5 Hz), in order to limit the effect of large oscillations on the weigh cell signal.

- A wooden bar is installed between the chute and the reservoir, to catch the impact of the overtopped water, further limiting those oscillations.

- The measures taken in the data acquisition of the AAU08 test series to achieve an accurate compensation for pumping (e.g. the binary signal) have also been used during the UG10 test series. However, the weigh cell signals have been studied in more detail in order to assemble the most accurate conjugate characteristic pump curve for each pumping event.

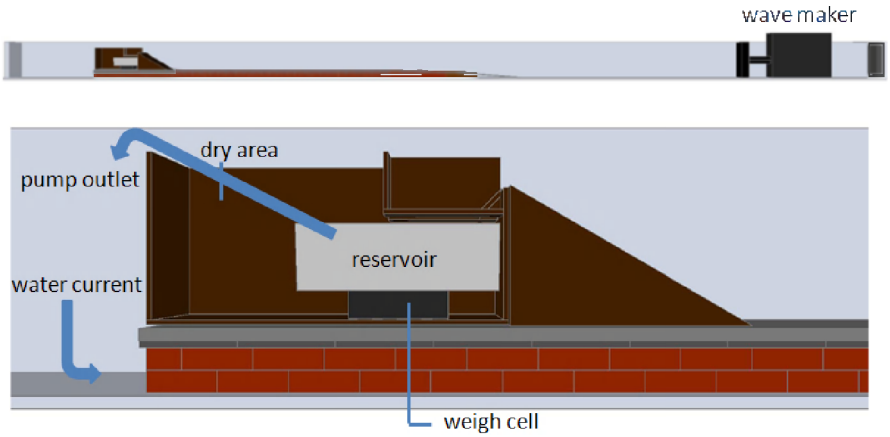

Figure 2.18: UG10 test set-up – side view.

Two additional photos of the UG10 test set-up are given below, showing the rear part (Fig. 2.19) and the front part of the test set-up (Fig. 2.20).

The overtopping detection system of the UG10 test set-up consists of a wave gauge instead of two wires with a limited length. Since their principles are identical, the methodology to derive the wave-by-wave overtopping volumes explained in section 2.4 (AAU08 test series), also applies for the UG10 test series. Additionally, the extended length of the two wires in the case of a wave gauge allows to directly link the height of the peaks of the overtopping detection signal to the size of the wave-by-wave overtopping volumes (Fig. 2.21). This aspect has not been further investigated in this PhD-research due to time limitations (see chapter 9).

A second wave gauge is positioned at the end of the chute (Fig. 2.20). This wave gauge exhibits a smaller time delay between the peaks in its signal and the increases in the cumulative curve. However, since the lower part of this second wave gauge was not covered by water for small overtopping waves, the output signal of the second wave gauge has not been used for analysis.

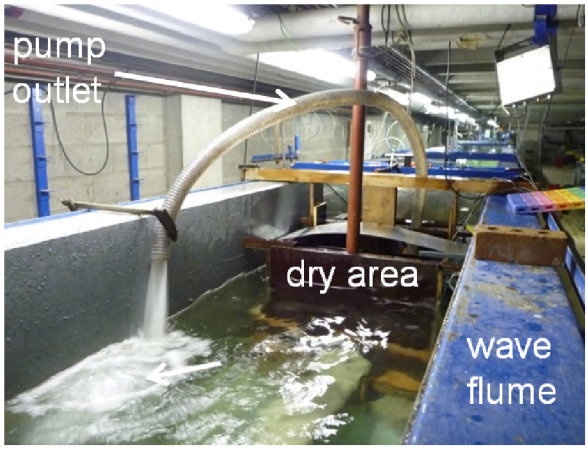

Figure 2.19: Rear view of the UG10 test set-up. The pump outlet transports water to the backside of the flume, from which it flows to the front of the flume below the structure.

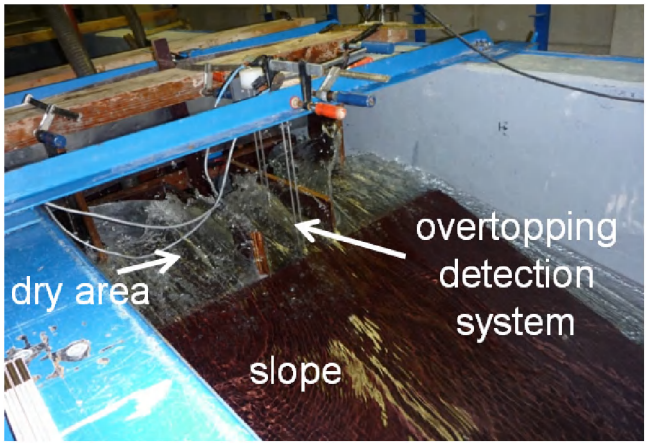

Figure 2.20: Front view of the UG10 test set-up. The width of the collection zone of the overtopped water is 0.20 m. The overtopping detection system is clearly visible.

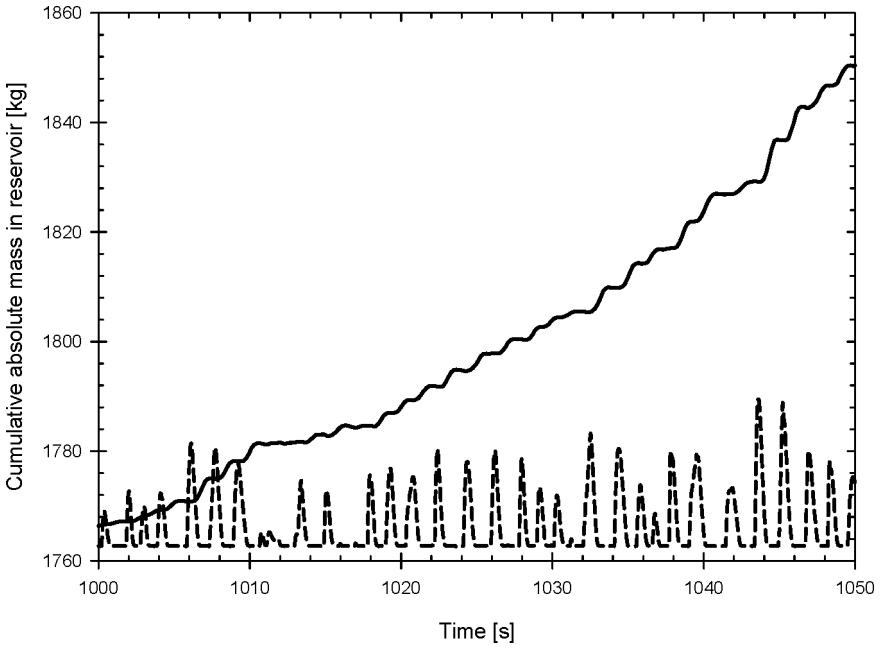

Figure 2.21: Typical example of output signal of overtopping detection system for UG10 test set-up, with the corresponding cumulative weigh cell signal.

Similar to section 2.4, the quality of the calculation of the wave-by-wave overtopping volumes is verified based on the size of the peaks in the curve of the time-differentiated cumulative mass in the reservoir over time (Fig. 2.22). The size of the negative and positive peaks is significantly reduced (down to -2 kg/s and 10 kg/s only) compared to the AAU08 test set-up for a similar test, confirming the positive effect of the adjustments. Accordingly, the wave-by-wave overtopping volumes can be determined more accurately. This is confirmed by a number of examples (section 2.6).

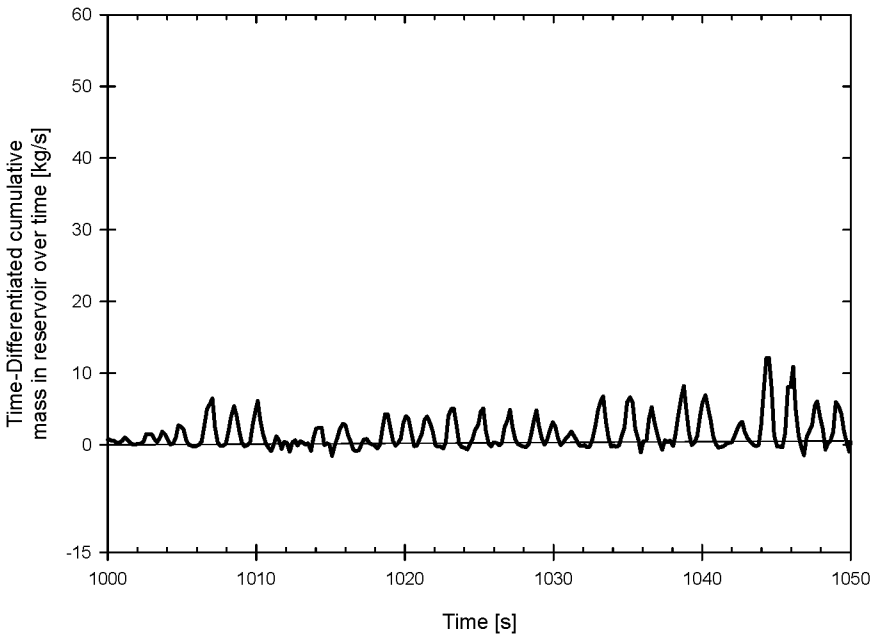

Figure 2.22: Time-differentiated cumulative mass in reservoir over time –UG10 test set-up.

2.6 Accuracy of the UG10 test set-up - Examples

The procedure to determine the wave-by-wave overtopping volumes (described in sections 2.2.3 and 2.4) has been programmed in Matlab® to analyze the test results of the AAU08 and UG10 test series. The code of the final Matlab®-script for the UG10 test series is given in Appendix B.

In order to verify the ability of this Matlab®-script to derive the wave-by-wave overtopping volumes accurately, two series of known water masses have been poured into the reservoir. Next, the wave-by-wave overtopping masses calculated by the Matlab®-script have been compared to the manually added overtopping masses.

In contrast to the AAU08 test series, the approach suggested in section 2.2.1 has not been used for the UG10 test series. Accordingly, Eq. (2.1a) has not been used in the Matlab®-script. Instead, an interpolation between the different values in the calibration curve, two-by-two, has been carried out (see Appendix B), since this approach results in more accurate predictions compared to a global interpolation between all data points in the calibration curve. The uncertainty on the calculated relative masses is only determined by the accuracy of the weigh cell used for determining the masses added to the reservoir (0.002 kg) and the accuracy of the weigh cell below the reservoir (0.005 kg). Nevertheless, the calculated absolute masses do not exhibit the accuracy of the weigh cell used for determining the added masses (e.g. 0.771 kg in Table 2.1).

In the first test series, relatively small masses of water have been added, also during pumping (Table 2.1). For each added mass, the corresponding absolute mass calculated by the Matlab®-script is given. Furthermore, the difference between the added and calculated absolute masses is given in the fourth column of Table 2.1. The fifth column mentions whether the mass is added during pumping or not.

Table 2.1: Accuracy of UG10 test set-up - Time series 1.

Mass Nr.	**Added mass [kg]**	**Calculated mass [kg]**	**Difference between added and calculated [kg]**	**Remarks**
1	0.604	0.602	-0.002	
2	0.714	0.771	0.057	during pumping
3	0.130	0.142	0.012	during pumping
4	0.468	0.466	-0.002	
5	0.022	0.022	0.000	
6	0.290	0.281	-0.009	

When no pumping occurs, the differences between the added and calculated masses are of the order of magnitude of the accuracy of the weigh cell used for determining the added masses. This means that when no pumping occurs, the Matlab®-script is able to determine both very small and relatively large overtopping masses.

During pumping, larger differences appear between the added and calculated masses of water, both for smaller and larger added masses. This is due to the spreading on the characteristic pump curve. The fact that the pumped absolute mass for the different pump curves, generated to determine the characteristic pump curve,

is positioned within ± 0.090 kg to the pumped absolute mass of the characteristic pump curve illustrates that spreading.

In the second test series, relatively large and small volumes have been added to the reservoir. In particular, a large overtopping volume (4.484 kg) has been added to the reservoir during pumping. The results for the second example are shown in Table 2.2.

Table 2.2: Accuracy of UG10 test set-up - Time series 2.

Mass Nr.	**Added mass [kg]**	**Calculated mass [kg]**	**Difference between added and calculated [kg]**	**Remarks**
1	1.662	1.653	-0.009	
2	0.016	0.014	-0.001	
3	4.484	4.445	-0.039	during pumping
4	1.652	1.623	-0.029	during pumping
5	0.306	0.315	0.009	
6	0.730	0.728	-0.002	
7	0.030	0.032	0.002	
8	0.586	0.571	-0.015	
9	0.012	0.014	0.002	
10	0.006	0.005	-0.001	

The findings are similar to the ones of the first test, i.e. the maximum difference between added and calculated masses occurs during pumping.

Based on Table 2.1 and Table 2.2, the following general conclusions are made concerning the accuracy of determination of the overtopping volumes by the Matlab®-script:

- When no pumping occurs, the accuracy of the calculated wave-by-wave overtopping volumes is determined by the reliability of the calibration curve. For the UG10 test series, this reliability is determined by the accuracy of the weigh cell used for determining the added masses. The reliability for the AAU08 test series is that of the linear regression line through the calibration curve, which means the accuracy of the calculated overtopping volumes is slightly lower for the AAU08 test series.

- During pumping, the accuracy of determination of the wave-by-wave overtopping volumes is determined by the spreading on the characteristic pump curve and the reliability of the calibration curve, since this curve has been used to translate the pump curve expressed in relative masses to the pump curve expressed in absolute masses. As mentioned in section 2.4, the spreading on the characteristic pump curve for the AAU08 test series is relatively high due to a number of "children's diseases" in the measurement set-up.

Both the accuracy of the weigh cell and the spreading on the characteristic pump curve are limited for the UG10 test series. Accordingly, the overtopping volumes are accurately calculated by the Matlab®-script described in Appendix B.

2.7 Conclusions

Two laboratory test set-ups have been developed during this PhD-research: AAU08 test series and UG10 test series. The test set-up of the UG10 test series is an improved version of the test set-up of the AAU08 test series and enables to measure large wave-by-wave overtopping volumes accurately. Both test set-ups are based on the weigh cell technique, which is traditionally used for measuring small wave overtopping masses at scale models of sea defense structures.

Since large average overtopping rates occur for steep low-crested slopes, a pump is suspended inside the reservoir which pumps water from the reservoir to the wave flume. The presence of the pump inside the reservoir requires a calibration curve between the real masses and the measured masses, and a compensation for pumping, in order to determine the cumulative real mass of water over a test run. The curve of the cumulative real mass of water over time is the basis for determining the average overtopping rates and wave-by-wave overtopping volumes.

An accurate determination of both parameters requires an accurate calibration curve and an accurate compensation for pumping. Hence, a number of additional adaptations have been carried out to the traditional weigh cell measurement technique. For the most accurate test set-up of the UG10 test series, these adaptations consist of structural adjustments and measures taken in the data acquisition system (a small sampling frequency for the weigh cell, a binary signal) and during the analysis of the output signals. The structural adjustments incorporate decreasing the length of the chute, installing a proper overtopping detection system, using a return valve for the pump, allowing wave overtopping over the whole width of the flume, guiding the outflow of the pump to the front of the wave flume below the structure, and limiting the oscillations of the water inside the reservoir.

A methodology has been developed to determine the average overtopping rates and large wave-by-wave overtopping volumes accurately for the adjusted test set-up and has been programmed in a Matlab®-script.

The effectiveness of the compensation for pumping has been illustrated by the small size of the negative peaks in the curve of the differentiated cumulative mass of water in the reservoir against time.

Furthermore, the applicability of the Matlab®-script to determine the wave-by-wave overtopping volumes accurately has been confirmed by comparing measured and calculated (by the Matlab®-script) overtopping masses for two test series with known measured overtopping masses.

3

Experimental tests - test conditions

In the previous chapter, two test set-ups are described that have been used to determine the overtopping behaviour of steep low-crested slopes: the AAU08 test set-up (section 2.4) and the UG10 test set-up (section 2.5). Chapter 3 describes the test conditions of each of the corresponding experimental test series, the AAU08 test series and UG10 test series. It includes a description of the wave characteristics, wave flumes and tested geometries.

3.1 Wave characteristics

The original scope of this PhD-research is the optimization of the performance of overtopping wave energy converters (OWECs) with a single level reservoir. Hence, in accordance to the experimental tests on OWECs with a single level reservoir carried out by Kofoed (2002), irregular waves have been generated for both the AAU08 test series and the UG10 test series based on the scatter diagram for a particular location in the Danish North Sea: Point 3 (Meyer 2002). This point is located 150 km off the Danish shore; the water depth is 39 m.

A scatter diagram shows the annual average frequencies of occurrence in time $FO_{j,l}$ [%] of all sea states at a particular location, for a specific acquisition period and wave direction. Each row in the scatter diagram corresponds to an interval of characteristic wave heights, with class representative H_j [m] (subscript *j*), while each column corresponds to an interval of characteristic wave periods, represented by T_l [s] (subscript *l*). Each cell of the scatter diagram is referred to as a *sea state*. The combinations of characteristic wave heights and wave periods each characterize a particular wave condition measured or simulated at the particular location. These

parameters can be either based on the time series of the water surface elevation (time domain), or on the corresponding wave spectrum (frequency domain).

In order to limit the number of sea states for preliminary design purposes, characteristic sea states have been defined. These sea states are a weighted average of the total number of sea states in the scatter diagram. For each wave height H_j, a weighted wave period has been defined as follows:

$$T_j = \sum_{l}^{N_T} T_l \, FO_{j,l} \tag{3.1}$$

where N_T [-] is the number of characteristic wave periods for each of the wave heights H_j in the scatter diagram. Typically, only the wave height intervals with a frequency of occurrence $FO_j = \sum_{l=1}^{N_T} FO_{j,l}$ [%] larger than 1% are considered.

By applying this method, five characteristic sea states have been found based on the omnidirectional annual average scatter diagram of Point 3 (Kofoed 2002). For each characteristic sea state, the significant wave height $H_{s,j}$, the peak wave period $T_{p,j}$, the frequency of occurrence in time FO_j and the wave power $P_{wave,j}$ [kW/m] are given (Table 3.1). A single peaked wave spectrum applies in Point 3. Therefore, the peak incident wave period is related to the spectral incident wave spectrum by $T_{p,j} = 1.1 T_{m-1,0,j}$ in this PhD-manuscript.

Table 3.1: Five characteristic sea states at Point 3 (Kofoed 2002).

Sea state number j	**$H_{s,j}$ [m]**	**$T_{p,j}$ [s]**	**Probability of occurrence FO_j [%]**	**Wave power $P_{wave,j}$ [kW/m]**
1	1.0	5.6	47.6	2.5
2	2.0	7.0	21.4	13.6
3	3.0	8.4	9.6	35.0
4	4.0	9.8	4.1	69.3
5	5.0	11.2	1.7	123.7

Note that the sum of the frequencies of occurrence over the five sea states is only 85 %. The sea states occurring at the remaining 15 % of the time correspond to significant wave heights that are either smaller than 0.5 m (± 14.0%) or larger than

5.5 m (± 1.0 %). These sea states are omitted by assuming that no potential energy is captured for the smaller wave heights and that the contribution of the larger wave heights to the overall hydraulic efficiency is negligible. Consequently, from the energy point of view, this is a conservative approach.

In order to generate the wave heights and wave periods from Table 3.1 in the wave flumes of the AAU08 and UG10 test series (sections 3.2 and 3.3), a Froude length scale of 1:30 is used for both test series. The scaled wave heights and wave periods are shown in Table 3.2.

Table 3.2: Five characteristic sea states at Point 3, scaled down with Froude length scale 1:30.

Sea state number *j*	**Reference name**	$H_{s,j}$ **[m]**	$T_{p,j}$ **[s]**	$s_{p,j}$ **[-]**	$s_{m\text{-}1,0,j}$ **[-]**
1	W11	0.033	1.022	0.020	0.024
2	W22	0.067	1.278	0.026	0.034
3	W33	0.100	1.534	0.027	0.033
4	W44	0.133	1.789	0.027	0.032
5	W55	0.167	2.045	0.026	0.031

Each of the characteristic sea states is given a reference name (first column in Table 3.2), which is used further in this document. The name contains two numbers, respectively referring to the wave height $H_{s,j}$ and wave period $T_{p,j}$ of the corresponding sea state. As an example, W33 corresponds to a sea state with a wave height $H_{s,3}$ = 0.100 m and a wave period $T_{p,3}$ = 1.534 s. These five characteristic sea states (W11 to W55) have been used during the experimental tests of the AAU08 test series. As mentioned in section 1.2, the range of application for the wave steepness of these sea states is rather small, with $s_{m-1,0} \approx 0.033$. In order to broaden this range of application for the UG10 test series, two measures have been taken:

- additional wave heights have been introduced: $H_{s,0}$ = 0.020 m (0.6 m in prototype) and $H_{s,6}$ = 0.185 m (5.6 m in prototype); and
- additional sea states, assembled from wave heights and wave periods of the five original characteristic sea states (Table 3.2) have been applied. Each wave period in Table 3.2 has been combined with three wave heights (Eq. 3.2), with j ranging from 1 to 5.

$$T_{p,j} \leftrightarrow \begin{cases} H_{s,j-1} \\ H_{s,j} \\ H_{s,j+1} \end{cases} \tag{3.2}$$

The resulting characteristic sea states used during the UG10 test series are given in Table 3.3.

Table 3.3: Characteristic sea states used during the UG10 test series.

Reference name	H_s **[m]**	T_p **[s]**	s_p **[-]**	$s_{m-1,0}$ **[-]**
W01	0.020	1.022	0.012	0.015
W11	0.033	1.022	0.020	0.024
W21	0.067	1.022	0.041	0.050
W12	0.033	1.278	0.013	0.016
W22	0.067	1.278	0.026	0.032
W32	0.100	1.278	0.039	0.047
W23	0.067	1.534	0.018	0.022
W33	0.100	1.534	0.027	0.033
W43	0.133	1.534	0.036	0.044
W34	0.100	1.789	0.020	0.024
W44	0.133	1.789	0.027	0.032
W54	0.167	1.789	0.033	0.040
W45	0.133	2.045	0.020	0.025
W55	0.167	2.045	0.026	0.031
W65	0.185	2.045	0.028	0.034

For each experimental test, waves have been generated based on the above sea states (Table 3.2 for AAU08 test series and Table 3.3 for UG10 test series) and by assuming a parameterised JONSWAP[1] spectrum with a peak enhancement factor 3.3. Furthermore, at least 1000 waves have been generated and analyzed for each experimental test to obtain average overtopping rates that are statistically independent of the number of waves of the test (Kortenhaus et al. 2004).

The next two sections describe the wave flumes and geometries which have been used for the AAU08 test series, section 3.2 and the UG10 test series, section 3.3.

[1] JONSWAP = Joint North Sea Wave Project (Hasselmann et al. 1973)

The effects of wave shoaling and wave breaking on the wave characteristics at the toe of the structure are discussed in section 3.4. Finally, section 3.5 elaborates on the scale effects on the average overtopping rates of steep low-crested slopes.

3.2 AAU08 test series – test conditions

The AAU08 test series have been carried out in a wave flume with dimensions 25 m x 1.2 m x 1.5 m (length x width x height) at the Department of Civil Engineering at Aalborg University, Denmark. The concrete bottom of the flume has a slope of approximately 1:60, reducing the height inside the wave flume from 1.5 m at the wave paddle to 1.1 m at the outer end of the wave flume. The flume is equipped with a piston-type wave maker with a stroke of 0.60 m.

The tested structures have a width of 0.5 m (section 2.4) and feature steep slopes that are partly fractioned. The upper slope has a fixed angle α_u [-] for which $\cot\alpha_u = 1.73$, and a height v_u [m] of 0.05 m or 0.10 m. The lower slope angle α_d [-] varies between $\cot\alpha_d = 1.73$ over $\cot\alpha_d = 1.19$ to $\cot\alpha_d = 0.84$ and has a fixed height v_d [m] of 0.500 m. The slopes are fractioned due to the presence of the overtopping detection system (described in section 2.4) which is fixed to the upper slope. For time-saving reasons, the overtopping detection system has not been removed from the crest of the slope, therefore requiring a fixed upper slope. The lower slope is altered independent from the upper slope and the dry area.

The characteristic slope angle α required for calculating the breaker parameter $\xi_{m-1,0}$ (Eq. 1.1) has been determined in a similar way compared to the mean angle α_{incl} of bermed sea defence structures defined in the CLASH database (Van der Meer et al. 2005a). The expressions for calculating the characteristic slope angle α for the AAU08 test series are given in appendix C.

The tested structures have been subjected to the sea states in Table 3.2. Variations in (relative) crest freeboard are achieved by changing the water depth and the height of the upper slope (Table 3.4).

Table 3.4: Crest freeboard heights R_c [m] for different water depths h_t and heights of upper slope h_u for AAU08 test set-up.

	Crest freeboard height R_c	
h_t [m]	**v_u = 0.050**	**v_u = 0.100**
0.450	0.100	0.150
0.475	0.075	0.125
0.500	0.050	0.100
0.525	0.025	0.075

The water depth at the toe of the structure has been varied between 0.450 m, 0.475 m, 0.500 m and 0.525 m. It is relatively large, in accordance to Eq. (1.8). This explains the rather large value of v_d. A definition sketch of the parameters that characterize the geometry of the structures tested during the AAU08 test series is shown in Fig. 3.1.

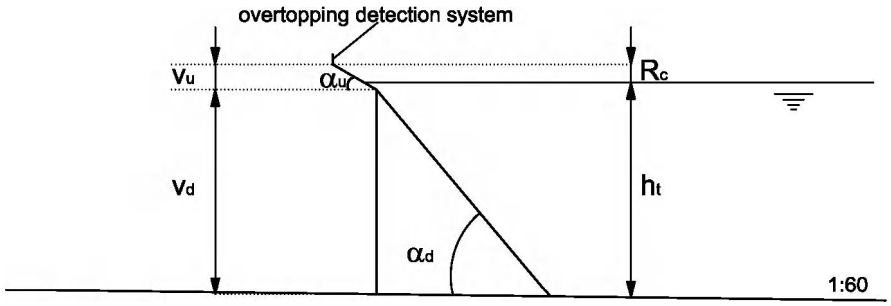

Figure 3.1: Parameters characterizing the geometry of the tested structures of the AAU08 test series.

In total, 207 tests (including replicates) have been carried out during the AAU08 test series, with wave characteristics based on Table 3.2, slopes with $\cot\alpha_d$ = 1.7, 1.19 and 0.84 and crest freeboards and water depths according to Table 3.4. The test matrix (design of experiments, DoE) of the AAU08 test series is shown in Table 3.5.

The corresponding test results have been gathered in the AAU08 dataset. For this dataset, the following ranges apply:

$$0.98 < \cot\alpha \leq 1.73 \tag{3.3}$$

$$3.1 < \xi_{m-1,0} < 5.6 \tag{3.4}$$

$$3.1 < \frac{h_t}{H_{m0}} < 18.9 \tag{3.5}$$

$$0.2 < \frac{R_c}{H_{m0}} < 2.0 \tag{3.6}$$

Note that the ranges of application of Eqs. (1.6) to (1.9) are fulfilled.

Table 3.5: Test matrix for the AAU08 test series.

3 slope angles α_d							
	8 crest freeboards						
		H_s **[m]**	T_p **[s]**				
			1.022	1.278	1.534	1.789	2.045
		0.033	W11				
		0.067		W22			
		0.100			W33		
		0.133				W44	
		0.167					W55

A cross section of the AAU08 test set-up is shown in Fig. 3.2 (WG stands for "wave gauge"). Photos of the AAU08 test set-up are shown in section 2.4.

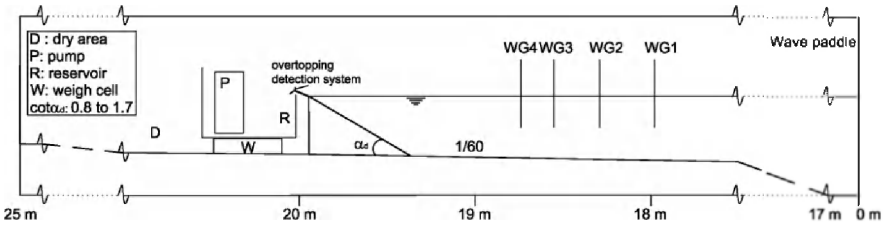

Figure 3.2: Cross section of test set-up of the AAU08 dataset (WG = "wave gauge").

The incident wave characteristics at the toe of the structure have been determined by performing a reflection analysis using the software package Wavelab™

(developed at Aalborg University, Denmark). This reflection analysis separates the incident and reflected waves based on the methodology described by Mansard and Funke (1980). This methodology requires the total water surface elevations at three wave gauges. Mansard and Funke (1980) have determined the limits for the distances between these three wave gauges and for the distance between the structure and the wave gauge closest to the structure. These limits depend on the characteristic wave lengths of the waves in the wave flume. Larger wave lengths correspond to larger the distances between the three wave gauges. Since the range of peak wave periods between the characteristic sea states is relatively large (Table 3.2), the distances between the wave gauges vary accordingly. Instead of changing the positions of the three wave gauges according to the peak wave periods, four wave gauges have been used during the AAU08 test series (i.e. WG1, WG2, WG3 and WG4 in Fig. 3.2). For each peak wave period, three out of the four wave gauges fulfil the requirements for the distances set by Mansard and Funke (1980).

A large dry area (D in Fig. 3.2) is positioned at the outer end of the wave flume (section 2.4). This area is accessible in order to make adjustments to the overtopping measurement set-up. The presence of the dry area reduces the area of the wave flume seaward of the structure to 20 m (Fig. 3.2).

The weigh cell (W in Fig. 3.2) has a capacity of 150.00 kg, and an accuracy of 0.01 kg. It should be noted that the output of the weigh cell to the data acquisition system does not consist of relative masses of water inside the reservoir, but of volts. Consequently, the calibration curve (section 2.2.1) is determined between the real mass of water inside the reservoir and the output of the weigh cell in volts. The pump is triggered by the weigh cell reaching a real mass of water of 70.00 kg inside the reservoir. On average, a mass of 37.30 kg is transported to the flume during the time of pumping, i.e. T_{pump} = 4.6 s. This corresponds to an average pump discharge of 30 m³/h (8.33 l/s). The dimensions of the reservoir of the AAU08 test set-up are given in appendix A.

3.3 UG10 test series – test conditions

The UG10 test series have been carried out in a wave flume with dimensions 30 m x 1.0 m x 1.2 m (length x width x height) at the Department of Civil Engineering of Ghent University. The flume is equipped with a piston-type wave maker which has a stroke of 1.5 m. In contrast to the wave flume used for the AAU08 test series, the bottom of this flume is horizontal. However, a foreshore is installed inside the wave flume, to allow transport of the pumped water below the structure (section 2.5). The foreshore consists of a rather short slope of 1:20, starting at a distance of 10 m from the wave paddle, followed by a horizontal part up to a

distance of 24 m from the paddle. This horizontal part reduces the depth of the flume by 0.27 m.

The tested structures feature uniform smooth impermeable steep slopes extending to the seabed and low crest freeboards. Nine slope angles are used, from *steep* to *mild*, varying between $\cot\alpha = 0.36$ and $\cot\alpha = 2.75$. The slopes can be altered independent from the dry area. Similar to the AAU08 test set-up large water depths have been used to avoid heavy depth-limited wave breaking. Due to the presence of the foreshore, even larger water depths had to be used, up to the limits of the range of application of the wave paddle. The crest of the structures has a fixed position, at 0.57 m above the horizontal part of the foreshore, i.e. the "point of rotation" for the slopes. Each of the slope angles is combined with three crest freeboards. A varying crest freeboard is achieved by varying the water depth on the horizontal part of the foreshore between 0.500 m, 0.525 m and 0.550 m. The corresponding values for the crest freeboard R_c are 0.070 m, 0.045 m and 0.020 m. An overview of the applied geometrical parameters is given in Table 3.6.

Table 3.6: Ranges of slope angle α , water depth at wave paddle h_{paddle} and near the toe of the structure h_t, and crest freeboard R_c for the UG10 test series.

Parameter	**Values**
$cot\ \alpha$ [-]	0.36, 0.58, 0.84, 1.00, 1.19, 1.43, 1.73, 2.14, 2.75
h_{paddle}	0.770, 0.795, 0.820
h_t	0.500, 0.525, 0.550
R_c [m]	0.070, 0.045, 0.020

A cross section of the UG10 test set-up is shown in Fig. 3.3. Photos of the UG10 test set-up are shown in section 2.5.

The different geometries (nine slope angles combined with three crest freeboards) have been subjected to irregular waves, characterized by the combinations of significant wave height H_s and peak period T_p shown in Table 3.3. The test matrix (design of experiments, DoE) is schematized in Table 3.7.

Table 3.7: Test matrix for the UG10 test series.

9 slope angles							
	3 crest freeboards						
		H_s **[m]**	T_p **[s]**				
			1.022	1.278	1.534	1.789	2.045
		0.020	W01				
		0.033	W11	W12			
		0.067	W21	W22	W23		
		0.100		W32	W33	W34	
		0.133			W43	W44	W45
		0.167				W54	W55
		0.185					W65

Similar to the AAU08 test series, a parameterized JONSWAP spectrum with peak enhancement factor 3.3 has been applied and at least 1000 waves have been generated for each experimental test.

In total, 366 tests (no replicates) have been carried out during the UG10 test series, with wave characteristics given in Table 3.7 and with slope angles, crest freeboards and water depths from Table 3.6. The test matrix in Table 3.7 allows to study the independent effects of slope angle, crest freeboard, and wave steepness on the overtopping behaviour of steep low-crested slopes in detail. The results are gathered in a dataset, referred to as the *UG10 dataset*. For this dataset, the following ranges apply:

$$0.36 \le \cot\alpha \le 2.75 \tag{3.7}$$

$$0.1 < \frac{R_c}{H_{m0}} \le 2.0 \tag{3.8}$$

$$2.6 < \frac{h_t}{H_{m0}} < 23.4 \tag{3.9}$$

$$0.02 < s_{m-1,0} < 0.05 \tag{3.10}$$

$$1.7 < \xi_{m-1,0} < 21.9 \tag{3.11}$$

Note that the ranges of application of Eqs. (1.8) and (1.9) are fulfilled. In order to validate the UG10 dataset against existing knowledge for traditional sea defence

structures, the range of application of $\cot\alpha$ in Eq.(1.6) has been extended to larger values (Eq. 3.7), resulting in values of the breaker parameter smaller than 2.0 in 17 tests (Eq. 3.11). Compared to the AAU08 dataset (Eqs. 3.3 – 3.6), the ranges are all broader.

The separation of the incident and reflected waves is carried out similar to the AAU08 test series, using the software package Wavelab™, which is based on the methodology of Mansard and Funke (1980). Two sets of three wave gauges have been installed (Fig. 3.3): one in front of the foreshore in the water depth h_{paddle} and the other in front of the structure, in the water depth h_t.

Furthermore, the active wave absorption system (Troch 2000) has been activated. This separates the incident and reflected waves in real time, based on the total water surface elevations at two wave gauges. Its purpose is to determine a correction signal that corresponds to the reflected waves travelling in the opposite direction. This signal is then added to the paddle movements to eliminate the reflected waves in real time. The methodology for the real time wave separation is based on the time domain method of (Frigaard and Brorsen 1995).

The presence of the dry area inside the wave flume reduces the area of the wave flume seaward of the structure to 22.5 m (Fig. 3.3). Due to the shape of the dry area, overtopping occurs over the total width of the wave flume (section 2.5). Correspondingly, the structures have been built over the total width of the wave flume. The width of the collection zone of the overtopped water is 0.20 m.

The weigh cell has a capacity of 100.000 kg, and an accuracy of 0.005 kg. A calibration curve is determined between the relative mass of water inside the reservoir and the cumulative absolute added mass (section 2.2.1). The pump is triggered by the weigh cell reaching a relative mass of water of 70 kg inside the reservoir. On average, a mass of 21.600 kg is transported to the flume during the intended time of pumping, i.e. 4.6 s (without the cooling down period, Fig. 2.5). This corresponds to an average pump discharge of 17 m^3/h (4.72 l/s).

The dimensions of the reservoir of the UG10 test set-up are given in appendix A.

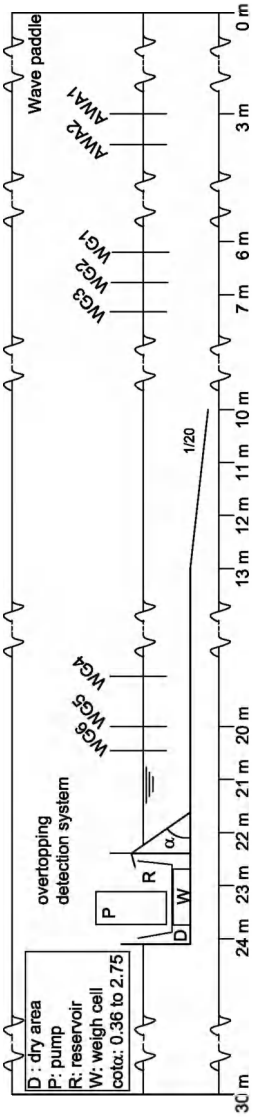

Figure 3.3: Cross section of test set-up of the UG10 dataset (WG – "wave gauge", AWA="wave gauge used for the active wave absorption system").

3.4 Effects of wave shoaling and wave breaking

The overtopping behaviour of steep low-crested slopes is determined by the characteristics of the waves occurring at the toe of the structure. Since the overtopping behaviour of steep low-crested slopes is studied for the wave characteristics in Table 3.2 for the AAU08 test series and in Table 3.3 for the UG10 test series, the waves at the toe of the tested structures should feature those intended characteristic wave height and wave period.

For the AAU08 test series, those characteristics have been used as input for the wave generation software of the wave flume. Based on the analysis of the waves at the toe of the structure, small deviations occur between the significant wave heights at the toe of the structure and the significant wave heights used as input for the wave paddle. Both smaller and larger significant wave heights appear at the toe of the structure compared to the input wave heights. No compensation has been used for these deviations. Hence, the significant wave heights at the toe of the tested structures deviate a little from the intended values in Table 3.2.

For the UG10 test series, the significant wave heights in the deeper part (± 0.80 m) of the wave flume seem to be larger than the input wave heights. Furthermore, the wave heights at the toe of the structures (water depths ± 0.50 m) are smaller than the wave heights in deeper water, but in general still larger than the input wave heights at the wave paddle. In order to compensate for these deviations for the UG10 test series and to achieve the significant wave heights from Table 3.3, a calibration between the input wave heights and the wave heights occurring at the toe of the structure has been carried out, based on tests without the tested structures but with an absorption beach instead.

The increases in significant wave height between the input wave heights at the wave paddle and the wave heights occurring in deeper water (± 0.80 m), are considered to be model effects. When analyzing the AAU08 and UG10 test results (chapter 5), only wave characteristics measured at the toe of the structures have been used.

The decreases in significant wave height between the values occurring at deeper water and the values at the toe of the structure for the UG10 test series can be attributed to the effects of wave shoaling and wave breaking. These aspects are discussed in the following two sections 3.4.1 and 3.4.2.

3.4.1 Wave shoaling

When waves travel from deep water to more shallow water, an increase in wave height occurs due to a reduction in the group velocity c_g, i.e. the energy propagation velocity of a wave, defined in Eq. 3.11 for linear waves. This phenomenon is referred to as wave shoaling (Goda 2000).

$$c_g = c\left(\frac{1}{2} + \frac{k\,h}{\sinh(k\,h)}\right) \tag{3.11}$$

The parameter c is the propagation velocity of the linear wave, defined as the ratio of the wave length L and the wave period T:

$$c = \frac{L}{T} \tag{3.12}$$

For linear waves, the wave length is defined by Eq. (3.13). When combining Eqs. (3.12) and (3.13), it appears that waves with different wave length generally correspond to different wave propagation velocities, i.e. a dispersive behaviour. Hence, Eq. (3.13) is referred to as the *dispersion relationship*. The parameter h is a generic water depth, while the parameter k is the wave number which is inversely proportional to the wave length (Eq. 3.14).

$$L = \frac{g\,T^2}{2\,\pi}\tanh(k\,h) \tag{3.13}$$

$$k = \frac{2\,\pi}{L} \tag{3.14}$$

The effect of wave shoaling is expressed by the shoaling coefficient K_S, which expresses the relative change in wave height when moving from deep water to more shallow water, as defined in Eq. (3.15) (Lykke Andersen and Frigaard 2008). It is based on the assumptions that:

- linear wave theory is valid both in deep water and more shallow water;
- no wave breaking and no current occurs;
- the waves are long-crested; and
- the wave period is unchanged between deep and more shallow water.

$$K_S\left(h,h_{deep}\right)=\frac{H}{H_{deep}}=\sqrt{\frac{c_{g,deep}}{c_g}} \tag{3.15}$$

The parameter H represents the wave height of the linear wave in the more shallow location; H_{deep} is the wave height in deep water. Based on Eqs. (3.11) to (3.14), the expression in Eq. (3.15) can be rewritten as:

$$K_S\left(h,h_{deep}\right)=\sqrt{\frac{\frac{1}{2}\frac{kh}{k_{deep}h}}{\left(\frac{1}{2}+\frac{kh}{\sinh\left(2kh\right)}\right)}} \tag{3.16}$$

with

$$kh\tanh\left(kh\right)=k_{deep}h \tag{3.17}$$

The derivation of the expressions for K_S and $k\,h$ in Eq. (3.16) and Eq. (3.17) is given in Appendix D. Both expressions have been plotted as a function of $k_{deep}\,h$ (Fig. 3.4). This figure explains the effect of wave shoaling for a general decrease in water depth. When a linear wave approaches more shallow water (decreasing value of h), the shoaling coefficient first drops slightly below $K_S=1.0$, before a sharp increase occurs to values above K_S=1.0 (Fig. 3.4). Accordingly, the wave height first slightly decreases compared to the wave height in deep water, while it becomes considerably larger when the water depth decreases further.

For the UG10 test series, wave shoaling affects the wave heights due to the presence of the foreshore, which reduces the water depth approximately from 0.80 m to 0.50 m. Based on Fig. 3.4, the decreases in significant wave height observed between the values occurring at deeper water and the values at the toe of the structure for the UG10 test series can be partly explained, using the parameters for the water depth and the wave length in Table 3.8.

The parameter $k\,h$ on the vertical axis of Fig. 3.4 is either $k_{m-1,0,t}\,h_t$ or $k_{m-1,0,paddle}\,h_{paddle}$.

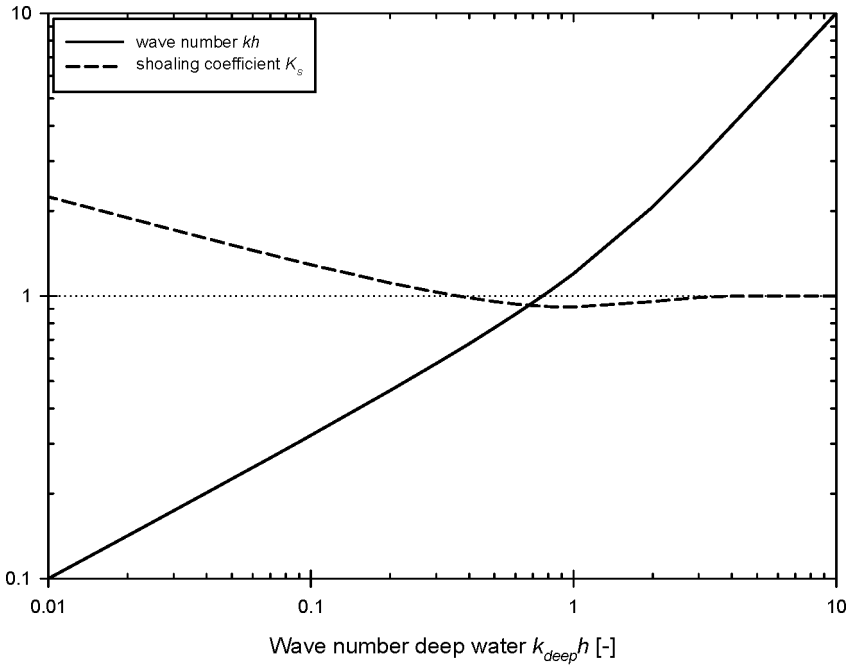

Figure 3.4: Wave shoaling, theoretical effect of wave number on the shoaling coefficient for linear waves.

The UG10 tests with smaller wave periods (T_p = 1.022 s, 1.278 s and 1.534 s) correspond to values of $k_{m-1,0,t}\,h_t$ ranging between 1.0 and 2.6, while the values of $k_{m-1,0,paddle}\,h_{paddle}$ range between 1.5 and 3.9. This is shown in Fig. 3.5, which illustrates that for a particular wave period $T_{m-1,0}$, the value of $k\,h$ at the paddle is larger than at the toe of the structure.

Table 3.8: Wave parameters used to explain effects of wave shoaling for the UG10 test results.

	Toe of the structure	**Deeper water**
h	h_t (±0.50 m)	h_{paddle} (±0.80 m)
L	$L_{m-1,0,t} = \frac{g T_{m-1,0}^2}{2\pi} \tanh\left(\frac{2\pi}{L_{m-1,0}} h_t\right)$	$L_{m-1,0,paddle} = \frac{g T_{m-1,0}^2}{2\pi} \tanh\left(\frac{2\pi}{L_{m-1,0,paddle}} h_{paddle}\right)$
k	$k_{m-1,0,t}$	$k_{m-1,0,paddle}$

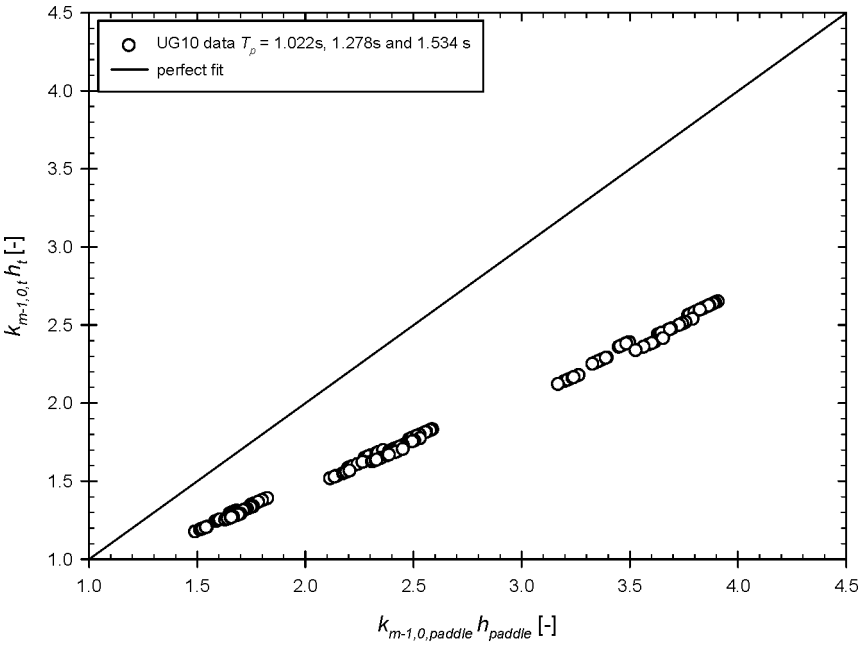

Figure 3.5: Differences in kh for the water depth at the toe of the structure versus the water depth at the wave paddle for the tests of the UG10 test series with T_p = 1.022 s, 1.278 s and 1.534 s.

Based on Fig. 3.4 and the values of $k_{m-1,0,t}\,h_t$ and $k_{m-1,0,paddle}\,h_{paddle}$ in Fig. 3.5, the values of $K_S\left(h_t, h_{deep}\right)$ are smaller than or equal to the corresponding values of $K_S\left(h_{paddle}, h_{deep}\right)$, as illustrated in Fig. 3.6. This explains the decrease in significant wave height between the water depth at the wave paddle and the toe of the structure for tests with smaller wave periods.

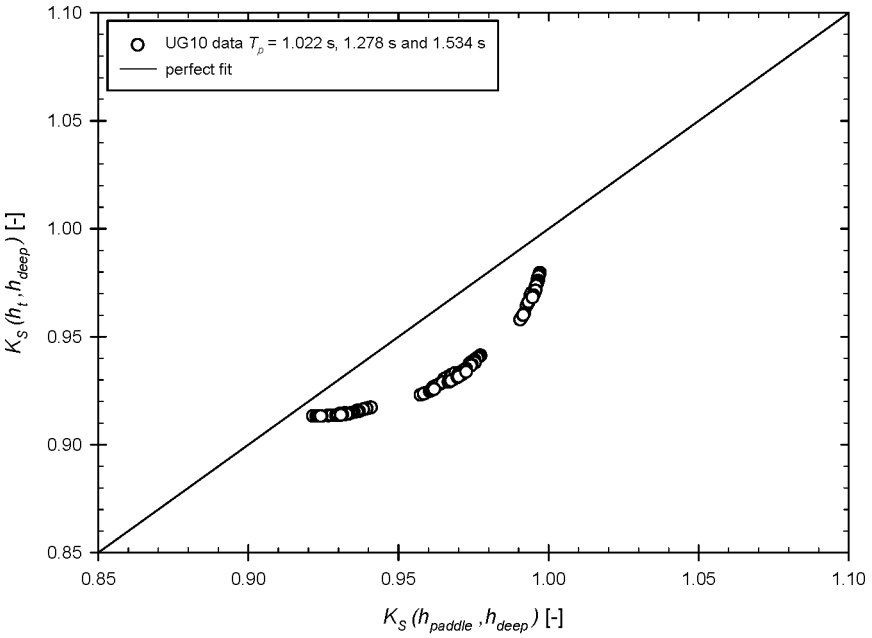

Figure 3.6: Differences in shoaling coefficient K_S for the water depth at the toe of the structure versus the water depth at the wave paddle for the tests of the UG10 test series with T_p = 1.022 s, 1.278 s and 1.534 s.

A similar reasoning applies to the UG10 tests with larger wave periods (T_p = 1.789 s and 2.045 s), resulting in Figs. 3.7 and 3.8. Although the shoaling coefficients for both the water depth at the toe of the structure and at the wave paddle compared to deep water are smaller than 1.0, it appears that an increase in the shoaling coefficient

occurs from $K_S\left(h_{paddle}, h_{deep}\right)$ to $K_S\left(h_t, h_{deep}\right)$. This means that for the tests with larger wave periods an increase in the significant wave height should occur between the water depth at the wave paddle and the water depth at the toe of the structure. However, a decrease in wave height has also been observed for those tests during the UG10 test series. This can be explained by the occurrence of wave breaking (section 3.4.2).

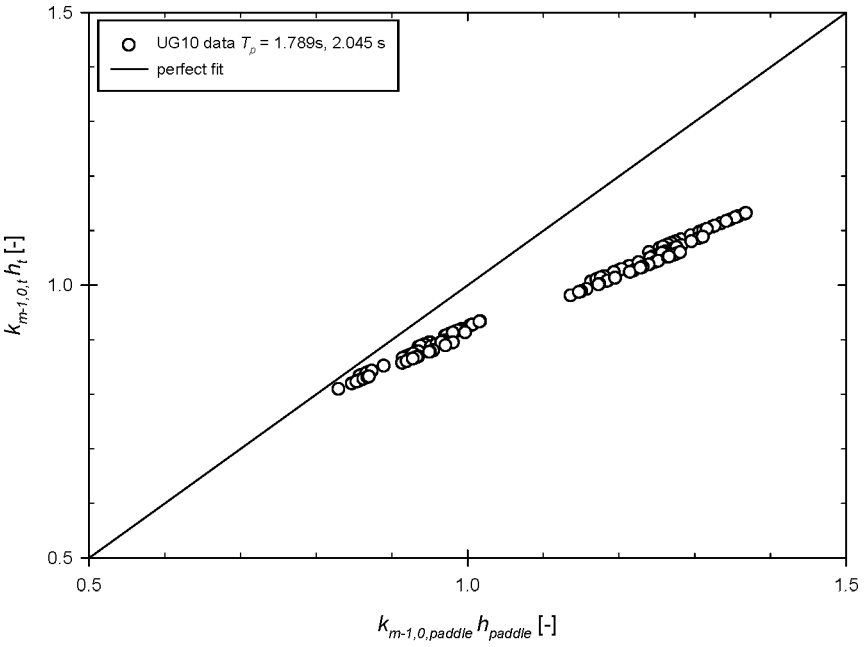

Figure 3.7: Differences in kh for the water depth at the toe of the structure versus the water depth at the wave paddle for the tests of the UG10 test series with T_p = 1.789 s and 2.045 s.

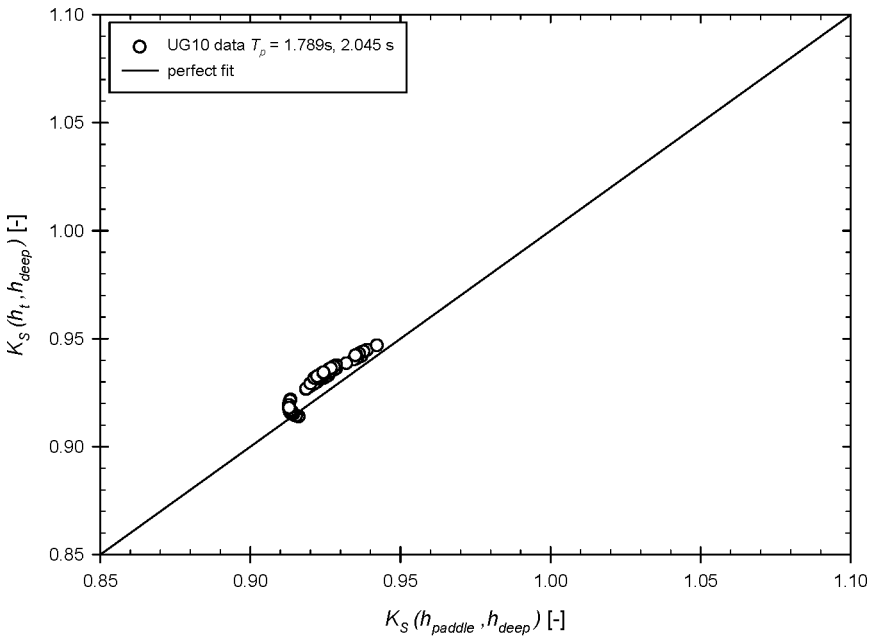

Figure 3.8: Differences in shoaling coefficient K_S for the water depth at the toe of the structure versus the water depth at the wave paddle for the tests of the UG10 test series with T_p = 1.789 s and 2.045 s.

3.4.2 Wave breaking

Based on Eq. (3.11), the major part of the UG10 tests corresponds to non-breaking (surging breaking) waves at the toe of the structure: $\xi_{m-1,0} > 2.0$ - 3.0. However, despite the fact that a wave train is categorized as non-breaking, individual waves of the wave train with the largest wave heights may break.

According to Nelson (1994), a regular wave train on a horizontal bottom with water depth h is affected by depth-induced breaking when its wave height H fulfils:

$$\frac{H}{h} > 0.55 \tag{3.18}$$

Equation (3.18) has been used to verify whether depth-induced wave breaking occurs for the UG10 tests, based on the maximum wave height occurring in deeper water, approximated by $2H_{m0,paddle}$, and on the water depth at the toe h_t. Consequently, depth-induced breaking occurs when:

$$\frac{h_t}{H_{m0,paddle}} < 3.6 \tag{3.19}$$

The ratio $h_t / H_{m0,paddle}$ has been calculated for each UG10 test. Using the above criterion (Eq. 3.19), breaking of the largest waves in the wave train on the horizontal part of the foreshore occurs for the UG10 tests with the largest significant wave heights (Table 3.3). This means, based on the fact that the larger wave heights are combined with larger wave periods for the UG10 test series, that a decrease in the significant wave height occurs from the water depth at the wave paddle to the water depth at the toe of the structure for the UG10 tests with larger wave periods. This is in contrast to Fig. 3.8, which predicts an increase in the significant wave height due to wave shoaling. Since the effect of depth-induced wave breaking is dominant, a decrease in significant wave height occurs:

$$H_{m0,paddle} > H_{m0} \tag{3.20}$$

Based on Eqs. (3.19) and Eq. (3.20), the condition $h_t / H_{m0} > 2.0$ (Eq. 1.8) is not sufficient to avoid depth-induced breaking of the largest waves in a wave train. However, this condition has only been imposed in chapter 1 to avoid the occurrence of large values of the breaker parameter $\xi_{m-1,0}$ due to small values of the wave steepness. Since only the largest waves break, the changes in the shape of the wave spectrum between the water depth at the wave paddle and the toe of the structure are expected to be relatively small. Furthermore, $H_{m0,paddle}$ is only slightly larger than H_{m0}. Hence, the value of the wave steepness $s_{m-1,0}$ will not strongly decrease due to the breaking of the largest waves.

Nevertheless, small variations in the spectral wave parameters occur, which means the effect of the (change in) water depth is included in those parameters. Accordingly, when using the spectral wave parameters, the water depth at the toe of

the structure h_t should not be taken into account as a separate parameter when studying the overtopping behaviour of steep low-crested slopes. Based on this observation and on Fig. 1.5, the average overtopping rate q and the exceedance probability P_V of the wave-by-wave overtopping volumes V_i of steep low-crested slopes are both function (denoted by f_1 and f_2) of the slope angle $\cot\alpha$, crest freeboard height R_c, spectral wave height H_{m0} and spectral wave period $T_{m-1,0}$ (Eq. 3.21).

$$q = f_1\left(\cot\alpha, R_c, H_{m0}, T_{m-1,0}\right) \tag{3.21a}$$

$$P_V = f_2\left(\cot\alpha, R_c, H_{m0}, T_{m-1,0}\right) \tag{3.21b}$$

Depth-induced breaking of the largest waves in a wave train also affects the distribution of the individual wave heights H_i. According to Battjes and Groenendijk (2000), wave heights on shallow foreshores do not follow the Rayleigh probability distribution proposed by Longuet-Higgins (1952). Based on laboratory data of wave heights on shallow foreshores, a model distribution consisting of two two-parameter Weibull probability distributions, i.e. the so-called *composite Weibull distribution*, has been proposed by Battjes and Groenendijk (2000).

The probability of the individual wave heights H_i to exceed a particular wave heigh $\tilde{H}$, assuming a two-parameter Weibull probability distribution function for the individual wave heights, is expressed in Eq. (3.21) (P_H is the exceedance probability and Pr stands for "probability").

$$P_{H,Weibull} = \Pr\left[H_i \geq \tilde{H}\right] = \exp\left(-\left(\frac{\tilde{H}}{a_H}\right)^{b_H}\right) \tag{3.21}$$

The coefficient b_H [-] determines the shape of the two-parameter Weibull distribution and is therefore referred to as the shape factor. The coefficient a_H represents an average individual wave height, hence scaling the individual wave heights in Eq. (3.21), and is therefore referred to as the scale factor.

The composite Weibull distribution consists of a Weibull distribution with a shape factor equal to 2.0 (i.e. the Rayleigh distribution, Eq. 3.22) for the smaller wave heights, and a Weibull distribution with a larger value of the shape factor (usually taken to be 3.6) for the larger wave heights. The parameter H_m is the mean individual wave height.

$$P_{H,Rayleigh} = \exp\left(-\frac{\pi}{4}\left(\frac{\tilde{H}}{H_m}\right)^2\right) \tag{3.22}$$

A comparison between (1) the distribution of the measured individual wave heights, (2) the Rayleigh distribution and (3) the composite Weibull distribution has been made for three tests of the UG10 test series. Two of those tests correspond to depth-limited breaking of the largest waves (Figs. 3.9a and 3.9b), while the third test features smaller wave heights without depth-limited breaking (Fig. 3.9c). It is clear that the data points in Figs. 3.9a and 3.9b are better described with the composite Weibull distribution than with the Rayleigh distribution. Hence, based on Fig. 3.9, the following conclusions can be made:

- the composite Weibull distribution is a better estimate for the distribution of the individual wave heights than the Rayleigh distribution for UG10 tests with larger wave heights;
- the agreement between the distribution of the measured wave heights and the composite Weibull distribution confirms the occurrence of depth-induced wave breaking.

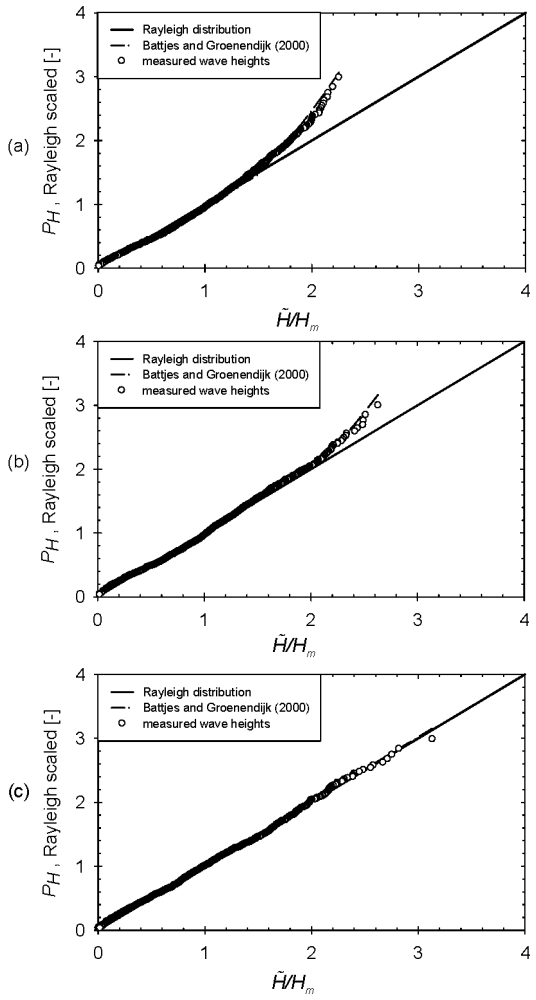

Figure 3.9: Distribution of wave heights at the toe of the structure for the UG10 tests with slope 1:1.4, water depth $h_t = 0.50$ m and wave characteristics according to (a) W55, (b) W45 and (c) W22.

3.5 Scale effects

A detailed study on the importance of scale effects on wave overtopping has been carried out during the CLASH project (De Rouck et al. 2009; Kortenhaus et al. 2004). It has been concluded that the scale effects are important for porous rubble slopes that require an adequate modelling of the porous flow and surface flow of the run-up wedge. Furthermore, when the overtopping rates are small, a surface tension effect occurs in the small scale tests. This effect is however unapparent in prototype.

Although relatively small wave heights have been used in a number of tests of the AAU08 and UG10 test series, the influence of scale effects is expected to be marginal since the tested structures feature smooth impermeable slopes. This is confirmed by previous research on structures with identical features (Kofoed 2002).

3.6 Conclusions

The wave characteristics, wave flumes and tested geometries for both the AAU08 and UG10 test series have been described in this chapter.

During testing, it appeared that differences occur between the significant wave heights at the wave paddle and at the toe of the structure. These differences have been investigated for the UG10 test series and appear to be due to wave shoaling and wave breaking.

Although the significant wave heights of a number of tests of the AAU08 and UG10 test series are relatively small, the influence of scale effects on the overtopping behaviour of steep low-crested slopes is expected to be small.

4

Average overtopping rates of steep low-crested slopes – existing knowledge

The main goal of this chapter is to introduce the most important prediction methods from literature that are able to predict average overtopping rates within the ranges of application of steep low-crested slopes. Prediction methods that are able to predict the overtopping behaviour of neighbouring structures (from a geometrical point of view) of steep low-crested slopes are also described.

4.1 Introduction

The major part of the existing knowledge on wave overtopping originates from research on sea defence structures, which are designed to minimize the amount of water overtopping their crests.

Since the 1950s, scale models of sea defence structures have been tested in wave flumes and wave basins in order to quantify their overtopping behaviour. Until 1980, mainly regular wave tests were carried out using a wave paddle with sinusoidal movements (e.g. Saville 1955). One of the first datasets of irregular wave test results was derived by Paape (1960) using a wind flume (the waves are generated by winds blowing over the water surface of the flume). Sibul and Tickner (1956) also used this technique to generate irregular waves.

Irregular wave generation using a wave paddle was only applied in the 1980s (e.g. Owen 1980). This method of generating irregular waves provides a much more realistic simulation of the waves in the open seas compared to the wind flume, leading to more accurate empirical prediction methods. Up to today, experiments in wave flumes or wave basins applying paddle generated irregular waves are a basic tool to determine the overtopping behaviour of sea defence structures.

Since the 1990s, numerical models have become a valuable tool to simulate wave overtopping at sea defence structures (Ingram 2005). These models solve the governing fluid dynamic equations in a specific fluid domain with specific boundary conditions. Examples are discussed and validated by Hu et al. (2000), Li et al. (2004), Reeve et al. (2008) and Losada et al. (2008).

The advantages of numerical models are numerous, including the high resolution of the output results in each grid point of the fluid domain, the lack of scale effects, the ability to model complex structures and the possibility to adapt structure geometries without large (time) costs. However, the large computational time for high precision simulations and the lack of extensive validation prevent numerical models to be a full alternative for experiments until now. The importance of numerical prediction models is expected to increase in the following years, through increased computational capacity of computers.

In the past decade, prototype measurements have been gathered during the CLASH project (De Rouck et al. 2009) for the overtopping behaviour of a number of sea defence structures with specific geometries. For example, wave overtopping has been quantified at:

- the Zeebrugge rubble mound breakwater (Troch et al. 2004);
- the Ostia shallow rubble mound breakwater (Franco et al. 2009);
- the Samphire Hoe vertical wall (Pullen et al. 2006); and
- the Petten mildly sloping dike (Hordijk 2003).

The prototype measurements are valuable to determine the scale effects of the small scale experiments in the wave flumes and wave basins (De Rouck et al. 2005).

The wave overtopping behaviour of a sea defence structure is traditionally characterized by the average overtopping rate per meter crest width of the structure q [m³/s/m], since wave-by-wave overtopping volumes are unevenly spread in time and in space. The design of the geometry of sea defence structures is mainly based on the limitation of the average overtopping rate q. The hydraulic efficiency of OWECs is also determined by the average overtopping rate (Eq. 1.5). Consequently, fundamental knowledge on the average overtopping rate is required for the design of any structure exposed to wave overtopping.

In the past 60 years, average overtopping rates q have been gathered for a wide range of structures and wave characteristics, both through measurements and simulations. For example, 10.532 irregular wave test results (last update in 2005) of experimental tests with small scale models of different (mainly) sea defence structures have been collected during the CLASH project and have been gathered in the CLASH database (Van der Meer et al. 2005a).

These measured and simulated average overtopping rates have been consequently used to derive a number of existing prediction models for the average overtopping rates. Section 4.2 gives an overview of the different types of prediction models for the average overtopping rate, while section 4.3 describes the most important prediction models that cover the ranges of application of steep low-crested slopes. The overtopping behaviour of (1) vertical walls with non-impacting waves and (2) structures with zero crest freeboard, which determine the asymptotic overtopping behaviour of steep low-crested slopes (from a geometrical point of view), is discussed in section 4.4. Finally, summarizing tables of the existing prediction models applicable to steep low-crested structures and their neighbouring structures are given in section 4.5.

4.2 Types of prediction models for average overtopping rates q

4.2.1 Direct comparison with test results from literature

A first estimate of the average overtopping rate q for a structure exposed to wave overtopping can be made by direct comparison with test results available in literature with similar geometry and wave characteristics as the studied structure.

4.2.2 Empirical prediction models

A second, more indirect prediction is achieved by empirical prediction models, which relate values of q (determined in the past for specific structures) to characteristic geometrical and hydraulic (linked to the wave characteristics) parameters. The empirical prediction models mainly consist of simple regression formulae that relate the dimensionless geometrical and hydraulic parameters to a dimensionless average overtopping rate with empirical regression coefficients, for a particular limited dataset. Commonly used simple regression formulae are in general derived based on a number of datasets, in order to be applicable to a wide variety of structure types. For example, a simple regression formula has been derived by Van der Meer and Janssen (1994) based on test results for mildly sloping dikes with different geometries (straight slope, berm, foreland, rough slope,…) and different wave conditions (normal wave attack, oblique wave attack, short-crested,…). This formula has been extended to an even wider range of structures by TAW (2002) and EurOtop (2007).

The expressions for commonly used simple regression formulae that predict the dimensionless average overtopping rate q are mainly based on exponential functions. Examples are given by the simple regression formulae of TAW (2002) and Owen (1980) for mildly sloping dikes and by Franco et al. (1994) and Allsop et al. (1995) for vertical walls.

A small number of simple regression formulae are based on the weir analogy, i.e. the average overtopping rate is expressed as the flow rate over a weir, which is not expressed using an exponential function. These models are commonly referred to as *weir-models*. A weir-model has been developed by Hedges and Reis (1998), based on the overtopping test results of Owen (1980) for mildly sloping dikes. Another example is the weir-model developed by Daemrich et al. (2006) which is based on regular wave test results with vertical walls, combined with the weir-model of Kikkawa et al. (1968) and the probability calculation method (Goda 2000).

Other empirical prediction models have been developed, using a diagram of the measured average overtopping rates as a function of one or more determining geometrical or hydraulic parameters. These models are referred to as *graphical prediction models*. Examples are given by Jensen and Sorensen (1979) and Goda (2000). The main disadvantage of the graphical prediction models is that they require interpolation of the diagram by the user.

The *run-up models* use information on the wave run up of the studied structure available in literature (assuming no overtopping occurs) to predict the average overtopping rates of the structure. Examples of these models are given by Ahrens (1977), De Waal and Van der Meer (1992) and Schüttrumpf (2001).

It should be noted that prototype measurements and numerical simulations mainly have been used for validation of small scale measurements. The majority of the empirical prediction models for q are based on small scale experimental test results. Consequently, prototype measurements and numerical simulations are not considered further in this PhD-manuscript.

4.2.3 Neural network prediction model

The empirical prediction models are only valid to predict the average overtopping rates for specific types of structures, with specific wave conditions. When the ranges of application of the corresponding datasets are exceeded, the predictions of these models are not accurate.

Generally, the expressions of the empirical prediction models only contain a limited number of geometrical and hydraulic parameters. Only the most dominant parameters are incorporated in the empirical prediction models. However, Van der Meer et al. (2005a) identified 31 parameters (17 geometrical, 11 hydraulic and 3 general parameters) for the description of each test of the CLASH database. Two neural network prediction models were almost simultaneously developed, based on the test results of the CLASH database, originating from the lack of a robust and reliable prediction method for wave overtopping at any type of structure. Van Gent et al. (2007) developed a neural network prediction model that consists of a single phase, while Verhaeghe et al. (2008) developed a 2-phases neural prediction model. The 2-phases model is composed of two neural networks: a *classifier* and a *quantifier*. The classifier determines whether the wave overtopping is significant or not. When the wave overtopping is significant, the average overtopping rate is calculated by the quantifier. The quantifier is comparable to the neural network prediction model by Van Gent et al. (2007), which is referred to as the *DHNN tool* (DHNN refers to Delft Hydraulics Neural Network) in this PhD-manuscript. Consequently, when the overtopping rates are significant, for example in the case of steep low-crested slopes, both the quantifier and the DHNN tool are expected to give a comparable output.

4.3 Predictions of q for steep low-crested slopes

The prediction models discussed in section 4.2 are traditionally applied to predict average overtopping rates of sea defence structures. The ability of each of the three types of prediction models to predict the average overtopping rates accurately for steep low-crested slopes is discussed in the following three sections:

- direct comparison with test results of the CLASH database (section 4.3.1);
- commonly used simple regression formulae for inclined structures (section 4.3.2); and
- the DHNN neural network prediction model (section 4.3.3).

4.3.1 Test results of the CLASH database

The requirements for steep low-crested slopes given in section 1.3 have been translated to assumptions for the 10.532 test results of the CLASH database (second column of Table 4.1):

Table 4.1: Assumptions for CLASH parameters – steep low-crested slopes.

Nr.	Assumption CLASH parameters	Number of tests remaining in the database
i	$\beta = 0.0°$	9224
ii	$B_{berm} = 0.0$ m	7591
iii	$\gamma_f = 1.0$	3097
iv	$CF = 1$ or 2	2846
v	$RF = 1$ or 2	1736
vi	$B_t = 0.0$ m	1372
vii	$h_t / H_{m0} > 2.0$	953
viii	$0.0 < R_c / H_{m0} \leq 2.0$	661
ix	$0.0 < \cot\alpha_{incl} \leq 2.0$	211
x	$\cot\alpha_u = \cot\alpha_d$	182

- the first assumption (i) corresponds to the requirement of normal wave attack. β [°] is the angle of wave attack compared to the normal to the structure.

- assumptions (ii) to (vi) mainly translate the requirement that the structures feature simple slopes:

  a) a zero-width berm (ii). B_{berm} [m] is the width of the berm;
  b) smooth impermeable slopes (iii). γ_f [-] is a parameter related to the roughness and permeability of the structure. γ_f equals 1.0 for smooth impermeable slopes;
  c) complexity factor CF [-] equal to 1 or 2 (iv). CF expresses how well the structure geometry is described by the structural parameters in the database: as good as exactly ($CF = 1$) or very well ($CF = 2$);
  d) width of the toe equal to zero (vi). B_t [m] is the width of the toe.

- only test results with a reliability factor RF [-] of 1 or 2 are considered (v). The factor RF indicates the reliability of the considered overtopping test. When RF equals 1, measurement and analysis have been performed in a reliable way. For $RF = 2$, the measurements have been overall reliable, although a number of estimations have been made or minor uncertainties have occurred.

- the assumptions (vii) to (ix) express the ranges of application for the relative water depth h_t / H_{m0} (Eq. 1.8), the relative crest freeboard R_c / H_{m0} (Eq. 1.9) and the characteristic average slope angle $\cot\alpha$ (Eq. 1.6).

- assumption (x) requires identical slope angles for the lower and upper parts of fractioned slopes. The tests with fractioned slopes remaining in the CLASH database after applying assumption (ix) all correspond to structures featuring a vertical wave wall. Note that the fractioned slopes of the AAU08 test series, described in chapter 3, also violate assumption (x). However, the only purpose of imposing assumption (x) to the CLASH test results is to avoid the occurrence of vertical wave walls.

The assumptions in Table 4.1 have been successively imposed to the CLASH database, starting from the 10.532 test results and increasingly restricting the database to test results which satisfy all assumptions in Table 4.1. The third column of Table 4.1 contains the number of test results remaining in the database after taking into account the corresponding assumption and the assumptions above it. The remaining 182 test results of the CLASH database after taking into account all assumptions in the order of Table 4.1 are referred to as the *CLASH_SL dataset* (steep (S) and low-crested (L)). It should be noted that all test results in the CLASH_SL dataset correspond to $\xi_{m-1,0} > 2.0$.

The CLASH_SL dataset originates from different references. An overview of the corresponding references and the ranges of application for $\cot\alpha$ and R_c / H_{m0} is given in Table 4.2.

Table 4.2: Overview of references and ranges of application for CLASH_SL test results.

CLASH nr.	**Reference**	**Number of test results**	***cot α***	R_c/H_{m0}
30	(Owen 1980)	43	1.0 - 2.0	0.6 - 2.0
35	(Bradbury et al. 1988)	14	2.0	1.0 - 2.0
42	(Coates et al. 1997)	59	2.0	0.5 – 2.0
218	(Perdijk 1987)	4	2.0	1.7 - 2.0
503 - 504 - 507	(Allsop et al. 2000)	33	0.1 - 0.2	1.3 - 1.9
703	(Kofoed 2002)	24	1.2	0.5 - 1.8
959	confidential	5	1.9 – 2.0	1.2 - 1.7

Based on Table 4.2, the following conclusions are drawn concerning the ability of the CLASH_SL dataset to predict the average overtopping rate for steep low-crested slopes:

- the number of test results is very small (182 / 10.532 = 1.7 %);
- the majority of the test results correspond either to $\cot\alpha \approx 2.0$, or to very steep slopes. Due to its low resolution for $\cot\alpha$, the CLASH_SL dataset is unable to predict the average overtopping rate for intermediate slopes;
- the range of application for R_c / H_{m0} is restricted to relative crest freeboards $R_c / H_{m0} \geq 0.5$. Consequently, the CLASH_SL dataset is not able to predict the average overtopping rates for structures with $0.0 < R_c / H_{m0} \leq 0.5$.

These *white spots* are also visible in the graphs of the ranges of application of the total CLASH database generated by Steendam et al. (2004).

Based on the above conclusions, direct comparison with test results of the CLASH_SL dataset is not a valuable tool to predict the overtopping behaviour of steep low-crested slopes.

4.3.2 Simple regression formulae for inclined structures

An important advantage of simple regression formulae is their ability to predict average overtopping rates for sets of geometrical and hydraulic parameters that are different to those of the test results of the corresponding dataset(s) (within the ranges of application of those dataset(s)).

A number of commonly used simple regression formulae for inclined structures that partly cover the ranges of application of steep low-crested slopes (section 1.3) are discussed in the three sections below.

4.3.2.1 EurOtop (2007)

Based on test results with small scale models of mildly sloping dikes with wide ranges of geometries and wave conditions (straight, smooth, deep, shallow, rough, oblique, bi-modal,…), Van der Meer and Janssen (1994) identified two different types of overtopping behaviour. The overtopping behaviour depends on the prevalent wave type: breaking or non-breaking (surging) waves. The transition between breaking and non-breaking waves occurs approximately at a breaker parameter $\xi_{m-1,0} = 2.0$, with non-breaking waves appearing for $\xi_{m-1,0} > 2.0$ (chapter 1).

Accordingly, Van der Meer and Janssen (1994) derived a set of two simple regression formulae, expressing the average overtopping rate as a function of the determining geometrical and hydraulic parameters for breaking and non-breaking waves. These equations originally contain the significant wave height $H_{1/3}$, defined as the average of the 1/3rd largest wave heights in a wave train, and the peak wave period T_p, i.e. the wave period corresponding to the peak of the wave spectrum. In order to take into account the effect of double-peaked or bi-modal spectra and flattened spectra due to wave breaking, these parameters subsequently have been replaced by the spectral wave height H_{m0} and the spectral wave period $T_{m-1,0}$. Adjusted expressions have been provided by TAW (2002) and EurOtop (2007), based on extended databases of test results.

The following formula applies for breaking waves on mildly sloping dikes (EurOtop 2007; TAW 2002):

$$\frac{q}{\sqrt{g\,H_{m0}^3}} = 0.067\sqrt{\frac{\tan\alpha}{s_{m-1,0}}}\,\gamma_b \exp\left[(-4.75)\frac{R_c}{H_{m0}}\frac{\sqrt{s_{m-1,0}}}{\tan\alpha}\frac{1}{\gamma_b\gamma_f\gamma_\beta\gamma_v}\right] \tag{4.1a}$$

with a maximum for non-breaking waves, of:

$$\frac{q}{\sqrt{g\,H_{m0}^3}} = 0.2\exp\left[(-2.6)\frac{R_c}{H_{m0}}\frac{1}{\gamma_f\gamma_\beta}\right] \tag{4.1b}$$

The γ-factors are reduction factors that take into account the effects of a berm (γ_b), the slope roughness (γ_f), oblique wave attack (γ_β) and a vertical wave wall (γ_v). Based on the requirements for the steep low-crested slopes (section 1.3), all γ-factors in Eq. (4.1) are equal to 1.0, simplifying both equations to:

$$\frac{q}{\sqrt{g\,H_{m0}^3}} = 0.067\sqrt{\frac{\tan\alpha}{s_{m-1,0}}}\exp\left[(-4.75)\frac{R_c}{H_{m0}}\frac{\sqrt{s_{m-1,0}}}{\tan\alpha}\right] \tag{4.2a}$$

$$\frac{q}{\sqrt{g\,H_{m0}^3}} = 0.2\exp\left[(-2.6)\frac{R_c}{H_{m0}}\right] \tag{4.2b}$$

The predicted value of the dimensionless average overtopping rate $q/\sqrt{g\,H_{m0}^3}$ for specific geometrical and hydraulic parameters is determined as the minimum of Eq. (4.2a) and Eq. (4.2b). Consequently, the value of $\xi_{m-1,0}$ corresponding to the transition between breaking and non-breaking waves is determined by the point of intersection between both equations in a graph of $q/\sqrt{g\,H_{m0}^3}$ against $\xi_{m-1,0}$. This point is only approximately located at $\xi_{m-1,0} = 2.0$, since it varies depending on the slope angle and the wave steepness.

The reliability of Eq. (4.2) is described by assuming the coefficients 4.8 and 2.6 are normally distributed stochastic variables with means 4.8 and 2.6 and a standard deviation σ. This is illustrated in Eq. (4.3) for the case of Eq. (4.2b). The parameter $z_{p/2}$ is a percentile of the standard normal distribution: p % of the observations is included in between $z_{p/2}$ and $-z_{p/2}$ for this distribution. For example, 90% of the observations in a standard normal distribution is included between $\pm z_{0.90/2}$, with $z_{0.90/2} = 1.645$.

$$\frac{q}{\sqrt{g\,H_{m0}^3}} = 0.2\exp\left[\left(-2.6 \pm z_{p/2}\cdot\sigma\right)\frac{R_c}{H_{m0}}\right] \tag{4.3}$$

The value of σ is determined by the requirement that 90 % of the test results used to derive Eq. (4.2b) should be positioned in between the values of the average overtopping rates determined by:

$$\frac{q}{\sqrt{g\,H_{m0}^3}} = 0.2\exp\left[\left(-2.6 \pm 1.645\cdot\sigma\right)\frac{R_c}{H_{m0}}\right] \tag{4.4}$$

Equation (4.4) represents the 90% prediction interval of Eq. (4.2b). The corresponding value of $\sigma =$ is 0.35. Similarly, σ equals 0.50 for the 90% prediction interval of Eq. (4.2a).

The ranges of application of Eq. (4.2a) and (4.2b) for the slope angle $\cot\alpha$ and the relative crest freeboard R_c/H_{m0} are given in Table 4.3. Note that the ranges of application for Eq. (4.2b) partly cover the ranges of application in Eq. (1.6) and Eq. (1.9). Consequently, Eq. (4.2b) can used to predict the average overtopping rates for steep low-crested slopes.

Table 4.3: Ranges of application of Eqs. (4.2a) and (4.2b) for $\cot\alpha$ *and* R_c / H_{m0}.

	$\cot\alpha$	R_c/H_{m0}
Eq. (4.2a)	2.5 – 7.0	0.2 – 1.8
Eq. (4.2b)	1.0 – 4.0	0.5 – 3.5

It is important to note that Eq. (4.2b) is only valid for large values of the breaker parameter $\xi_{m-1,0}$ caused by large values of the slope angle α. It underestimates the average overtopping rates when large values of $\xi_{m-1,0}$ occur corresponding to small values of the wave steepness due to very heavy breaking in shallow waters (EurOtop 2007).

4.3.2.2 Kofoed (2002)

Based on experimental tests with scale models of fixed overtopping wave energy converters (OWECs) with a limited draft and a single level reservoir with a uniform slope, Kofoed (2002) added correction factors to Eq. (4.2b), resulting in Eq. (4.5).

$$\frac{q}{\sqrt{g\,H_{m0}^3}} = \lambda_{dr}\lambda_{\alpha}\lambda_{s}\,0.2\exp\left[\left(-2.6\right)\frac{R_c}{H_{m0}}\right] \tag{4.5}$$

The factor λ_{dr} (Eq. 4.6) takes into account the effect of the limited draft d_r [m], i.e. the vertical dimension of the submerged part of the OWEC, of the floating OWECs on the average overtopping rate (k_p in Eq. 4.6 is the wave number based on the peak wave period, while κ is a coefficient controlling the degree of influence of the limited draft (0.4 by best fit)). The factor λ_{dr} equals 1.0 when the slope extends to the bottom, which is the case for the steep low-crested slopes considered in this PhD-research.

$$\lambda_{dr} = 1-\kappa\frac{\sinh\left(2\,k_p\,h_t\left(1-\frac{d_r}{h_t}\right)\right)+2\,k_p\,h_t\left(1-\frac{d_r}{h_t}\right)}{\sinh\left(2\,k_p\,h_t\right)+2\,k_p\,h_t} \tag{4.6}$$

The factor λ_{α} includes the decrease in average overtopping rate observed by Kofoed (2002) for slopes deviating from the optimal slope angle $\alpha_{\circ}$ = 30°:

$$\lambda_\alpha = \left[\cos\left(\alpha_\circ - 30°\right)\right]^3 \tag{4.7}$$

Equation (4.7) introduces a weak dependency of the average overtopping rate on the slope angle.

Finally, the factor λ_s takes into account the observation that the relationship between $q/\sqrt{g H_{m0}^3}$ and R_c / H_{m0} is no longer exponential for relative crest freeboards $R_c / H_{m0} < 0.75$:

$$\lambda_s = \begin{cases} 0.40 \sin\left(\frac{2}{3}\pi \frac{R_c}{H_{m0}}\right) + 0.60 & \frac{R_c}{H_{m0}} < 0.75 \\ 1 & \frac{R_c}{H_{m0}} \geq 0.75 \end{cases} \tag{4.8}$$

λ_s has been calibrated using test results of Schüttrumpf (2001) for structures with a zero crest freeboard ($R_c / H_{m0} = 0.0$) and with $3.0 \leq \cot\alpha \leq 6.0$.

The ranges of application of Eqs. (4.5) to (4.8) for $\cot\alpha$ and R_c / H_{m0} are: $0.58 \leq \cot\alpha \leq 2.75$ and $0.15 \leq R_c / H_{m0} \leq 2.00$. Hence, the set of equations by Kofoed (2002) extends the ranges of application of Eq. (4.2b) to steeper slopes and to smaller relative crest freeboards. Hence, these equations can be applied to predict the average overtopping rates for steep low-crested slopes.

It should be noted that the test conditions of the UG10 test series (section 3.3) are similar to the conditions of the tests carried out by Kofoed (2002). However, the structures studied in the UG10 test series feature slopes extending to the bottom of the seabed, in contrast to the limited draft used by Kofoed (2002). Kofoed (2002) only tested one geometry (with $\cot\alpha = 1.19$) that features a slope extending to the sea bottom, corresponding to CLASH number 703 (Table 4.2). When only the tests for that geometry are considered, the ranges of application for R_c / H_{m0} are narrower than the ranges mentioned above.

4.3.2.3 Owen (1980)

Owen (1980) derived a simple regression formula, based on small scale experiments with uniform mildly sloping dikes subjected to normal wave attack (Eq. 4.9). The dataset used to derive this equation contains 24% of the 182 test results of the CLASH_SL dataset.

$$\frac{q}{g\,T_m\,H_s} = Q_0 \exp\left(-b_{Owen}\frac{R_c}{T_m\sqrt{g\,H_s}}\right) \tag{4.9}$$

Other dimensionless expressions (incorporating different wave characteristics) are used for the average overtopping rate q and the crest freeboard R_c compared to the expressions in the two above sections 4.3.2.1 and 4.3.2.2. The parameter T_m [s] is the mean zero-crossing wave period of the incident waves at the toe of the structure, while H_s [m] is the incident significant wave height $H_{1/3}$ at that same position.

The coefficients Q_0 and b_{Owen} in Eq. (4.9) are empirical constants, their values depend on the slope angle α of the structure. Owen (1980) derived and interpolated values of Q_0 and b_{Owen} for slopes with $1.0 \le \cot\alpha \le 5.0$ (Table 4.4).

Table 4.4: Overview of parameters Q_0 and b_{Owen} (Owen 1980) as a function of the slope angle.

cot α	Q_0	b_{Owen}
1.0	0.0079	20.1
1.5	0.0088	19.9
2.0	0.0094	21.6
2.5	0.010	24.5
3.0	0.011	28.7
3.5	0.011	34.1
4.0	0.012	41.0
4.5	0.012	47.7
5.0	0.013	55.6

Average overtopping rates have been measured by Owen (1980) during 100 wave periods for each test, which has at least five replicates. These replicates enabled to determine the standard deviation of the measured average overtopping rates about the

mean (Eq. 4.9). The reliability of Eq. (4.9) is described by the *overtopping discharge factor* (Owen 1980). This factor has been derived based on the spreading of the natural logarithms of the measured dimensionless average overtopping rates, assuming these logarithms exhibit a normal probability distribution about the mean value of Eq. (4.9). This is expressed in Eq. (4.10), which uses the percentiles of the standard normal distribution $z_{p/2}$ described in section 4.3.2.1.

$$\ln\left(\frac{q}{g\,T_m\,H_s}\right)_p = \ln\left(\frac{q}{g\,T_m\,H_s}\right)_{pred} \pm z_{p/2}\cdot\sigma \tag{4.10}$$

For example, the 90% prediction interval of Eq. (4.9) is determined by:

$$\left(\frac{q}{g\,T_m\,H_s}\right)_{90\%} = \left(\frac{q}{g\,T_m\,H_s}\right)_{pred} \exp\left(\pm 1.645\cdot\sigma\right) \tag{4.11}$$

A standard deviation $\sigma = 0.70$ has been found by fitting the measured average overtopping rates to Eq. (4.10) for different values of p (Owen 1980). Hence, the overtopping discharge factor corresponding to the upper boundary of the 90% prediction interval is defined by $\exp(1.645\cdot 0.70) = 3.2$. Based on Eq. (4.11), the dimensionless average overtopping rate with a probability of exceedance of 5% (95%) is found by multiplying (dividing) the dimensionless average overtopping rate (Eq. 4.9) by a factor 3.2. Values of the overtopping discharge factor corresponding to different probabilities of exceedance have been derived in a similar way (Table 4.5).

The range of application of Eq. (4.9) for $\cot\alpha$ is $1.0 \le \cot\alpha \le 5.0$, while the range of application for $R_c/\left(\sqrt{g\,H_s}T_m\right)$ is $0.05 < R_c/\left(\sqrt{g\,H_s}T_m\right) < 0.30$. Furthermore, Eq. (4.9) is only valid for rather large values of the wave steepness $s_m = 2\pi H_s/\left(g\,T_m^2\right)$: $0.04 < s_m < 0.06$.

In order to compare the predictions of Eq. (4.9) to the predictions of Eqs. (4.2b) and (4.5), the expressions of the dimensionless average overtopping rate and relative crest freeboard in Eq. (4.9) are transformed into $q/\sqrt{g\,H_s^3}$ and R_c/H_s respectively. Hence, Eq. (4.9) can be rewritten as:

$$\frac{q}{\sqrt{g\,H_s^3}} = \frac{Q_0\sqrt{2\pi}}{\sqrt{s_m}}\exp\left(-\frac{b_{Owen}}{\sqrt{2\pi}}\sqrt{s_m}\frac{R_c}{H_s}\right) \tag{4.12}$$

In this context, the significant wave height in Eq. (4.9) is assumed to be equal to the spectral wave height H_{m0}. In theory, this is only valid when the individual wave heights are Rayleigh distributed.

Table 4.5: Overtopping discharge factor expressing the reliability of the prediction formula of Owen (1980).

Probability of exceedance [%]	**Overtopping discharge factor[-]**
50	1.0
20	1.8
10	2.4
5.0	3.2
2.0	4.2
1.0	5.1
0.50	6.1
0.20	7.5
0.10	8.7

There is a clear similarity between Eq. (4.12) and Eq. (4.2a), which applies to breaking waves, since the coefficients Q_0 and b_{Owen} can be expressed as a function of the tangent of the slope angle. Accordingly, Eq. (4.9) (and thus Eq. (4.12)) has no maximum for non-breaking waves, which may lead to overpredictions for steep slopes (EurOtop 2007).

4.3.3 DHNN - Neural network

Van Gent et al. (2007) developed the neural network prediction model, i.e. the DHNN tool, which has been trained using the majority of the test results of the CLASH database. Not all 10.532 test results have been included. All test results with a reliability factor $RF = 4$ or a complexity factor $CF = 4$ have been left out. Elimination of the inconsistencies in the database further reduced the CLASH database to 8.372 test results, including all 182 test results in Table 4.2.

Moreover, the input of the neural network prediction model did not consist of the 31 parameters identified by Van der Meer et al. (2005a), but of 15 parameters: 3 parameters describing the wave field and 12 parameters describing the geometry of the structure. Consequently, the DHNN tool has been trained based on 16 (15 input parameters and 1 output) times 8.372 input values.

The ranges of application of the DHNN tool for the slope angle and relative crest freeboard are: $0.0 \leq \cot\alpha \leq 7.0$ and $0.0 \leq R_c / H_{m0} \leq 6.4$. The reliability of the DHNN tool is described by a number of percentiles for $q/\sqrt{g H_{m0}^3}$ that are part of the output of the DHNN tool for a particular input.

Although the number of tests of the CLASH_SL dataset is limited (182 test results, section 4.3.1), the DHNN tool has the ability to interpolate between the test results for which it is trained, similar to simple regression formulae. The slopes of steep low-crested structures are situated in between those of mildly sloping dikes and vertical walls (section 1.1.3), while the crest freeboards are positioned in between a zero crest freeboard and crest freeboards typical for sea defence structures. Consequently, the average overtopping rates are also expected to be situated in between the average overtopping rates of these *neighbouring* (from a geometrical point of view) *structures*. Due to the presence of test results for the neighbouring structures in the 8.372 test results that have been used to train the DHNN tool, predictions of the average overtopping rates for steep low-crested slopes are expected to be relatively accurate.

4.3.4 Contribution of the geometrical and hydraulic parameters

Based on Eq. (3.21a) (chapter 3), the average overtopping rate of steep low-crested slopes is a function of the slope angle, crest freeboard, wave height and wave period. The expression of the generic function f_1 in Eq. (3.21a) should use dimensionless parameters consisting of the geometrical and hydraulic parameters, in order to obtain expressions independent of the scale of the test and of the design conditions. In this PhD-manuscript, the following dimensionless parameters are used, in accordance with section 4.3.2.1:

- the dimensionless average overtopping rate $q/\sqrt{g H_{m0}^3}$;
- the cotangent of the slope angle $\cot\alpha$;
- the relative crest freeboard R_c / H_{m0}, which includes the effect of the crest freeboard and the wave height; and

- the wave steepness $s_{m-1,0} = H_{m0} / L_{m-1,0}$, which includes the effect of the wave height and the wave period.

Consequently, the expression for the dimensionless average overtopping rate for steep low-crested slopes is expressed by (f is a generic function):

$$\frac{q}{\sqrt{g H_{m0}^3}} = f\left(\cot\alpha, \frac{R_c}{H_{m0}}, s_{m-1,0}\right) \tag{4.13}$$

Since the expressions in section 4.3.2 all partly cover the ranges of application of steep low-crested slopes, these expressions give more information on the expression of the generic function f in Eq. (4.13). Looking at these expressions, it is unclear whether all dimensionless parameters in the right hand side of Eq. (4.13) should be taken into account. All formulae in section 4.3.2 include the effect of the relative crest freeboard R_c / H_{m0}, but disagree on the inclusion of the effects of the slope angle and the wave period (wave steepness):

- according to Eq. (4.2b), the effects of the slope angle and wave period on the average overtopping rate of structures corresponding to non-breaking waves are negligible;

- on the other hand, Eqs. (4.5) to (4.8) predict a weak dependency of the average overtopping rates on the slope angle. The effect of the wave period on the average overtopping rate is also neglected;

- based on Eq. (4.12), the effect of the wave period on the average overtopping rate is not negligible. The effect of the slope angle is included through the factors Q_0 and b_{Owen} (Table 4.4).

Furthermore, a number of interactions occur between the dimensionless parameters in Eq. (4.13) for the formulae in section 4.3.2:

- the argument of the exponential function in Eq. (4.12) shows there is an interaction between the effect of the slope angle, the effect of the wave period and the effect of the relative crest freeboard on the dimensionless average overtopping rate $q / \sqrt{g H_{m0}^3}$;

- for $R_c / H_{m0} \geq 0.75$, the effect of the slope angle is only present outside the argument of the exponential function (hence not interacting with the effect of the relative crest freeboard) in Eq. (4.5) through the use of the factor λ_α. On the other hand, λ_s is not equal to 1.0 for $R_c / H_{m0} < 0.75$, resulting in an interaction between the effect of the slope angle and the effect of the relative crest freeboard.

The DHNN tool includes the effects of all geometrical and hydraulic parameters and their interactions. Consequently, predictions by the DHNN tool should be compared to the predictions of the empirical formulae in section 4.3.2 to determine which of the parameters $\cot\alpha$, R_c / H_{m0} and $s_{m-1,0}$ affect the average overtopping rate of steep low-crested slopes and to identify the significant interactions between these parameters.

The limited number of test results in the CLASH_SL database (182) justifies the new experimental tests which have been carried out during this PhD-research. The test matrices of the AAU08 and UG10 test series (Tables 3.5 and 3.7) particularly allow to study the independent effects of the three determining parameters and their interactions. A comparison between these test results and their predictions by the empirical formulae from section 4.3.2 and by the DHNN tool for the effects of slope angle, relative crest freeboard and wave period and the interactions between these parameters is shown and discussed in chapter 5.

4.4 Asymptotic overtopping behaviour

4.4.1 Asymptotic behaviour of vertical walls (cot α = 0.0)

As mentioned above, the overtopping behaviour of vertical walls is considered to be asymptotic for the overtopping behaviour of very steep slopes. According to EurOtop (2007), two different types of overtopping behaviour occur at vertical walls, depending on the value of the impulsiveness parameter $h*$ (Eq. 4.14).

$$h* = 1.3 \frac{h_t}{H_{m0}} \frac{h_t}{L_{m-1,0}} \tag{4.14}$$

When $h* > 0.3$, *non-impulsive* or *pulsating* conditions occur. This corresponds to large values of h_t / H_{m0} and $h_t / L_{m-1,0}$. The overtopping behaviour in non-impulsive conditions is dominated by green water overtopping.

On the other hand, when $h^* < 0.2$, *impulsive* conditions dominate at a vertical wall. Under impulsive conditions, the overtopping behaviour is characterized by violently breaking waves against the wall, giving rise to an up rushing jet of water.

In the transition zone, $0.2 \leq h^* \leq 0.3$, the maximum of the average overtopping rates calculated by both formulae for non-impulsive and impulsive conditions applies.

Since the water depth is assumed to be rather large for the structures studied in this PhD-research (Eq. 1.8), empirical formulae for non-impulsive conditions are applied to determine the asymptotic overtopping behaviour of very steep slopes. Two commonly used empirical formulae that predict the average overtopping rate at vertical walls for non-impulsive conditions are given below (Eqs. 4.15 and 4.16).
Franco et al. (1994) derived Eq. (4.15) based on small scale experimental tests with caisson breakwaters (vertical walls) in relatively deep water ($h_t / H_{m0} > 3.0$) with non-impulsive waves and normal wave attack.

$$\frac{q}{\sqrt{g H_{m0}^3}} = 0.2 \exp\left[\left(-4.3\right) \frac{R_c}{H_{m0}} \right] \tag{4.15}$$

The reliability of Eq. (4.15) is described by assuming the coefficient 4.3 is a normally distributed stochastic parameter with mean 4.3 and standard deviation $\sigma =$ 0.30. This standard deviation is derived similarly compared to the standard deviations of Eqs. (4.2a) and (4.2b).

The range of application of Eq. (4.15) for the relative crest freeboard R_c / H_{m0} is $0.8 < R_c / H_{m0} < 3.0$.

EurOtop (2007) mentions a different formula (Eq. 4.16), derived based on test results with wider ranges of application for the relative crest freeboard and for the wave characteristics than Eq. (4.15).

$$\frac{q}{\sqrt{g H_{m0}^3}} = 0.04 \exp\left[\left(-2.6\right) \frac{R_c}{H_{m0}} \right] \tag{4.16}$$

The reliability of Eq. (4.16) is described by assuming that the coefficient 2.6 is a normally distributed stochastic parameter with mean 2.6 and standard deviation $\sigma =$ 0.80. The range of application for the relative crest freeboard is $0.1 < R_c / H_{m0} < 3.5$. Equation (4.16) is based on the prediction formula by Allsop et

al. (1995) (Eq. 4.17), which has been extended to a larger number of datasets. Equations (4.16) and (4.17) give similar predicted values.

$$\frac{q}{\sqrt{g\,H_{m0}^3}} = 0.05 \exp\left[\left(-2.8\right)\frac{R_c}{H_{m0}}\right] \tag{4.17}$$

4.4.2 Asymptotic behaviour of structures with a zero crest freeboard ($R_c/H_{m0} = 0.0$)

Test results with slopes $\cot\alpha = 0.0$ and $\cot\alpha = 1.5$ (Smid et al. 2001) and with $3.0 \le \cot\alpha \le 6.0$ (Schüttrumpf 2001) are available for structures with a zero crest freeboard. An empirical formula based on the test results of Schüttrumpf (2001) is provided by EurOtop (2007); its expression is given for $\xi_{m-1,0} \ge 2.0$ in Eq. (4.18).

$$\frac{q}{\sqrt{g\,H_{m0}^3}} = \left(0.136 - \frac{0.226}{\xi_{m-1,0}^3}\right) \tag{4.18}$$

It should be noted that the test results of Smid et al. (2001) have a reliability factor *RF* of 4 (unreliable) in the CLASH database. However, these are the only available tests on steep slopes and vertical walls with zero crest freeboards and they are also mentioned in EurOtop (2007). Hence, the test results by Smid et al. (2001) are used in this PhD-research to predict the average overtopping rate at steep slopes and vertical walls with zero crest freeboards.

4.5 Overview of prediction models for steep low-crested slopes and neighbouring structures

An overview of the prediction models described above that are applicable to steep low-crested slopes is shown in Table 4.6.

Table 4.7 gives an overview of the empirical formulae and test results that determine the asymptotic behaviour for steep low-crested slopes (vertical walls and structures with a zero crest freeboard).

Table 4.6: Summary of prediction models applicable to steep low-crested slopes.

Eq. Nr.	**Reference (in figures)**	$cot\ \alpha$ [-]	R_c/H_{m0} [-]	$\frac{R_c}{\sqrt{gH_s}T_m}$ [-]
Eq. (4.2b)	non-breaking, EurOtop (2007)	1.0 – 4.0	0.5 – 3.5	-
Eq. (4.5)	OWECs, Kofoed (2002)	0.58 – 2.75	0.15 – 2.0	-
Eq. (4.9)	smooth slopes, Owen (1980)	1.0 – 5.0	-	0.05 – 0.30
-	DHNN	0.0 – 7.0	0.0 – 7.0	-

Table 4.7: Summary of prediction models applicable to neighbouring structures (vertical wall, zero crest freeboard).

Eq. Nr.	**Reference (in figures)**	$cot\ \alpha$ [-]	R_c/H_{m0} [-]
Eq. (4.15)	vertical wall, Franco et al. (1994)	0.0	0.8 – 3.0
Eq. (4.16)	vertical wall, EurOtop (2007)	0.0	0.1 – 3.5
-	test results, Smid et al. (2001)	0.0 , 1.5	0.0

4.6 Conclusions

An overview of the existing knowledge on the average overtopping rates of steep low-crested slopes has been given in this chapter. A number of commonly used prediction models, originally developed for sea defence structures, appear to be valid within the ranges of application of steep low-crested slopes: the CLASH_SL dataset, the simple regression formulae by EurOtop (2007) for inclined structures, Kofoed (2002) and Owen (1980), and the DHNN tool. The ranges of application and reliability of these models have been described.

Furthermore, prediction models for the overtopping behaviour of vertical walls under non-impulsive wave attack and of structures with zero crest freeboard have been given, since these structures determine the asymptotic (from a geometrical point of view) overtopping behaviour for steep low-crested slopes.

5

Average overtopping rates of steep low-crested slopes – experimental test results

The main goal of this chapter is to present the average overtopping rates measured at both the AAU08 test set-up and the UG10 test set-up (described in chapter 2 and 3) and to compare these measurements with predicted overtopping rates by the prediction models from chapter 4. More specific, the relative importance of the effects of the slope angle, relative crest freeboard and wave period on the average overtopping rates of steep low-crested slopes and the interactions between these parameters are shown and discussed. The ability of the prediction models from chapter 4 to predict these three effects and the interactions between the three dominating parameters has been investigated. Finally, a new set of empirical prediction formulae is proposed at the end of this chapter.

5.1 Introduction

The prediction models from literature do not agree on the effects of the slope angle, relative crest freeboard and wave period on the average overtopping rates of steep low-crested slopes and on the interactions between these three parameters (section 4.3.4). The test results of the AAU08 and UG10 dataset allow to verify the relative importance of these parameters and to investigate their interactions. All AAU08 test results are shown in a log-linear graph of the dimensionless average overtopping rate $q/\sqrt{gH_{m0}^3}$ against the relative crest freeboard R_c/H_{m0} in Fig. 5.1. The UG10 test results are shown in a similar graph in Fig. 5.2. The data points are

categorized by the bottom slope angle α_d for the AAU08 test results (Fig. 5.1) and by the slope angle α for the UG10 test results (Fig. 5.2).

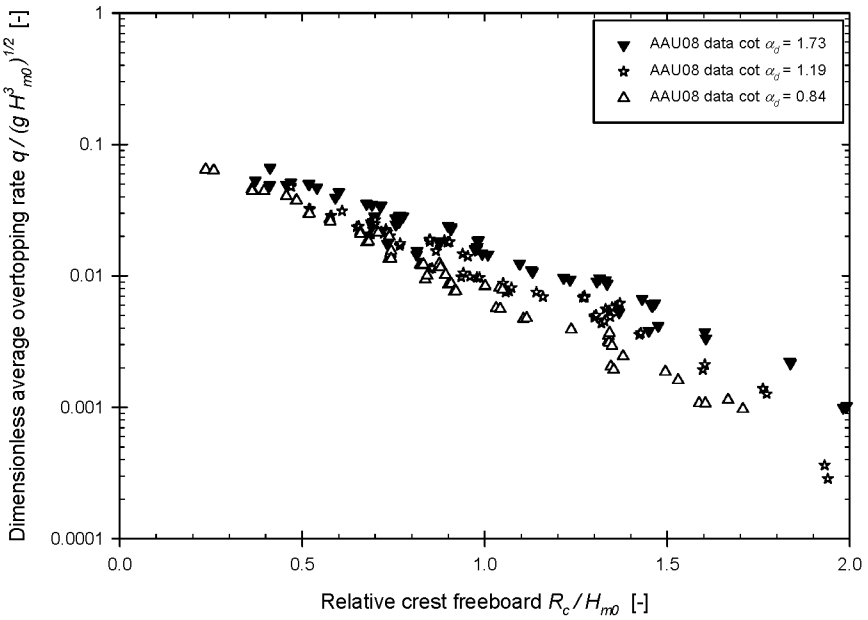

Figure 5.1: Dimensionless average overtopping rate (logarithmic scale) as a function of the relative crest freeboard (linear scale) for the test results of the AAU08 dataset, with R_c / H_{m0} varying between 0.0 and 2.0.

Both graphs show that the dimensionless average overtopping rate of steep low-crested slopes is dominated by the slope angle and the relative crest freeboard:

- for a particular slope angle (α_d or α), the dimensionless average overtopping rate is mainly affected by the relative crest freeboard: an increase in R_c / H_{m0} causes a decrease in $q / \sqrt{g H_{m0}^3}$. The effect of the wave period is only present in the spreading around the trend line of the data points for a particular slope angle.

That spreading also contains the effect of differences in the characteristic slope angle α for a particular value of α_d in Fig. 5.1;

- for a particular relative crest freeboard, the dimensionless average overtopping rate is mainly affected by the slope angle. Generally, it appears that a decrease of the slope angle α corresponds to an increase of $q/\sqrt{g\,H_{m0}^3}$. At first sight, the wave period does not affect this general trend.

Hence, the effect of the wave period is small compared to the effects of the slope angle and the relative crest freeboard, and its interactions with those two effects are small. This is in contrast to the findings by Owen (1980) (section 4.3.4.3).

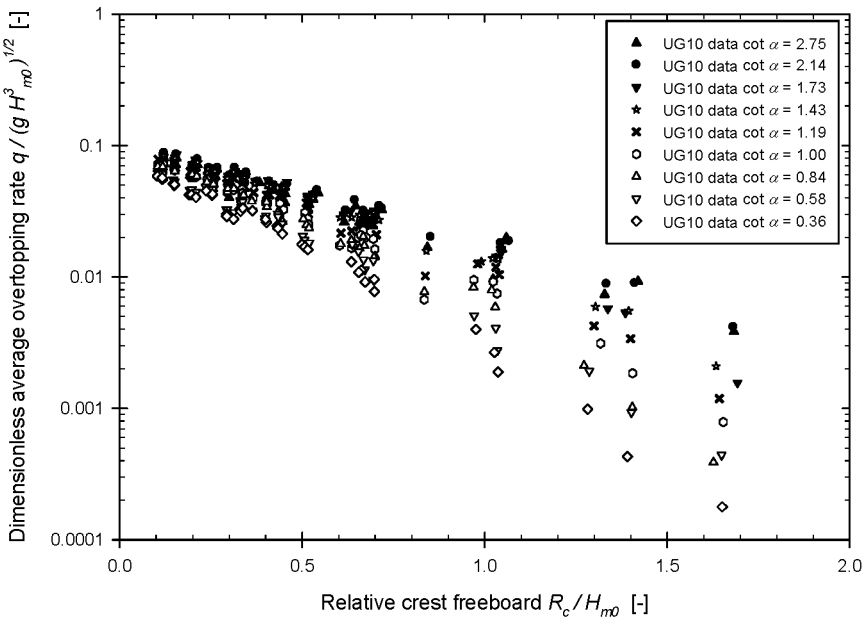

Figure 5.2: Dimensionless average overtopping rate (logarithmic scale) as a function of the relative crest freeboard (linear scale) for the test results of the UG10 dataset, with R_c / H_{m0} varying between 0.0 and 2.0.

On the other hand, a clear interaction is visible in Figs. 5.1 and 5.2 between the effects of the slope angle and the relative crest freeboard. The slope of the trend line of the data points for a particular slope angle and its intersection point with the vertical axis are dependent on the value of that slope angle. Correspondingly, the effect of the slope angle on $q/\sqrt{g H_{m0}^3}$ is larger for larger relative crest freeboards.

This interaction is further investigated in sections 5.2 and 5.3, based on a comparison between the AAU08 and UG10 test results and the predictions of the models in Table 4.6 and Table 4.7. Since the effect of the wave period and its interactions with the effects of the slope angle and relative crest freeboard on $q/\sqrt{g H_{m0}^3}$ are relatively small, the effect of the wave period is not considered in first instance. Hence, the value of the wave period is chosen arbitrarily in sections 5.2 and 5.3. The effect of the slope angle on $q/\sqrt{g H_{m0}^3}$ is studied in section 5.2, for a number of relative crest freeboards. This allows to study the independent effect of the slope angle and the interactions between the relative crest freeboard and the effect of the slope angle in detail. Section 5.3 studies the effect of the relative crest freeboard on $q/\sqrt{g H_{m0}^3}$ for a number of slope angles, enabling to investigate the independent effect of the relative crest freeboard and its interactions with the slope angle.

The contradiction between the limited effect of the wave period for the AAU08 and UG10 test results on the one hand and the relatively large contribution of the wave period to the average overtopping rate of smooth slopes according to Owen (1980) (Eq. 4.9) on the other hand requires a detailed study on the effect of the wave period on $q/\sqrt{g H_{m0}^3}$ for steep low-crested slopes. This is the subject of section 5.4.

Furthermore, the interaction between the wave period and the effect of the slope angle is studied in detail in section 5.5, concerning the value of the optimal slope angle, which corresponds to the maximum average overtopping rate.

Conclusions concerning the interactions between the three dominating parameters (slope angle, relative crest freeboard and wave period) on the average overtopping rates of steep low-crested slopes and concerning the ability of the prediction models from chapter 4 to predict these rates are drawn in section 5.6. Finally, section 5.7 describes the derivation of a set of new empirical prediction formulae which results in more accurate predictions for the average overtopping rate of steep low-crested slopes compared to the existing prediction models.

5.2 Effect of slope angle on overtopping rate of steep low-crested slopes

The effect of the slope angle α on the average overtopping rate of steep low-crested slopes is studied below for three different values of the relative crest freeboard R_c / H_{m0}: 0.45 (Example 1), 0.67 (Example 2) and 1.36 (Example 3). These three values are chosen, since UG10 test results are available for those relative crest freeboards. Furthermore, a relatively wide variety of relative crest freeboards is covered by these values.

The crest freeboards used for the AAU08 test series and the UG10 test series are not identical. The AAU08 data points in the three examples (Examples 1 to 3) below correspond to slightly larger relative crest freeboards. Hence, the average overtopping rates of these data points are slightly overpredicted by the prediction models from literature (Table 4.6), which have been determined for the relative crest freeboards of the UG10 test results.

The graphs in which the AAU08 test results are compared to the predictions by the DHNN tool are an exception to this. All predicted values in those graphs are based on the relative crest freeboard of the AAU08 test series.

5.2.1 Example 1 - $R_c / H_{m0} = 0.45$

The measured dimensionless average overtopping rates of the AAU08 dataset with $R_c / H_{m0} = 0.50$ and the UG10 test results with $R_c / H_{m0} = 0.45$ (Table 5.1) are compared to predicted values by the simple regression formulae of EurOtop (2007) (Eq. 4.2b) and of Kofoed (2002) (Eqs. 4.5 to 4.8) for $R_c / H_{m0} = 0.45$ in Fig. 5.3. The prediction lines for both formulae are drawn within their ranges of application for $\cot\alpha$ (Table 4.6). The 90% prediction interval of Eq. (4.2b) is also added to Fig. 5.3 (*short-dashed* lines). Note that the predictions by Eq. (4.2b) are added although its ranges of application for R_c / H_{m0} are violated.

Furthermore, the dimensionless average overtopping rate for a vertical wall ($\cot\alpha = 0.0$) predicted by EurOtop (2007) (Eq. 4.16) is shown (white triangle on the vertical axis). The straight *dotted* lines connect the 90% prediction interval of Eq. (4.16) to the 90% prediction interval of Eq. (4.2b).

Table 5.1: Geometrical and hydraulic parameters for studying the independent effect of the slope angle on the average overtopping rate of steep low-crested slopes – Example 1.

Parameter	UG10	AAU08
R_c / H_{m0}	0.45	0.50
R_c	0.045 m	0.050 m
H_{m0}	0.10 m	0.10 m
T_p	1.534 s	1.534 s

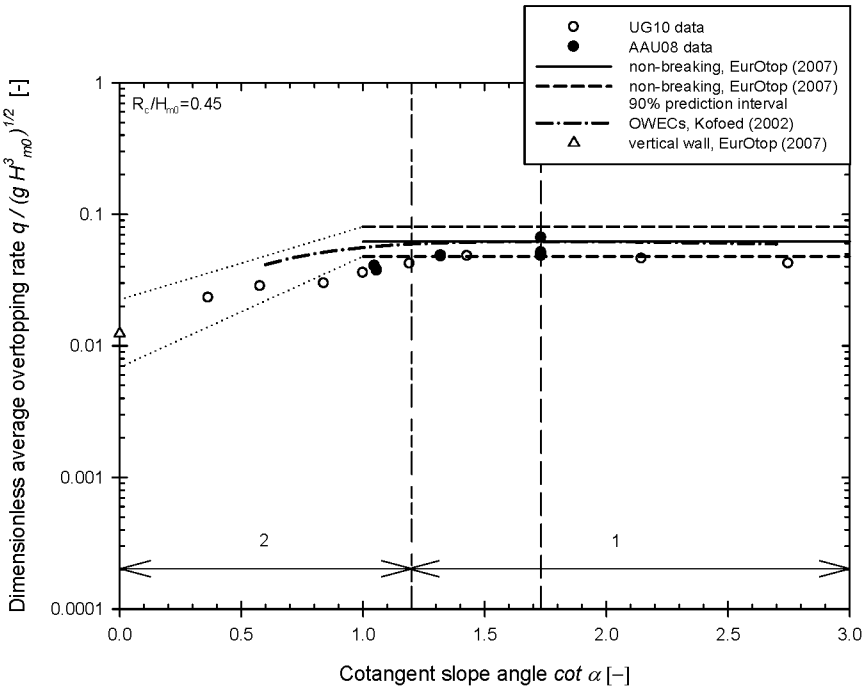

Figure 5.3: Measured average overtopping rate (logarithmic scale) for Example 1 as a function of the slope angle (linear scale), with $\cot\alpha$ *varying between 0.0 and 3.0. Predictions by EurOtop (2007) and Kofoed (2002) are added.*

Based on the trend described by the data points of the AAU08 and UG10 datasets in Fig. 5.3, two zones of different overtopping behaviour are identified for Example 1, separated by a vertical *long-short-short*-dashed line and marked by 1 and 2:

- zone 1 contains *milder slopes*, for which the overtopping behaviour is characterized by large dimensionless average overtopping rates with a weak dependency on the slope angle.

- zone 2 contains test results with *steeper slopes* for which a significant decrease in the overtopping rate occurs for increasing slope angle, from the overtopping rates for milder slopes towards the dimensionless average overtopping rate predicted by EurOtop (2007) for vertical walls. These data points describe a straight line rather than a curved line in the log-linear graph of Fig. 5.3, suggesting that a positive exponential function may express the relationship between the dimensionless average overtopping rate $q/\sqrt{g\,H_{m0}^3}$ and $\cot\alpha$ for steeper slopes.

The transition between both zones occurs at $\cot\alpha = 1.2$ for Example 1, which is the abscissa of the intersection point between the data points of the AAU08 and UG10 datasets and the lower boundary of the 90% prediction interval of Eq. (4.2b) (marked by the vertical *long-short-short* -dashed line).

The weak dependency of the test results on the slope angle in zone 1 is confirmed by Eq. (4.5) (Kofoed 2002), which slightly overpredicts the corresponding average overtopping rates. Kofoed (2002) also predicts the occurrence of a single optimal slope angle ($\cot\alpha = 1.73$), which results in the maximum average overtopping rate (*long-dashed* vertical line in Fig. 5.3).

Equation (4.2b) tends to overpredict the average overtopping rates in zone 1. This is caused by the violation of its ranges of application for R_c/H_{m0}.

The log-linear graph in Fig. 5.4 is similar to Fig. 5.3, in which predictions by Kofoed (2002) are replaced with predictions by the simple regression formula of Owen (1980) (Eq. 4.9), within its range of application for $\cot\alpha$. Furthermore, the 90% prediction interval of Eq. (4.9) is added to Fig. 5.4 (marked by the *dash-dot-dot* lines).

The significant wave height $H_{1/3}$ in Eq. (4.9) is assumed to be equal to H_{m0}, which is less accurate for the tests of the AAU08 and UG10 dataset without Rayleigh distributed wave heights (section 3.4.2). The AAU08 and UG10 test results shown in Examples 1 to 3 all correspond to Rayleigh distributed wave heights.

Similar to Eq. (4.5) (Kofoed 2002), the simple regression formula by Owen (1980) also predicts a weak dependency of the overtopping rates on the slope angle for milder slopes (zone 1) and the existence of a single optimal slope angle, $\cot\alpha = 1.73$ (Fig. 5.4). Since the data points in zone 1 are positioned within the 90% prediction interval of Eq. (4.9), the effect of the slope angle is not negligible according to Owen (1980).

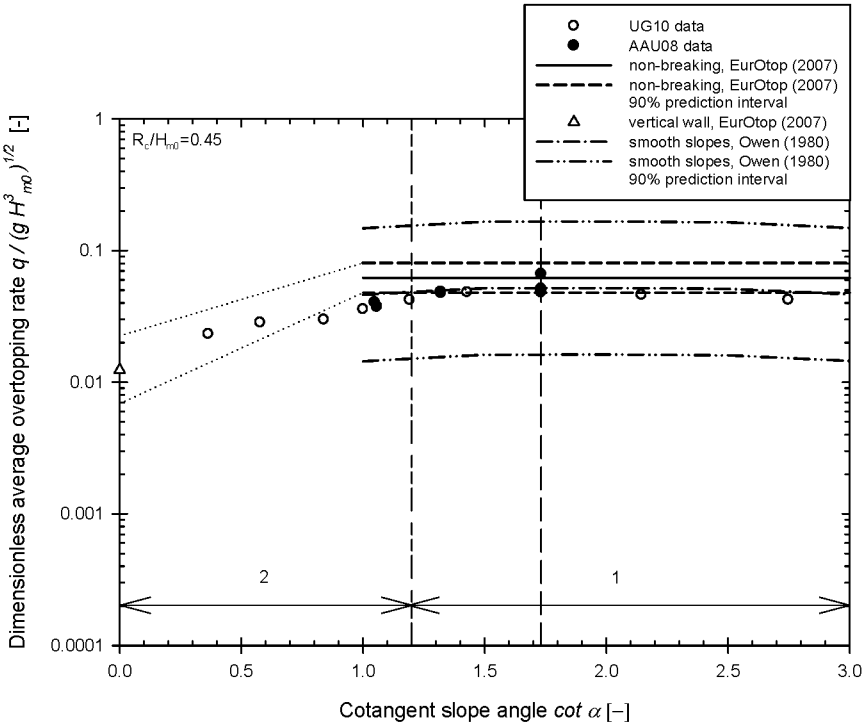

Figure 5.4: Measured average overtopping rate (logarithmic scale) for Example 1 as a function of the slope angle (linear scale), with $\cot\alpha$ *varying between 0.0 and 3.0. Predictions by EurOtop (2007) and Owen (1980) are added.*

Finally, the measured average overtopping rates for Example 1 are compared to their predicted values of the DHNN tool in Fig. 5.5 and Fig. 5.6, for the AAU08 and UG10 test results respectively. The predicted average overtopping rates in Fig. 5.5 are based on the relative crest freeboard of the AAU08 test series ($R_c / H_{m0} = 0.50$).

The horizontal axis of Fig. 5.5 corresponds to the characteristic slope angle for the fractioned slopes of the AAU08 test series. Note that the DHNN tool is able to take into account the fractioned slopes through a zero-width berm. This feature was used when determining the predictions of the AAU08 test results by the DHNN tool.

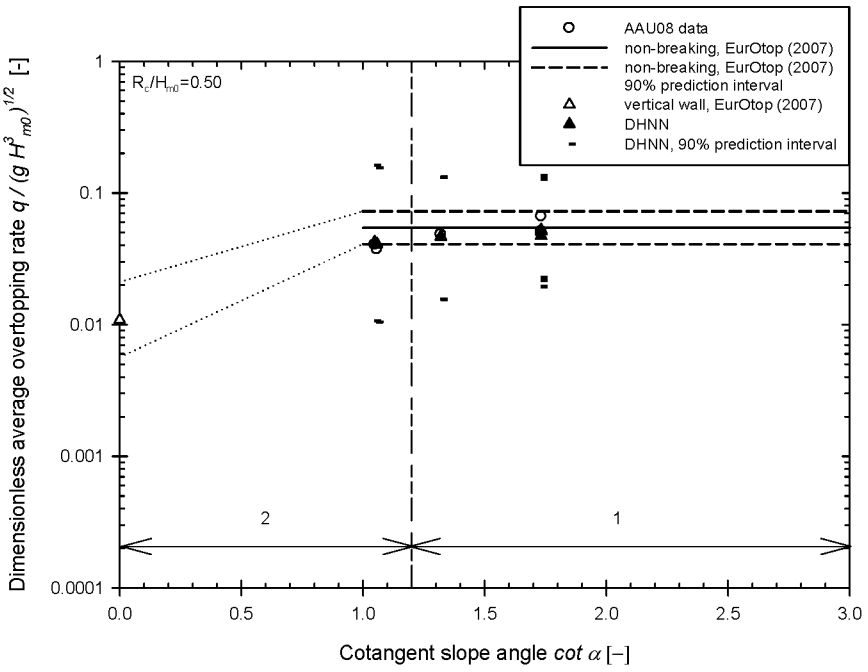

Figure 5.5: Measured average overtopping rate (logarithmic scale) for the AAU08 test results of Example 1 as a function of the slope angle (linear scale), with $\cot\alpha$ *varying between 0.0 and 3.0. Predictions by EurOtop (2007) and the DHNN tool are added.*

The mean predictions by the DHNN tool approach the measured average overtopping rates quite well for both the AAU08 and UG10 test results and for both zones of milder and steeper slopes (Figs. 5.5 and 5.6). This shows that the DHNN tool gives rather accurate predictions for Example 1, although its predictions are based on an interpolation between test results of the CLASH database for vertical walls and for mild slopes.

Based on Figs. 5.3 to 5.6, the following conclusions are drawn concerning Example 1:

- a weak dependency on the slope angle occurs for the average overtopping rates of the AAU08 and UG10 test results for milder slopes (zone 1). This weak dependency is also predicted by Eqs. (4.5) and (4.9), and by the DHNN tool;
- the mean predictions by Eq. (4.9) and by the DHNN tool are quite accurate. Eq. (4.5) tends to overpredict the average overtopping rates;

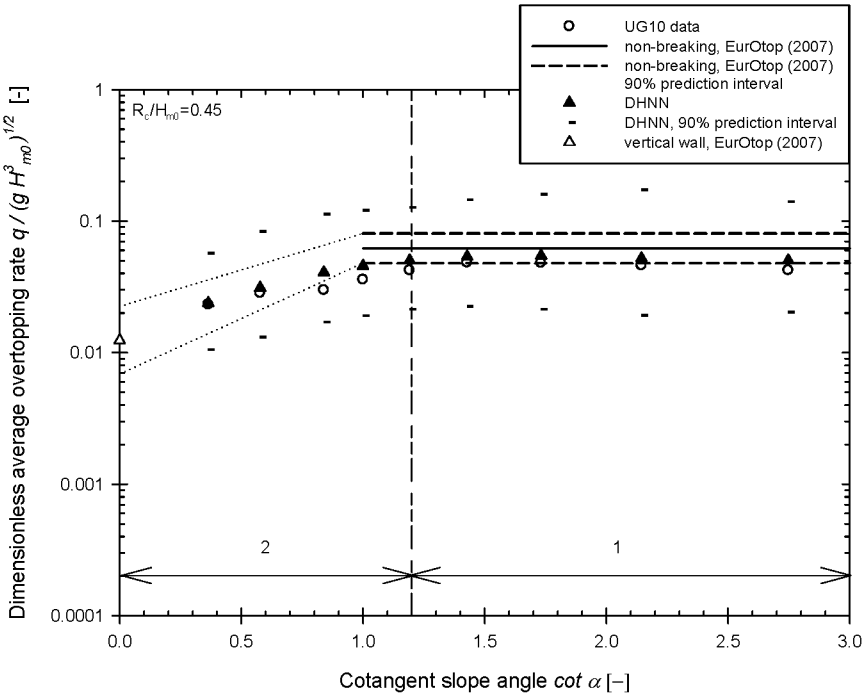

Figure 5.6: Measured average overtopping rate (logarithmic scale) for the UG10 test results of Example 1 as a function of the slope angle (linear scale), with $\cot\alpha$ *varying between 0.0 and 3.0. Predictions by EurOtop (2007) and the DHNN tool are added.*

- Eq. (4.2b) overpredicts the average overtopping rates due to the violation of its ranges of application for R_c / H_{m0};

- a significant decrease in average overtopping rate occurs for steeper slopes (zone 2) with increasing slope angle. The mean predictions of the DHNN tool accurately predict that decrease.

5.2.2 Example 2 - $R_c / H_{m0} = 0.67$

Graphs similar to section 5.2.1 are shown below for Example 2. The characteristics of the AAU08 and UG10 test results for Example 2 are given in Table 5.2.

Table 5.2: Geometrical and hydraulic parameters for studying the independent effect of the slope angle on the average overtopping rate of steep low-crested slopes – Example 2.

Parameter	UG10	AAU08
R_c / H_{m0}	0.67	0.75
R_c	0.045 m	0.050 m
H_{m0}	0.067 m	0.067 m
T_p	1.278 s	1.278 s

Based on Figs. 5.7 to 5.10, the effect of the slope angle on the average overtopping rate for Example 2 is similar to that of Example 1. Again, a weak dependency of the average overtopping rates occurs for milder slopes (zone 1), while steeper slopes (zone 2) correspond to a decrease in overtopping rate from the overtopping rate for milder slopes towards that of a vertical wall following a quasi-linear trend line.

However, the slope of the descending trend line of the UG10 data points in zone 2 is steeper compared to the corresponding slope for Example 1 (e.g. when comparing Fig. 5.7 to Fig. 5.3). This is caused by the larger difference between the dimensionless average overtopping rates for milder slopes on the one hand and vertical walls on the other hand for Example 2. Correspondingly, the effect of the slope angle on the overtopping rates for steeper slopes is larger for larger values of the relative crest freeboard. This is in agreement with Figs. 5.1 and 5.2 (section 5.1).

Furthermore, the intersection point between the descending trend line of the test results for steeper slopes and the lower boundary of the 90% prediction interval of Eq. (4.2b) is positioned at a lower value of $\cot\alpha$ for Example 2 than for Example 1: $\cot\alpha$ = 1.0 (vertical *long-short-short* -dashed line). This is caused by the increased

width of the 90% prediction interval of Eq. (4.2b) for an increased value of the relative crest freeboard.

Thirdly, since the data points of the AAU08 and UG10 datasets with $1.0 < \cot\alpha < 3.0$ are located within the 90% prediction interval of Eq. (4.2b) in Fig. 5.7, the effect of the slope angle on the overtopping rate is negligible according to EurOtop (2007). On the other hand, those data points are also positioned inside the 90% prediction interval of Eq. (4.9) (Fig. 5.8). This means that the effect of the slope angle, although it is rather weak, should not be neglected (Owen 1980). The mean predictions by Owen (1980) tend to overpredict the measured overtopping rates for milder slopes in Fig. 5.8.

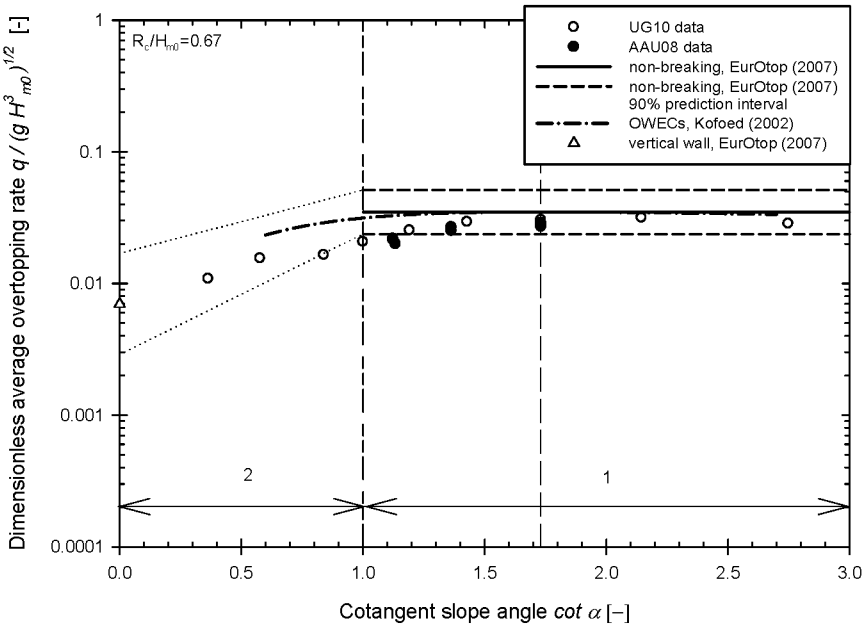

Figure 5.7: Measured average overtopping rate (logarithmic scale) of Example 2 as a function of the slope angle (linear scale), with $\cot\alpha$ *varying between 0.0 and 3.0. Predictions by EurOtop (2007) and Kofoed (2002) are added.*

Similar to Example 1, the mean predictions of the DHNN tool are quite accurate for Example 2, both for milder and steeper slopes (Figs. 5.9 and 5.10). Only a small overprediction of the overtopping rates of the AAU08 and UG10 test results occurs by the mean predictions of the DHNN tool.

The conclusions drawn at the end of section 5.2.1 for Example 1 are also largely valid for Example 2. However, the ranges of application of Eq. (4.2b) for R_c / H_{m0} are not violated in Example 2. This results in a contradiction concerning the significance of the effect of the slope angle between the predictions of Eq. (4.2b) on the one hand and by Eq. (4.9) and the DHNN tool on the other hand.

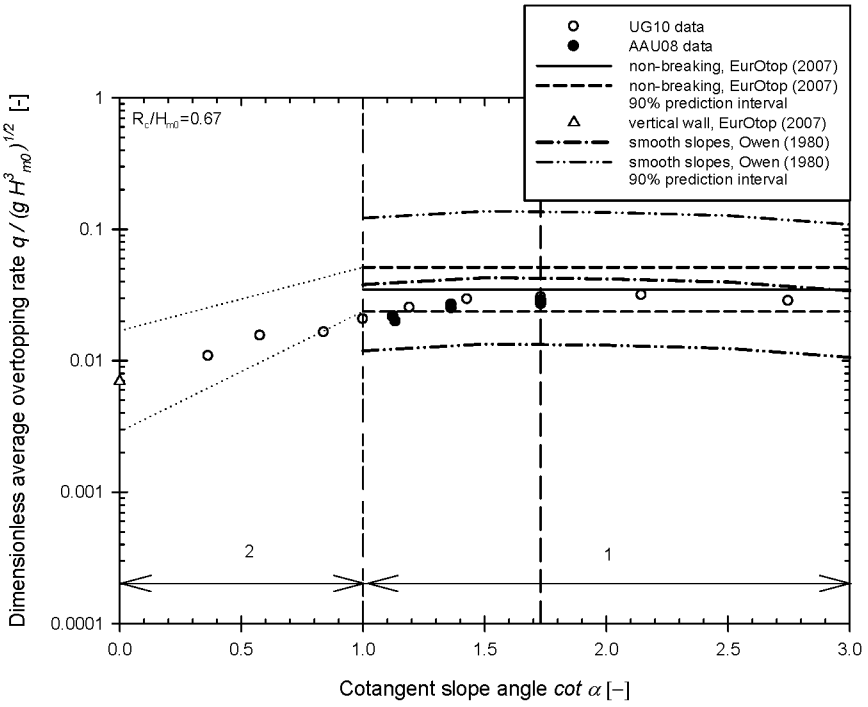

Figure 5.8: Measured average overtopping rate (logarithmic scale) for Example 2 as a function of the slope angle (linear scale), with $\cot\alpha$ *varying between 0.0 and 3.0. Predictions by EurOtop (2007) and Owen (1980) are added.*

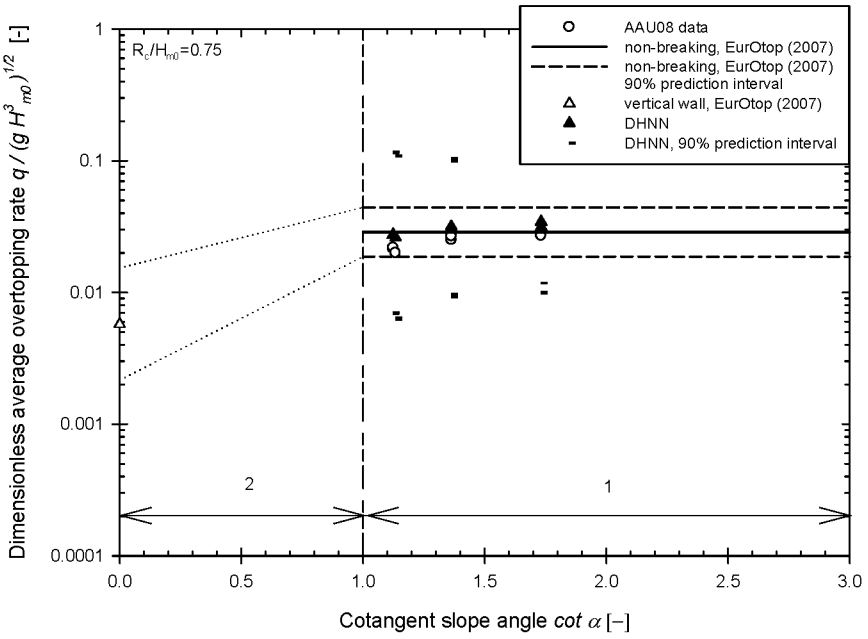

Figure 5.9: Measured average overtopping rate (logarithmic scale) for the AAU08 test results of Example 2 as a function of the slope angle (linear scale), with $\cot\alpha$ *varying between 0.0 and 3.0. Predictions by EurOtop (2007) and the DHNN tool are added.*

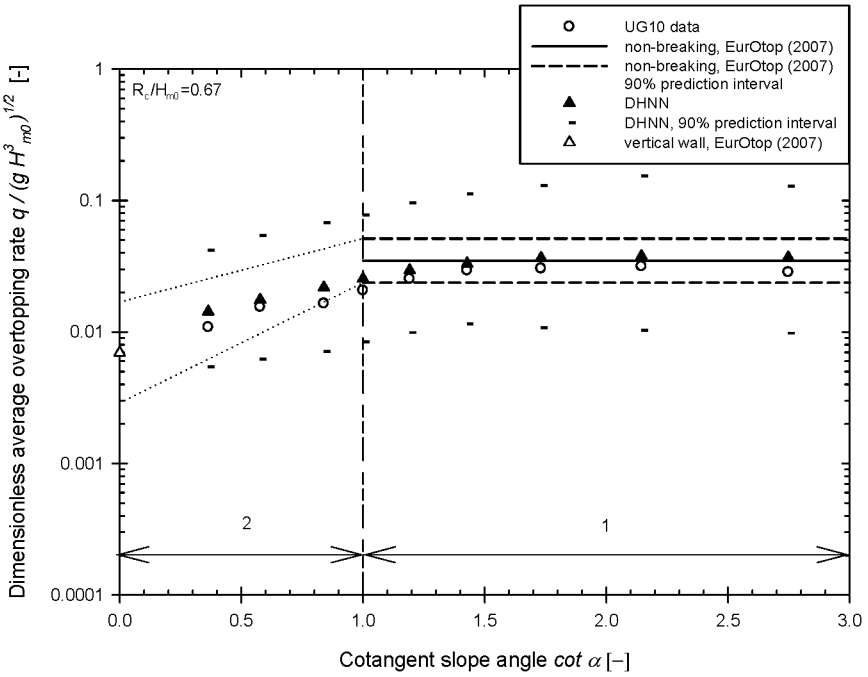

Figure 5.10: Measured average overtopping rate (logarithmic scale) for the UG10 test results of Example 2 as a function of the slope angle (linear scale), with $\cot\alpha$ *varying between 0.0 and 3.0. Predictions by EurOtop (2007) and the DHNN tool are added.*

5.2.3 Example 3 - R_c / H_{m0} = 1.36

Figures 5.11 to 5.14 are similar to Figs. 5.3 to 5.6, but for test results of the AAU08 and UG10 datasets with characteristics defined in Table 5.3.

The relative crest freeboard of Example 3 fulfils the ranges of application of R_c / H_{m0} for Eq. (4.15) (Table 4.7). Hence, predictions of the dimensionless average overtopping rate for vertical walls ($\cot\alpha = 0.0$) by Eq. (4.15) (Franco et al. 1994) are added to the graphs in this section (white square on vertical axis).

Table 5.3: Geometrical and hydraulic parameters for studying the independent effect of the slope angle on the average overtopping rate of steep low-crested slopes – Example 3.

Parameter	UG10	AAU08
R_c / H_{m0}	1.36	1.52
R_c	0.045 m	0.050 m
H_{m0}	0.033 m	0.033 m
T_p	1.022 s	1.022 s

In general, similar observations are made in this section compared to the two previous sections 5.2.1 and 5.2.2. In particular, the following conclusions are drawn for Example 3:

- since the relative crest freeboard is larger compared to Example 2, the slope of the descending trend line of the data points for steeper slopes (zone 2) is even steeper than for Example 2;

- the 90% prediction interval of Eq. (4.2b) is wider for Example 3 than for Example 2. Hence, the abscissa of the intersection point between the descending trend line of the data points for steeper slopes and the lower boundary of the 90% prediction interval of Eq. (4.2b) (extended to steeper slopes) is positioned at a steeper slope ($\cot\alpha$ = 0.80) for Example 3 (vertical *long-short-short* -dashed line);

- although the data points of the UG10 dataset with milder slopes are positioned within the 90% prediction interval of Eq. (4.2b), these points clearly describe a curved line in Fig. 5.11, reaching a maximum for $\cot\alpha \approx 2.14$;

- the empirical prediction formula of Owen (1980) overpredicts the dimensionless average overtopping rates for Example 3 (Fig. 5.12). This is caused by the low value of the wave steepness ($s_{m-1,0}$ = 0.024) for Example 3, which is below the lower boundary of the range of application of the simple regression formula by Owen (1980) for the wave steepness: $s_{m-1,0} \approx 0.030$[1] (section 4.3.2.3). The mean

[1] Based on $T_p / T_m = 1.25$ (JONSWAP spectrum with peak enhancement factor 3.3) and assuming $T_p / T_{m-1,0} = 1.1$ (single peaked spectrum).

prediction line by Owen (1980) is quite accurate for the milder slopes of Examples 1 and 2, since these examples correspond to values of the wave steepness $s_{m-1,0} \approx 0.031$;

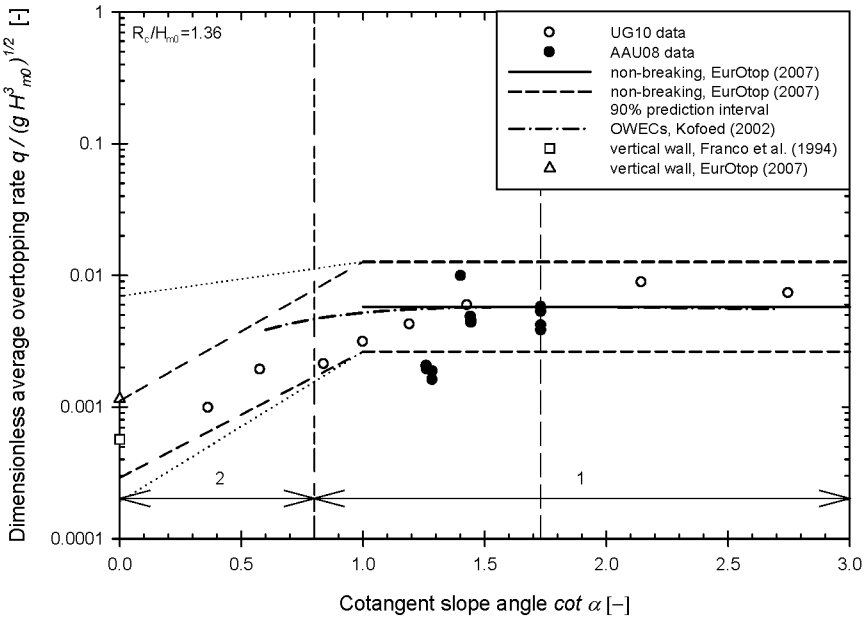

Figure 5.11: Measured average overtopping rate (logarithmic scale) for the UG10 test results of Example 3 as a function of the slope angle (linear scale), with $\cot\alpha$ *varying between 0.0 and 3.0. Predictions by EurOtop (2007), Franco et al. (1994) and Kofoed (2002) are added.*

- the mean predictions by the DHNN tool for the AAU08 and UG10 test results (Figs. 5.13 and 5.14) approach the measured overtopping rates quite well for the milder slopes, but clearly overpredict the measured overtopping rates for steeper slopes ($\cot\alpha < 1.0$). However, the data points are still positioned within the 90% prediction interval (which is relatively wide for the larger relative crest freeboards) of the DHNN tool. This means that no significant deviations occur between the predictions of the DHNN tool and the UG10 test results.

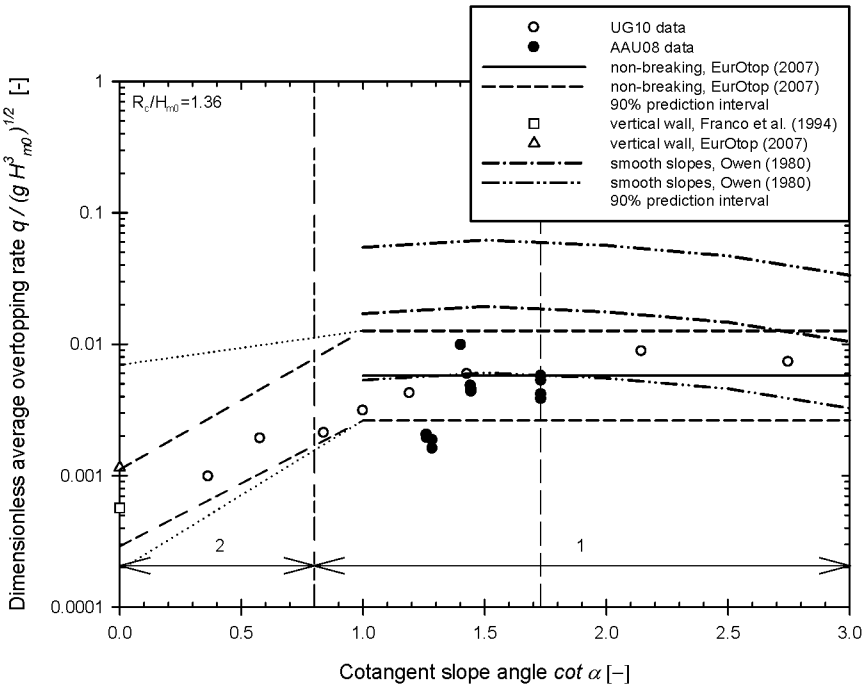

Figure 5.12: Measured average overtopping rate (logarithmic scale) for Example 3 as a function of the slope angle (linear scale), with $\cot\alpha$ *varying between 0.0 and 3.0. Predictions by EurOtop (2007), Franco et al. (1994) and Owen (1980) are added.*

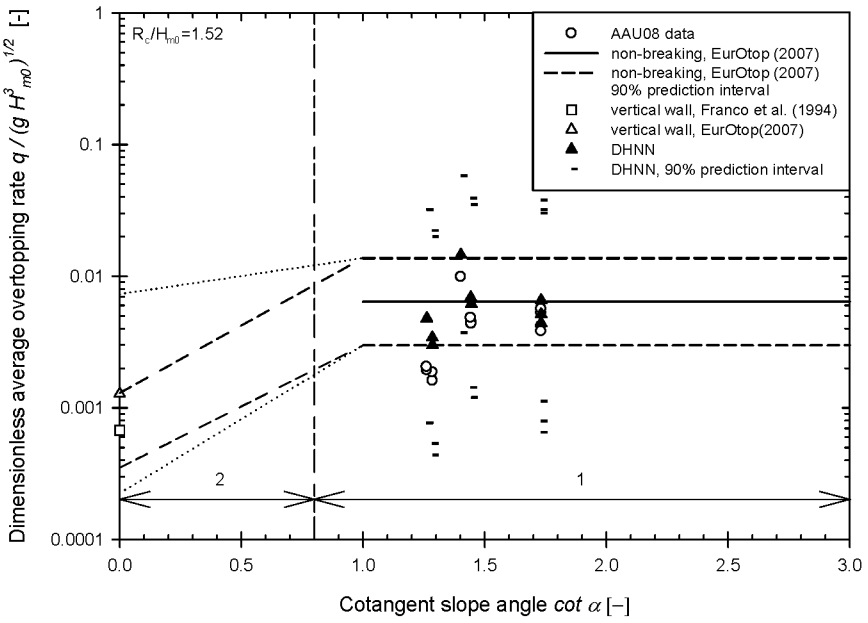

Figure 5.13: Measured average overtopping rate (logarithmic scale) for the AAU08 dataset of Example 3 as a function of the slope angle (linear scale), with $\cot\alpha$ *varying between 0.0 and 3.0. Predictions by EurOtop (2007), Franco et al. (1994) and the DHNN tool are added.*

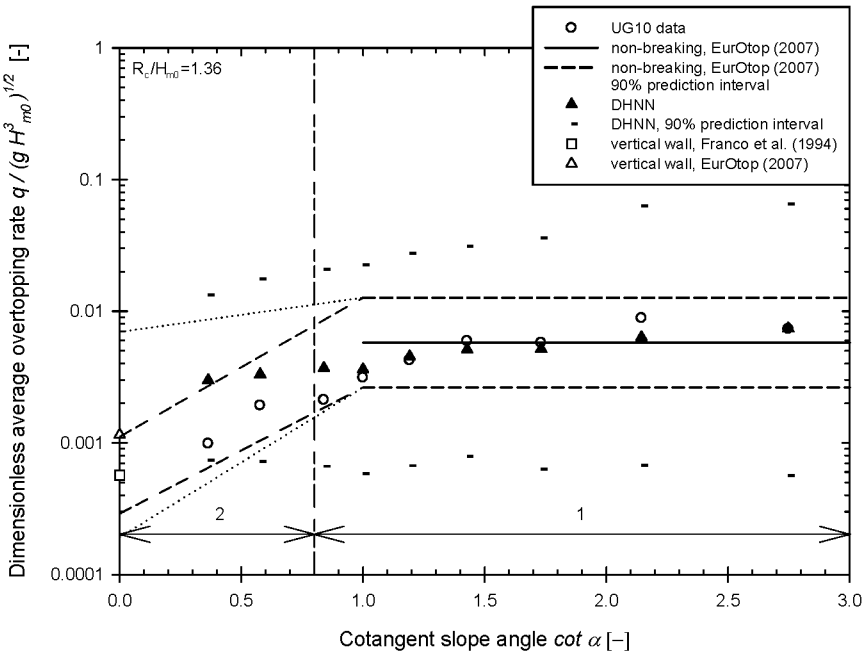

Figure 5.14: Measured average overtopping rate (logarithmic scale) for the UG10 dataset of Example 3 as a function of the slope angle (linear scale), with $\cot\alpha$ *varying between 0.0 and 3.0. Predictions by EurOtop (2007), Franco et al. (1994) and the DHNN tool are added.*

5.2.4 Conclusions on the effect of the slope angle and the interaction with the relative crest freeboard

5.2.4.1 Conclusions on the effect of the slope angle

Two zones of different overtopping behaviour have been identified for each of the examples in sections 5.2.1 and 5.2.3 based on the data points corresponding to the AAU08 and UG10 test results. Zone 1 contains milder slopes with a weak dependency on the slope angle. The corresponding data points describe a gentle parabolic-shaped curve, reaching a maximum for a specific slope angle and further

decreasing towards steeper slopes. Zone 2 contains data points corresponding to steeper slopes and exhibits a large dependency on the slope angle. A sharp decrease in average overtopping rate occurs for increasing slope angle, following a quasi-linear trend line which descends from the gentle parabolic curve for milder slopes towards the overtopping rates for vertical walls predicted by EurOtop (2007) and Franco et al. (1994).

5.2.4.2 Conclusions on interaction between relative crest freeboard and the effect of the slope angle

The interaction between the relative crest freeboard and the effect of the slope angle on the overtopping rate is considerable. Figure 5.15 summarizes the observations from sections 5.2.1 to 5.2.3, using two illustrative examples with relative crest freeboards $R_c / H_{m0} = 0.60$ and 1.40.

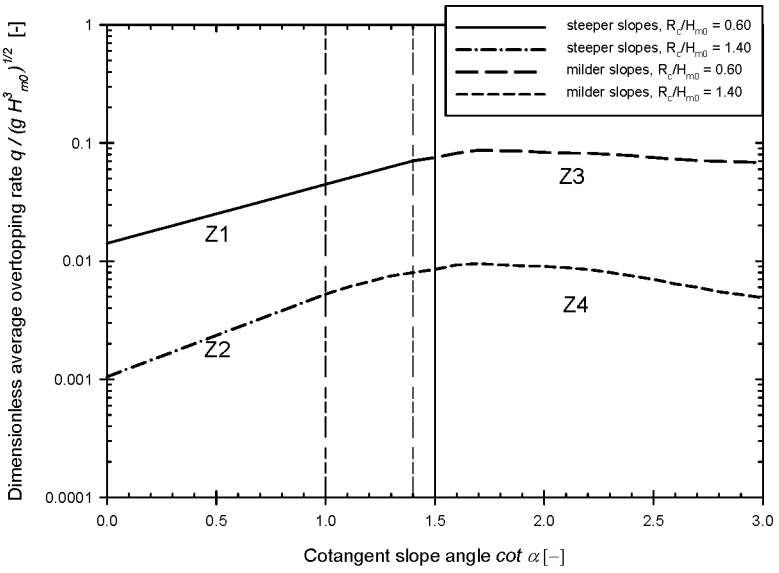

Figure 5.15: Dimensionless average overtopping rate (logarithmic scale) as a function of the slope angle (linear scale), with $\cot\alpha$ *varying between 0.0 and 3.0. Illustrative examples summarizing the conclusions from Examples 1 to 3.*

It is clear that the dependency of the overtopping rates on the slope angle increases for larger relative crest freeboards, both for steeper slopes and milder slopes (Fig. 5.15). Hence, it is worthwhile to take a look at the effect of the slope angle on the average overtopping rate of structures with a zero crest freeboard (Fig. 5.16).

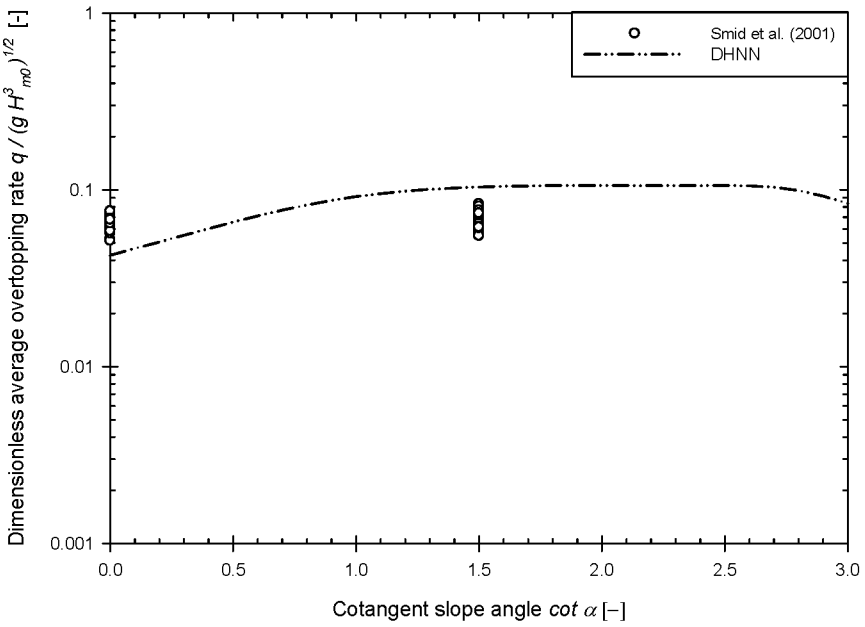

Figure 5.16: Average overtopping rate (logarithmic scale) as a function of the slope angle (linear scale), with $\cot\alpha$ *varying between 0.0 and 3.0, for the test results by Smid et al. (2001) and predictions by the DHNN tool are added.*

Based on Fig. 5.16, only a very weak dependency of the average overtopping rate on the slope angle is expected for structures with a zero crest freeboard, both for steeper and milder slopes.

The test results of Smid et al. (2001) predict an independency of the average overtopping rate on the slope angle, with a constant value of $q/\sqrt{gH_{m0}^3} = 0.062$. On the other hand, a decrease in the average overtopping rate is predicted by the DHNN

tool for slope angles increasing from $\cot\alpha = 1.0$ to $\cot\alpha = 0.0$ (similar to Examples 1 to 3). It is noted that the test results of Smid et al. (2001) have not been used for training the DHNN tool. This explains the differences between both corresponding predictions. Since Eq. (4.17) (Schüttrumpf 2001) predicts a dependency of the average overtopping rate on the slope angle for mild slopes ($3.0 \le \cot\alpha \le 6.0$), the existence of a constant average overtopping rate for steep slopes is questionable.

In conclusion, the very weak dependency on the slope angle for R_c / H_{m0} = 0.0 observed in Fig. 5.16 confirms the interaction between the effects of $\cot\alpha$ and R_c / H_{m0} on the dimensionless average overtopping rate $q / \sqrt{g H_{m0}^3}$ for steep low-crested structures.

5.2.4.3 Conclusions on ability of prediction models to predict the effect of the slope angle and the interactions with the relative crest freeboard

The ability of the prediction models from Table 4.6 to predict the effect of the slope angle on the average overtopping rate for the AAU08 and UG10 test results depends on the values of the slope angle and the relative crest freeboard. A division is made into four zones (Fig. 5.15):

- **zone Z1** (*solid* line) corresponds to **steeper slopes with small relative crest freeboards characterized by a significant effect of the slope angle**. The DHNN tool is the only prediction method which is able to predict the overtopping rates for the steeper slopes, since these slopes are positioned outside the range of application of $\cot\alpha$ for the prediction methods in section 4.3.2. As illustrated for Examples 1 and 2, the mean predictions of the UG10 test results by the DHNN tool are relatively accurate in zone Z1;

- on the other hand, the mean predictions by the DHNN tool overpredict the average overtopping rates for **steeper slopes with larger relative crest freeboards** (i.e. **zone Z2**, *dash-dot* line), **characterized by a significant effect of the slope angle which is larger than in zone Z1**. This is illustrated in Example 3 (Fig. 5.14). The average overtopping rate of the UG10 data points decreases for increasing slope angle towards the predicted values for vertical walls on the vertical axis. On the other hand, the intersection of the trend line of the predicted values for steeper slopes by the DHNN tool intersects the vertical axis above the data points for vertical walls.
  Nevertheless, the UG10 data points are still positioned within the 90% prediction interval of the DHNN tool, which is quite wide for the relatively high crest freeboard in Example 3. This means that the deviations between the predictions

by the DHNN tool and the UG10 test results are not significant. Hence, the DHNN tool can be used to predict the average overtopping rates;

- **milder slopes with small relative crest freeboards** correspond to the **zone Z3** (*long-dashed* line). The AAU08 and UG10 test results only show a **weak dependency on the slope angle** in that zone (Examples 1 and 2). The overtopping rates are quite accurately predicted by Eq. (4.9) (Owen 1980), within its ranges of application for the wave steepness, and by the DHNN tool (mean predictions). The simple regression formula of Kofoed (2002) and EurOtop (2007) tend to overpredict the average overtopping rates for very small relative crest freeboards (Example 1).
  Since the data points corresponding to milder slopes and low relative crest freeboards in Example 2 are positioned inside the 90% prediction interval of Eq. (4.2b), the overtopping rates are assumed to be accurately predicted by Eq. (4.2b) (EurOtop 2007), which suggests the overtopping rate to be independent of the slope angle. This is in contrast to the predicted (weak) effect of the slope angle by Eq. (4.5), Eq (4.9) and by the DHNN tool;

- based on Example 3, the **effect of the slope angle** on the overtopping rates for **milder slopes with large relative crest freeboards** is **not negligible** (**zone Z4**) (*short-dashed* line). Since the data points of Example 3 are positioned within the 90% prediction interval of Eq. (4.2b), the effect of the slope angle on the average overtopping rate however is assumed to be negligible. This is again in contrast to the mean predictions by the DHNN tool and the predictions by Eq. (4.5).

In summary, a disagreement concerning the effect of the slope angle on the average overtopping rate occurs between the test results and (1) the mean predictions by Eq. (4.2b) in the zones Z3 and Z4, and (2) the mean predictions by the DHNN tool in the zone Z2.

In this context, it is important to note that both Eq. (4.2b) and the DHNN tool are determined or trained for a broad range of geometries of coastal structures subjected to a wide range of wave conditions. Hence, the uncertainty on the predictions is relatively large, resulting in rather wide 90% prediction intervals. The width of those intervals is expected to decrease when only straight smooth impermeable slopes exposed to normal wave attack are considered, i.e. applicable to the type of structures considered in this PhD-research.

Moreover, a larger variety of structures has been included for larger crest freeboards compared to lower relative crest freeboards when deriving Eq. (4.2b) and when training the DHNN tool. Consequently, the prediction interval is expected to be relatively narrower for larger relative crest freeboards when only taking into account

straight smooth impermeable coastal structures compared to the original prediction interval.

However, when restricting the test results originally used to derive Eq. (4.2b) to the subset of straight smooth impermeable slopes with normal wave attack, a rather large spreading still occurs. A standard deviation σ = 0.34 has been found for the coefficient -2.6 in Eq. (4.2b) for this subset. Possible reasons for the rather large scatter are differences in waves, structures and overtopping measurements between the different test results. By eliminating these model effects, a decrease in the standard deviation should occur and the 90% prediction interval of Eq. (4.2b) in the figures of the examples above should be narrower when only considering straight smooth impermeable coastal structures, without model effects.

Based on this reasoning, the effect of the slope angle may become significant for zones Z3 and Z4, for which the mean predictions by the DHNN tool are in good agreement with the AAU08 and UG10 test results. Furthermore, Eq. (4.2b) may also overpredict the average overtopping rates for the larger relative crest freeboards in zone Z3.

On the other hand, reducing the dataset used for training the DHNN tool (section 5.4.4) to straight smooth impermeable slopes with normal wave attack conflicts with the principle of the DHNN tool to be applicable for a wide range of structure. The price paid for this wide applicability is the wide 90% prediction interval.

The clear trend of the UG10 data points towards the predicted average overtopping rates for vertical walls in Example 3 confirm the less accurate predictions by the DHNN tool in zone Z2. More accurate predictions would be achieved in zone Z2 when training the DHNN tool using a database which incorporates the UG10 test results.

In conclusion, The DHNN tool is able to predict the effects of the slope angle and the relative crest freeboard and their interactions for the UG10 test results relatively accurately, except for zone Z2. When neglecting the effect of the slope angle in zone Z4, Eq. (4.2b) is also able to predict the average overtopping rate accurately. An overview is given in Table 5.4.

Table 5.4: Overview of applicable prediction models for each of the zones Z1 to Z4.

Zone	**Applicable prediction model**	
Z1	DHNN	
Z2	DHNN overpredicts	
Z3	DHNN	
Z4	Eq. (4.2b)	DHNN

5.2.4.4 Conclusions on transition point between milder and steeper slopes

The slope angle which constitutes the transition between the steeper and milder slopes is defined as the abscissa of the intersection point of the linear trend line in the log-linear plot of the data points corresponding to steeper slopes and the lower boundary of the 90% prediction interval of Eq. (4.2b). Since the slope of the linear trend line and the width of the 90% prediction interval differ depending on the value of the relative crest freeboard, the transition point also depends on the relative crest freeboard. Examples 1 to 3 suggest that the transition slope angle increases when the relative crest freeboard increases (illustrated in Fig. 5.15).

However, based on the reasoning in section 5.2.4.3, the width of the 90% prediction interval of Eq. (4.2b) should be reduced when only considering straight smooth impermeable coastal structures (without model effects) and the reduction should be relatively larger for larger relative crest freeboards than for smaller relative crest freeboards. Hence, the transition point between steeper and milder slopes should shift towards larger values of $\cot\alpha$ and the dependency of the transition slope angle on the relative crest freeboard should be relatively small. Therefore, the transition slope is assumed to be $\cot\alpha = 1.5$, marked by the vertical solid line in Fig. 5.15.

5.3 Effect of relative crest freeboard on overtopping rate of steep low-crested slopes

The effect of the relative crest freeboard on the average overtopping rate for the AAU08 and UG10 test results is shown in Fig. 5.1 and Fig. 5.2 respectively. It is clear that a decrease in the relative crest freeboard results in an increase in the average overtopping rate. The results of a comparison of the measured average overtopping rates and the predictions by the models from Tables 4.6 and 4.7 are given in this section for the UG10 test results. The AAU08 test results are not discussed in this section due to their smaller ranges of application of the slope angle and relative crest freeboard compared to the UG10 test results.

The four zones Z1 to Z4 in Fig. 5.15 can also be identified in Fig. 5.2, as shown in Fig. 5.17. Hence, the conclusions concerning the ability of the prediction models from chapter 4 to predict the dimensionless average overtopping rates accurately in each of the zones (section 5.2.4.3) also apply here. This is verified for the zones Z3 and Z4 in section 5.3.1 and for zones Z1 and Z2 in section 5.3.2.

Furthermore, the transition slope angle between the zones Z1 - Z2 on the one hand and Z3 – Z4 on the other hand has been studied in section 5.2.4.4. However, the

transition value of the relative crest freeboard between the zones Z1-Z3 (small relative crest freeboards) and Z2-Z4 (large relative crest freeboards) is still unknown. This is also discussed in the two sections below (sections 5.3.1 and 5.3.2).

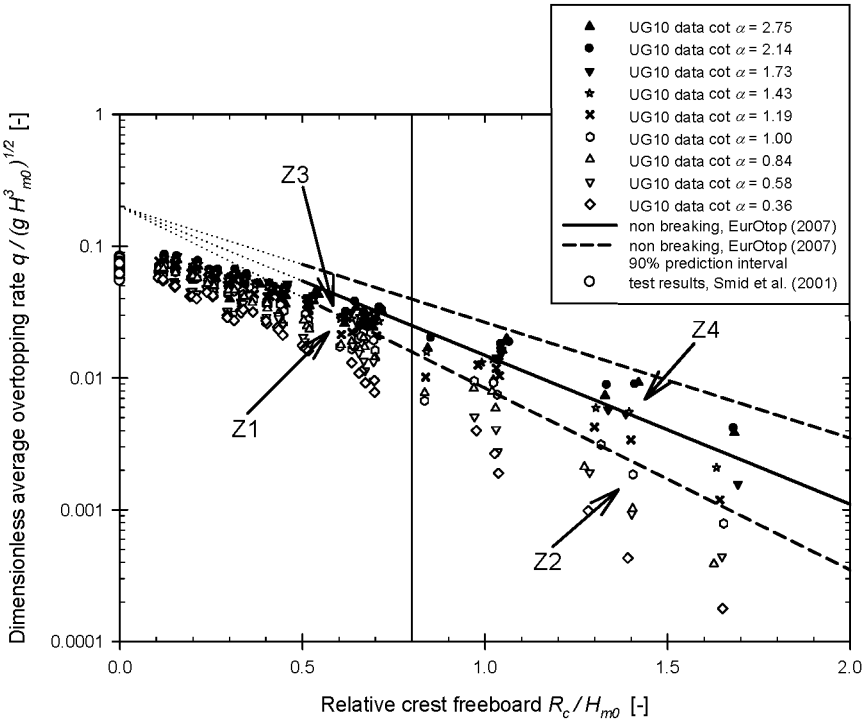

Figure 5.17: Dimensionless average overtopping rate (logarithmic scale) as a function of the relative crest freeboard (linear scale) for the test results of the UG10 dataset, with R_c / H_{m0} varying between 0.0 and 2.0. Predictions by EurOtop (2007) are added.

5.3.1 Zones Z3 and Z4

Based on the conclusions in section 5.2.4.3, Eq. (4.2b) tends to overpredict the overtopping rates in zone Z3, for smaller relative crest freeboards. This is confirmed when plotting the UG10 test results with $\cot\alpha > 1.5$ and the predictions of Eq. (4.2b) against the relative crest freeboard (Fig. 5.18).

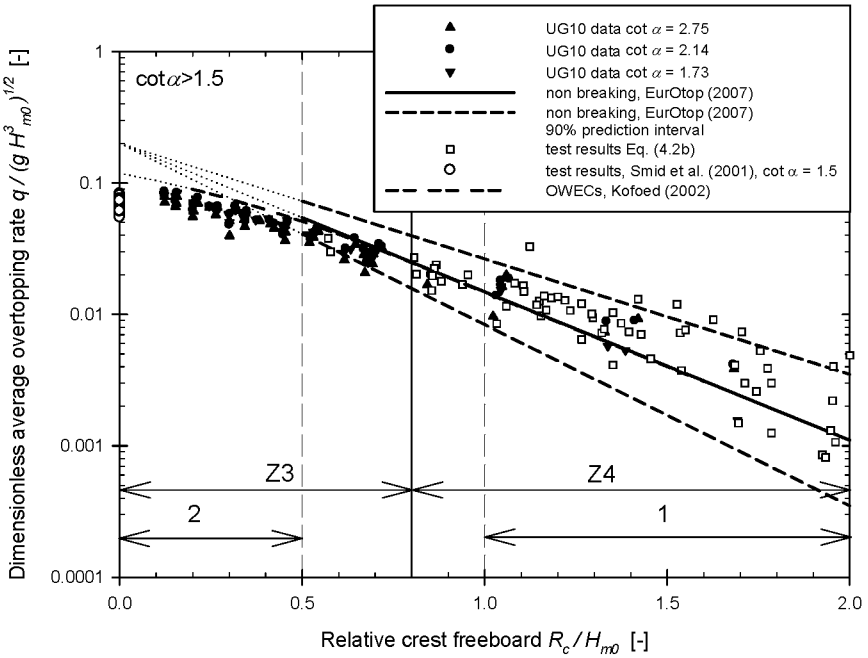

Figure 5.18: Dimensionless average overtopping rate (logarithmic scale) as a function of the relative crest freeboard (linear scale) for the test results of the UG10 dataset with $\cot\alpha > 1.5$, with R_c / H_{m0} varying between 0.0 and 2.0. Original test results for derivation of Eq. (4.2b) are added.

Test results for smooth impermeable steep slopes with $\cot\alpha = 1.0$ and $\cot\alpha = 2.0$ used for deriving Eq. (4.2b) are also added to Fig. 5.18. Only a small number of those test results feature a relative crest freeboard $R_c / H_{m0} < 1.0$.

Three different zones of overtopping behaviour are identified for the UG10 test results in Fig. 5.18: $1.0 \leq R_c / H_{m0} \leq 2.0$ (zone 1), $0.0 \leq R_c / H_{m0} \leq 0.5$ (zone 2) and the transition zone in between, $0.5 < R_c / H_{m0} < 1.0$.

In the first zone, all UG10 data points (black symbols) are located within the 90% prediction interval of Eq. (4.2b). This means that the effect of R_c / H_{m0} on $q / \sqrt{g H_{m0}^3}$ is accurately described by the exponential function of Eq. (4.2b).

In the second zone ($0.0 \leq R_c / H_{m0} \leq 0.5$), the UG10 data points significantly deviate from Eq. (4.2b) towards the test results of Smid et al. (2001) with a zero crest freeboard. The relationship between $q / \sqrt{g H_{m0}^3}$ and R_c / H_{m0} appears to be approximately linear in the log-linear graph for zone 2, suggesting that an exponential function may be fitted through the data points.

In between both zones, a transition zone occurs ($0.5 \leq R_c / H_{m0} \leq 1.0$). Since the 90% prediction interval of Eq. (4.2b) is expected to be narrower than shown in Fig. 5.18 when only considering straight smooth impermeable slopes, the UG10 data points are expected to significantly deviate from Eq. (4.2b) for a value of R_c / H_{m0} larger than 0.5. Based on all data points in Fig. 5.18 and assuming a narrower 90% prediction interval for Eq. (4.2b), this equation is assumed to overpredict the average overtopping rate of steep low-crested structures for $R_c / H_{m0} < 0.8$. Correspondingly, this is the transition value between the zones Z3 and Z4.

Based on Fig. 5.18, the predictions by Eq. (4.5), assuming a slope $\cot\alpha = 1.73$, are located below the prediction line of Eq (4.2b) in zone Z3, caused by the presence of the factor λ_s. However, this factor appears to be insufficient to describe the deviating behaviour of the UG10 data points with $R_c / H_{m0} < 0.8$. This is due to the fact that test results of Schüttrumpf (2001) for structures featuring zero crest freeboards and milder slopes, which are positioned above the test results of Smid et al. (2001), have been used by Kofoed (2002) for calibration.

On the other hand, the mean prediction line by Owen (1980) ($\cot\alpha = 1.5$ and $s_m = 0.05$) is in good agreement with the average overtopping rates for the UG10 test results, particularly for the UG10 test results in zone Z3 (Fig. 5.19). Moreover, it intersects the vertical axis approximately at the test results of Smid et al. (2001). Similar to Fig. 5.12 for Example 3, it tends to overpredict the average overtopping rate for larger relative crest freeboards (zone Z4). The trend of the UG10 test results with $R_c / H_{m0} < 0.8$ is confirmed by the mean prediction line of the DHNN tool for $\cot\alpha = 1.5$ (Fig. 5.20), which interpolates between test results with low relative crest

freeboards and test results with zero crest freeboards. The prediction line also intersects the vertical axis around the location of the test results of Smid et al. (2001).

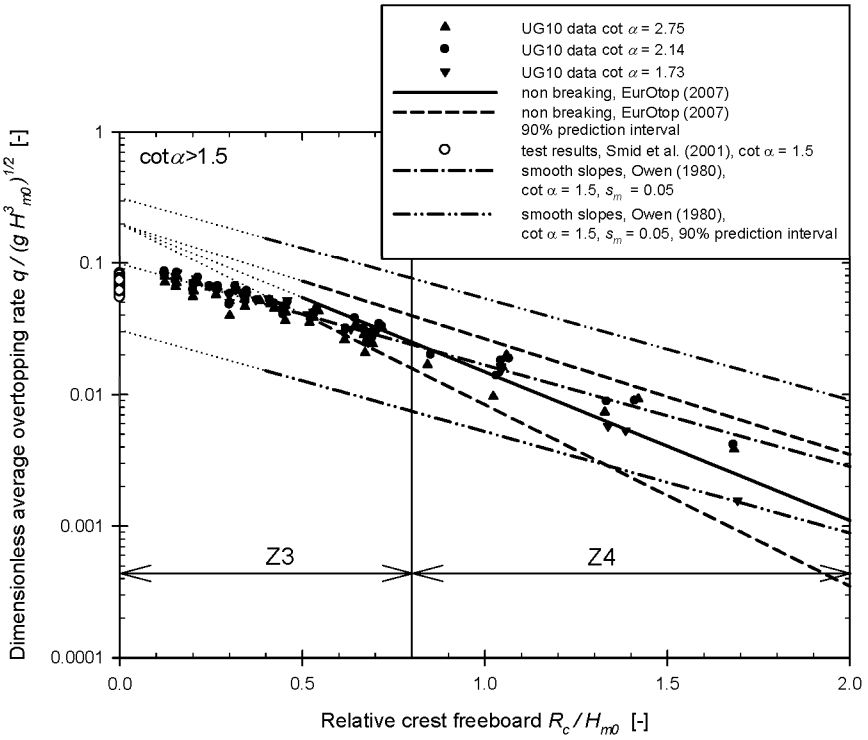

Figure 5.19: Dimensionless average overtopping rate (logarithmic scale) as a function of the relative crest freeboard (linear scale) for the test results of the UG10 dataset with $\cot\alpha > 1.5$, *with* R_c / H_{m0} *varying between 0.0 and 2.0.*

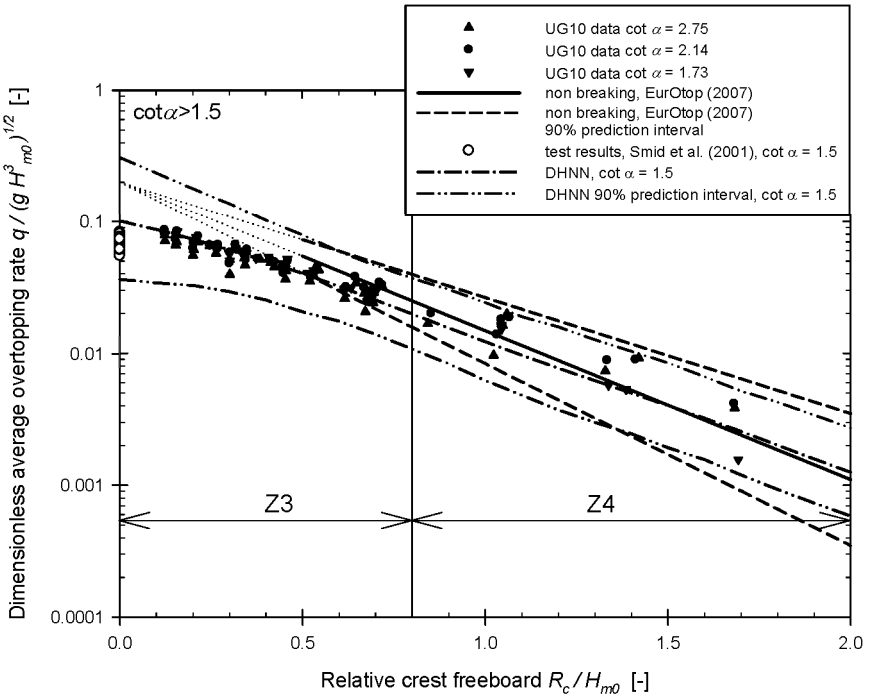

Figure 5.20: Dimensionless average overtopping rate (logarithmic scale) as a function of the relative crest freeboard (linear scale) for the test results of the UG10 dataset with $\cot\alpha > 1.5$*, with* R_c / H_{m0} *varying between 0.0 and 2.0.*

In conclusion, the overtopping behaviour of smooth impermeable uniform slopes in zones Z3 and Z4 is not described sufficiently accurate by a single straight line in a log-linear graph of the average overtopping rate as a function of the relative crest freeboard. This is similar to the case of breaking waves, where the average overtopping rate follows a curved line when plotted in a log-linear graph as a function of the relative crest freeboard (Battjes 1974).

5.3.2 Zones Z1 and Z2

In zones Z1 and Z2, a significant effect of the slope angle is seen, which increases for increasing relative crest freeboard (section 5.2.4.3). This is also visible in Fig. 5.17. The data points in zones Z1 and Z2 are marked using white symbols. The piecewise overtopping behaviour mentioned in section 5.3.1 for zones Z3 and Z4 is confirmed for each of the slope angles, with data points describing a linear trend in the log-linear plot for $0.0 \leq R_c / H_{m0} \leq 0.8$ and a steeper linear trend for $0.8 \leq R_c / H_{m0} \leq 2.0$. Consequently, the transition between the zones Z1 and Z2 also occurs at $R_c / H_{m0} = 0.8$.

Based on section 5.2.4.4 and the observations above, the transition points for the slope angle and relative crest freeboard are determined and the following ranges of application apply for the different zones Z1 to Z4:

Table 5.5 Overview of ranges of application for the slope angle and relative crest freeboard of each of the zones Z1 to Z4

	$R_c/H_{m0} \leq 0.8$	$R_c/H_{m0} \geq 0.8$
cot α < 1.5	zone Z1	zone Z2
cot α > 1.5	zone Z3	zone Z4

A change in slope angle does not affect the shape of the trend line connecting the data points for a specific slope angle (Fig. 5.17). However, the slopes of the corresponding linear trend lines differ depending on the value of the slope angle, becoming steeper for larger values of the slope angle. As a result, the vertical spreading of the data points in Fig. 5.17, which is largely caused by differences in slope angle, increases for increasing relative crest freeboard R_c / H_{m0}.

Based on section 5.2.4.4, the data points in zones Z1 and Z2 are assumed to be positioned outside the narrower 90% prediction interval of Eq. (4.2b). Only the DHNN tool is able to predict the dimensionless average overtopping rates in zones Z1 and Z2, with an overprediction by the mean prediction line of the DHNN tool in zone Z2. This is also visible in Fig. 5.21, which shows the measured and predicted average overtopping rates for $\cot\alpha = 0.84$.

It is also interesting to have a look at the effect of the relative crest freeboard on the overtopping behaviour for the asymptotic case of a vertical wall ($\cot\alpha = 0.0$), to verify whether the double-linear trend lines also occur for that case. Hence, predictions by Eq. (4.15), Eq. (4.16) and the DHNN tool are compared to test results

of the CLASH database for plain vertical walls with non-impulsive conditions (Fig. 5.22). These test results include the test results for a zero crest freeboard by Smid et al. (2001).

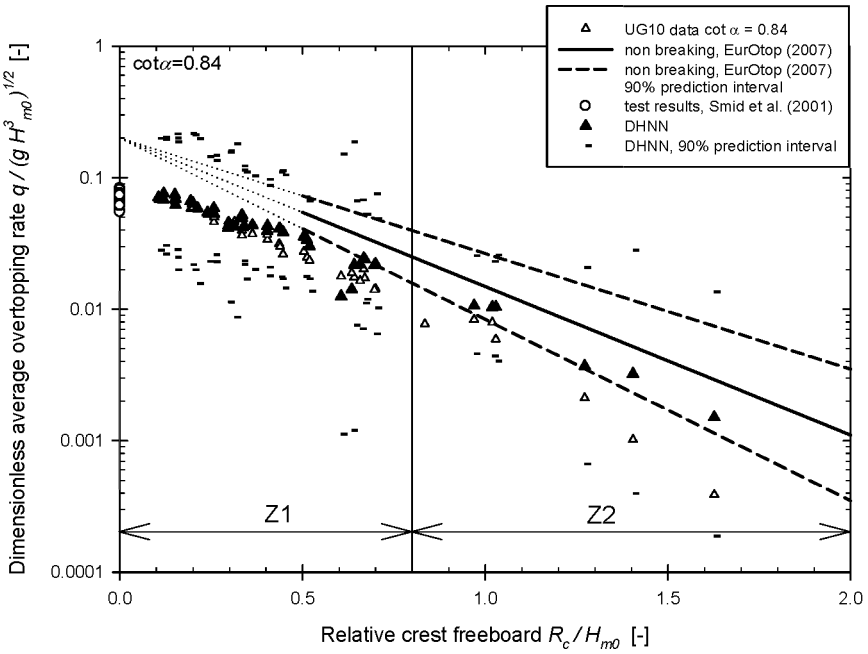

Figure 5.21: Dimensionless average overtopping rate (logarithmic scale) as a function of the relative crest freeboard (linear scale) for the test results of the UG10 dataset with $\cot\alpha = 0.84$*, with* R_c / H_{m0} *varying between 0.0 and 2.0. Predictions by the DHNN tool are added.*

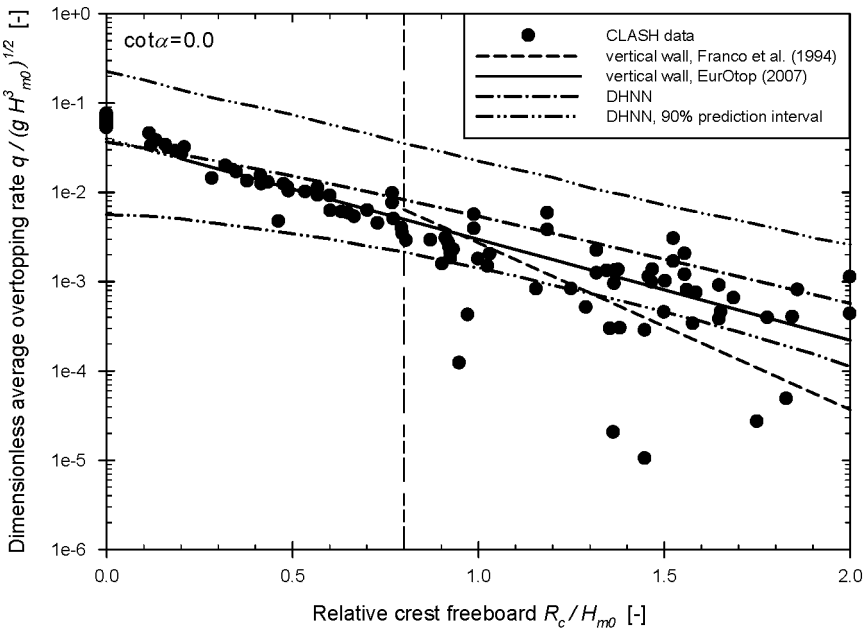

Figure 5.22: Dimensionless average overtopping rate (logarithmic scale) as a function of the relative crest freeboard (linear scale) for $\cot\alpha = 0.0$*, with* R_c / H_{m0} *varying between 0.0 and 2.0.*

Two zones are identified in Fig. 5.22 based on the CLASH test results: (1) a zone with relatively little scatter for smaller relative crest freeboards, and (2) a zone with larger scatter for larger relative crest freeboards. The transition between both zones occurs approximately at $R_c / H_{m0} = 0.8$ (*long-short-short*-dashed line).

The measured average overtopping rates for $R_c / H_{m0} < 0.8$ are relatively accurately predicted by Eq. (4.16) and by the DHNN tool. However, the predicted average overtopping rate of the DHNN tool for a zero crest freeboard and the extension of Eq. (4.16) for $R_c / H_{m0} = 0.0$ are positioned below the test results of

Smid et al. (2001). It is clear that the latter test results have not been used in the training of the DHNN tool and in the derivation of the empirical prediction formula in Eq. (4.16).

A large scatter occurs in the zone of larger relative crest freeboards, resulting in inconsistencies in the predictions. The average overtopping rate predicted by Eq. (4.15), which is only valid in this zone of larger scatter, is smaller than that predicted by Eq. (4.16) and the DHNN tool.

It should be noted that both prediction lines of Eq. (4.16) and the DHNN tool approximately correspond to a straight line for $0.0 \leq R_c / H_{m0} \leq 2.0$, suggesting that the effect of the relative crest freeboard on the average overtopping rate of vertical walls is described by a single straight line.

5.4 Effect of wave steepness on overtopping rate of steep low crested structures

Based on Fig. 5.1 and Fig. 5.2, the effect of the wave period is expected to be small. Hence, its effect has been omitted in the two sections above (5.2 and 5.3), when studying the effects of the slope angle and relative crest freeboard. However, Eq. (4.9) (Owen 1980) explicitly incorporates the wave period in its expression for the average overtopping rate, which means the effect of the wave period may be important.

The effect of the wave period is investigated in detail in this section. The wave period is expressed in a dimensionless form using the wave steepness $s_{m-1,0}$. The effect of the wave steepness combines the effects of the wave height H_{m0} and of the wave period $T_{m-1,0}$.

The wave height H_{m0} is part of the denominators of the dimensionless average overtopping rate $q/\sqrt{g H_{m0}^3}$ and of the dimensionless crest freeboard R_c / H_{m0} in the empirical prediction formulae of Tables 4.6 and 4.7. Accordingly, for specific values of the wave period $T_{m-1,0}$, crest freeboard R_c and slope angle $\cot\alpha$, an increase in wave height results in an increase in average overtopping rate q.

On the other hand, the wave period is not part of those formulae, except for Eq. (4.9). This means that most of the considered prediction methods assume that the effect of the wave period on the overtopping behaviour at steep slopes with non-breaking waves and at vertical walls with non-impacting waves is negligible.

The independent effect of the wave period on the average overtopping rate of steep low-crested structures is studied based on the UG10 test results. The AAU08 test results are not considered here due to their limited range of wave steepness. The dimensionless average overtopping rate $q/\sqrt{g H_{m0}^3}$ (logarithmic scale) for test results of the UG10 dataset with R_c = 0.07 m and $\cot\alpha$ = 1.73 is plotted versus the wave steepness $s_{m-1,0}$ (linear scale) in Fig. 5.23. The UG10 data points are categorized according to the wave height H_{m0}, which varies from 0.067 m, 0.100 m to 0.133 m. The corresponding values of the relative crest freeboard R_c/H_{m0} are 1.04, 0.70 and 0.54. Values of $q/\sqrt{g H_{m0}^3}$ predicted by Eq. (4.2b) and by Eq. (4.9) for H_{m0} = 0.067 m (R_c/H_{m0} =1.04) are added to Fig. 5.23, with their 90% prediction intervals.

Figure 5.24 is similar to Fig. 5.23, for which the predictions by Eq. (4.9) have been replaced with the predictions of the DHNN tool.

The differences in the dimensionless average overtopping rate $q/\sqrt{g H_{m0}^3}$ between the data points in both Figs. 5.23 and 5.24 are mainly due to variations in wave height (and thus in relative crest freeboard). Only very small differences occur between the data points for a particular relative crest freeboard, resulting in quasi-horizontal trend lines. Since these trend lines are quasi-parallel, the interaction between the wave period and the relative crest freeboard is negligible.

The data points corresponding to H_{m0} = 0.067 m are closely aligned with the horizontal prediction line of Eq. (4.2b) and with the prediction line of the DHNN tool (Fig. 5.24). On the other hand, Eq. (4.9) predicts an increase in $q/\sqrt{g H_{m0}^3}$ for an increase in wave period (Fig. 5.23). Note that the solid mean prediction line of Owen (1980) is positioned for its major part inside the 90% prediction interval of Eq. (4.2b). This observation raises the question whether the effect of the wave period is significant or not. Moreover, for large wave periods, corresponding to small values of the wave steepness, overpredictions of the measured values of $q/\sqrt{g H_{m0}^3}$ occur by Eq. (4.9). The overpredictions by Eq. (4.9) for small wave steepnesses have been confirmed by experiments carried out by Hawkes (1999), in which measured average overtopping rates for a wind sea (with large wave steepness) and a swell sea (with small wave steepness) have been compared to predicted rates by the (semi-) empirical formulae of Owen (1980), EurOtop (2007) and Hedges and Reis (1998) for structures with slopes of 1:2 and 1:4.

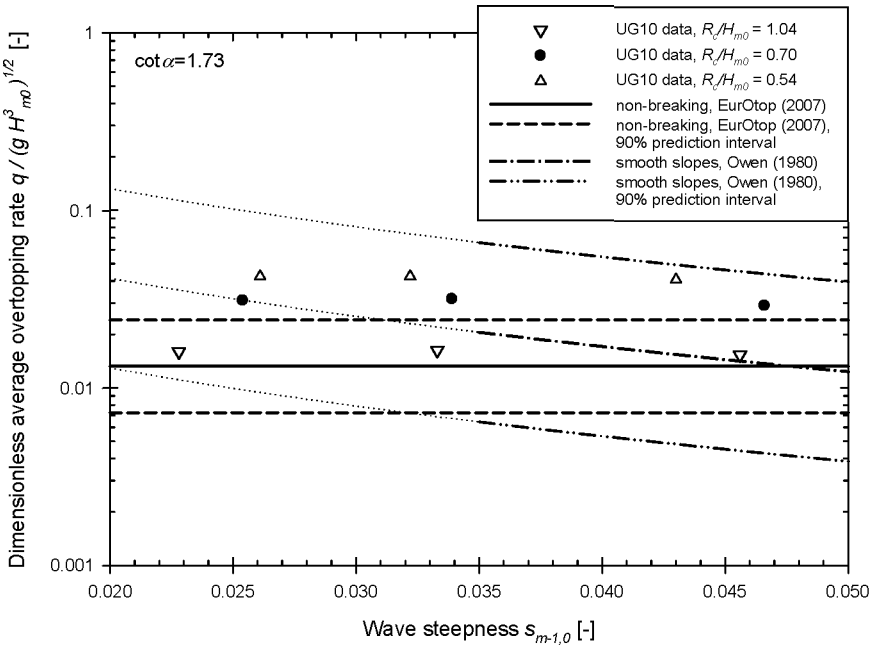

Figure 5.23: Dimensionless average overtopping rate (logarithmic scale) as a function of the wave steepness (linear scale) for $\cot\alpha = 1.73$*, with* $s_{m-1,0}$ *varying between 0.02 and 0.05.*

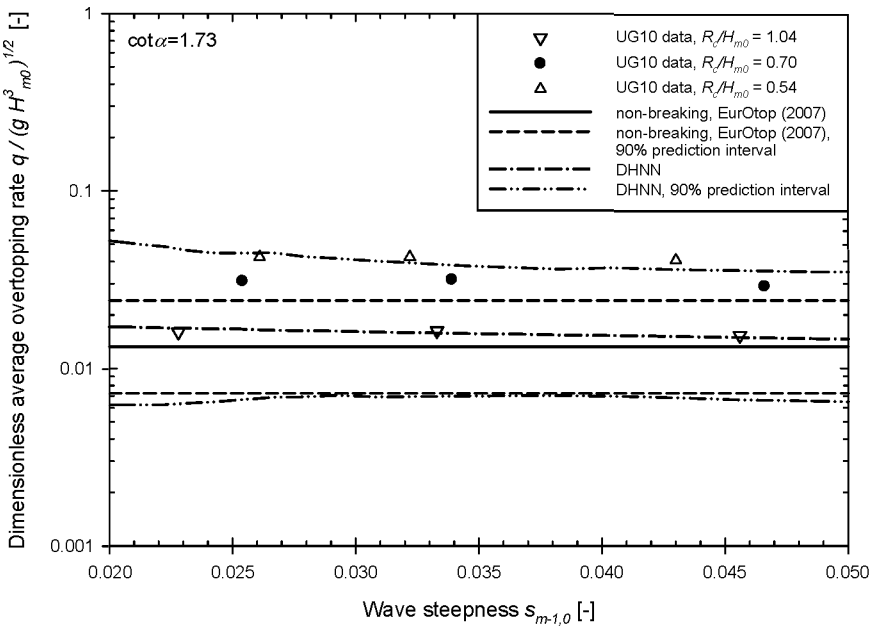

Figure 5.24: Dimensionless average overtopping rate (logarithmic scale) as a function of the wave steepness (linear scale) for $\cot\alpha = 1.73$*, with* $s_{m-1,0}$ *varying between 0.02 and 0.05.*

A graph similar to Fig. 5.24 is shown for $\cot\alpha = 0.84$ in Fig. 5.25. Since this slope angle does not fit the ranges of application of Eq. (4.9), predictions by this equation are not visualized.

The UG10 data points in Fig. 5.25 indicate that an increase in wave period results in a slight decrease in the average overtopping rate for $\cot\alpha = 0.84$. This is in contrast to Eq. (4.2b) and the DHNN tool which predict a quasi-horizontal line.

Eq. (4.2b) clearly overpredicts the average overtopping rates with R_c / H_{m0} = 1.04 in Fig. 5.25, since the corresponding UG10 data are positioned in zone Z2. Accordingly, also the DHNN tool tends to overpredict the average

overtopping rates, which appears to be effectively the case for the largest wave periods (smallest wave steepness).

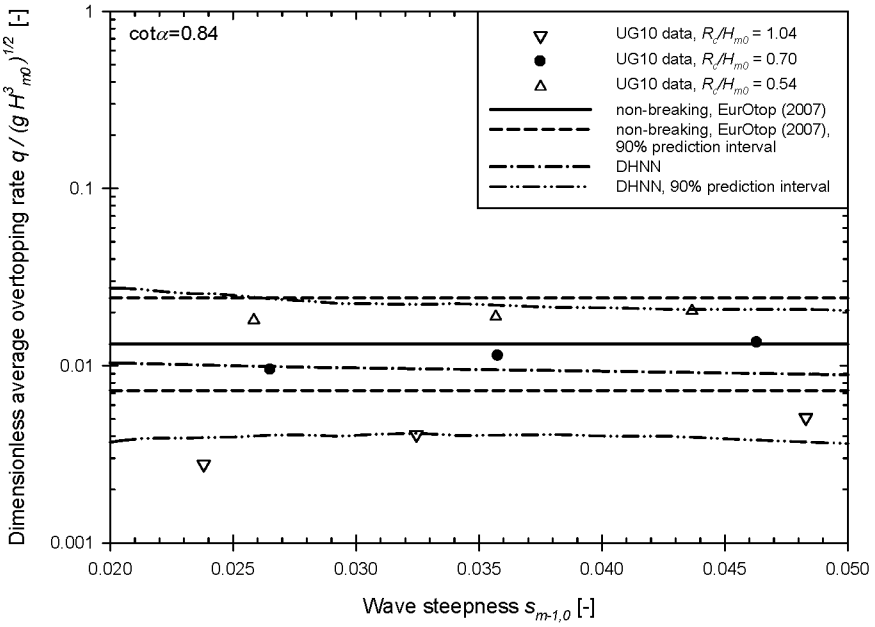

Figure 5.25: Dimensionless average overtopping rate (logarithmic scale) as a function of the wave steepness (linear scale) for $\cot\alpha = 0.84$*, with* $s_{m-1,0}$ *varying between 0.02 and 0.05.*

The increasing trend of the data points in Fig. 5.25 for a particular relative crest freeboard contradicts the decreasing trend predicted by Eq. (4.9) for milder slopes in Fig. 5.23. This suggests that there is an interaction between the wave period and the effect of the slope angle, which is studied in section 5.5.

The vertical spreading of the data points of the UG10 dataset in the graphs in section 5.4 for a particular wave height is much smaller than the vertical spreading of the graphs in sections 5.2 and 5.3. This confirms that the effect of the wave period on the average overtopping rate of steep low-crested structures is limited compared to the effects of the relative crest freeboards and the slope angle, as suggested in section 5.1.

5.5 Optimal slope angle

5.5.1 Existence of optimal slope angle

The optimal slope angle corresponds to the maximum average overtopping rate. Since the largest average overtopping rates are found in zones Z3 and Z4, the maximum average overtopping rate should be found in the range $1.5 < \cot\alpha < 3.0$. As discussed in section 5.2.4.3, it is unclear whether the effect of the slope angle is significant in the zones Z3 and Z4 or not. Accordingly, there is either a zone of optimal slope angles ($1.5 < \cot\alpha < 3.0$), or a single optimal slope angle.

The following references predict the occurrence of a single optimal slope angle:

- Kofoed (2002) and Owen (1980) predict a maximum average overtopping rate for $\cot\alpha = 1.73$ ($\alpha_\circ = 30°$);
- Goda (2009) suggests an optimal slope with $\cot\alpha = 2.0$ ($\alpha_\circ = 27°$);
- according to Sibul and Tickner (1956), the *critical* slope angle $\alpha_\circ$ corresponding to maximum run-up height equals 28° to 30°.

The simple regression formulae of Kofoed (2002) (Eq. 4.5) and Owen (1980) (Eq. 4.9) are based on datasets of test results with more limited ranges of structures compared to the dataset which is used to develop Eq. (4.2b). This confirms that by narrowing the 90% prediction interval of Eq. (4.2b) (when only considering straight smooth sea defence structures), the effect of the slope angle on the average overtopping rate should become significant. In this reasoning, the empirical coefficients in Eq. (4.2b) are assumed to be unvariable when only considering straight smooth sea defence structures. This is justified by the fact that identical values of those coefficients have been suggested by Van der Meer and Janssen (1994), based on a more limited database compared to EurOtop (2007).

5.5.2 Value of the optimal slope angle – interaction between wave period and effect of the slope angle

Assuming that the effect of the slope angle for milder slopes ($1.5 < \cot\alpha < 3.0$) is not negligible, an optimal slope angle exists. According to the references mentioned in section 5.5.1, the value of the optimal slope angle should correspond approximately to $\cot\alpha = 1.73$ ($\alpha_\circ = 30°$). The UG10 test results with $R_c / H_{m0} = 1.04$ (zone Z4)

confirm that the maximum overtopping rate is approximately located at $\cot\alpha = 1.73$ (solid line in Fig. 5.26). The AAU08 test results are not used to determine the optimal slope angle due to their limited range of slope angles.

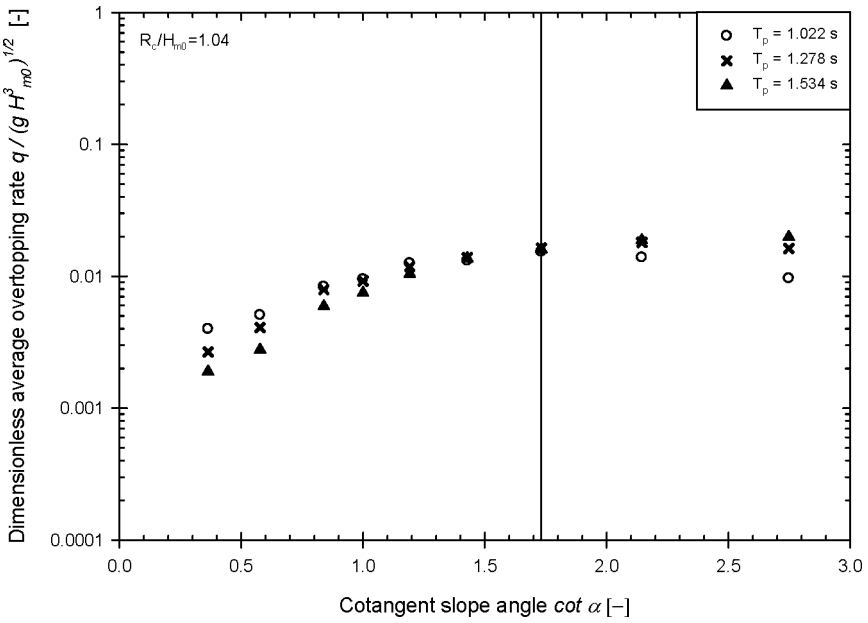

Figure 5.26: Measured average overtopping rate (logarithmic scale) for $R_c = 0.070$ *m and* $H_{m0} = 0.067$ *m as a function of the slope angle (linear scale), with* $\cot\alpha$ *varying between 0.0 and 3.0. Data points are categorized by the wave period.*

However, the value of the optimal slope angle appears to be dependent on the value of the peak wave period. This means that although the interaction between the wave period and the effect of the slope angle on the overtopping rates appears to be very small at first sight (section 5.1), it does affect the value of the optimal slope angle. Furthermore, the interaction exhibits an increased dependency on the wave period for steeper and milder slopes, with a minimum interaction for $\cot\alpha = 1.73$. This explains the increase in average overtopping rate for decreasing wave period seen in Fig. 5.25 for $\cot\alpha = 0.84$.

Based on Fig. 5.26, the cotangent of the optimal slope angle increases for increasing value of the peak wave period, corresponding to a decreasing wave steepness. Accordingly, a specific wave steepness corresponds to a specific optimal slope angle. This suggests that the effect of the breaker parameter (which incorporates the effects of the slope angle and the wave steepness) on the optimal slope angle is important. A log-linear plot of the dimensionless average overtopping rate $q/\sqrt{g H_{m0}^3}$ (logarithmic scale) as a function of the breaker parameter $\xi_{m-1,0}$ (linear scale) is shown in Fig. 5.27 for the identical subset of test results of the UG10 dataset as in Fig. 5.26. The data points are also categorized by the peak wave period T_p.

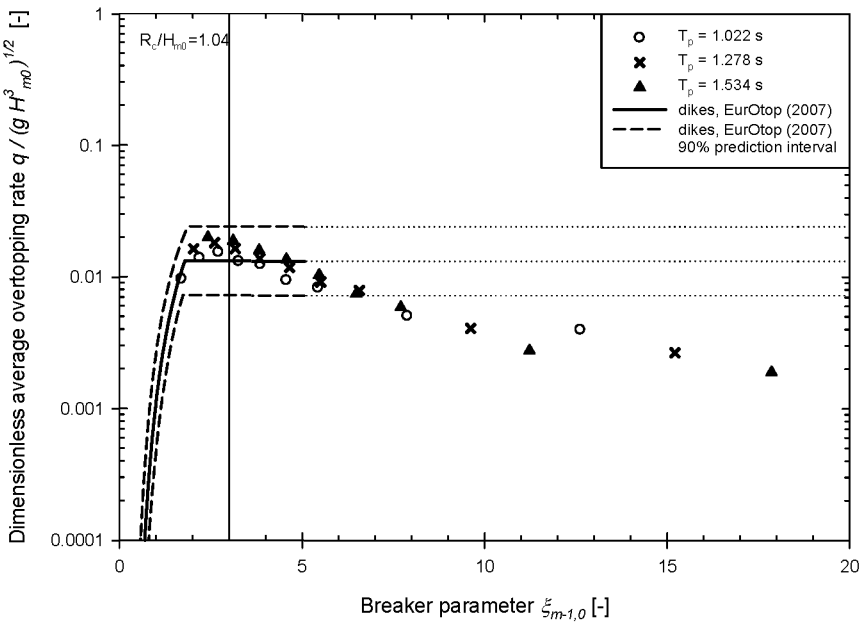

Figure 5.27: Measured average overtopping rate (logarithmic scale) for $R_c = 0.070$ *m and* $H_{m0} = 0.067$ *m as a function of the breaker parameter* $\xi_{m-1,0}$ *(linear scale). Data points are categorized by the wave period.*

Predictions by Eqs. (4.2a) and Eq. (4.2b) are added within their ranges of application for the breaker parameter ($\xi_{m-1,0} < 5.0$), assuming a wave period $T_p = 1.5$ s. When applying narrower 90% prediction intervals for these equations, the effect of the breaker parameter is expected to be significant for $\xi_{m-1,0} < 5.0$, with an optimal breaker parameter positioned at $\xi_{m-1,0} \approx 3.0$ (indicated by the vertical solid line).

The interactions between the wave period and the effect of the slope angle are smaller for UG10 test results with a smaller relative crest freeboard, $R_c / H_{m0} = 0.67$ (Fig. 5.28), positioned in zone Z3.

Hence, the choice of the optimal slope angle is less confined when considering those UG10 test results. Nevertheless, the optimal breaker parameter is assumed to be $\xi_{m-1,0} \approx 3.0$ (Fig. 5.29).

Based on Fig. 5.27 and Fig. 5.29, a maximum average overtopping rate is achieved for a particular sea state (subscript *j*) with a specific wave steepness $s_{m-1,0,j}$, when the slope angle fulfils $\xi_{m-1,0,j} \approx 3.0$:

$$\cot \alpha_{opt,j} \approx \frac{1}{3.0 \sqrt{s_{m-1,0,j}}} \tag{5.1}$$

This is in agreement with the optimal slope angle proposed by Kofoed (2002): $\cot \alpha = 1.73$ ($\alpha_\circ = 30°$). The characteristic sea states used during the experimental tests of Kofoed (2002) all correspond to a wave steepness $s_{m-1,0} \approx 0.033$. Hence, applying Eq. (5.1), the corresponding $\alpha_{\circ,opt}$ equals 29 °.

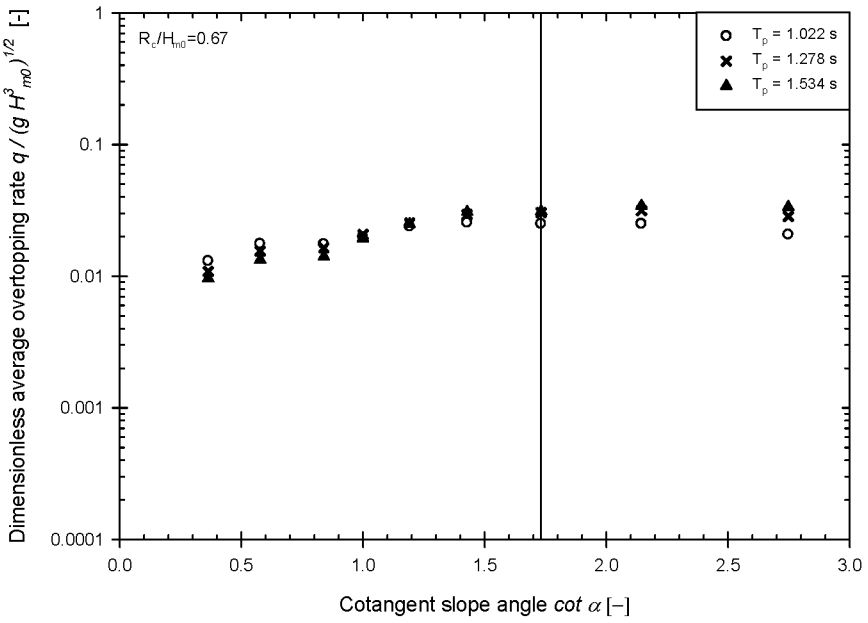

Figure 5.28: Measured average overtopping rate (logarithmic scale) for $R_c = 0.045$ *m and* $H_{m0} = 0.067$ *m as a function of the slope angle (linear scale), with* $\cot\alpha$ *varying between 0.0 and 3.0. Data points are categorized by the wave period.*

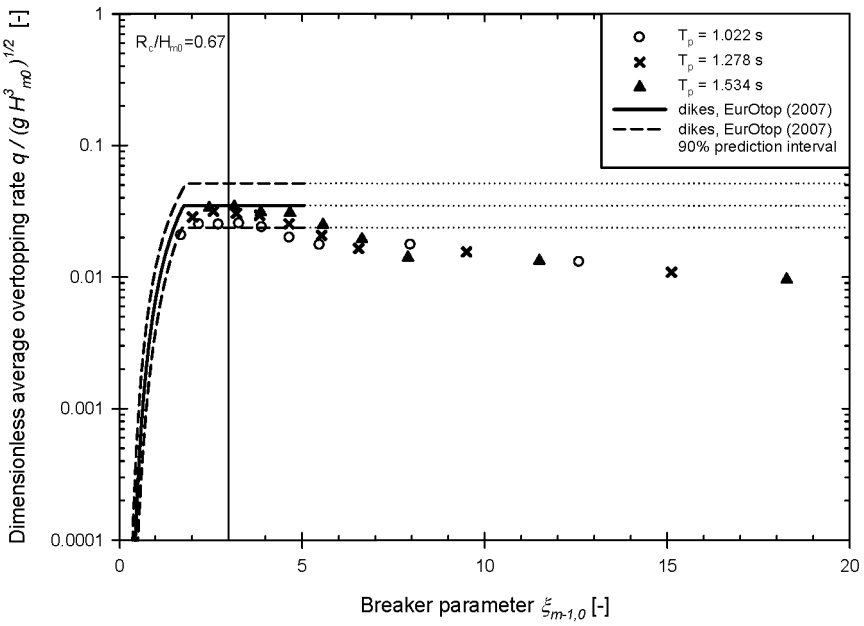

Figure 5.29: Measured average overtopping rate (logarithmic scale) for $R_c = 0.045$ *m and* $H_{m0} = 0.067$ *m as a function of the breaker parameter* $\xi_{m-1,0}$ *(linear scale). Data points are categorized by the wave period.*

5.5.3 Value of the optimal slope angle – interaction between relative crest freeboard and effect of the slope angle

The interaction between the relative crest freeboard and the effect of the slope angle is discussed in section 5.2.4.2. However, its effect on the optimal slope angle in particular is treated here.

The examples in Fig. 5.27 and Fig. 5.29 suggest that the value of the optimal breaker parameter is not affected by the relative crest freeboard. Figure 5.30 shows the effect of the relative crest freeboard on the optimal slope angle for UG10 test results with $H_{m0} = 0.067$ m, $T_p = 1.5$ s and relative crest freeboards $R_c = 0.020$ m,

0.045 m and 0.070 m, covering both zones Z3 and Z4. The interaction between the relative crest freeboard and the effect of the slope angle mainly consists of a change in slope angle of the slope of the trend lines of the data points with $\cot\alpha < 1.50$ for a particular relative crest freeboard. The effect of the relative crest freeboard on the optimal slope angle is negligible (Fig. 5.30) compared to the effect of the wave period on the optimal slope angle (Fig. 5.26).

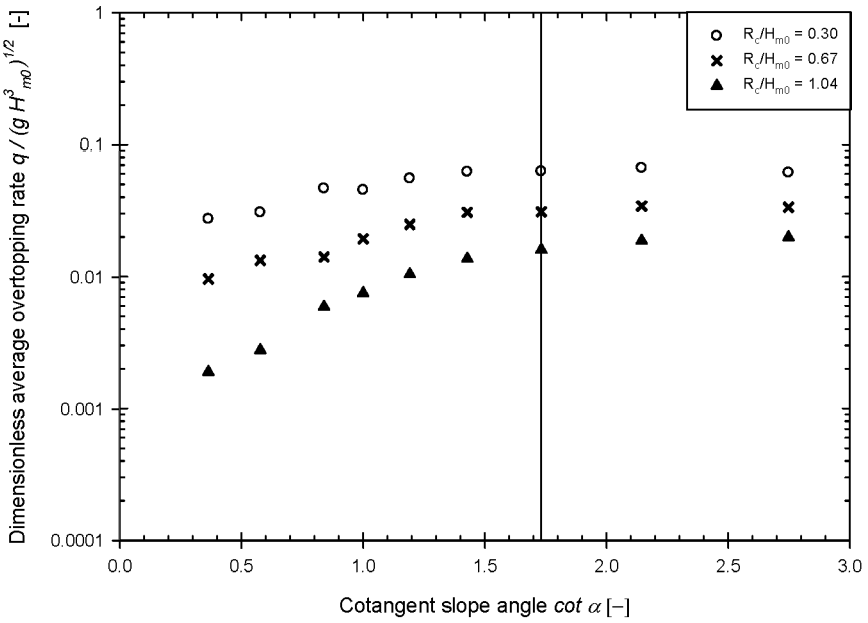

Figure 5.30: Measured average overtopping rate (logarithmic scale) for $H_{m0} = 0.067$ m and $T_p = 1.5$ s and as a function of the slope angle (linear scale), with $\cot\alpha$ varying between 0.0 and 4.0. Data points are categorized by the relative crest freeboard.

5.6 Conclusions on interactions and predictions

5.6.1 Summary of interactions

The sections above discuss the interactions between the three dominating parameters (slope angle, relative crest freeboard and wave period) for the overtopping behaviour of steep low-crested structures. An overview of these interactions is given in Table 5.6.

Table 5.6: Overview of applicable prediction models for each of the zones Z1 to Z4.

Parameters	Interaction
wave period vs slope angle	• at first sight, none (section 5.1) • at second sight (section 5.5): o effect on optimal slope angle o larger effect of wave period on average overtopping rate for steeper and milder slopes
wave period vs relative crest freeboard	neglected (sections 5.1 and 5.4)
relative crest freeboard vs slope angle	• a larger relative crest freeboard corresponds to a larger effect of the slope angle (sections 5.2 and 5.3) • negligible effect on optimal slope angle (section 5.5)

5.6.2 Conclusions on predictions

As shown in Table 5.4, the DHNN tool appears to be the most accurate existing prediction model for the UG10 test results. However, the predictions of the average overtopping rates for steep low-crested slopes by the DHNN tool are subject to a number of shortcomings:

- deviations occur between the mean predictions of the DHNN tool and the UG10 test results in zone Z2;

- based on Fig. 5.25 (section 5.4), the DHNN tool is unable to predict the interaction between the wave period and the slope angle.

Furthermore, the predictions of the DHNN tool feature a wide 90% prediction interval, since the neural network has been trained using test results for a large range of structures and wave characteristics, which means a large uncertainty exists for the output of the DHNN tool.

Moreover, the DHNN tool requires a number of calculations to gain physical insights, while an empirical formula has the advantage that physical insights can be gained based on its expression.

Enhanced by the limited number of parameters affecting the overtopping behaviour of steep low-crested slopes and by the drawbacks of the DHNN tool, a set of new simple regression prediction formulae has been derived based on the UG10 test results, as described in section 5.7. Test results of the AAU08 dataset have not been incorporated for deriving these formulae due to the wider ranges of application for the slope angle, crest freeboard and wave steepness of the UG10 dataset and based on the fact that the UG10 test results are derived for uniform, non-fractioned slopes.

5.7 Derivation of a set of new prediction formulae

Four different prediction formulae have been derived for each of the zones Z1 to Z4, which mathematically express the observed overtopping behaviour for each of these zones explicitly. Due to the uncertainty concerning the existence of an optimal slope angle in zones Z3 and Z4, two approaches are followed in this PhD-manuscript when deriving the new simple regression prediction formulae in zones Z3 and Z4:

- the first approach neglects the effect of the slope angle for milder slopes, which is particularly applicable to smaller relative crest freeboards. In this approach, the constant average overtopping rate predicted by Eq. (4.2b) is valid for milder slopes ($1.5 < \cot\alpha < 3.0$) with $R_c / H_{m0} \geq 0.8$;

- the second approach assumes the effect of the slope angle is significant for milder slopes ($1.5 < \cot\alpha < 3.0$). This is particularly valid for the larger relative crest freeboards. Consequently, a single optimal slope angle occurs and the effect of the wave period on that optimal slope angle should be taken into account.

Since the effect of the slope angle is significant in the zones Z1 and Z2, it has been taken into account in the corresponding prediction formulae.

On the other hand, the effect of the wave period on the average overtopping rate for steeper and milder slopes (all zones, Table 5.6) has been neglected. This slightly increases the spreading on the new prediction formulae for those slopes.

Furthermore, the asymptotic overtopping behaviour for structures with a zero crest freeboard has been taken into account when determining the expressions for the prediction formulae in zones Z1 and Z3. The asymptotic behaviour for vertical walls under non-impulsive wave attack has been considered when deriving the prediction formulae in zones Z1 and Z2.

5.7.1 General shape of prediction formulae

The identification of the general shape of the expressions for the dimensionless average overtopping rate $q/\sqrt{gH_{m0}^3}$ is based on the log-linear graph of $q/\sqrt{gH_{m0}^3}$ versus R_c/H_{m0} in Fig. 5.17. For a particular value of $\cot\alpha$, a double-exponential relationship exists between $q/\sqrt{gH_{m0}^3}$ and R_c/H_{m0} (i.e. a double-linear relationship in a log-linear graph). The transition point between both exponential relationships is positioned at $R_c/H_{m0} = 0.8$.

The typical expression for the exponential relationship between $q/\sqrt{gH_{m0}^3}$ and R_c/H_{m0} used in literature (EurOtop 2007; Owen 1980) is:

$$\frac{q}{\sqrt{g\,H_{m0}^3}} = A\exp\left(B\frac{R_c}{H_{m0}}\right) \tag{5.2}$$

The coefficients A and B are empirical coefficients; A determines the point of intersection of the linear trend line with the vertical axis at $R_c/H_{m0} = 0.0$, while the coefficient B determines the slope angle of the corresponding linear prediction line in the log-linear graph.

Since the effect of the wave period on the average overtopping rate of steep low-crested structures is neglected for zones Z1 and Z2, the point of intersection with the vertical axis and slope angle of the trend lines for a particular slope angle only depends on the value of the slope angle. This means that the coefficients A and B are a function of the slope angle in zones Z1 and Z2 (Table 5.7).

When not taking into account the effect of the slope angle in zones Z3 and Z4, the coefficients A and B are empirical constants. Otherwise, the coefficients A and B are a function of (1) the slope angle and (2) the wave period, since it has an effect on the optimal slope angle (Table 5.7).

Table 5.7: Dependency of the empirical coefficients in Eq. (5.2) for different zones.

		$R_c/H_{m0} \leq 0.8$	$R_c/H_{m0} \geq 0.8$
cot α < 1.5		Zone Z1 $\cot\alpha$	Zone Z2 $\cot\alpha$
cot α > 1.5	no $\cot\alpha$	Zone Z3 constant	Zone Z4 constant
	$\cot\alpha$	Zone Z3 $\cot\alpha$ and $T_{m-1,0}$	Zone Z4 R_c / H_{m0} and $T_{m-1,0}$

The expressions and values for the coefficients A and B for each of the zones are derived in the following sections. Section 5.7.2 treats the expressions for the zones Z1 and Z2, while the expressions for zones Z3 and Z4 are discussed in sections 5.7.3 and 5.7.4, for the approach without and with taking into account the effect of the slope angle respectively.

5.7.2 Prediction formulae in zones Z1 and Z2

The procedure to derive the expressions for the coefficients A and B in zones Z1 and Z2 as a function of the slope angle is explained here. Taking the logarithm of both sides of Eq. (5.2) yields Eq. (5.3) (the coefficients A and B have either a subscript Z1 or Z2).

$$\ln\left(\frac{q}{\sqrt{g\,H_{m0}^3}}\right) = A' + B\frac{R_c}{H_{m0}} \tag{5.3a}$$

$$A = \exp(A') \tag{5.3b}$$

Sets of values of the coefficients A' and B in Eq. (5.3a) are determined using a linear regression analysis applied to each subset of the UG10 dataset with identical

values of the slope angle, separately for zone Z1 and zone Z2. The corresponding values of the coefficient A are obtained using Eq. (5.3b).

The sets of values of the coefficients A_{Z1} and B_{Z1} for zone Z1 (Table 5.8) have been calculated applying this methodology. The values of A_{Z1} and B_{Z1} for $\cot\alpha$ = 0.0, provided in Table 5.8, have been established applying a different reasoning. The coefficient A_{Z1} = 0.062 corresponds to the dimensionless average overtopping rate predicted by Smid et al. (2001) for vertical walls with a zero crest freeboard: $q/\sqrt{gH_{m0}^3}$ = 0.062. The coefficient B_{Z1} for $\cot\alpha$ = 0.0 is determined using linear regression analysis based on Eq. (5.3a) and taking into account the coefficient A_{Z1} = 0.062, for the subset of the CLASH database for plain vertical walls with non-impulsive wave attack and with $R_c/H_{m0} \leq 0.8$. This subset includes the test results for a zero crest freeboard by Smid et al. (2001) (Fig. 5.22).

Table 5.8: Values of the coefficients A_{Z1} and B_{Z1} as a function of the slope angle.

cot α	**A_{Z1}**	**B_{Z1}**
1.43	0.104	-1.920
1.19	0.099	-2.140
1.00	0.094	-2.386
0.84	0.096	-2.627
0.58	0.082	-2.713
0.36	0.082	-3.066
0.00	0.062	-3.451

The sets of values of the coefficients A_{Z2} and B_{Z2} for zone Z2 (Table 5.9) are achieved in a similar way compared to the coefficients A_{Z1} and B_{Z1}. Additionally, the prediction formulae for zones Z1 and Z2 are assumed to give an identical value of $q/\sqrt{gH_{m0}^3}$ for R_c/H_{m0} = 0.8. Hence, the following relationship between A'_{Z2} and B_{Z2} has been applied when determining the values of the coefficients A_{Z2} and B_{Z2} in Table 5.9:

$$A'_{Z2} = \ln\left(\frac{q}{\sqrt{g\,H_{m0}^3}}\right)_{0.8,Z1} - B_{Z2}\,0.8 \qquad (5.4)$$

Values of the coefficients A_{Z2} and B_{Z2} for $\cot\alpha = 0.0$ are not given in Table 5.9, since the relationship between $q/\sqrt{gH_{m0}^3}$ and R_c/H_{m0} is unclear for the test results of the CLASH database for plain vertical walls with non-impulsive conditions and with $R_c/H_{m0} \geq 0.8$, due to the rather large scatter (Fig. 5.22).

Table 5.9: Values of the coefficients A_{Z2} and B_{Z2} as a function of the slope angle.

cot α	**A_{Z2}**	**B_{Z2}**
1.43	0.197	-2.643
1.19	0.189	-2.948
1.00	0.181	-3.176
0.84	0.259	-3.868
0.58	0.159	-3.661
0.36	0.217	-4.409

The values of the coefficient A_{Z2} in Table 5.9 are positioned around the value 0.2 for all slope angles in the UG10 test series. Therefore, the coefficient A_{Z2} is assumed to be a constant: $A_{Z2} = 0.2$. The corresponding values of the coefficient B_{Z2}, referred to as $B_{Z2\_0.2}$, are determined by expressing (1) that the dimensionless average overtopping rate at $R_c/H_{m0} = 0.0$ takes the value of $A_{Z2} = 0.2$, $\left(q/\sqrt{gH_{m0}^3}\right)_{0.0,Z2} = 0.2$, and (2) that the prediction formulae for zone Z1 and zone Z2 are assumed to give an identical value of $q/\sqrt{gH_{m0}^3}$ for $R_c/H_{m0} = 0.8$: $\left(q/\sqrt{gH_{m0}^3}\right)_{0.8,Z1} = \left(q/\sqrt{gH_{m0}^3}\right)_{0.8,Z2}$. The value of the coefficient A_{Z2} for $\cot\alpha = 0.0$ is also assumed to be 0.2. Accordingly, this methodology is also applied to determine the value of the coefficient $B_{Z2\_0.2}$ for $\cot\alpha = 0.0$. The corresponding values of $B_{Z2\_0.2}$ are given in Table 5.10.

Eventually, the expressions for the coefficients A and B as a function of the slope angle for zones Z1 and Z2 are achieved by fitting a curve through the values of A and B for the different slope angles.

Table 5.10: Values of the coefficients A_{Z2} and B_{Z2} as a function of the slope angle, assuming the coefficient A_{Z2}=0.2.

cot α	A_{Z2}	$B_{Z2\ 0.2}$
1.43	0.200	-2.662
1.19	0.200	-3.015
1.00	0.200	-3.301
0.84	0.200	-3.545
0.58	0.200	-3.951
0.36	0.200	-4.306
0.00	0.200	-4.914

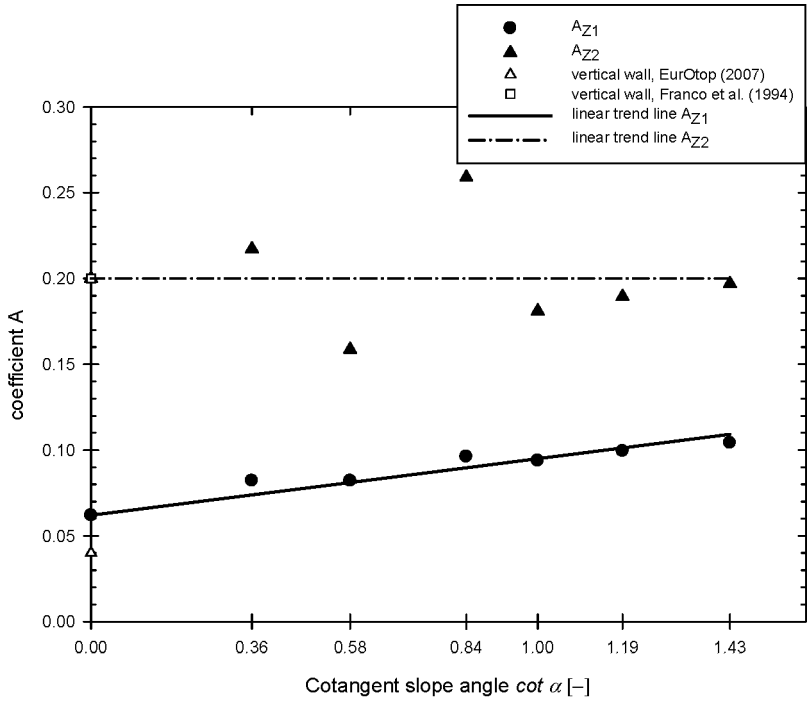

Figure 5.31: Coefficient A for zones Z1 and Z2 as a function of the slope angle, with cot α *varying between 0.00 and 1.43.*

The values of the coefficients A_{Z1} and A_{Z2} from Table 5.8 and Table 5.9 are shown as a function of $\cot\alpha$ in Fig. 5.31. For $\cot\alpha = 0.0$ the coefficients A corresponding to Eq. (4.15) ($A_{Z2} = 0.2$) and Eq. (4.16) ($A = 0.04$, valid for zones Z1 and Z2) are given, marked on the vertical axis using a white square and a white triangle respectively. A similar graph is shown in Fig. 5.32 for the coefficient B.

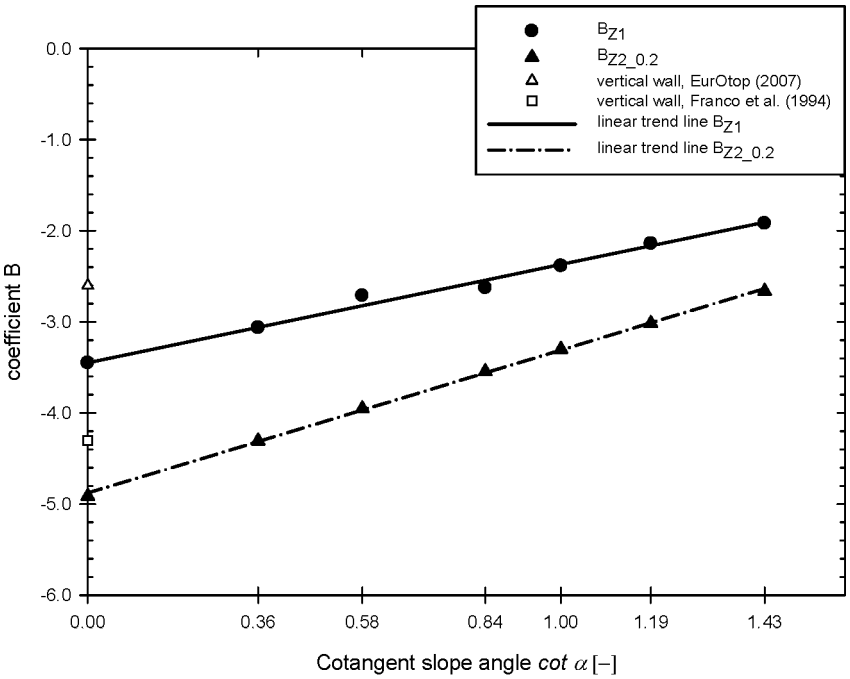

Figure 5.32: Coefficient B for zones Z1 and Z2 (assuming A_{Z2} equals 0.2) as a function of the slope angle, with $\cot\alpha$ varying between 0.00 and 1.43.

As illustrated in Fig. 5.31 and Fig. 5.32, the coefficients A_{Z1}, B_{Z1} and $B_{Z2\_0.2}$ approximately follow a linear trend when plotted as a function of the cotangent of the slope angle $\cot\alpha$. Accordingly, these coefficients are expressed as a linear function of $\cot\alpha$. The corresponding expressions are given in Eqs. (5.5) and (5.6). The range of application for the slope angle of Eq. (5.5) and Eq. (5.6) is $0.0 \le \cot\alpha \le 1.43$. The

range of application for the relative crest freeboard of Eq. (5.5) is $0.0 \le R_c / H_{m0} \le 0.8$, while it is $0.8 \le R_c / H_{m0} \le 2.0$ for Eq. (5.6).

$$\left(\frac{q}{\sqrt{g H_{m0}^3}}\right)_{Z1} = (0.033\cot\alpha + 0.062)\exp\left((1.08\cot\alpha - 3.45)\frac{R_c}{H_{m0}}\right) \qquad (5.5)$$

$$\left(\frac{q}{\sqrt{g H_{m0}^3}}\right)_{Z2} = 0.2\exp\left((1.57\cot\alpha - 4.88)\frac{R_c}{H_{m0}}\right) \qquad (5.6)$$

Note that the intersection between the linear trend line of the coefficient $B_{Z2\_0.2}$ and the vertical axis in Fig. 5.32 (positioned at -4.914) is relatively close to the coefficient B = -4.3 of Eq. (4.15). Combining this observation with the constant value of 0.2 for the coefficient A_{Z2}, it appears that the empirical formula of Eq. (4.15) is a relatively accurate prediction formula for the average overtopping rate at vertical walls with non-impulsive wave attack and with $R_c / H_{m0} \ge$ 0.8. This finding is inconsistent with the validity of Eq. (4.16). The reason for this inconsistency is unclear and therefore subject for further research.

5.7.3 Prediction formulae in zones Z3 and Z4 - when neglecting the effect of the slope angle

When neglecting the effect of the slope angle for $\cot\alpha >$ 1.5, the coefficients A and B in Eq. (5.3) are empirical constants.

Since all UG10 data points are located within the 90% prediction interval of Eq. (4.2b) in zone Z4, a new prediction formula for zone Z4 has not been derived. Hence, the empirical constants A_{Z4} and B_{Z4} in zone Z4 are known: A_{Z4} = 0.2 and B_{Z4} = -2.6 (Eq. 4.2b).

Furthermore, a number of restrictions apply to the coefficients A_{Z3} and B_{Z3} in zone Z3:

- the prediction formula for zone Z3 is assumed to give an identical average overtopping rate for R_c / H_{m0} = 0.8 as Eq. (4.2b) (zone Z4);

- based on the test results of Smid et al. (2001) for structures with a zero crest freeboard and $\cot\alpha$ = 1.5, the value of $q/\sqrt{gH_{m0}^3}$ corresponding to R_c/H_{m0} = 0.0 is expected to be equal to 0.062. However, this disagrees with the linear trend followed by the coefficients A_{Z1} in Fig. 5.31: applying Eq. (5.6) for $\cot\alpha = 1.5$, a value of $q/\sqrt{gH_{m0}^3}$ = 0.11 is found. Consequently, the hypothesis of a constant average overtopping rate for steep slopes with a zero crest freeboard (Smid et al. 2001) is rejected.

Hence, the coefficient A_{Z3} is given the value 0.11, while the restriction for the predicted dimensionless average overtopping rate at R_c/H_{m0} = 0.8 determines the coefficient B_{Z3}. The corresponding prediction formula is given in Eq. (5.7). The value of B_{Z3} is approximately equal to the calculated value of B_{Z1} for $\cot\alpha = 1.5$.

$$\left(\frac{q}{\sqrt{gH_{m0}^3}}\right)_{Z3} = 0.11\exp\left(-1.85\frac{R_c}{H_{m0}}\right) \tag{5.7}$$

The ranges of application for Eq. (5.7) are $1.73 \le \cot\alpha \le 2.75$ and $0.0 \le R_c/H_{m0} \le 0.8$.

5.7.4 Prediction formulae in zones Z3 and Z4 - when taking into account the effect of the slope angle

When assuming the effect of the slope angle on the overtopping rate is significant in zones Z3 and Z4, the occurrence of a maximum average overtopping rate for $\xi_{m-1,0}$ = 3.0 (section 5.3.2) should be incorporated in the simple regression prediction formulae for both zones. Applying a methodology similar to section 5.7.2 does not result in appropriate expressions, since the value of the optimal slope angles varies over the relative crest freeboard, fulfilling Eq. (5.1). After several curve fittings, the following expression is proposed for the dimensionless average overtopping rate in zones Z3 and Z4, when taking into account the effect of the slope angle:

$$\begin{cases} \dfrac{q}{\sqrt{g H_{m0}^3}} = A \exp\left(B \dfrac{R_c}{H_{m0}} \right) \\ A = A_1 \left(\cos\left(\dfrac{\xi_{m-1,0} - 3.0}{A_2} \right) \right)^3 \\ B = \text{constant} \end{cases} \tag{5.8}$$

The coefficients A_1, A_2 and B are empirical coefficients which are determined by non-linear regression analysis of the subset of the UG10 dataset with $1.73 \leq \cot\alpha \leq 2.75$ and with $0.11 \leq R_c / H_{m0} \leq 0.80$ for zone Z3, while with $0.80 \leq R_c / H_{m0} \leq 2.0$ for zone Z4.

The expression achieved through non-linear regression analysis by SPSS 16 (IBM® 2010) for zone Z4 is given in Eq. (5.9). The coefficient $A_{1,Z4}$ is given the value 0.2, in accordance with Fig. 5.31. The expression for zone Z3 is found by assuming $A_{1,Z3}$ takes the value 0.11 (similar to Eq. 5.7) and by fulfilling the continuity requirement for $R_c / H_{m0} = 0.80$ (Eq. 5.10).

$$\left(\frac{q}{\sqrt{g H_{m0}^3}} \right)_{Z4} = 0.2 \left(\cos\left(\frac{\xi_{m-1,0} - 3.0}{3.0} \right) \right)^3 \exp\left(-2.4 \frac{R_c}{H_{m0}} \right) \tag{5.9}$$

$$\left(\frac{q}{\sqrt{g H_{m0}^3}} \right)_{Z3} = 0.11 \left(\cos\left(\frac{\xi_{m-1,0} - 3.0}{3.0} \right) \right)^3 \exp\left(-1.7 \frac{R_c}{H_{m0}} \right) \tag{5.10}$$

5.7.5 Overview of new prediction formulae

An overview of the new prediction formulae for steep low-crested slopes with their ranges of application for the slope angle and the relative crest freeboard is shown in Table 5.11. These formulae are referred to as the *UG10 formulae*.

Table 5.11: Overview of UG10 formulae.

		$0.0 \leq R_c/H_{m0} \leq 0.8$	$0.8 \leq R_c/H_{m0} \leq 2.0$
$0.0 \leq \cot\alpha \leq 1.43$		Zone Z1 – Eq. (5.5)	Zone Z2 – Eq. (5.6)
$1.73 \leq \cot\alpha \leq 2.75$	no $\cot\alpha$	Zone Z3 – Eq. (5.7)	Zone Z4 – Eq. (4.2b)
	$\cot\alpha$	Zone Z3 – Eq. (5.10)	Zone Z4 – Eq. (5.9)

5.7.6 Reliability of new expressions

The reliability of the UG10 prediction formulae derived above is expressed using an overtopping discharge factor, similar to Owen (1980). In a first step, the root-mean-square error *rmse* is calculated as defined in Eq. (5.11):

$$rmse = \sqrt{\frac{1}{N_{test}} \sum_{r=1}^{N_{test}} \left(\log\left(\frac{q_{meas}}{\sqrt{g H_{m0}^3}} \right)_r - \log\left(\frac{q_{pred}}{\sqrt{g H_{m0}^3}} \right)_r \right)^2} \qquad (5.11)$$

N_{test} is the number of test results (subscript r) in the subset of the UG10 dataset for which the particular UG10 formula is derived. A small *rmse* means that a large part of the variability of the dataset is accounted for by the prediction formula. The values of the root-mean-square error *rmse* of the UG10 formulae are given in Table 5.12. All values in Table 5.12 are relatively small.

The effect of taking into account the slope angle in the prediction formulae for zones Z3 and Z4 appears when comparing the *rmse* values:

- the predictions are more accurate when the effect of the slope angle is incorporated in the prediction formula (smaller *rmse*-values);
- the relatively small *rmse*-values of Eq. (4.2b) and Eq. (5.7) confirm that the dependency on the slope angle is relatively weak;
- the decrease in *rmse* is smaller for zone Z3 compared to Z4 due to the more limited effect of the slope angle in zone Z3.

Table 5.12: Overview of rmse-values for UG10 formulae.

		$0.0 \leq R_c/H_{m0} \leq 0.8$	$0.8 \leq R_c/H_{m0} \leq 2.0$
$0.0 \leq \cot\alpha \leq 1.43$		0.042	0.10
$1.73 \leq \cot\alpha \leq 2.75$	no $\cot\alpha$	0.057	0.15
	$\cot\alpha$	0.045	0.10

Based on Eq. (5.11), the *rmse* – value is the standard deviation of the measured dimensionless average overtopping rates about the predicted dimensionless average overtopping rates in a log-log plot. The log-log plot containing measured and predicted dimensionless average overtopping rates for zone Z1 is shown in Fig. 5.33.

When assuming the logarithms of the measured dimensionless average overtopping rates exhibit a normal probability distribution about the logarithms of the predicted dimensionless average overtopping rates, 68% of the measured overtopping rates should be located within the interval defined by:

$$\log\left(\frac{q_{meas}}{\sqrt{g\,H_{m0}^3}}\right)_{68\%} = \log\left(\frac{q_{pred}}{\sqrt{g\,H_{m0}^3}}\right) \pm rmse \tag{5.12}$$

Consequently, the lower and upper overtopping rates of the 68% prediction interval are defined by Eq. (5.13). The corresponding lines, which are parallel to the line of perfect fit, are added to Fig. 5.33.

$$\begin{cases} \left(\frac{q_{meas}}{\sqrt{g\,H_{m0}^3}}\right)_{68\%,upper} = \left(\frac{q_{pred}}{\sqrt{g\,H_{m0}^3}}\right) 10^{rmse} \\ \left(\frac{q_{meas}}{\sqrt{g\,H_{m0}^3}}\right)_{68\%,lower} = \left(\frac{q_{pred}}{\sqrt{g\,H_{m0}^3}}\right) / 10^{rmse} \end{cases} \tag{5.13}$$

Other prediction intervals are defined similarly, based on the percentiles of the standard normal distribution. Hence, the following expressions apply to the 90% prediction interval:

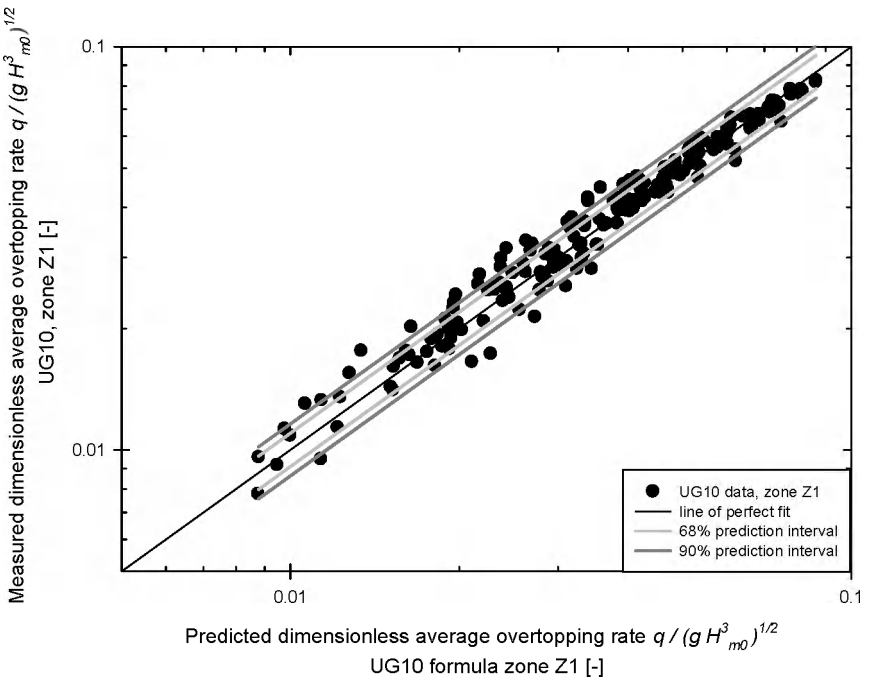

Figure 5.33: Measured overtopping rates for zone Z1 against the predicted overtopping rates by the UG10 formula for zone Z1. The line of perfect fit is added.

$$\log\left(\frac{q_{meas}}{\sqrt{g\,H_{m0}^3}}\right)_{90\%} = \log\left(\frac{q_{pred}}{\sqrt{g\,H_{m0}^3}}\right) \pm 1.645\,rmse \tag{5.14}$$

$$\Rightarrow \begin{cases} \left(\dfrac{q_{meas}}{\sqrt{g\,H_{m0}^3}}\right)_{90\%,upper} = \left(\dfrac{q_{pred}}{\sqrt{g\,H_{m0}^3}}\right) 10^{1.645\,rmse} \\ \left(\dfrac{q_{meas}}{\sqrt{g\,H_{m0}^3}}\right)_{90\%,lower} = \left(\dfrac{q_{pred}}{\sqrt{g\,H_{m0}^3}}\right) / 10^{1.645\,rmse} \end{cases} \tag{5.15}$$

The 90% prediction interval is also added to Fig. 5.33 for zone Z1, corresponding to lines parallel to the line of perfect fit, wider than the 68% prediction interval.

The factor $10^{z_{p/2}\cdot rmse}$ is referred to as the *overtopping discharge factor*, similar to the factor defined by Owen (1980) (section 4.4.1.3). Note that the common logarithm has been used in this section, while the natural logarithm is used by Owen (1980).

Based on the *rmse*-values in Table 5.12, the overtopping discharge factors corresponding to the 90% prediction interval have been determined for each of the zones Z1 to Z4 (Table 5.13).

For example, the 90% prediction interval for zone Z1 is bounded by:

$$\Rightarrow \begin{cases} \left(\dfrac{q_{meas}}{\sqrt{g\,H_{m0}^3}}\right)_{90\%,upper} = \left(\dfrac{q_{pred}}{\sqrt{g\,H_{m0}^3}}\right) 1.16 \\ \left(\dfrac{q_{meas}}{\sqrt{g\,H_{m0}^3}}\right)_{90\%,lower} = \left(\dfrac{q_{pred}}{\sqrt{g\,H_{m0}^3}}\right) / 1.16 \end{cases} \tag{5.16}$$

Similar definitions as in Eq. (5.16) are used below (section 5.7.8) to visualize the reliability of the UG10 formulae.

Note that instead of using the dimensionless average overtopping rates also the non-dimensionless average overtopping rates can be used:

$$\log\left(\frac{q_{meas}}{\sqrt{g\,H_{m0}^3}}\right) - \log\left(\frac{q_{pred}}{\sqrt{g\,H_{m0}^3}}\right) \tag{5.17a}$$

$$= \left[\log\left(q_{meas}\right) - \log\left(\sqrt{g\,H_{m0}^3}\right)\right] - \left[\log\left(q_{pred}\right) - \log\left(\sqrt{g\,H_{m0}^3}\right)\right] \tag{5.17b}$$

$$= \log\left(q_{meas}\right) - \log\left(q_{pred}\right) \tag{5.17c}$$

Furthermore, it should be noted that the 90% prediction interval of Eq. (4.2b) is expressed by taking into account a standard deviation for the coefficient B in Eq. (4.2b). Consequently, the width of the 90% prediction interval increases continuously for increasing relative crest freeboard. This trend is also expected intrinsically. On the other hand, the reliability of Eq. (4.9), the DHNN tool and the UG10 formulae is expressed using an overtopping discharge factor. Hence, the 90% prediction interval is parallel compared to the prediction line.

The 90% prediction intervals in zones Z2 and Z4 are wider compared to the 90% confidence intervals in zones Z1and Z3 respectively. This suggests that the spreading

of the overtopping rates predicted by the UG10 formulae increases for larger relative crest freeboards, confirming the intrinsically expected increase in spreading.

Table 5.13: Overview of overtopping discharge factors for UG10 formulae.

		$0.0 \leq R_c/H_{m0} \leq 0.8$	$0.8 \leq R_c/H_{m0} \leq 2.0$
$0.0 \leq \cot\alpha \leq 1.43$		1.16	1.46
$1.73 \leq \cot\alpha \leq 2.75$	no $\cot\alpha$	1.25	1.74
	$\cot\alpha$	1.19	1.49

5.7.7 Important remarks on new set of prediction formulae

The transition point for $\cot\alpha$ between zone Z1 (zone Z2) and zone Z3 (zone Z4) has been set to 1.5. However, no results in the UG10 dataset are available for the exact value of $\cot\alpha = 1.5$. As a consequence, Eqs. (5.5) and Eq. (5.6) are only valid up to $\cot\alpha = 1.43$, while Eq. (5.7), Eq. (4.2b), Eq. (5.9) and Eq. (5.10) are only valid for values of $\cot\alpha$ larger than 1.73. In the range $1.43 < \cot\alpha < 1.73$, the minimum of both values of $q/\sqrt{g H_{m0}^3}$ determined by the expressions for $\cot\alpha < 1.5$ and $\cot\alpha > 1.5$ should be taken.

5.7.8 Graphical output of new set of prediction formulae

The figures below illustrate the validity of the UG10 formulae. The graphs in Fig. 5.34 and Fig. 5.35 are identical to Fig. 5.3 (Example 1), except that the prediction line corresponding to Eq. (4.5) is replaced by the prediction lines of the UG10 formulae from Table 5.11 for $R_c/H_{m0} = 0.45$, with and without taking into account the effect of the slope angle in zone Z3 respectively. Since Example 1 corresponds to a relative crest freeboard $R_c/H_{m0} = 0.45$, the UG10 prediction formulae for zone Z1 and Z3 apply.

The 90% prediction interval of the UG10 formulae is also added. As expected, the data points approach the UG10 formulae well. Furthermore, the 90% prediction

intervals of the UG10 formulae are narrower compared to the 90% prediction interval of Eq. (4.2b). This is expected to be due to the fact that the range of structures is wider for Eq. (4.2b) and due to the presence of model effects between the different datasets used for deriving Eq. (4.2b).

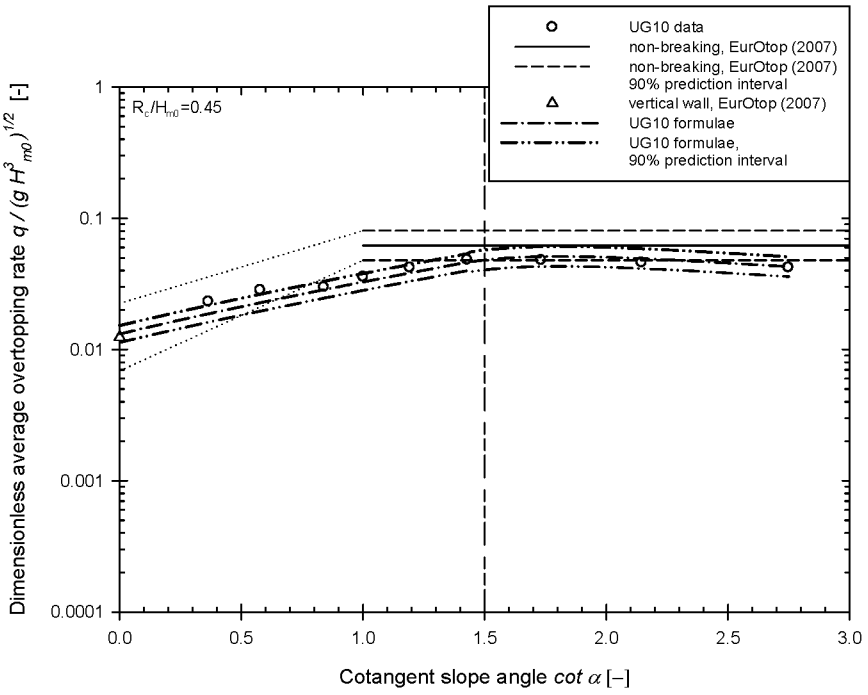

Figure 5.34: Measured average overtopping rate (logarithmic scale) for Example 1 as a function of the slope angle (linear scale), with $\cot\alpha$ *varying between 0.0 and 3.0. Predictions by EurOtop (2007) and UG10 formulae are added.*

The effect of the relative crest freeboard on the dimensionless average overtopping rate is shown in a log-linear graph in both Fig. 5.36 for test results of the UG10 dataset with $\cot\alpha$ = 0.84 and in Figs. 5.37 and 5.38 for $\cot\alpha = 2.14$. The prediction lines corresponding to the UG10 formulae (Table 5.11) are also given in these figures. Furthermore, predictions by the DHNN tool and by Eq. (4.2b), within its range of application for R_c / H_{m0}, are added to these figures for comparison. The 90% prediction intervals of all prediction models are also shown.

Since $\cot\alpha < 1.5$ in Fig. 5.36, the UG10 formulae corresponding to zones Z1 and Z2 apply.

On the other hand, since $\cot\alpha > 1.5$ in Figs. 5.37 and 5.38, the UG10 formulae corresponding to zones Z3 and Z4 apply. The effect of the slope angle is incorporated in Fig. 5.37 and neglected in Fig. 5.38.

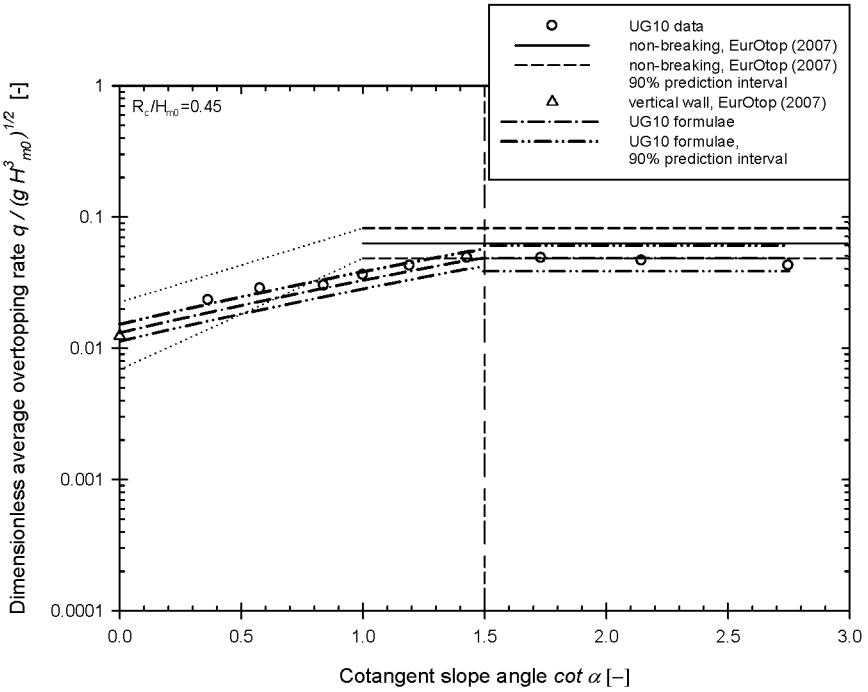

Figure 5.35: Measured average overtopping rate (logarithmic scale) for Example 1 as a function of the slope angle (linear scale), with $\cot\alpha$ *varying between 0.0 and 3.0. Predictions by EurOtop (2007) and UG10 formulae are added. No effect of the slope angle in zone Z3.*

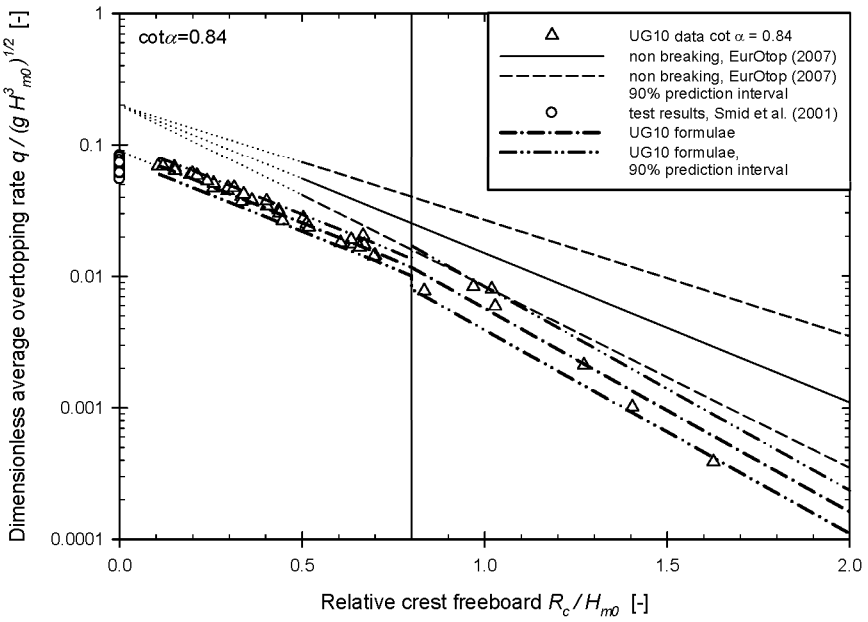

Figure 5.36: Dimensionless average overtopping rate (logarithmic scale) as a function of the relative crest freeboard (linear scale) for the test results of the UG10 dataset with $\cot\alpha = 0.84$*, with* R_c / H_{m0} *varying between 0.0 and 2.0. Predictions by EurOtop (2007) and UG10 formulae are added.*

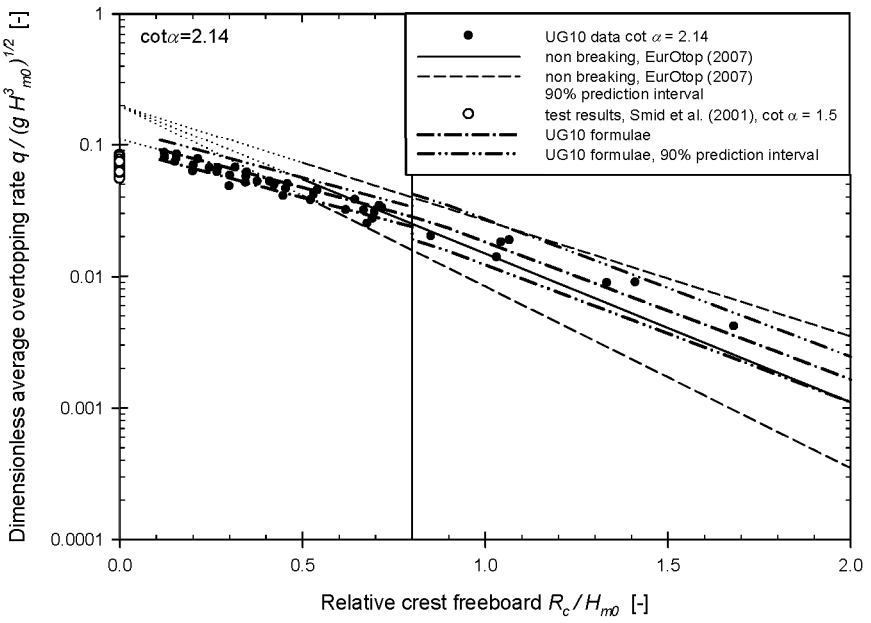

Figure 5.37: Dimensionless average overtopping rate (logarithmic scale) as a function of the relative crest freeboard (linear scale) for the test results of the AAU08 and UG10 dataset with $\cot\alpha = 2.14$ *and* R_c / H_{m0} *varying between 0.0 and 2.0. Predictions by EurOtop (2007) and UG10 formulae are added, incorporating the effect of the slope angle for zone Z3 and Z4.*

In general, a good agreement exists between the data points of the UG10 dataset and the UG10 formulae in Figs. 5.36 to 5.38. Furthermore, it appears that:

- the 90% prediction intervals of the UG10 formulae are narrower than the 90% prediction interval of Eq. (4.2b);
- the UG10 formulae are particularly more accurate than Eq. (4.2b) for small relative crest freeboards (zones Z1 and Z3);
- incorporating the effect of the slope angle (Fig. 5.37) is particularly important for the accuracy of prediction of the data points in zone Z4.

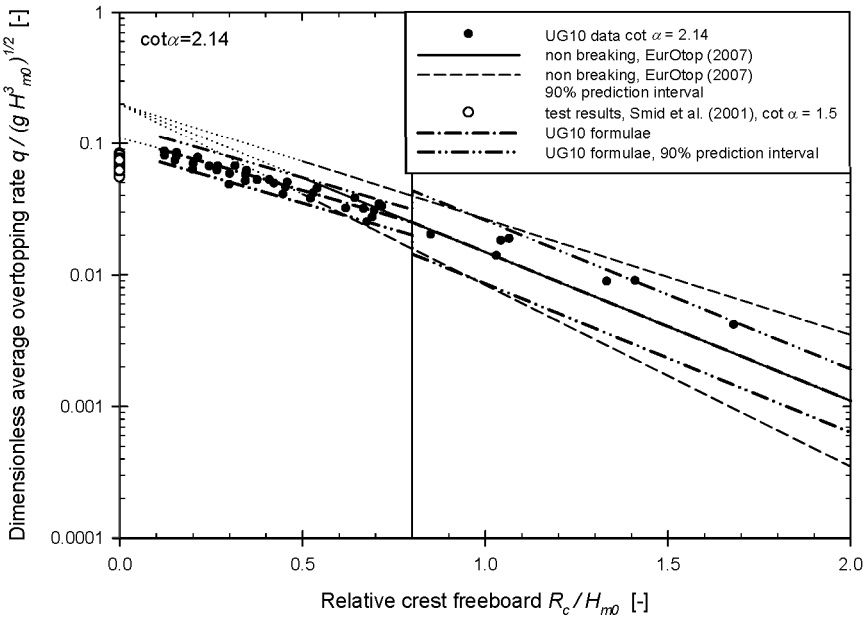

Figure 5.38: Dimensionless average overtopping rate (logarithmic scale) as a function of the relative crest freeboard (linear scale) for the test results of the AAU08 and UG10 dataset with $\cot\alpha = 2.14$*, with* R_c / H_{m0} *varying between 0.0 and 2.0. Predictions by EurOtop (2007) and UG10 formulae are added, neglecting the effect of the slope angle for zone Z3.*

5.8 Conclusions

The independent effects of the slope angle, relative crest freeboard and wave period on the average overtopping rates of steep low-crested slopes, and their interactions, have been studied based on the test results of the AAU08 and UG10 datasets, which describe wide ranges of application of the slope angle, relative crest freeboard and wave steepness.

Furthermore, a comparison with commonly used prediction models, described in chapter 4, has been carried out.

Two zones of different overtopping behaviour have been identified for the slope angle, separated by $\cot\alpha = 1.5$. Slopes with $1.5 < \cot\alpha < 3.0$ correspond to the largest average overtopping rates, for which a weak dependency on the slope angle occurs. When assuming that this dependency is significant, a maximum average overtopping rate occurs for $\xi_{m-1,0} = 3.0$. On the other hand, when $\cot\alpha < 1.5$, a sharp decrease in average overtopping rate occurs for increasing slope angle towards the predicted rate for vertical walls under non-impulsive wave attack.

Furthermore, also two zones of different overtopping behaviour have been identified for the relative crest freeboard, separated by $R_c / H_{m0} = 0.80$. The slope of the linear trend line of the data points with $R_c / H_{m0} < 0.80$ in a log-linear graph is milder compared to the slope of the linear trend line of the data points with $R_c / H_{m0} > 0.80$.

The interaction between the effect of the slope angle and the effect of the relative crest freeboard is expressed by an increased effect of the slope angle for larger relative crest freeboards. When the relative crest freeboard becomes very small, the effect of the slope angle is also very small.

Combining the zones of different overtopping behaviour for the slope angle and relative crest freeboards results in the following four zones:

- zone Z1: $0.0 \le \cot\alpha \le 1.43$ and $0.0 \le R_c / H_{m0} \le 0.8$
- zone Z2: $0.0 \le \cot\alpha \le 1.43$ and $0.8 \le R_c / H_{m0} \le 2.0$
- zone Z3: $1.73 \le \cot\alpha \le 2.75$ and $0.0 \le R_c / H_{m0} \le 0.8$
- zone Z4: $1.73 \le \cot\alpha \le 2.75$ and $0.8 \le R_c / H_{m0} \le 2.0$

None of the prediction models described in chapter 4 is able to predict the average overtopping rates accurately for all of the zones Z1 to Z4. The DHNN tool is the most accurate prediction model, but tends to overpredict the average overtopping rates in zone Z2 and has wide 90% prediction intervals due to its wide ranges of application.

Enhanced by the ability to incorporate physical insights in an empirical formula, a set of new prediction formulae, the UG10 formulae, has been derived based on the UG10 test results. The UG10 formulae have been visualized for a number of graphs, illustrating that the UG10 formulae are able to predict the independent effects of the slope angle and the crest freeboard, and their interactions, accurately for steep low-crested slopes with broad ranges of application for the slope angle, crest freeboard and wave steepness.

For the zones Z3 and Z4, two expressions have been derived, incorporating or neglecting the effect of the slope angle. The differences between the average overtopping rates determined by both expressions are small, but predictions are more accurate when incorporating the effect of the slope angle.

6

Wave reflection at steep low-crested slopes

In this chapter, the reflection coefficients measured during the UG10 test series (chapter 2 and 3) are compared to predicted reflection coefficients (based on existing empirical prediction formulae) for smooth impermeable slopes. In particular, the effect of a low crest freeboard on the reflection coefficient and the relation between wave overtopping and wave reflection are investigated.

6.1 Introduction

Traditionally, wave reflection is of minor importance in the design of sea defence structures compared to e.g. wave overtopping and wave transmission. Although wave reflection has been studied since the 1940s, the underlying goal was mainly to determine the characteristics of the waves incident to a sea defence structure by separating the incident and reflected waves, not to study wave reflection itself. The incident wave characteristics successively were used to set up empirical prediction formulae for e.g. wave overtopping and wave transmission.

Similar to wave overtopping, wave reflection was originally studied for regular waves. In the 1980s, irregular wave generation using reflection compensation (active absorption) was introduced. Since then, the unfavourable effects of high reflection coefficients - causing dangerous sea states close to harbour entrances, intensified sediment scour and increased loads on the sea defence structure - have been acknowledged.

Correspondingly, the number of studies focussing on wave reflection is relatively limited compared to the large amount of studies on wave overtopping (chapter 4).

The major part of these studies analyzes the reflective behaviour of a particular type of sea defence structure, mainly smooth impermeable slopes and rubble mound breakwaters. Since the smooth impermeable steep slopes with low crest freeboards (studied in this PhD-manuscript) are intended to be built into sea defence structures (chapter 1), their reflective behaviour also needs to be investigated. Existing prediction formulae for the reflective behaviour of smooth impermeable steep slopes may give an indication of the reflective behaviour of steep low-crested slopes. An overview of these formulae is given in the following section 6.2.

In section 6.3, the reflection coefficients K_r [-] determined during the UG10 test series are compared to predictions by formulae from section 6.2. In particular, the measured and predicted effects of the wave height, slope angle, wave period, breaker parameter and relative crest freeboard have been investigated. A new prediction formula, which takes into account the effect of a small relative crest freeboard on the reflection coefficient, is proposed in section 6.4. Finally, in section 6.5, the relationship between the reflection coefficient K_r [-] and the dimensionless average overtopping rate $q/\sqrt{g H_{m0}^3}$ [-] is discussed, based on the UG10 test results.

The reflection coefficients for the AAU08 test series have not been analyzed due to the wider ranges of application of the UG10 test results.

As mentioned in section 3.3, frequency-averaged reflection coefficients have been determined for each test of the UG10 dataset, based on a separation of the incident and reflected waves using the measured total elevations at three wave gauges and the algorithm by Mansard and Funke (1980).

6.2 Literature study on reflective behaviour of smooth impermeable slopes

6.2.1 Non-overtopped slopes

According to Battjes (1974), the main parameter affecting the reflective behaviour of smooth impermeable non-overtopped slopes subjected to normal monochromatic breaking waves is the breaker parameter $\xi = \tan\alpha / \sqrt{2\pi H / (g T^2)}$. A theoretical expression for the reflection coefficient K_r [-] as a function of ξ has been derived for those conditions (Eq. 6.1). Breaking waves occur for $\xi < 2.3$, whereas non-breaking waves correspond to $\xi > 2.3$ (Battjes 1974).

$$K_r = 0.1\xi^2 \quad (\xi < 2.3) \tag{6.1}$$

However, the expression in Eq. (6.1) does not have a proper limitation for the reflection coefficient when used for non-breaking waves, i.e. outside its ranges of applicability (Seelig and Ahrens 1981). The reflection coefficient should be asymptotically equal to 1.0 for large values of the breaker parameter, for the case of a vertical wall. An adjusted expression for K_r, which takes into account this physical bound has been proposed by Seelig and Ahrens (1981) (Eq. 6.2). This expression is referred to as the *improved Battjes formula* in this PhD-manuscript.

$$K_r = \tanh\left(0.1\xi^2\right) \tag{6.2}$$

Note that Eq. (6.2) approaches Eq. (6.1) for $\xi < 2.3$, while it has an asymptotic value of 1.0 for large values of the breaker parameter. Correspondingly, the expression in Eq. (6.2) is also valid for monochromatic non-breaking waves.

Next to the physical bound that the reflection coefficient should be approximately equal to 1.0 for breaker parameters increasing to infinity, i.e. the asymptotic value for vertical non-overtopped walls, another physical bound applies. When the breaker parameter approaches zero, i.e. in the absence of a structure, the reflection also approaches zero.

Seelig and Ahrens (1981) also investigated the reflective behaviour of a large variety of sea defence structures (beaches, revetments and breakwaters) subjected to irregular waves under normal wave attack. This study confirms that the breaker parameter is the main parameter that affects the reflection coefficients of smooth impermeable sea defence structures. A prediction formula (Eq. 6.3a) was derived for the reflection coefficient K_r of smooth impermeable non-overtopped slopes, based on test results with irregular waves obtained by Ahrens (1980). The corresponding formula, using the breaker parameter $\xi_{m-1,0}$ based on the energy wave period, is given in Eq. (6.3b).

Eventually, the reflection coefficient for a particular breaker parameter ξ_p is determined by the minimum of the predicted values by Eq. (6.3a) and by $K_r = \tanh\left(0.1\xi_p^2\right)$ (Seelig and Ahrens 1981). This approach shows less error in the predictions of the test results of Ahrens (1980) compared to using only Eq. (6.2).

$$K_{r,S\&A} = \frac{\xi_p^2}{\xi_p^2 + 5.5} \tag{6.3a}$$

$$K_{r,S\&A} = \frac{\xi_{m-1,0}^2}{\xi_{m-1,0}^2 + 5.0} \tag{6.3b}$$

The ranges of application of the test results of Ahrens (1980) for the slope $\cot\alpha$ and the breaker parameter $\xi_{m-1,0}$ are: $1.5 \le \cot\alpha \le 2.5$ and $1.0 \le \xi_{m-1,0} \le 6.2$.

Recently, more than 4.000 test results of reflection coefficients, originating from the DELOS[1] and CLASH projects mainly, have been gathered in a wave reflection database (Zanuttigh and Van der Meer 2006). Based on this database, the expression in Eq. (6.3b) has been reviewed in an attempt to set up a generally applicable formula for a wide variety of structures (Zanuttigh and Van der Meer 2008). The following conclusions have been drawn:

- Eq. (6.3b) is well suited to predict the reflection coefficients for smooth impermeable slopes. A root mean square error *rmse* (Eq. 6.4) of 0.058 was found. The subscript r runs through the number of tests N_{test};

$$rmse = \sqrt{\frac{1}{N_{test}} \sum_{r=1}^{N_{test}} \left[K_{r,meas,r} - K_{r,pred,r} \right]^2} \tag{6.4}$$

- the expression in Eq. (6.3b) should be adapted for rock permeable slopes and rock impermeable slopes.

A new expression has been proposed using a hyperbolic tangent function with coefficients C and D that depend on the type of structure (Eq. 6.5a), resulting in a better fit for the rock slopes (Zanuttigh and Van der Meer 2008). The expression in Eq. (6.5a) has also been used for smooth impermeable slopes. The corresponding values of the coefficients C and D (Eq. 6.5b) are determined by interpolating between 134 test results with smooth slopes that hardly overtop. The *rmse* of the new expression for smooth impermeable slopes is 0.040.

$$K_{r,Z\&V} = \tanh\left(C \xi_{m-1,0}^D \right) \tag{6.5a}$$

[1] Environmental Design of Low Crested Coastal Defence Structures. Fifth Framework Programme of the EU, Contract n. EVK3-CT-00041. www.delos.unibo.it.

$$\begin{cases} C = 0.16 \\ D = 1.43 \end{cases} \tag{6.5b}$$

The ranges of application for $\cot\alpha$, $\xi_{m-1,0}$ and R_c / H_{m0} of the 134 test results that were used to develop Eq. (6.5) are: $1.5 \le \cot\alpha \le 4.0$, $1.0 \le \xi_{m-1,0} \le 4.1$ and $0.58 \le R_c / H_{m0} \le 4.5$. According to Zanuttigh and Van der Meer (2008), structures are hardly overtopped when the relative crest freeboard R_c / H_{m0} is larger than 0.5. This explains the range of application of Eq. (6.5) for R_c / H_{m0}. Equation (6.5) is valid both for non-breaking and breaking waves.

Seelig and Ahrens (1981) provide a reduction factor to be used together with Eq. (6.3) for breaking waves.

The reflection coefficients predicted by Eqs. (6.1) to (6.3) and Eq. (6.5) are shown as a function of the breaker parameter in Fig. 6.1.

As mentioned above, the prediction formula by Battjes (1974) clearly provides unrealistically high reflection coefficients for monochromatic non-breaking waves (outside its range of applicability, $\xi > 2.3$), hence resulting in the derivation of Eq. (6.2).

On the other hand, the two physical bounds - K_r = 1.0 for large breaker parameters and K_r = 0.0 for $\xi_{m-1,0}$ = 0.0 - are fulfilled by Eq. (6.2), Eq. (6.3) and Eq. (6.5). Although the asymptotic boundaries are identical for all three formulae, different predictions occur for values of the breaker parameter larger than 3.0. Each of the formulae corresponds to a different value of the breaker parameter for which the asymptotic value of K_r = 1.0 is approximately reached. The improved Battjes formula reaches that asymptote for a breaker parameter $\xi = 6.0$, while the prediction line of Eq. (6.5) reaches the asymptote at a breaker parameter $\xi_{m-1,0}$ = 9.0. The prediction formula by Seelig and Ahrens (1981) only reaches the asymptote for very large values of the breaker parameter. Correspondingly, the prediction line of the improved Battjes formula is positioned above the prediction line of Eq. (6.5) in the zone of breaker parameters larger than 3.0, while this last prediction line is positioned above the prediction line corresponding to Eq. (6.3b).

The predictions by the improved Battjes formula are limited to monochromatic waves, and Eq. (6.3b) is based on a smaller database compared to Eq. (6.5). Hence, Eq. (6.5) is expected to give the most accurate predictions of the reflection coefficient K_r for smooth impermeable non-overtopped slopes.

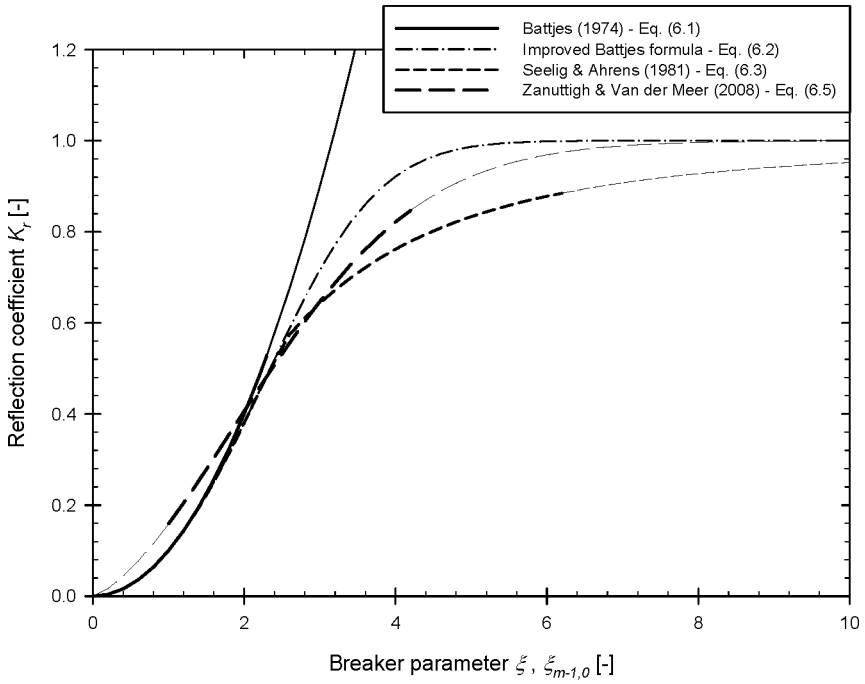

Figure 6.1: Effect of breaker parameter on the reflection coefficient of smooth impermeable non-overtopped slopes predicted by empirical formulae found in literature.

6.2.2 Overtopped slopes

The prediction formulae for the reflection coefficients given above (Eqs 6.1 to 6.3 and Eq. 6.5) are only valid when the relative crest freeboard of the tested smooth impermeable structures is large enough to prevent wave overtopping. Accordingly, it is unclear whether these formulae are still able to predict the reflection coefficients accurately for smooth impermeable steep low-crested slopes (studied in this manuscript) when significant wave overtopping occurs.

Recently, a study on the reflective behaviour of the overtopping wave energy converter SSG (chapter 1) has been carried out (Zanuttigh et al. 2009) based on test results obtained for a scale model of the SSG with only two reservoirs (Margheritini et al. 2009b). Since the SSG is designed to extract energy from the waves, it features small relative crest freeboards R_c / H_{m0} and steep slopes. The following conclusions have been drawn concerning the reflective behaviour of the two-reservoir SSG:

- the reflection coefficients of the two-reservoir SSG for all tests by Margheritini et al. (2009b) are larger than 0.50, with an average of 0.68. This is of the same order of magnitude as the reflection coefficients of caisson breakwaters (0.45 to 0.90);

- the prediction formulae for non-overtopped slopes by Seelig and Ahrens (1981) (Eq. 6.3b), and Zanuttigh and Van der Meer (2008) (Eq. 6.5), overpredict the reflection coefficients of the two-reservoir SSG. The smallest overestimations are achieved when applying Eq. (6.3b);

- the overestimation is caused by the capturing of water inside the reservoirs of the SSG. More accurate predictions have been achieved by applying a reduction factor, based on the test results of Margheritini et al. (2009b) and on the geometry of the two-reservoir SSG, to Eq. (6.5) (Zanuttigh et al. 2009).

Van der Meer et al. (2005b) studied the reflective behaviour of low-crested rubble mound breakwaters (LCS) as part of the DELOS project. This study confirms the reduction in reflection coefficient for smaller relative crest freeboards. Reflection coefficients acquired during four different test series with LCS have been compared to reflection coefficients predicted by empirical formulae for non-overtopped rubble mound breakwaters available in the Rock Manual (CUR/CIRIA 1991). The measured reflection coefficients appeared to be smaller than the predicted reflection coefficients and the following preliminary conclusions were drawn:

- the deviations between measured and predicted reflection coefficients are dominantly determined by the relative crest freeboard R_c / H_{m0} and become significant for a relative crest freeboard $R_c / H_{m0} < 0.5$;

- the overpredictions of the prediction formulae for small values of R_c / H_{m0} increase linearly for decreasing relative crest freeboard.

Correspondingly, a reduction factor $f_{r,1}$ has been proposed, expressing these preliminary conclusions:

$$f_{r,1} = \begin{cases} 0.2\dfrac{R_c}{H_{m0}} + 0.9 & \dfrac{R_c}{H_{m0}} < 0.5 \\ 1.0 & \dfrac{R_c}{H_{m0}} \geq 0.5 \end{cases} \tag{6.6}$$

A similar reduction factor, denoted by $f_{r,2}$, was proposed by Zanuttigh and Van der Meer (2008) based on a wider dataset of test results of rock permeable slopes, which partly overlaps the dataset used to predict Eq. (6.6), and based on a prediction formula of the type of Eq. (6.5) with coefficients for rock slopes. The expression for $f_{r,2}$ is given in Eq. (6.7). The corresponding *rmse* is 0.047.

$$f_{r,2} = \begin{cases} 0.37\dfrac{R_c}{H_{m0}} + 0.67 & -1.0 \leq \dfrac{R_c}{H_{m0}} < 0.9 \\ 1.0 & \dfrac{R_c}{H_{m0}} \geq 0.9 \end{cases} \tag{6.7}$$

Note that for both low-crested structures, i.e. the SSG and the LCS, the reflection coefficients have been predicted by applying a reduction factor to a prediction formula for non-overtopped slopes. Consequently, it is likely that Eq. (6.3b) and Eq. (6.5) also overpredict the reflection coefficients for the smooth impermeable low-crested slopes studied in this PhD-manuscript. Van der Meer et al. (2005b) suggest that those reflection coefficients should be predicted by applying the reduction factor $f_{r,1}$ (Eq. 6.6) to prediction formulae for the reflection coefficients of non-overtopped smooth impermeable slopes available in the Rock Manual (a.o. Eq. 6.3b). A validation of the applicability of this methodology for smooth impermeable low-crested slopes has however not been found in literature.

Since the predictions of the reflection coefficients for non-overtopped smooth impermeable slopes by Eq. (6.5) are assumed to be more accurate than the predictions by Eq. (6.3), a more accurate methodology probably consists of predicting the reflection coefficients for non-overtopped smooth impermeable slopes using Eq. (6.5), and applying a reduction factor for the relatively small crest freeboards.

In order to verify the validity of this methodology, the reflection coefficients of the UG10 test series are compared to their predictions by Eq. (6.3b) and Eq. (6.5) (see following section 6.3). In particular, the test matrix of the UG10 test series enables to identify the independent effects of the determining parameters for steep

low-crested slopes - wave height, slope angle, wave period and crest freeboard - on the corresponding reflection coefficients.

6.3 Effect of determining parameters on reflection coefficients of steep low-crested slopes

Postma (1989) studied the suitability of the breaker parameter to describe the independent effects of the wave height, slope angle and wave period on the reflection coefficient for rock slopes. The effect of the wave height on the reflection coefficient of rock slopes appears to be rather weak: a small decrease in the reflection coefficient occurred with increased wave height for rock slopes. According to Postma (1989), this small effect is caused by energy dissipation along the slope surface due to drag forces and by local flattening of the rock slope due to testing beyond the limits of armour stability, both resulting in less reflection. Correspondingly, the application of a breaker parameter leads to an overestimation of the effect of the wave height on the reflection coefficient for rock slopes, thus introducing a larger scatter in the predictions.

Based on section 6.2.1, the breaker parameter is expected to describe the independent effects of the wave height, slope angle and wave period well for non-overtopped smooth impermeable slopes. The following three sections (6.3.1 to 6.3.3) show those independent effects based on the UG10 test results with a relatively high crest freeboard. Section 6.3.4 discusses the effect of the breaker parameter on the reflection coefficients of the UG10 test series. These four sections (6.3.1 to 6.3.4) enable to verify the ability of the breaker parameter to accurately take into account the independent effects. The effect of a small relative crest freeboard is also discussed in section 6.3.4.

6.3.1 Effect of wave height on reflection coefficients of steep slopes

The effect of the wave height on the reflection coefficient of steep low-crested slopes is shown in Fig. 6.2 for tests of the UG10 dataset with $\cot\alpha$ = 1.7, T_p = 1.5 s and R_c = 0.070 m. The relative crest freeboards R_c / H_{m0} corresponding to the three test results are 0.51, 0.70 and 1.04. Predicted reflection coefficients by Eq. (6.3b) and Eq. (6.5), and its 90% prediction interval, were added to Fig. 6.2. No reduction

factors have been applied to these prediction formulae, although the UG10 data point with the largest wave height exceeds the ranges of application of Eq. (6.5) for R_c / H_{m0}.

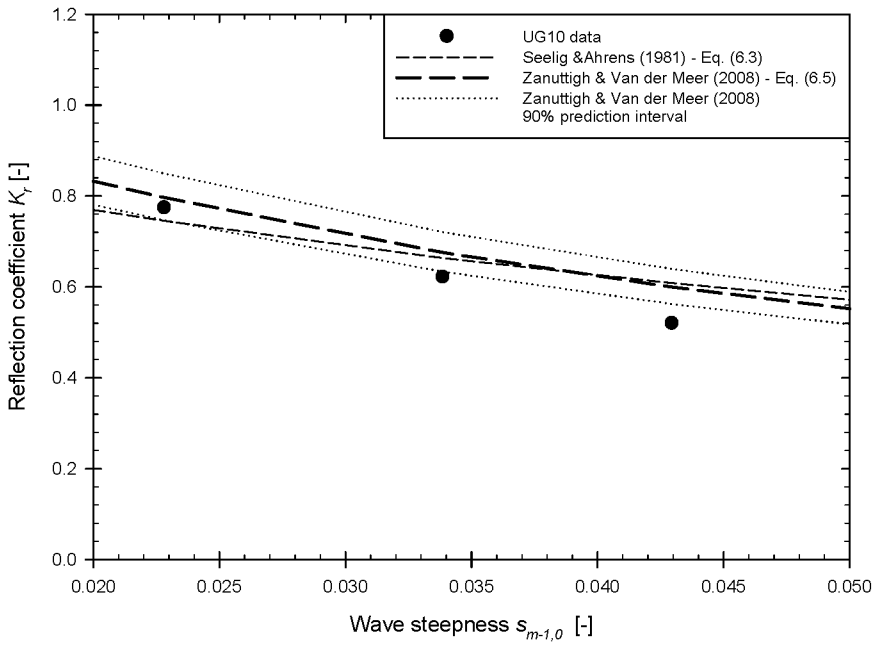

Figure 6.2: Measured reflection coefficients as a function of the wave steepness, for tests of the UG10 dataset with $\cot\alpha$ *= 1.7,* T_p *= 1.5 s and* R_c *= 0.070 m. Predicted values by Eq. (6.3b) and Eq.(6.5) are added.*

For the particular example in Fig. 6.2, an increase in wave height corresponds to a decrease of the reflection coefficient. Based on similar graphs for other sets of $\cot\alpha$, T_p and R_c, these conclusions appear to be generally valid (Eq. 6.8) for the total ranges of application covered by the UG10 dataset.

$$H_{m0} \uparrow \quad \Rightarrow \quad K_r \downarrow \tag{6.8}$$

The prediction lines of Eq. (6.3b) and Eq. (6.5) (Fig. 6.2) confirm this decreasing trend, but overpredict the reflection coefficients of the two test results with the smaller relative crest freeboards (even though the ranges of application of these prediction formulae are only violated by the test result with the largest wave height). Consequently, it can be concluded that Eq. (6.5) overpredicts the reflection coefficient for values of the relative crest freeboard even larger than 0.58. The overestimations by Eq. (6.3b) are slightly smaller.

6.3.2 Effect of slope angle on reflection coefficients of steep slopes

The independent effect of the slope angle on the reflection coefficient of steep low-crested slopes is visualized in Fig. 6.3.

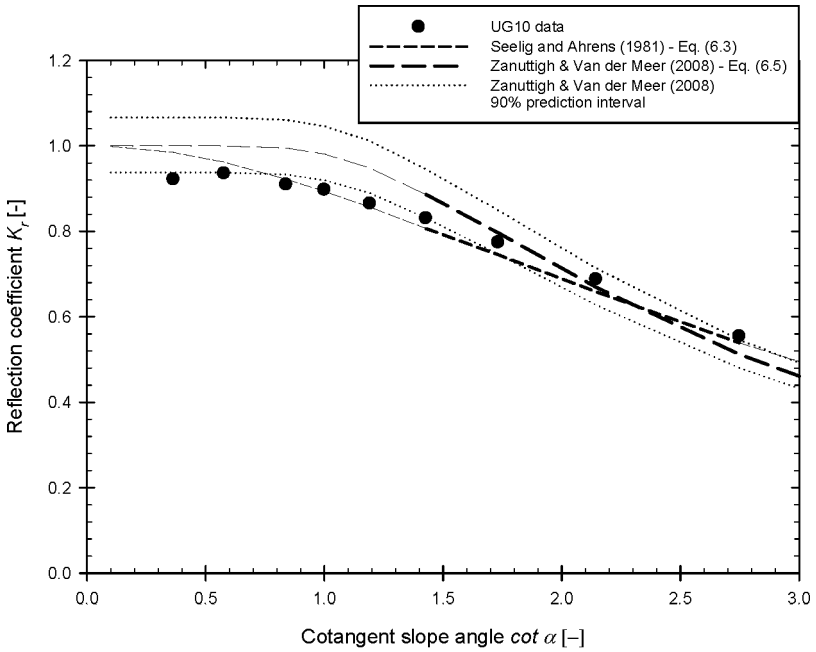

Figure 6.3: Measured reflection coefficients as a function of the cotangent of the slope angle $\cot\alpha$ *for tests of the UG10 dataset with* $H_{m0} = 0.067$ *m,* $T_p = 1.5$ *s and* $R_c = 0.070$ *m. Predicted values by Eq. (6.3b) and Eq. (6.5) are added.*

This figure shows a graph of measured reflection coefficients as a function of the cotangent of the slope angle $\cot\alpha$ for tests of the UG10 dataset with H_{m0} = 0.067 m, T_p = 1.5 s and R_c = 0.070 m. The corresponding value of the relative crest freeboard R_c / H_{m0} is 1.04. Predicted reflection coefficients (by Eq. (6.3b) and Eq. (6.5) with its 90% prediction interval) were added to Fig. 6.3 for comparison. Again, no reduction factors were applied to these prediction formulae.

Note that the test results of the UG10 dataset with slopes steeper than 1:1.5 are positioned outside the ranges of application of Eq. (6.3b) and Eq. (6.5) for $\cot\alpha$. The corresponding prediction lines are marked with a thinner line for those slope angles.

In general, a steeper slope corresponds to a larger reflection coefficient for the example in Fig. 6.3. Graphs for different sets of H_{m0}, T_p and R_c confirm these conclusions. Accordingly, Eq. (6.9) is valid for the total range of application covered by the UG10 dataset (for identical values of the wave height, wave period and crest freeboard).

$$\cot\alpha \uparrow \quad \Rightarrow \quad K_r \downarrow \tag{6.9}$$

This is confirmed by the prediction lines of Eq. (6.3b) and Eq. (6.5), which reach a theoretical maximum of 1.0 for non-overtopped vertical walls with $\cot\alpha$ = 0.0. The predictions by Eq. (6.5) are accurate for milder slopes: the data points with $\cot\alpha$ > 1.5 are positioned within the 90% prediction interval of Eq. (6.5). However, Eq. (6.5) overpredicts the reflection coefficients for slopes that are steeper than 1:1.5, outside its ranges of application for the slope angle. On the other hand, the predictions by Eq. (6.3b) are relatively accurate for the total range of slope angles (Fig. 6.3).

6.3.3 Effect of wave period on reflection coefficients of steep slopes

The independent effect of the wave period on the reflection coefficient is shown in Fig. 6.4, i.e. a graph of measured reflection coefficients as a function of the wave steepness for tests of the UG10 dataset with $\cot\alpha$ = 1.7, H_{m0} = 0.067 m and R_c = 0.070 m. The corresponding value of the relative crest freeboard R_c / H_{m0} is 1.04. Again, predicted reflection coefficients by Eq. (6.3b) and Eq. (6.5), together

with its 90% prediction interval, are added for comparison. No reduction factors have been applied.

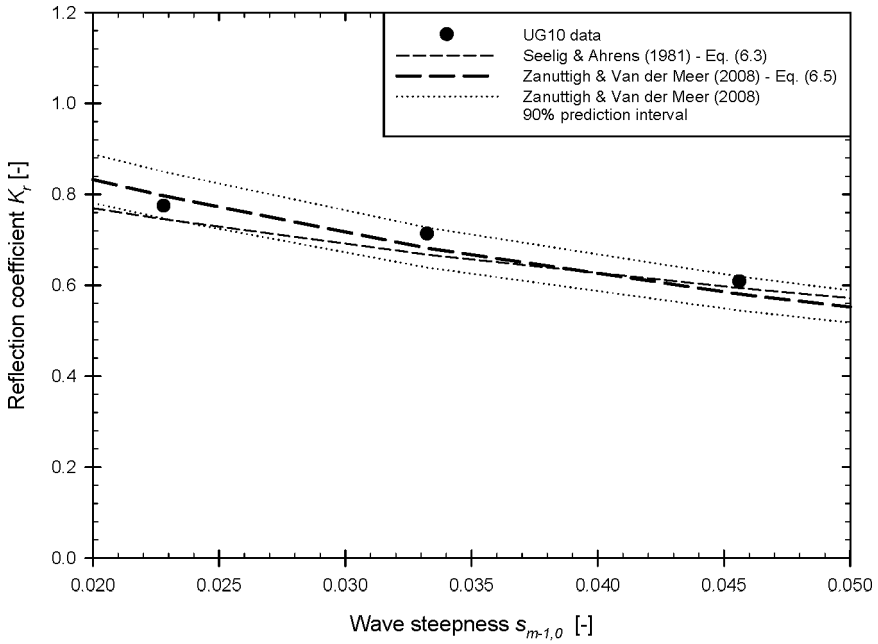

Figure 6.4: Measured reflection coefficients as a function of the wave steepness for tests of the UG10 dataset with $\cot\alpha$ *= 1.7,* H_{m0} *= 0.067 m and* R_c *= 0.070 m. Predicted values by Eq. (6.3b) and Eq. (6.5) are added.*

Based on the example in Fig. 6.4, an increase of the wave period corresponds to an increasing reflection coefficient. Similar graphs for other sets of $\cot\alpha$, H_{m0} and R_c confirm these conclusions. This means that Eq. (6.10) is valid for the total ranges of application covered by the UG10 dataset (for identical values of wave height, slope angle and crest freeboard).

$$T_p \uparrow \quad \Rightarrow \quad K_r \uparrow \tag{6.10}$$

The decreasing trend followed by the data points in Fig. 6.4 is quite accurately predicted by Eq. (6.5); all UG10 test results are positioned within the 90% prediction interval of Eq. (6.5). The predictions of Eq. (6.3b) are less accurate.

The proportionality between the wave period and the reflection coefficient was also encountered by Postma (1989), who studied the reflective behaviour of rock slopes under random wave attack.

6.3.4 Effect of breaker parameter and relative crest freeboard on the reflection coefficients of steep low-crested slopes

When comparing Fig. 6.2 to Fig. 6.4, it seems that the effects of the wave height and wave period are equivalent in size for steep smooth impermeable slopes. This is confirmed by the predictions of Eq. (6.3b) and Eq. (6.5), which are based on the breaker parameter. Furthermore, taking into account the good agreement between measured and predicted values of the reflection coefficient in Fig. 6.3, the breaker parameter appears to be able to describe the independent effects of the wave height, slope angle and wave period well for non-overtopped smooth impermeable slopes, in contrast to the observation by Postma (1989) for rock slopes.

Based on Eqs. (6.8) to (6.10), an increase in the breaker parameter $\xi_{m-1,0}$ should cause an increase in the reflection coefficient. This is confirmed by Fig. 6.1 and by Fig. 6.5, which shows the reflection coefficients as a function of the breaker parameter $\xi_{m-1,0}$ for tests of the UG10 dataset with H_{m0} = 0.067 m. The data points are categorized by the crest freeboard R_c, within the following categories: R_c = 0.020 m (R_c / H_{m0} = 0.30), 0.045 m (R_c / H_{m0} = 0.67) and 0.070 m (R_c / H_{m0} = 1.04).

Reflection coefficients predicted by Eq. (6.3b) and Eq. (6.5), together with its 90% prediction interval, are added for comparison. Both equations are also plotted outside their ranges of application for $\xi_{m-1,0}$. Note that the UG10 test results with R_c = 0.020 m correspond to relative crest freeboards smaller than 0.58, i.e. outside the ranges of application of Eq. (6.5) for R_c / H_{m0} (Fig. 6.5).

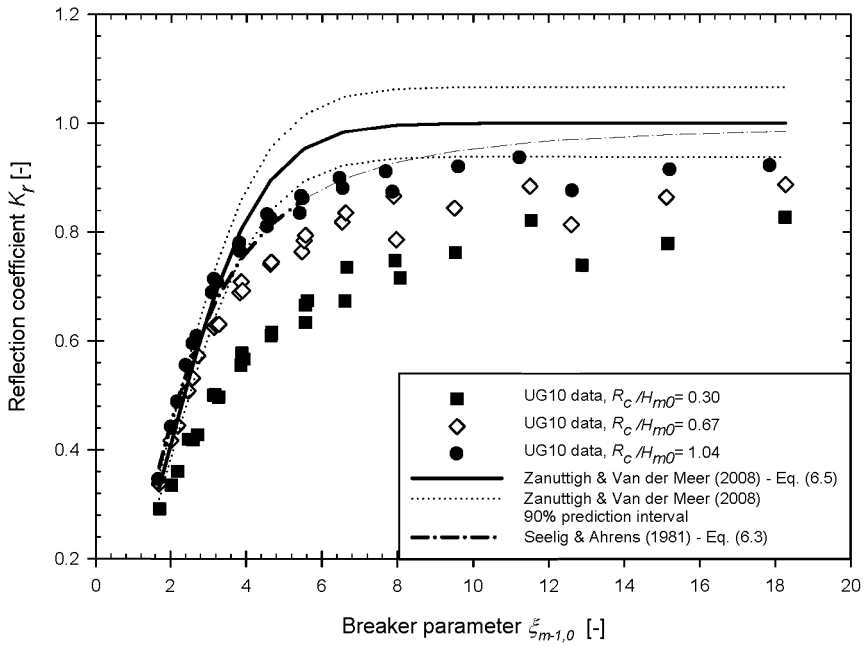

Figure 6.5: Measured reflection coefficients as a function of the breaker parameter for tests of the UG10 dataset with H_{m0} = 0.067 m and R_c = 0.020 m, 0.045 m and 0.070 m. Predicted values by Eq. (6.3b) and Eq. (6.5) are added. Test results categorized by the relative crest freeboard.

A number of conclusions are drawn based on Fig. 6.5:

- similar to the SSG, large values of the reflection coefficients occur. The measured coefficients vary between 0.3 (typical for traditional rubble mount breakwaters) and almost 1.0 (typical for a vertical wall), depending on the values of the breaker parameter and the relative crest freeboard. This means that scour is possibly induced at the toe of the structure, which may result in failure. Consequently, a rocky toe protection or perforated screens need to be used to reduce the induced scour at the toe of the structure. The elevation of these structures should not be

too high in order to avoid wave breaking and dissipation of incident wave energy. A smaller reflection coefficient reduces the size and cost of the toe protection;

- an increase in breaker parameter causes an increase in reflection coefficient, even for the UG10 test results with relative crest freeboards smaller than 0.50;

- both Eq. (6.3b) and Eq. (6.5) quite accurately predict the measured reflection coefficients for a relative crest freeboard $R_c / H_{m0} = 1.04$, within their ranges of application for $\xi_{m-1,0}$. However, these formulae overpredict the measured reflection coefficients for larger values of $\xi_{m-1,0}$ (larger than 6.2 for Eq. (6.3b) and larger than 4.1 for Eq. (6.5)). Furthermore, the deviations between measured and predicted reflection coefficients increase for increasing value of the breaker parameter. Significant overpredictions by Eq. (6.5) occur for $\xi_{m-1,0} > 8.0$;

- both Eq. (6.3b) and Eq. (6.5) overpredict the measured reflection coefficients for the relative crest freeboard $R_c / H_{m0} = 0.67$ for breaker parameters $\xi_{m-1,0} > 3.0$. The measured reflection coefficients for $R_c / H_{m0} = 0.30$ are overpredicted by Eq. (6.3b) and Eq. (6.5) over the total range of $\xi_{m-1,0}$ in Fig. 6.5;

- for a specific value of the breaker parameter, an increase in relative crest freeboard causes an increase in the reflection coefficient. This is also illustrated in Fig. 6.6, which shows the measured reflection coefficients as a function of the relative crest freeboard for tests of the UG10 dataset with $\cot\alpha =$ 1.7, $H_{m0} =$ 0.067 m and $T_p =$ 1.5 s. Predicted values of the reflection coefficients by Eq. (6.3b) and Eq. (6.5), with its 90% prediction interval, are added to Fig. 6.6 for comparison. Since no reduction factors have been applied to these prediction formulae, they overpredict the reflection coefficients for smaller relative crest freeboards. Based on Fig. 6.6, these overestimations are significant for relative crest freeboards smaller than 0.9, similar the value of obtained by Zanuttigh and Van der Meer (2008) (Eq. 6.7). This is in accordance with the observations made above (Fig. 6.2).

- the asymptotic value of the reflection coefficient for large values of the breaker parameter depends on the value of the relative crest freeboard, and is only approximately equal to 1.0 for large relative crest freeboards. Theoretically, the reflection coefficient is equal to 1.0 for vertical walls (breaker parameter equals infinity) without wave overtopping. However, when significant wave overtopping

occurs at a vertical wall, the corresponding reflection coefficient becomes smaller than 1.0. This is illustrated by Young and Testik (2011), in which an example of a vertical wall with zero crest freeboard subjected to regular waves is shown, which corresponds to a reflection coefficient equal to 0.65.

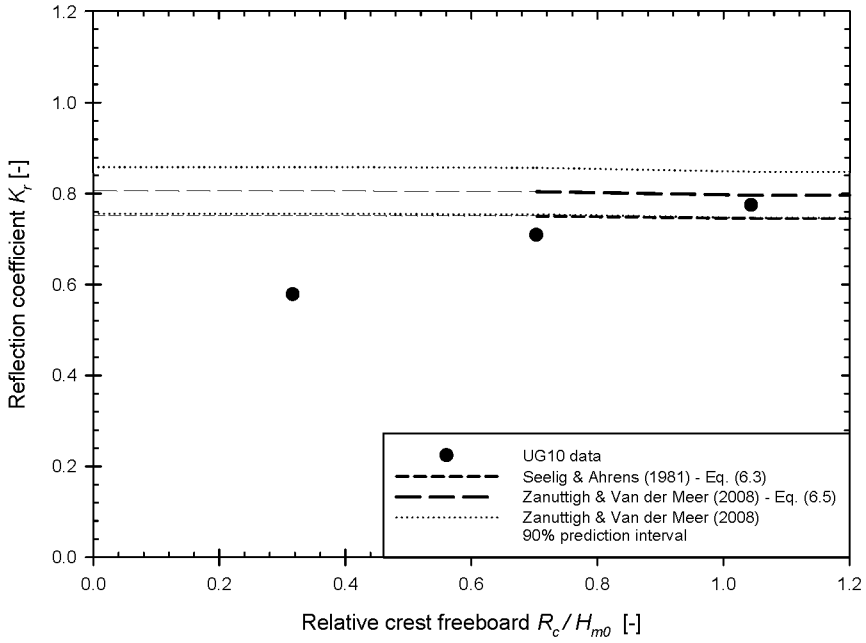

Figure 6.6: Measured reflection coefficients as a function of the relative crest freeboard for tests of the UG10 dataset with $\cot\alpha = 1.7$, $H_{m0} = 0.067$ *m and* $T_p = 1.5$ *s. Predicted values by Eq. (6.3b) and Eq. (6.5) are added.*

In conclusion, existing prediction formulae overpredict the reflection coefficient for large breaker parameters and relatively small crest freeboards.

Hence, a new empirical production formula has been derived in this PhD-research. The last two conclusions demonstrate that there is an interaction between the effect of the relative crest freeboard and the effect of the breaker parameter for smooth impermeable steep low-crested slopes. As mentioned above, a similar interaction has

been observed for rock slopes. This is taken into account by applying a reduction factor to a prediction formula of the reflection coefficient for non-overtopped rock slopes. This methodology could also be applied for steep low-crested slopes (Fig. 6.5). The new prediction formula thus consists of an expression for K_r as a function of the breaker parameter $\xi_{m-1,0}$ for relatively large crest freeboards, to which a reduction factor is applied for smaller relative crest freeboards. In that sense, the methodology suggested at the end of section 6.2 could be considered, i.e. applying a reduction factor for small values of R_c / H_{m0} to Eq. (6.5). However, the significant overpredictions of the reflection coefficients for larger breaker parameters by Eq. (6.5) require the derivation of a prediction formula that is able to predict the reflection coefficients more accurately than Eq. (6.5) for the total range of breaker parameters of the UG10 dataset and for relatively large crest freeboards. Furthermore, the expression for the reduction factor has to be determined. The derivation of the new prediction formula for K_r is discussed in the following section.

6.4 New prediction formula for reflection coefficients of steep low-crested slopes

Based on the observations in section 6.3, the reflection coefficient of steep low-crested slopes is a function of the breaker parameter $\xi_{m-1,0}$, to which a reduction factor f_R is applied for small relative crest freeboards R_c / H_{m0} (Eq. 6.11) (f is a random function).

$$K_r = f_R \, f\left(\xi_{m-1,0}\right) \tag{6.11}$$

Since the predictions of the UG10 test results by Eq. (6.3b) are in general more accurate than the predictions by Eq. (6.5) (sections 6.3.1 to 6.3.4), Eq. (6.3b) is selected as the expression for f :

$$K_r = f_R \frac{\xi_{m-1,0}^2}{\xi_{m-1,0}^2 + 5.0} \tag{6.12}$$

In order to achieve more information on the expression for the reduction factor f_R , a graph visualizing the ratio of the measured reflection coefficients of the UG10

test series and their predicted values using Eq. (6.3b) ($K_r / K_{r,S\&A}$) as a function of the relative crest freeboard was generated (Fig. 6.7). The data points in Fig. 6.7 are categorized by the slope angle. The reduction factors $f_{r,1}$ (Eq. 6.6) and $f_{r,2}$ (Eq. 6.7), with its 90% prediction interval, are added for comparison.

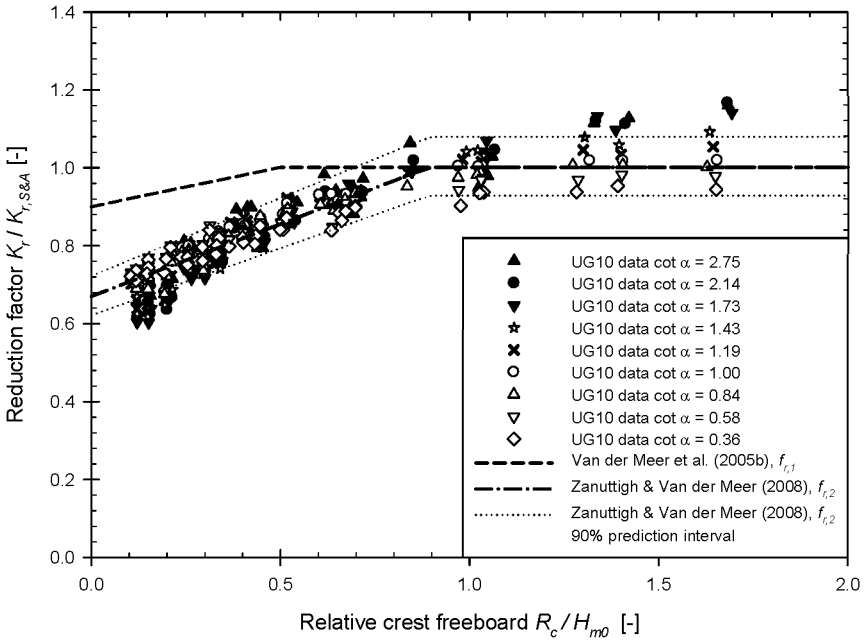

Figure 6.7: Ratio of measured and predicted (Eq. 6.3b) reflection coefficients as a function of the relative crest freeboard for all tests of the UG10 dataset. Reduction factors $f_{r,1}$, Eq. (6.6), and $f_{r,2}$, Eq. (6.7), together with its 90% prediction interval, are added for comparison.

$K_r / K_{r,S\&A}$ is smaller than 1.0 for relative crest freeboards smaller than approximately $R_c / H_{m0} = 0.9$ (see also Fig. 6.6). Since $f_{r,1}$ is only smaller than 1.0 for values of $R_c / H_{m0} < 0.5$ (short-dashed line in Fig. 6.7), this reduction factor is

not able to describe the reduced reflection coefficient for UG10 test results with smaller relative crest freeboards accurately.

On the other hand, $f_{r,2}$ predicts the reduction in reflection coefficient for $R_c / H_{m0} < 1.0$ quite accurately, although it is originally derived for rock slopes. The reduction factor $f_{r,2}$ becomes 1.0 for a relative crest freeboard $R_c / H_{m0} = 0.9$ (Eq. 6.7).

Due to the good agreement between the data points in Fig. 6.7 with $R_c / H_{m0} < 0.9$ and the reduction factor $f_{r,2}$, the new prediction formula for the reflection coefficients of steep low-crested slopes is:

$$K_r = f_{r,2} \frac{\xi_{m-1,0}^2}{\xi_{m-1,0}^2 + 5.0} \tag{6.13}$$

For relative crest freeboards $R_c / H_{m0} \geq 0.9$, Eq. (6.13) reduces to Eq. (6.3b).

The corresponding *rmse* (Eq. 6.4) for the measured reflection coefficients of the UG10 test series equals 0.031. This low value of the *rmse* confirms that Eq. (6.13) is able to predict the reflection coefficients of steep low-crested slopes accurately.

Furthermore, the following two important remarks concerning Fig. 6.7 are made:

- it is clear that the effect of the relative crest freeboard is dominant over the effects of the slope angle and the wave period. This means that for relatively small crest freeboards, an increase of the relative crest freeboard corresponds to an increase of the reflection coefficient, even when the slope angle and wave period are not identical;
- the parameters affecting the reflection coefficient of steep low-crested slopes (i.e. the breaker parameter $\xi_{m-1,0}$ and the relative crest freeboard R_c / H_{m0}) are also the two parameters that affect the dimensionless average overtopping rate of steep low-crested slopes (section 5.4). This suggests that there is a relationship between the average overtopping rate and the reflection coefficient for steep low-crested slopes. This is the subject of the following section 6.5.

6.5 Relationship between average overtopping rates and reflection coefficients of steep low-crested slopes

Based on Fig. 6.8, one could conclude that an increase of the dimensionless average overtopping rate $q/\sqrt{g H_{m0}^3}$ corresponds to a decrease of the reflection coefficient K_r (Eq. 6.14).

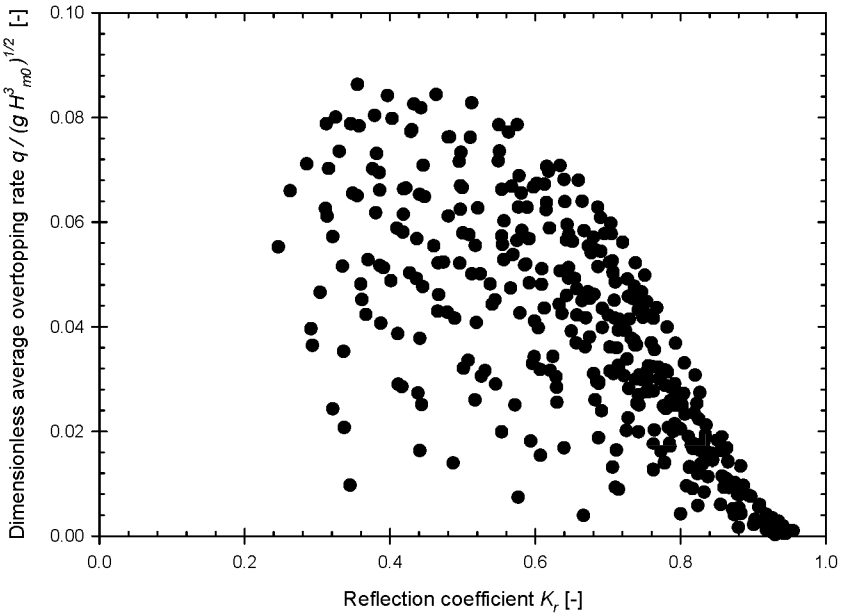

Figure 6.8: Average overtopping rate $q/\sqrt{g H_{m0}^3}$ as a function of the reflection coefficients for all tests of the UG10 dataset.

$$\frac{q}{\sqrt{g\,H_{m0}^3}}\uparrow \quad \Rightarrow \quad K_r \downarrow \tag{6.14}$$

However, spreading occurs among the data points. Therefore, the relationship between $q/\sqrt{g\,H_{m0}^3}$ and K_r is studied in detail, based on the differences between the effects of the slope angle, crest freeboard and wave period on the reflection coefficient on the one hand (section 6.3) and on the dimensionless average overtopping rate on the other hand (chapter 5):

1. an increase of the cotangent of the slope angle (i.e. the slope becoming milder) corresponds to a decrease of the reflection coefficient, over the total range of slope angles of the UG10 dataset (section 6.3.2). This is in contrast with the dimensionless average overtopping rate, which reaches a maximum for a particular slope angle;

2. an increase of the relative crest freeboard causes an increase of the reflection coefficient (Fig. 6.2 and Fig. 6.6) and a decrease of the dimensionless average overtopping rate. This effect agrees well with Eq. (6.14);

3. finally, an increase in wave period causes an increase in reflection coefficient, for all tests of the UG10 dataset (section 6.3.3). On the other hand, the effect of the wave period on the dimensionless average overtopping rate depends on the slope of the structure (Fig. 5.26). For milder slopes, an increase in wave period causes an increase in the dimensionless average overtopping rate, while for steeper slopes an increase in wave period causes a decrease in the dimensionless average overtopping rate.

Both effects of the slope angle and wave period undermine the generality of the conclusion in Eq. (6.14). This can be explained based on an energy balance, since the underlying reason is the effect of wave breaking. The interrelation between wave reflection, dissipation and transmission has been pointed out by Seelig and Ahrens (1981) and is given in Eq. (6.15).

$$1 = K_r^2 + K_d^2 + K_t^2 \tag{6.15}$$

K_d^2 [-] is the ratio of the wave energy lost through dissipation to the total incident wave energy, while K_t [-] is the transmission coefficient. This coefficient includes transmission through a permeable structure and transmission by overtopping for a low-crested structure. Due to the fact that the slope of the structures considered in

this PhD-manuscript is impermeable and extends to the bottom of the seabed, energy loss through wave transmission is absent. Consequently, K_t^2 is only determined by wave overtopping; it is denoted by K_{OT}^2 [-].

In the case of non-breaking waves, the dissipation term K_d^2 becomes negligible, resulting in Eq. (6.16).

$$1 = K_r^2 + K_{OT}^2 \tag{6.16}$$

On the other hand, for the case of breaking waves, the dissipation term is significant and the energy balance equation becomes more complex:

$$1 = K_r^2 + K_d^2 + K_{OT}^2 \tag{6.17}$$

It is clear that an increase in wave overtopping causes a decrease in the reflection coefficient for non-breaking waves (Eq. 6.16). This is confirmed by Fig. 6.9, which is limited to the test results of the UG10 dataset with $\xi_{m-1,0} \geq 3.0$, i.e. the transition value between non-breaking and breaking waves (according to chapter 5). The horizontal spreading is caused by the wave period; its effect on the reflection coefficient is larger than on the average overtopping rate (Fig. 6.9).

The transition from non-breaking waves to breaking waves corresponds to the introduction of an energy dissipation term K_d^2 in the energy balance equation (Eq. 6.16 to Eq. 6.17). This has a number of consequences:

- in the case of breaking waves, the dimensionless average overtopping rate increases for increasing slope angle, since the dissipation term K_d^2 in Eq. (6.17) decreases. When the slope is sufficiently steep, this term becomes zero. Consequently, Eq. (6.17) reduces to Eq. (6.16), and the term K_{OT}^2 is at its maximum. When the slope becomes even steeper, K_r increases and the term K_{OT}^2 decreases again. This explains the existence of an optimal slope angle;

- an increase in wave period increases the reflection coefficient. For steeper slopes, corresponding to non-breaking waves, this means that the average overtopping rate should decrease (Eq. 6.16). For milder slopes, which correspond to breaking waves, the increase in wave period increases the breaker parameter. Hence, less energy is dissipated through wave breaking and the dimensionless average overtopping rate should increase. Both conclusions are confirmed by Fig. 5.26;

- when more wave breaking occurs, smaller reflection coefficients and smaller average overtopping rates should be found (Eq. 6.17).

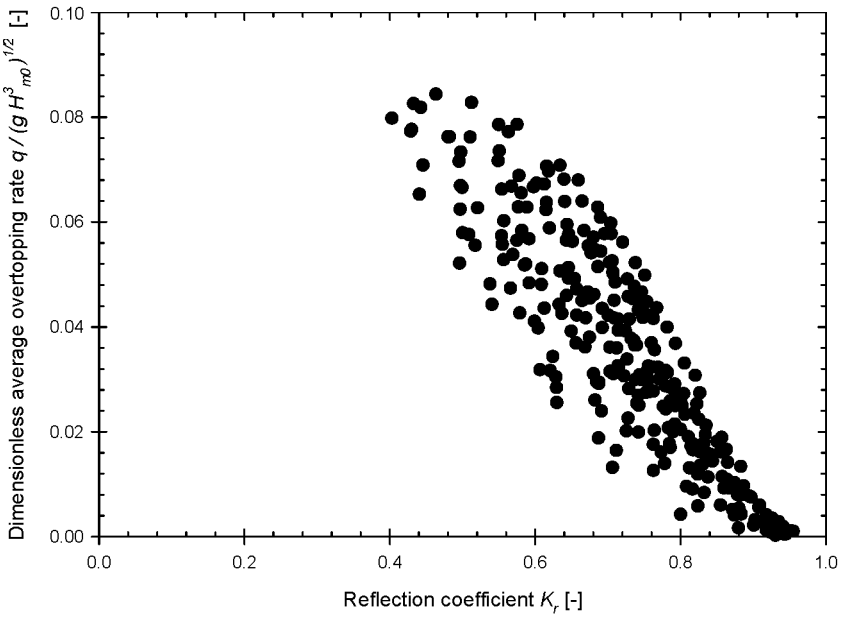

Figure 6.9: Average overtopping rate $q/\sqrt{g H_{m0}^3}$ as a function of the reflection coefficients for all tests of the UG10 dataset with $\xi_{m-1,0} \geq 3.0$.

Consequently, it is clear that the conclusion that an increase in average overtopping rate corresponds to a decrease in reflection coefficient is only generally valid for non-breaking waves.

However, when an increase in the relative crest freeboard R_c / H_{m0} of structures with a relatively low crest freeboard occurs, which is large compared to the changes in slope angle and wave period, the reflection coefficient increases (Fig. 6.7) while the dimensionless average overtopping rate decreases (Fig. 5.17). This is expressed in Eq. (6.18).

$$\frac{R_c}{H_{m0}} \uparrow \quad \Rightarrow \begin{cases} \dfrac{q}{\sqrt{g H_{m0}^3}} \downarrow \\ K_r \uparrow \end{cases} \tag{6.18}$$

Accordingly, the following conclusion is valid for non-breaking and breaking waves: when the average overtopping rate of a structure with a relatively small crest freeboard decreases (increases) due to an increase (decrease) in relative crest freeboard, which is large compared to the changes in slope angle and wave period, the reflection coefficient increases (decreases). A similar conclusion has been drawn by Van der Meer et al. (2005b).

Equation (6.18) can also be explained based on the energy balance of Eq. (6.17). When only an increase occurs in crest freeboard R_c, the contribution of the dissipation term to the energy balance is not affected. Accordingly, the inverse proportionality between $q/\sqrt{g H_{m0}^3}$ and K_r appears. On the other hand, when only the wave height increases for constant slope angle, wave period and crest freeboard, the amount of wave breaking increases. However, since the amount of incident energy increases as well, the changes in K_d^2 are expected to be rather small.

6.6 Conclusions

The reflective behaviour of steep low-crested slopes has been studied in this chapter, based on the reflection coefficients determined for the UG10 test results and based on predicted values from literature.

The approach suggested in literature to predict the reflection coefficient of low-crested structures consists of applying a reduction factor for smaller relative crest freeboards to a prediction formula for non-overtopped structures. This approach has been applied in literature for rock slopes, but not for smooth impermeable structures with small relative crest freeboards. Therefore a new prediction formula for K_r at steep low-crested structures has been suggested in this chapter.

A number of empirical formulae that predict the reflection coefficient for smooth, impermeable non-overtopped slopes are available in literature. Similar to those prediction formulae, the reflection coefficients of the UG10 test results are mainly determined by the breaker parameter for relatively large crest freeboards: an increase in breaker parameter causes an increase in reflection coefficient. The prediction formula by Seelig and Ahrens (1981) predicts the test results of the UG10 dataset with relatively large crest freeboards quite accurately. Furthermore, it appears that a reduction in reflection coefficients occurs for $R_c/H_{m0} < 0.9$, following the reduction

factor suggested by Zanuttigh and Van der Meer (2008) quite accurately. Hence, the new prediction formula combines the prediction formula by Seelig and Ahrens (1981) for smooth impermeable non-overtopped slopes and the reduction factor suggested by Zanuttigh and Van der Meer (2008) for rock permeable overtopped slopes.

Due to the analogy with the dimensionless average overtopping rate, the relationship between $q/\sqrt{g H_{m0}^3}$ and K_r has been studied. Based on the UG10 test results and an energy balance equation, it appears that an increase in $q/\sqrt{g H_{m0}^3}$ causes a decrease in K_r for non-breaking waves. Furthermore, an identical conclusion is valid for structures with a relatively small crest freeboard subjected to breaking waves, when the increase in average overtopping rate is determined by a decrease in relative crest freeboard.

7

Optimization of the performance of Overtopping Wave Energy Converters by geometry control

The main goal of this chapter is to present the results of a study on the effect of geometry control on the hydraulic performance of the overtopping wave energy converters (OWECs) considered in this PhD-manuscript. The study is based on the knowledge gained in chapters 5 and 6 on the relationship between geometry and average overtopping rate on the one hand, and the reflection coefficient on the other hand for steep low-crested slopes.

7.1 Introduction

The design of the slope of an OWEC for a particular deployment site, characterized by a number of characteristic sea states, is based on a maximization of the overall hydraulic efficiency (Eq. 1.5). The expression for the overall hydraulic efficiency for a single reservoir OWEC is:

$$\eta_{hydr,overall} = \frac{\sum_{j=1}^{N_{SS}} \rho g \, q_j \, R_{c,j} \, FO_j}{\sum_{j=1}^{N_{SS}} \frac{\rho g^2}{64\pi} H_{m0,j}^2 \, T_{m-1,0,j} \, FO_j} \tag{7.1a}$$

$$P_{hydr,overall} = \sum_{j=1}^{N_{SS}} \rho g \, q_{reservoir\,j} \, R_{c,j} \, FO_j \tag{7.1b}$$

In order to maximize the right hand side of Eq. (7.1a), its numerator - referred to as the hydraulic power $P_{hydr,overall}$ [kW/m] (Eq. 7.1b) - should be maximal. Consequently, after dividing and multiplying the numerator by the wave power $P_{wave,j}$ (Eq. 1.4), the following sum needs to be maximized: $\sum_{j=1}^{N_{SS}} \eta_{hydr,j} FO_j P_{wave,j}$, in which:

$$\eta_{hydr,j} = \frac{P_{hydr,j}}{P_{wave,j}} = \frac{\rho g q_j R_{c,j}}{\frac{\rho g^2}{64\pi} H_{m0,j}^2 T_{m-1,0,j}} \tag{7.2}$$

Traditionally, the slope angle and crest freeboard of an OWEC with a fixed geometry are determined by the characteristic sea states at the deployment site with the largest products $FO_j P_{wave,j}$. Hence, the geometry is only adapted to a limited number of sea states. Geometry control implies that the geometry of the slope is adapted to the characteristics of each sea state, in order to obtain a larger overall hydraulic efficiency compared to a fixed geometry. Hence, geometry control requires the maximization of the hydraulic power $P_{hydr,j}$ for each of the sea states (subscript *j*). Note that the crest freeboard $R_{c,j}$ also has a subscript *j* (Eqs. 7.1 and 7.2), since this value also depends on the sea state when geometry control is applied.

One of the main goals of this chapter is to study whether applying geometry control results in a significant increase in the overall hydraulic efficiency for the non-floating OWECs studied in this PhD-research. Furthermore, the effect of geometry control on the reflective behaviour of those OWECs is studied.

The knowledge gathered in chapters 5 and 6 allows to determine the optimal geometry of an OWEC for each sea state, resulting in the maximum hydraulic efficiency and power for that sea state (Eq. 7.2), and the corresponding reflection coefficient. This aspect is discussed in the first section below (section 7.2).

The effect of five different geometry control scenarios on the overall hydraulic efficiency, overall hydraulic power (power is more tangible than efficiency regarding energy output of OWECs) and reflection coefficient of OWECs has been studied at three hypothetical deployment sites. The scenarios are described in section 7.3, while the data for the deployment sites are given in section 7.4.

It should be noted that the UG10 prediction formulae for $q/\sqrt{g H_{m0}^3}$ (Eqs. 5.9 and 5.10), which consider the existence of a single slope angle corresponding to the

maximum average overtopping rate, are used in this chapter because these formulae result in the most accurate predictions. Note that the range of wave steepness of the UG10 test results is not valid for swells. Hence, the conclusions drawn in this chapter are only applicable to wind seas. Furthermore, the following important remarks are made regarding geometry control:

- the optimal geometry is determined based on a maximization of the hydraulic efficiency. The total efficiency of an OWEC is also determined by the efficiency of the reservoir, turbines efficiency and generator efficiency. Furthermore, the capacities of the generator and turbines also affect the value of the practical crest freeboard (e.g. the turbines should be able to handle the flow rates). However, these efficiencies and capacities are not considered when designing the optimal slope geometry;

- geometry control requires the adaptation of the geometry to each sea state. This involves that part of the power gained from the ocean waves is not transferred to the grid, but is used to adapt the slope geometry;

- when a location is dominated by one sea state, geometry control is not efficient.

7.2 Optimal geometry for a sea state

7.2.1 General

The optimal geometry for a sea state is determined by the values of $\cot\alpha_j$ and $R_{c,j}$ (j is the subscript for the sea state) which lead to a maximum hydraulic power[1] $P_{hydr,j}$. A maximization of the right hand side of Eq. (7.2) requires a maximization of the product $q_j R_{c,j}$, with q_j being dependent on $\cot\alpha_j$ and $R_{c,j}$ (chapter 5). Note that this also results in a maximization of the hydraulic efficiency, since $P_{hydr,j}$ is the numerator of the right hand side of Eq. (7.2).

It is clear that the crest freeboard plays an important role in maximizing $q_j R_{c,j}$. When using a low crest freeboard, large average overtopping rates occur, but with rather low potential energy, resulting in low values of the hydraulic efficiency. On the other hand, a high crest freeboard increases the potential energy of the

[1] Note that the *optimal* slope angle discussed in section 5.5 corresponds to the maximum average overtopping rate, not to the maximum hydraulic power.

overtopping water, but the amount of overtopping is reduced. Consequently, an optimum crest freeboard exists, for which the average overtopping rate q_j needs to be maximized. Based on Fig. 5.17, the value of $q/\sqrt{g H_{m0}^3}$ corresponding to the maximum value of $q_j R_{c,j}$ is found in zone Z3 or zone Z4. Accordingly, based on the expressions for the dimensionless average overtopping rate in zones Z3 and Z4, the following expression is valid for $q_j R_{c,j}$:

$$q_j R_{c,j} = F_1 F_2 \tag{7.3a}$$

where

$$F_1 = \left[\cos\left(\frac{\xi_{m-1,0,j} - 3.0}{3.0} \right) \right]^3 \tag{7.3b}$$

$$F_2 = A \exp\left(B \frac{R_{c,j}}{H_{m0,j}} \right) R_{c,j} \sqrt{g H_{m0,j}^3} \tag{7.3c}$$

The values of the empirical coefficients A and B are dependent on the zone (Eq. 5.9 or Eq. 5.10). Since the effect of the slope angle and crest freeboard are independent in Eq. (7.3), the optimal values of both parameters are determined independently. The optimal slope angle is based on a maximization of the factor $F_1 = \left[\cos\left(\left(\xi_{m-1,0,j} - 3.0 \right) / 3.0 \right) \right]^3$. This introduces the concept of an adaptive slope angle (section 7.2.2).

The optimal crest freeboard maximizes the factor $F_2 = A \exp\left(B R_{c,j} / H_{m0,j} \right) R_{c,j} \sqrt{g H_{m0,j}^3}$, which introduces the concept of an adaptive crest freeboard (section 7.2.3).

7.2.2 Adaptive slope angle

It is clear that the factor F_1 is maximal when the breaker parameter $\xi_{m-1,0,j}$ takes the value 3.0. This requirement for the breaker parameter determines the optimal slope angle for a specific sea state (Eq. 7.4), resulting in the maximum average overtopping rate for that particular sea state and a specific crest freeboard.

$$\tan\alpha_{j,opt} = 3.0\sqrt{s_{m-1,0,j}} \tag{7.4}$$

Note that the optimal slope angle only depends on the wave steepness of the sea state. When the waves are steeper, the optimal slope is also steeper. The concept of an adaptive slope angle entails the application of the optimal slope angle (Eq. 7.4) for each of the characteristic sea states of a deployment site.

Deployment of the steep low-crested slopes with a fixed crest freeboard in a location at sea with little variation in wave steepness consequently only results in a small gain in performance when applying an adaptive slope angle compared to a fixed slope angle.

7.2.3 Adaptive crest freeboard

The optimal crest freeboard is determined by maximizing the factor F_2. This is achieved by setting the derivative of F_2 to $R_{c,j}$ equal to zero:

$$\frac{dF_2}{dR_{c,j}} = 0 \tag{7.5}$$

$$\Rightarrow \frac{d\left(\sqrt{g H_{m0,j}^3}\, A R_{c,j} \exp\left(B\frac{R_{c,j}}{H_{m0,j}}\right)\right)}{dR_{c,j}} = 0 \tag{7.6}$$

$$\Rightarrow \exp\left(B\frac{R_{c,j}}{H_{m0,j}}\right)\left[A + A R_{c,j}\frac{B}{H_{m0,j}}\right] = 0 \tag{7.7}$$

$$\Rightarrow \left[A + A R_{c,j}\frac{B}{H_{m0,j}}\right] = 0 \tag{7.8}$$

$$\Rightarrow \left(\frac{R_{c,j}}{H_{m0,j}}\right)_{opt} = -\frac{1}{B} \tag{7.9}$$

The coefficient B takes the value -1.7 for zone Z3, while it is -2.4 for zone Z4. Since the optimal relative crest freeboard (Eq. 7.9) is smaller than 0.8 for both values

of B, the optimal zone is Z3. Consequently, the value of the optimal crest freeboard fulfils Eq. (7.10).

$$\left(\frac{R_{c,j}}{H_{m0,j}}\right)_{opt} = 0.59 \tag{7.10}$$

The analytically obtained value of the optimal relative crest freeboard (Eq. 7.10) is confirmed by plotting the hydraulic efficiency (Eq. 7.2) as a function of the relative crest freeboard for test results of the UG10 dataset, for example with slope angle $\cot\alpha = 1.4$ and a breaker parameter $\xi_{m-1,0} \approx 3.0$ (Fig. 7.1). The maximum hydraulic efficiency occurs for a relative crest freeboard $R_c / H_{m0} \approx 0.59$.

An adaptive relative crest freeboard implies that the crest freeboard of steep low-crested slopes is adapted for each sea state, based on the condition that $\left(R_{c,j} / H_{m0,j}\right)_{opt} = 0.59$.

Different existing prediction formulae could be used to predict the average overtopping rate, resulting in different values of the optimal relative crest freeboard. When Eq. (4.2b) is applied in zone Z3, an optimal relative crest freeboard of 1/2.6 = 0.38 is found. The larger value of $\left(R_{c,j} / H_{m0,j}\right)_{opt}$ in Eq. (7.10) is caused by the deviation of the test results of the UG10 dataset below the prediction line of Eq. (4.2b) for relative crest freeboards R_c / H_{m0} smaller than 0.80 (e.g. Fig. 5.19).

The optimal relative crest freeboard predicted based on Eq. (4.5) (Kofoed 2002), assuming the correction factors λ_{dr} and λ_{α} are equal to 1.0, is expected to be closer to 0.59, since this formula takes into account a deviation below Eq. (4.2b) for smaller relative crest freeboards, through the use of λ_s (Eq. 4.8). The optimal relative crest freeboard based on Eq. (4.5) is derived as follows:

$$\frac{d\left(\sqrt{g H_{m0,j}^3}\,\lambda_{s,j}\,0.2\exp\left((-2.6)\frac{R_{c,j}}{H_{m0,j}}\right)R_{c,j}\right)}{dR_{c,j}} = 0 \tag{7.11a}$$

$$\Rightarrow \left(R_{c,j} / H_{m0,j}\right)_{opt} = 0.48 \tag{7.11b}$$

The value of the optimal relative crest freeboard in Eq. (7.11b) is indeed larger than 0.38 and tends towards the value of 0.59 in Eq. (7.10).

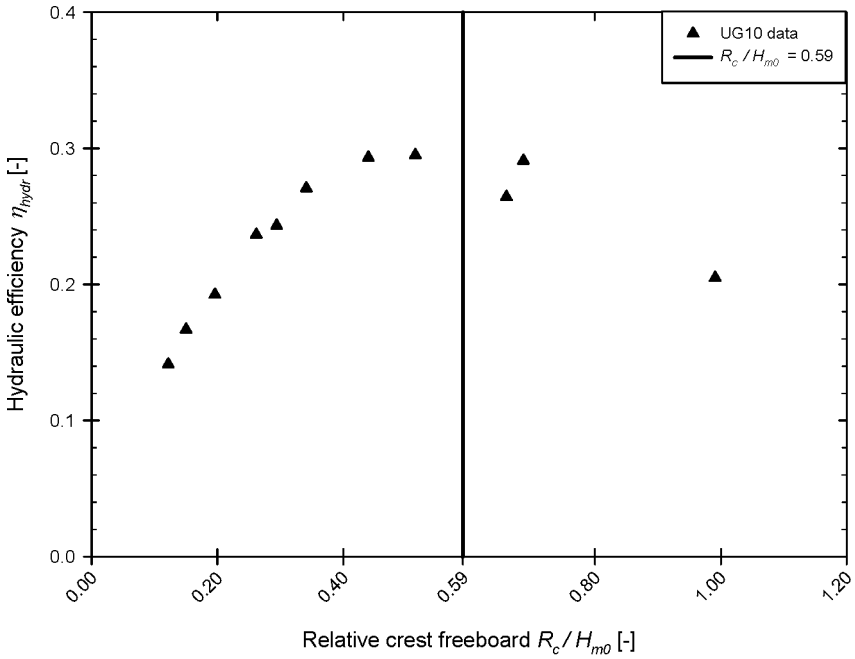

Figure 7.1: Hydraulic efficiency as a function of the relative crest freeboard, for test results of the UG10 dataset with $\cot\alpha = 1.4$ *and* $\xi_{m-1,0} = 3.0$.

7.2.4 Hydraulic efficiency for optimal geometry

Based on sections 7.2.2 and 7.2.3, the optimal geometry (resulting in maximum hydraulic power and efficiency for a particular sea state) is achieved when: $\tan\alpha_j = 3.0\sqrt{s_{m-1,0,j}}$ and $R_{c,j} / H_{m0,j} = 0.59$. Since the optimal geometry is clearly positioned in zone Z3, the point of optimal geometry corresponds to a dimensionless average overtopping rate expressed by (using Eq. 5.10):

$$\left(q_j / \sqrt{gH_{m0,j}^3}\right)_{opt} = 0.11\exp\left(-1.7 \cdot 0.59\right) = 0.04 \qquad (7.12)$$

This value of $q/\sqrt{gH_{m0}^3}$ is referred to as the *optimal dimensionless average overtopping rate*. The corresponding point of optimal geometry is indicated with a grey dot in Fig. 7.2 (similar to Fig. 5.17).

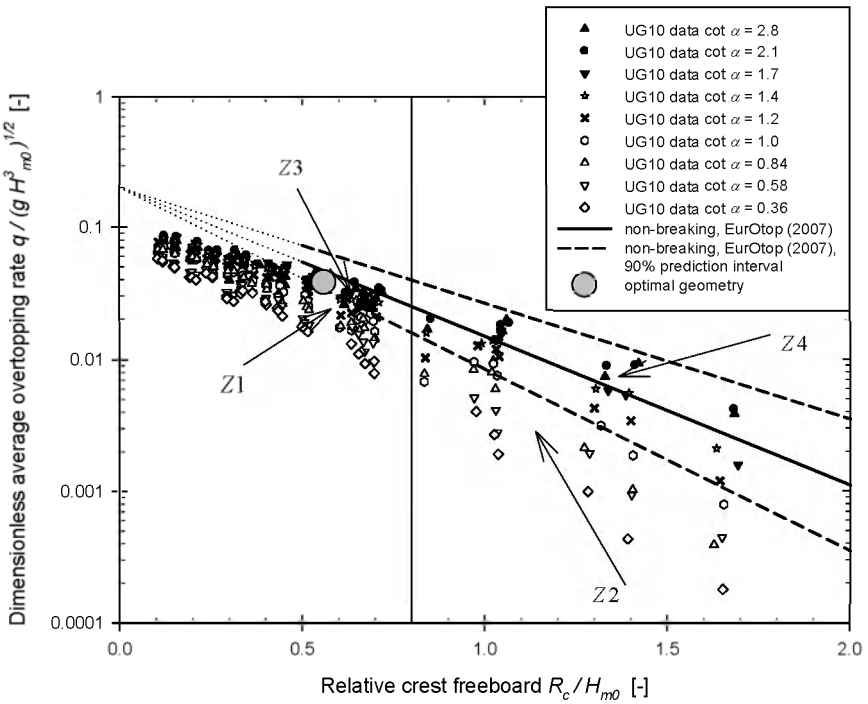

Figure 7.2: Dimensionless average overtopping rate (logarithmic scale) as a function of the relative crest freeboard (linear scale) for the test results of the UG10 dataset, with R_c / H_{m0} varying between 0.0 and 2.0. Indication of point of optimal geometry by grey dot.

Successively, the expression for the maximum hydraulic efficiency at the point of optimal geometry is derived as:

$$\left(\eta_{hydr,j}\right)_{opt} = \frac{\rho g\left[\sqrt{gH_{m0,j}^3}\,0.04\right]R_{c,j}}{\frac{\rho g^2}{64\pi}H_{m0,j}^2 T_{m-1,0,j}} \tag{7.13a}$$

$$= \frac{\left[\sqrt{H_{m0,j}}\,0.04\right]0.59}{\frac{\sqrt{g}}{64\pi}T_{m-1,0,j}} \tag{7.13b}$$

$$= 1.9\sqrt{s_{m-1,0,j}} \tag{7.13c}$$

It appears that the maximum hydraulic efficiency for a specific sea state only depends on the wave steepness of that sea state. When the waves are steeper, the maximum hydraulic efficiency will be larger.

7.2.5 Reflection coefficient for optimal geometry

The reflection coefficient $\left(K_{r,j}\right)_{opt}$ corresponding to the maximum hydraulic power and efficiency for a particular sea state is calculated based on Eq. (6.12):

$$\left(K_{r,j}\right)_{opt} = \left(0.37\cdot 0.59 + 0.67\right)\frac{\left(3.0\right)^2}{\left(3.0\right)^2 + 5.0} = 0.57 \tag{7.14}$$

This reflection coefficient is referred to as the *optimal reflection coefficient* and is visualized with a grey dot in Fig. 7.3 (similar to Fig. 6.5). Since the optimal reflection coefficient is still rather large, a proper toe protection needs to be applied at the toe of the OWECs studied in the PhD-research.

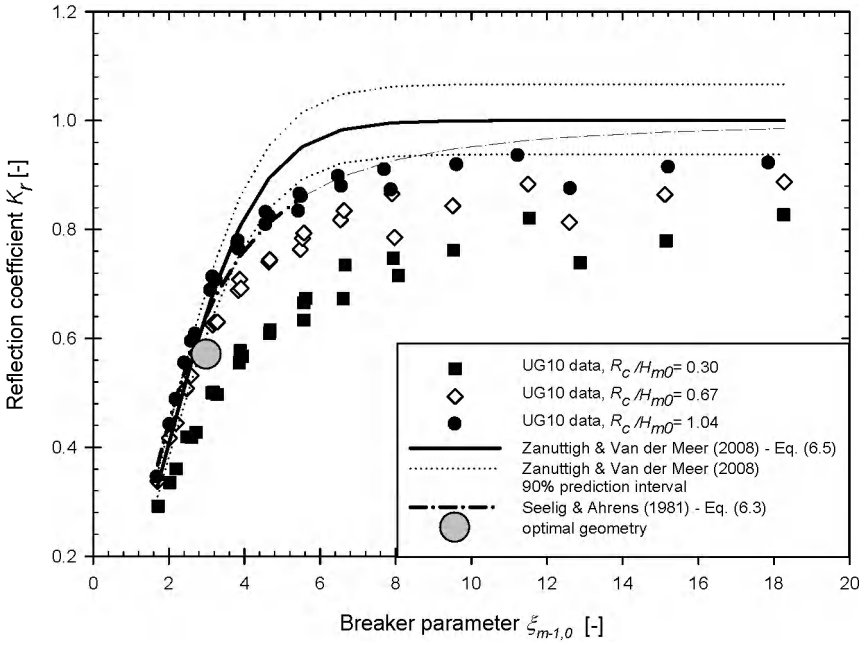

Figure 7.3: Reflection coefficient as a function of the breaker parameter for test results of the UG10 dataset. Indication of point of optimal geometry by grey dot.

7.3 Geometry control – different scenarios

Applying the optimal geometry (section 7.2) to the different characteristic sea states at a particular deployment site (i.e. geometry control in its strict sense) requires an adaptation of both the slope angle and crest freeboard to its optimal values for each sea state. The OWECs studied in this PhD-research however are less flexible concerning geometry control compared to floating OWECs. Hence, the realization of this adaptation is not straightforward.

Therefore, a number of additional geometry control scenarios are suggested. These scenarios violate the strict definition of geometry control, thus resulting in a hydraulic efficiency which is smaller than the maximum hydraulic efficiency derived in section 7.2.4. In total, five geometry control scenarios have been used in this PhD-research to investigate the effect of geometry control on the overall hydraulic efficiency and reflective behaviour of OWECs. Each of these scenarios is described below.

7.3.1 Scenario 1: Adaptive slope angle and adaptive crest freeboard (S1)

An optimal geometry is applied for each sea state: $\tan\alpha_j = 3.0\sqrt{s_{m-1,0,j}}$ and $R_{c,j} / H_{m0,j} = 0.59$ for each j. This scenario requires a vertical motion of the crest of the structure and a rotation of the slope independent of the crest freeboard (Fig. 7.4). The combination of these movements is not straightforward in practice.

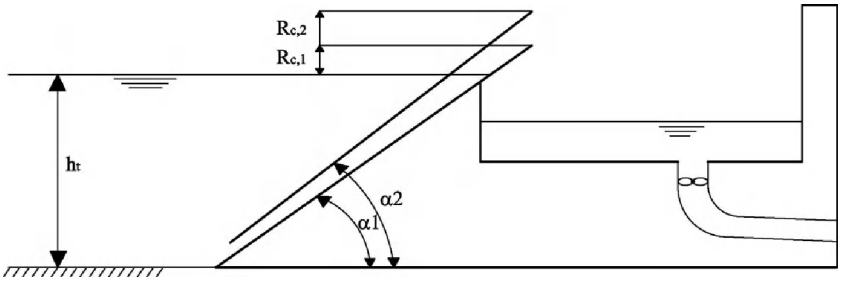

Figure 7.4: Scenario 1 - Geometry control by adaptive slope angle and adaptive crest freeboard (S1).

7.3.2 Scenario 2: Adaptive slope angle (S2)

In this scenario, only an adaptive slope angle is applied, fulfilling the condition $\tan\alpha_j = 3.0\sqrt{s_{m-1,0,j}}$, combined with a fixed crest freeboard (Fig. 7.5). The variation in slope angle is achieved by applying a hinge point at the crest of the slope. The value of the fixed crest freeboard is based on a maximization of the overall hydraulic power, as expressed in Eqs. (7.15) and (7.16).

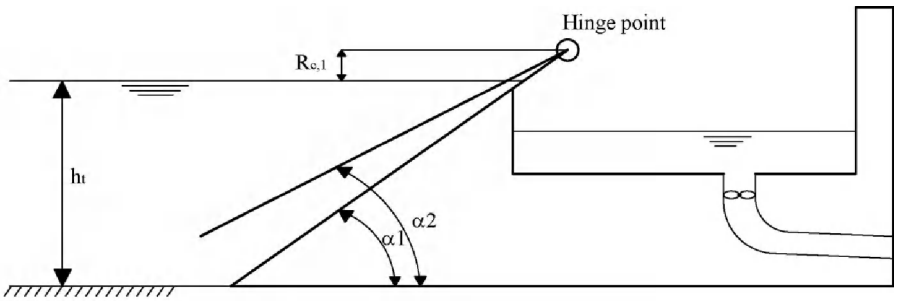

Figure 7.5: Scenario 2 - Geometry control by adaptive slope angle (S2).

$$\frac{dP_{hydr,overall}}{dR_c} = 0 \tag{7.15}$$

$$\Rightarrow \frac{d}{dR_c}\left(\sum_{j=1}^{N_{zz}} \rho g\, q_j\, R_c\, FO_j\right) = 0 \tag{7.16}$$

The fixed crest freeboard is not optimal for each sea state, and it is unclear whether the dimensionless average overtopping rate is located in zone Z3 or Z4. Taking into account the fulfilment of the condition $\tan\alpha_j = 3.0\sqrt{s_{m-1,0,j}}$ for scenario 2, the average overtopping rate is thus expressed by:

$$q_j = A_j \exp\left(B_j \frac{R_c}{H_{m0,j}}\right)\sqrt{g H_{m0,j}^3} \tag{7.17}$$

The coefficients A_j and B_j depend on the sea state and therefore are given the subscript j. When $R_{c,j}/H_{m0,j} \leq 0.8$, $A_j = 0.11$ and B_j = -1.7, while $A_j = 0.2$ and B_j = -2.4 when $R_{c,j}/H_{m0,j} > 0.8$. Hence, Eq. (7.16) can be rewritten as:

$$\frac{d}{dR_c}\left(\sum_{j=1}^{N_{ss}}\left[A_j \exp\left(B_j \frac{R_c}{H_{m0,j}}\right)\right]\sqrt{g H_{m0,j}^3} R_c FO_j\right) = 0 \tag{7.18}$$

$$\Rightarrow \sum_{j=1}^{N_{ss}} q_j FO_j \left[B_j \frac{R_c}{H_{m0,j}} + 1\right] = 0 \tag{7.19}$$

The fixed crest freeboard for scenario 2 is found by solving Eq. (7.19) for R_c, using numerical methods that are implemented in MS Excel© (Solver add-in) and in Maple™ (fsolve function).

The resulting fixed crest freeboard is largely determined by the sea states with the largest products $FO_j P_{wave,j}$ and approaches the optimal crest freeboards for those sea states relatively closely.

7.3.3 Scenario 3: Adaptive crest freeboard (S3)

This scenario combines a fixed slope angle with the optimal crest freeboard for each sea state, i.e. fulfilling the condition $R_{c,j}/H_{m0,j} = 0.59$ (Fig. 7.6).

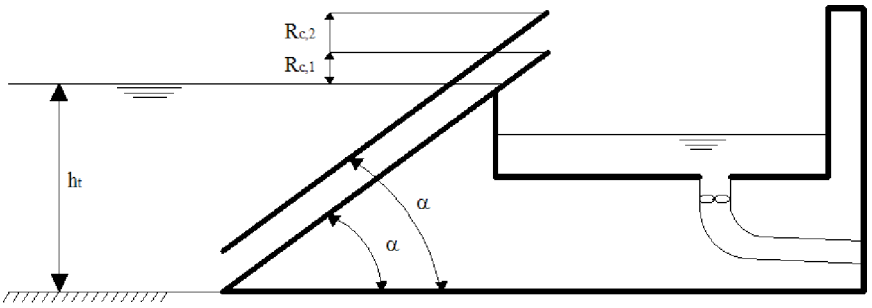

Figure 7.6: Scenario 3 - Geometry control by adaptive crest freeboard (S3).

The value of the fixed slope angle is determined by maximizing the overall hydraulic power (Eq. 7.20 and Eq. 7.21).

$$\frac{dP_{hydr,overall}}{d\tan\alpha} = 0 \tag{7.20}$$

$$\Rightarrow \frac{d}{d\tan\alpha}\left(\sum_{j=1}^{N_{SS}} \rho g\, q_j\, R_{c,j}\, FO_j\right) = 0 \tag{7.21}$$

The fixed slope angle is not optimal for each sea state. However, since the optimal slopes for each of the different sea states range between $\cot\alpha = 1.5$ and $\cot\alpha = 3.0$ roughly, the differences between the optimal slope angles and the fixed slope angle for scenario 3 are relatively small. Hence, the expression for the average overtopping rate of zone Z3 applies for scenario 3. Consequently, Eq. (7.21) can be rewritten as:

$$\Rightarrow \sum_{j=1}^{N_{SS}}\left[0.11\exp\left(-1.7\frac{R_{c,j}}{H_{m0,j}}\right)\right] R_{c,j}\, FO_j \sqrt{g\, H_{m0}^3}\, \frac{d}{d\tan\alpha}\left(\cos\left(\frac{\frac{\tan\alpha}{\sqrt{s_{m-1,0,j}}} - 3.0}{3.0}\right)\right)^3 = 0 \tag{7.22}$$

$$\Rightarrow \sum_{j=1}^{N_{SS}} q_j\, FO_j \left[\frac{R_{c,j}}{\sqrt{s_{m-1,0,j}}}\left(-\tan\left(\frac{\frac{\tan\alpha}{\sqrt{s_{m-1,0,j}}} - 3.0}{3.0}\right)\right)\right] = 0 \tag{7.23}$$

The fixed slope angle for scenario 3 is found by solving Eq. (7.23) for $\tan\alpha$, using numerical methods (MS Excel© and Maple™). Intrinsically, the fixed slope angle is determined by the sea states with the largest values of $FO_j\, P_{wave,j}$.

Although this geometry control strategy is more simple than scenario 1, realizing the vertical movement of the crest of the slope required for scenario 3 is also not straightforward in practice.

7.3.4 Scenario 4: Fixed slope angle and fixed crest freeboard (S4)

No geometry control is applied in this particular scenario (Fig. 7.7).

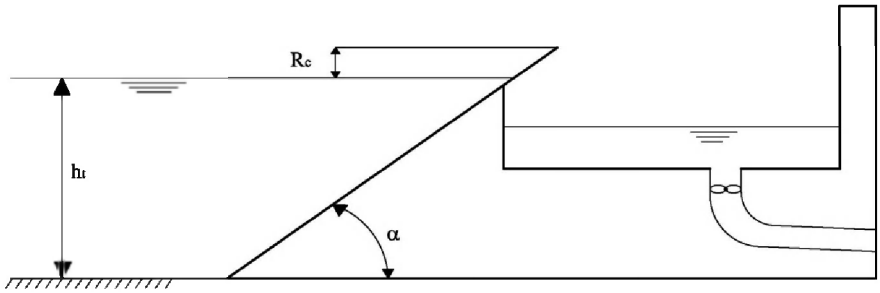

Figure 7.7: Scenario 4 - No geometry control – Fixed slope angle and fixed crest freeboard (S4).

The values of the fixed slope angle and crest freeboard are determined by maximizing the overall hydraulic efficiency. This means that the partial derivatives of the overall hydraulic power for the slope angle and the crest freeboard should be zero (Eq. 7.24).

$$\begin{cases} \dfrac{\partial}{\partial \tan\alpha}\left(\sum_{j=1}^{N_{sg}} \rho g\, q_j\, R_c\, FO_j\right) = 0 \\ \dfrac{\partial}{\partial R_c}\left(\sum_{j=1}^{N_{sg}} \rho g\, q_j\, R_c\, FO_j\right) = 0 \end{cases} \tag{7.24}$$

Based on Eq. (7.19) and Eq. (7.23), this system can be rewritten as:

$$\begin{cases} \sum_{j=1}^{N_{sg}} q_j\, FO_j \left[\dfrac{R_c}{\sqrt{s_{m-1,0,j}}} \left(-\tan\left(\dfrac{\dfrac{\tan\alpha}{\sqrt{s_{m-1,0,j}}} - 3.0}{3.0} \right) \right) \right] = 0 \\ \sum_{j=1}^{N_{sg}} q_j\, FO_j \left[B_j \dfrac{R_c}{H_{m0,j}} + 1 \right] = 0 \end{cases} \tag{7.25}$$

The fixed slope angle and crest freeboard for scenario 4 are found by solving the system in Eq. (7.25) for $\tan\alpha$ and R_c. This system can be solved using numerical methods, based on a minimization of the sum of squares in the left hand sides of the two equations in the system.

7.3.5 Scenario 5: Adaptive crest freeboard, hinge at bottom (S5)

In this scenario, the adaptive crest freeboard is realized by using a hinge point at the bottom of the slope (Fig. 7.8), which results in a combined control of the slope angle and the crest freeboard.

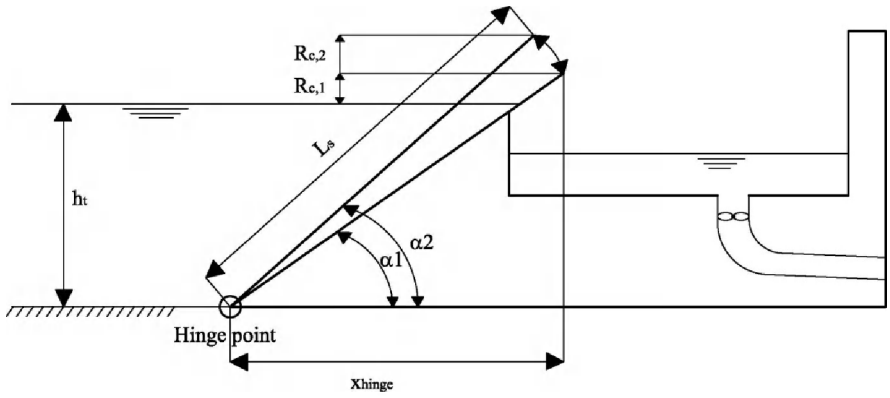

Figure 7.8: Scenario 5 - Geometry control by installing a hinge point at the bottom of the slope – determining parameters (S5).

An increase in wave height results in an increase of the optimal crest freeboard (Eq. 7.10) ($R_{c,1}$ to $R_{c,2}$) and, in correspondence to Fig. 7.8, the slope becomes steeper (α_1 to α_2). Since an increase in wave height also corresponds to an increase of the optimal slope angle (Eq. 7.4), the installation of the hinge at the bottom of the slope has a positive effect on the overall hydraulic efficiency.

The slope angles are directly related to the length of the slope, denoted by L_s, through Eq. (7.26) or Eq. (7.27), based on trigonometry.

$$\sin\alpha_j = \frac{h_t + R_{c,j}}{L_s} \tag{7.26}$$

$$\tan\alpha_j = \frac{h_t + R_{c,j}}{\sqrt{L_s^2 - \left(h_t + R_{c,j}\right)^2}} \tag{7.27}$$

The fixed slope length is determined by maximizing the overall hydraulic power. Accordingly, the constant value of L_s is determined by setting the derivative equal to zero (Eq. 7.28 and Eq. 7.29), similar to sections 7.3.2 and 7.3.3.

$$\frac{dP_{hydr,overall}}{dL_s} = 0 \tag{7.28}$$

$$\Rightarrow \frac{d}{dL_s}\left(\sum_{j=1}^{N_{SS}} \rho g\, q_j\, R_{c,j}\, FO_j\right) = 0 \tag{7.29}$$

Applying the expression for the average overtopping rate for zone Z3 (similar reasoning as for scenario 3) and taking into account Eq. (7.27), Eq. (7.29) can be rewritten as:

$$\Rightarrow \sum_{j=1}^{N_{SS}}\left[0.11\exp\left(-1.7\frac{R_{c,j}}{H_{m0,j}}\right)\right] R_{c,j}\, FO_j \sqrt{g\, H_{m0,j}^3}\, \frac{d}{dL_s}\left(\cos\left(\frac{\dfrac{h_t + R_{c,j}}{\sqrt{L_s^2 - \left(h_t + R_{c,j}\right)^2}\sqrt{s_{m-1,0,j}}} - 3.0}{3.0}\right)\right)^3 = 0 \tag{7.30}$$

$$\Rightarrow \sum_{j=1}^{N_{SS}} q_j\, FO_j \left[\frac{R_{c,j}\left(h_t + R_{c,j}\right) L_s}{\left(L_s^2 - \left(h_t + R_{c,j}\right)^2\right)^{3/2}\sqrt{s_{m-1,0,j}}}\left(\tan\left(\frac{\dfrac{h_t + R_{c,j}}{\sqrt{L_s^2 - \left(h_t + R_{c,j}\right)^2}\sqrt{s_{m-1,0,j}}} - 3.0}{3.0}\right)\right)\right] = 0 \tag{7.31}$$

The fixed slope length for scenario 5 is found by solving Eq. (7.31) for L_s, using numerical methods.

Once the fixed slope length is known, the position of the hinge point is determined by using the smallest crest freeboard $R_{c,1}$ (corresponding to sea state 1):

$$x_{hinge} = \sqrt{L_s^2 - \left(h_t + R_{c,1}\right)^2} \tag{7.32}$$

The origin of the horizontal distance x_{hinge} is positioned at the intersection of the vertical line through the crest of the slope corresponding to sea state 1 and the sea bottom (Fig. 7.8).

7.3.6 Overview of scenarios

The following table summarizes the characteristics of the five scenarios described above:

Table 7.1: Characteristics of the five scenarios of geometry control.

Scenario No.	Acronym	Slope angle	Crest freeboard
1	S1	Adaptive	Adaptive
2	S2	Adaptive	Fixed
3	S3	Fixed	Adaptive
4	S4	Fixed	Fixed
5	S5	Linked to crest freeboard	Adaptive

7.4 Application to a number of hypothetical deployment sites

Each of the five scenarios described in section 7.3 has been applied to a number of hypothetical deployment sites (section 7.4.1), in order to study the effect of geometry

control on the overall hydraulic efficiency (section 7.4.3), overall hydraulic power (section 7.4.4) and reflective behaviour (section 7.4.5) of OWECs. Since scenario 4 corresponds to a fixed geometry, the outcomes of the four other scenarios are compared to that scenario.

The simulations for the three possible deployments sites are based on the formulae derived in section 7.3, which are based on the formulae in chapters 5 and 6. It is again emphasized that those formulae only apply for sheltered areas, since the values of the wave steepness used during the UG10 test series are only valid for wind seas (see chapter 3). This means that the formulae are not applicable to OWECs positioned in swells.

7.4.1 Chosen deployment sites

Three nearshore locations have been chosen (Table 7.2): Ostend (Belgian Continental Shelf), MPN (Dutch Continental Shelf) and Fjaltring (Danish Continental Shelf). All three locations are located relatively close to shore, in areas which are not exposed to large swells due to the sheltering effect of the UK from large period ocean waves.

Table 7.2: Important characteristics for three possible deployment sites.

Deployment Site	**Average Annual available wave power [kW/m]**	**Mean water depth [m]**	**Shortest distance to shore [km]**	**Data acquisition period**
Ostend, BE	1.66	6	1	1997-2005
MPN, NL	5.42	18	8	1979-2002
Fjaltring, DK	7.00	20	4	1979-1993

Research on the wave characteristics for these three locations has been carried out based on the analysis of signals of wave measurement equipment. The acquisition periods for the wave data used below for the three possible deployment sites are added to Table 7.2.

The average annual available wave power in Ostend is rather low (i.e. 1.66 kW/m), while the wave power at MPN and Fjaltring is larger (i.e. 5.42 kW/m and 7.00 kW/m).

Omni-directional annual average scatter diagrams are available for each deployment site. The methodology explained in section 3.1 to determine the characteristic sea states based on a scatter diagram has been applied for each location. These sea states are given below in Table 7.3 (Ostend), Table 7.4 (MPN) and Table 7.5 (Fjaltring). The energy period $T_{m-1,0}$ is taken for the wave period characterizing the sea states instead of the peak period T_p (Table 3.1), since the energy period is incorporated in the prediction formulae from chapters 5 and 6. Note that for all deployment sites, the sea states with the smallest wave power are most dominantly present. The sea states with the largest power only occur during a limited amount of time.

Table 7.3: Characteristic sea states for location on the Belgian Continental Shelf (Ostend), h_t = 6 m, source scatter diagram: Flemish Ministry of Transport and Public Works, Agency for Maritime and Coastal Services – Coastal Division.

ID Sea state j	**1**	**2**	**3**	**4**	**5**
$H_{m0,j}$ [m]	0.25	0.75	1.25	1.75	2.25
$T_{m-1,0}$ [s]	4.19	4.60	5.18	5.94	6.59
$P_{wave,j}$ [kW/m]	0.1	1.2	3.9	8.7	16.0
FO_j [%]	49.20	35.89	10.12	3.08	1.18
$s_{m-1,0,j}$ [-]	0.009	0.023	0.030	0.032	0.033

Table 7.4: Characteristic sea states for location on the Dutch Continental Shelf (MPN), $h_t = 18m$, source scatter diagram: Rijkswaterstaat (2010).

ID Sea state j	**1**	**2**	**3**	**4**
$H_{m0,j}$ [m]	0.5	1.5	2.5	3.5
$T_{m-1,0}$ [s]	4.62	5.49	6.49	7.46
$P_{wave,j}$ [kW/m]	0.55	5.91	19.41	43.76
FO_j [%]	59.84	30.42	7.70	1.64
$s_{m-1,0,j}$ [-]	0.015	0.032	0.038	0.040

Table 7.5: Characteristic sea states for location on Danish Continental Shelf (Fjaltring), $h_t = 20m$, source scatter diagram: RAMBØLL et al. (1999).

ID Sea state j	1	2	3	4	5	6	7	8
$H_{m0,j}$ [m]	0.25	0.75	1.25	1.75	2.25	2.75	3.25	3.75
$T_{m-1,0}$ [s]	3.76	4.56	5.19	5.94	6.56	7.34	7.78	8.41
$P_{wave,j}$ kW/m]	0.1	1.3	4.0	8.9	16.3	27.2	40.3	58.0
FO_j [%]	20.8	31.5	20.1	11.9	7.1	4.4	2.5	1.2
$s_{m-1,0,j}$ [-]	0.011	0.023	0.030	0.032	0.033	0.033	0.034	0.034

Note that in reality a variation of the still water level (SWL) occurs at these three hypothetical deployment sites due to tides. The case study in this chapter omits any tidal variation and therefore is merely an academic exercise. The presence of a tidal change of the SWL may result in a considerable reduction of the power output of fixed OWECs (Margheritini 2009).

7.4.2 Fixed geometry components for scenarios 2 to 5

In order to derive the overall hydraulic efficiency $\eta_{hydr,overall}$ and overall hydraulic power $P_{hydr,overall}$ for scenarios 2 to 5, the fixed geometry components for these scenarios were determined based on the formulae in section 7.3 (Table 7.6).

The values of the geometrical parameters in Table 7.6 are largely determined by the approximate fulfilment of the optimal conditions $\tan\alpha_j = 3.0\sqrt{s_{m-1,0,j}}$ and $R_{c,j}/H_{m0,j} = 0.59$ for the sea states with the largest values of $FO_j P_{wave,j}$. The differences between the three locations are thus explained based on parameters that represent the wave characteristics of the sea states with the largest $FO_j P_{wave,j}$ for a particular location. Therefore, a sea state averaged wave height (Eq. 7.33) and a sea state averaged wave steepness (Eq. 7.34) have been defined. The corresponding values for the three possible deployment sites are given in Table 7.7.

Table 7.6: Fixed geometrical parameters for scenarios 2 to 5 at the three possible deployment sites.

Deployment Site	**Fixed crest freeboard scenario 2 [m]**	**Cotangent fixed slope angle scenario 3 [-]**	**Fixed crest freeboard scenario 4 [m]**	**Cotangent fixed slope angle scenario 4 [-]**	**Fixed slope length scenario 5 [m]**
Ostend, BE	0.64	2.04	0.64	2.00	17.39
MPN, NL	1.05	1.78	1.07	1.79	39.81
Fjaltring, DK	1.17	1.87	1.17	1.85	39.85

$$\widehat{H}_{m0} = \sum_{j=1}^{N_{SS}} \frac{FO_j P_{wave,j}}{\sum_{j=1}^{N_{SS}} FO_j P_{wave,j}} H_{m0,j} \tag{7.33}$$

$$\widehat{s}_{m-1,0} = \sum_{j=1}^{N_{SS}} \frac{FO_j P_{wave,j}}{\sum_{j=1}^{N_{SS}} FO_j P_{wave,j}} s_{m-1,0,j} \tag{7.34}$$

Table 7.7: Sea state averaged wave height and wave steepness for different test locations.

Deployment Site	$\widehat{H}_{m0}$	$\widehat{s}_{m-1,0}$
Ostend, BE	1.28	0.027
MPN, NL	2.03	0.034
Fjaltring, DK	5.20	0.032

In accordance to Eq. (7.4), a larger sea state averaged wave steepness should correspond to a larger value of the fixed slope angle. Furthermore, based on Eq. (7.10)

an increase in the sea state averaged wave height is expected to cause an increase in the fixed relative crest freeboard. This is confirmed when Table 7.6 and Table 7.7 are compared. The fixed crest freeboard increases when moving from Ostend to MPN and to Fjaltring, both for scenarios 2 and 4, corresponding to the increase in sea state averaged wave height shown in Table 7.7. The optimal slope angle varies together with the sea state averaged wave steepness (Table 7.7) for the scenarios 3 and 4.

The optimal slope length is related to the slope angle and the crest freeboard (Eqs. 7.26 and 7.27) and consequently depends on both the sea state averaged wave height and wave steepness. The combination of both parameters results in an increase in optimal slope length from Ostend to MPN, and in a small increase in optimal slope length from MPN to Fjaltring.

Furthermore, it appears that the optimal crest freeboard and slope angle of scenario 4 (fixed slope angle and crest freeboard) are approximately equal to the crest freeboard of scenario 2 (fixed crest freeboard) and the optimal slope angle of scenario 3 (fixed slope angle) respectively. Both similarities are due to the limited effect of the slope angle on the average overtopping rate (and thus on the overall hydraulic efficiency and power) in zones Z3 and Z4 (see chapter 5).

7.4.3 Effect of different geometry control scenarios on overall hydraulic efficiency

The overall hydraulic efficiency has been calculated based on Eq. (7.1) for each of the five scenarios at the possible deployment sites. The resulting graph for Ostend is shown in Fig. 7.9.

The mean overall hydraulic efficiency corresponding to the fixed geometry of scenario 4 is 24.2 % for the deployment site in Ostend. Applying an adaptive slope angle (S2) increases the mean overall hydraulic efficiency up to 24.5 %, while applying an adaptive crest freeboard (S3) results in a mean efficiency of 26.3 %. This shows that the effect of an adaptive crest freeboard on the overall hydraulic efficiency is larger than the effect of an adaptive slope angle. This observation can be explained by the weak dependency of the average overtopping rate on the slope angle in the zone around the optimal slope angle. The slope angle of the fixed geometry deviates from the optimal slope angle, but since the effect of the slope angle on the average overtopping rate is rather small, the effect of this deviation is limited compared to the effect of deviations in crest freeboard. The mean overall hydraulic efficiency can be further increased by applying an adaptive crest freeboard with a hinge at the bottom of the slope (S5), up to 26.7 %. This value is larger than the value obtained in scenario 3 due to the positive effect of the slope angle.

The largest mean overall hydraulic efficiency is achieved when combining an adaptive slope angle and an adaptive crest freeboard (S1): 27.1 %.

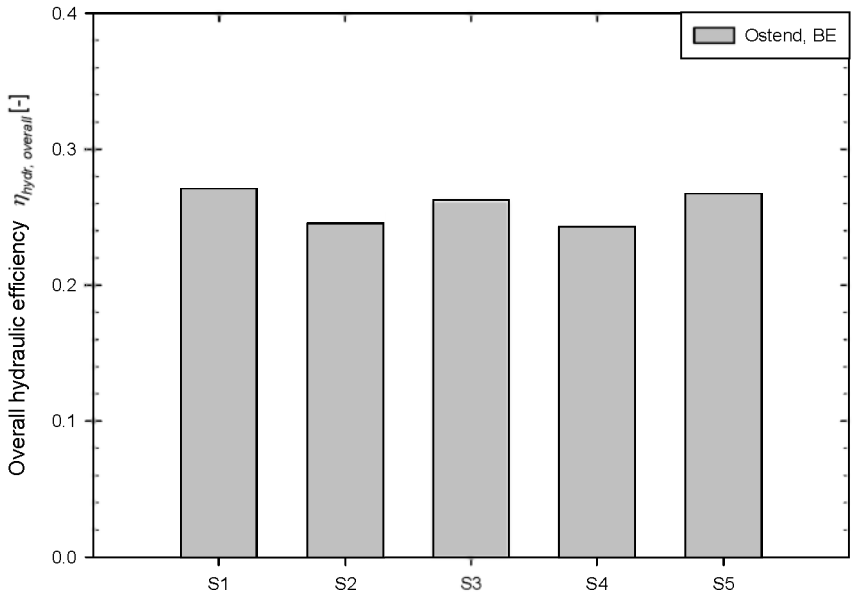

Figure 7.9: Comparison between effects of five scenarios on the overall hydraulic efficiency for test site in Ostend, Belgian Continental Shelf.

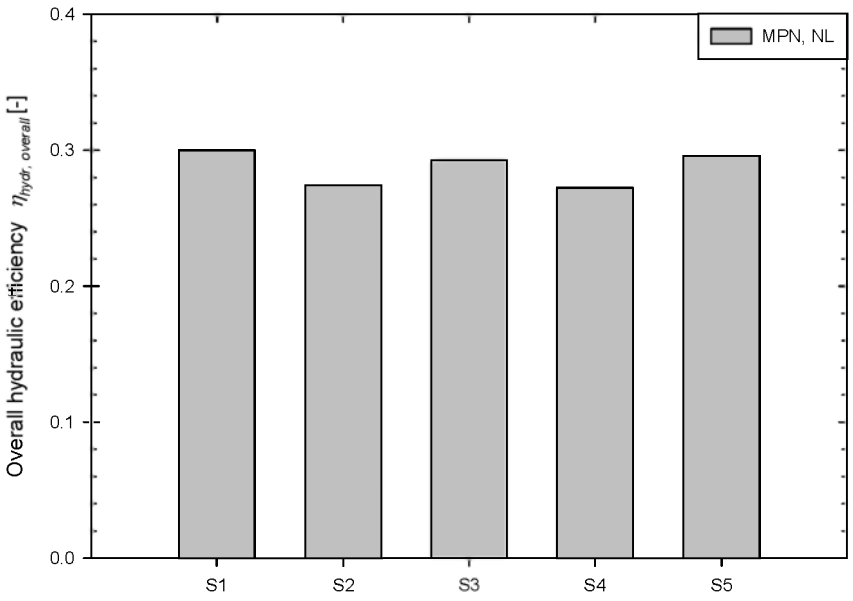

Figure 7.10: Comparison between effects of five scenarios on the overall hydraulic efficiency for test site at MPN, Dutch Continental Shelf.

Similar graphs have been generated for the possible deployment sites at MPN, NL (Fig. 7.10), and Fjaltring, DK (Fig. 7.11). Based on these figures, the conclusions for the other two sites are similar to the conclusions for Ostend. The general conclusion thus is drawn that an adaptive crest freeboard increases the overall hydraulic efficiency considerably, while an adaptive slope angle only has a small effect. Similar conclusions are expected to be valid for the overall hydraulic power. Since power is more tangible than efficiency, the gain in overall hydraulic power by using geometry control is explicitly studied in section 7.4.4.

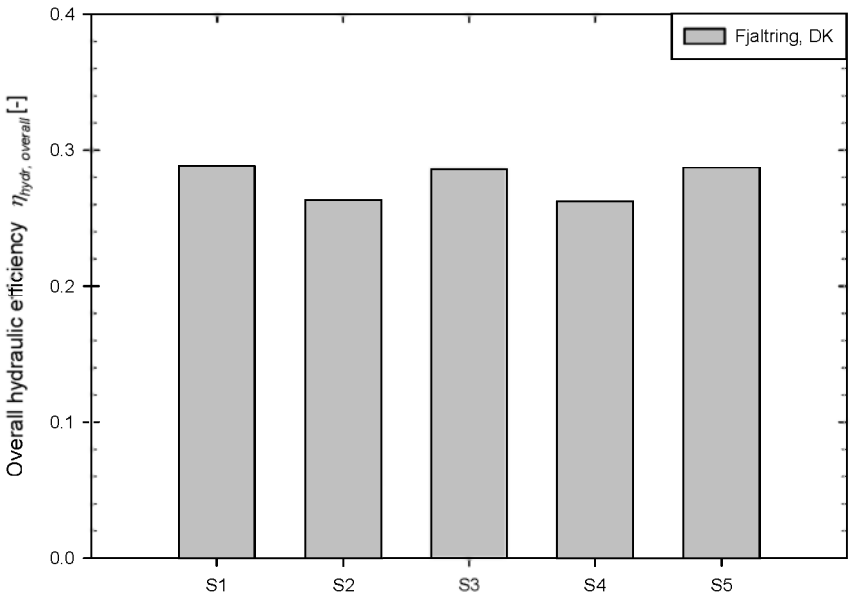

Figure 7.11: Comparison between effects of five scenarios on the overall hydraulic power for test site in Fjaltring, Danish Continental Shelf.

The difference in mean overall hydraulic efficiency for scenario 1 between the different deployment sites is shown in Fig. 7.12. It appears that the mean overall hydraulic efficiency increases when moving from Ostend to MPN, while it slightly decreases when moving from MPN to Fjaltring. This trend is similar to the trend of the sea state averaged wave steepness (Table 7.7). The relationship between the wave steepness and the overall hydraulic efficiency for scenario 1 is given in Eq. 7.13c, explaining the differences in Fig. 7.12.

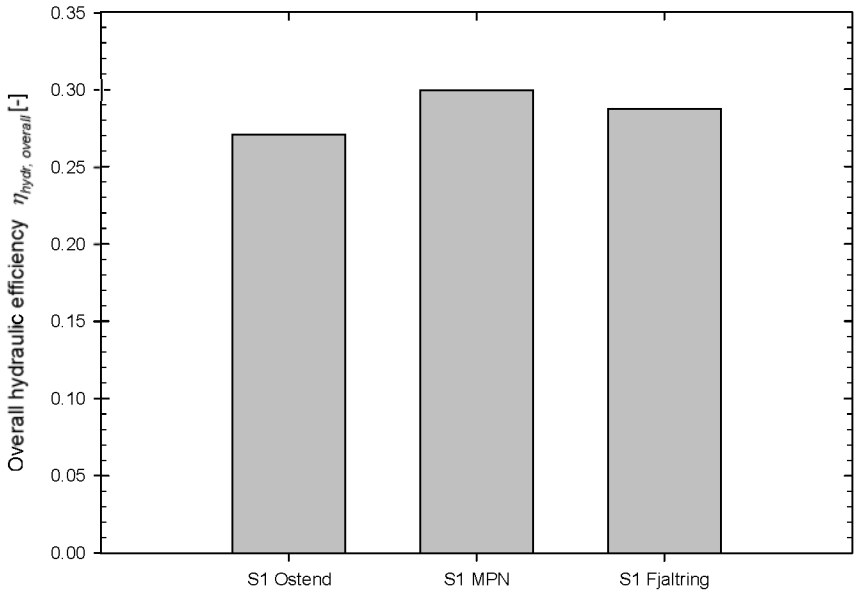

Figure 7.12: Comparison between mean overall hydraulic efficiency of scenario 1 for test sites in Ostend, MPN and Fjaltring.

7.4.4 Effect of different geometry control scenarios on overall hydraulic power

The mean overall hydraulic power obtained based on Eq. 7.34 for each of the scenarios is shown in Fig. 7.13 for the deployment site in Ostend. The mean overall hydraulic power for scenario 4 equals 0.33 kW/m. Compared to this fixed geometry, applying an adaptive slope angle increases the mean power only slightly, while applying an adaptive crest freeboard increases the mean power by 8 % up to 0.36 kW/m. This confirms that the relative crest freeboard has a larger effect than the slope angle around its optimum. The gained mean overall hydraulic power can be further increased by applying an adaptive crest freeboard with a hinge at the bottom of the slope (scenario 5) due to the positive effect of the slope angle. The increase is

10 % compared to the fixed scenario. The largest mean overall hydraulic power is achieved when an adaptive slope angle is combined with an adaptive crest freeboard. The power is increased by 12% to 0.37 kW/m.

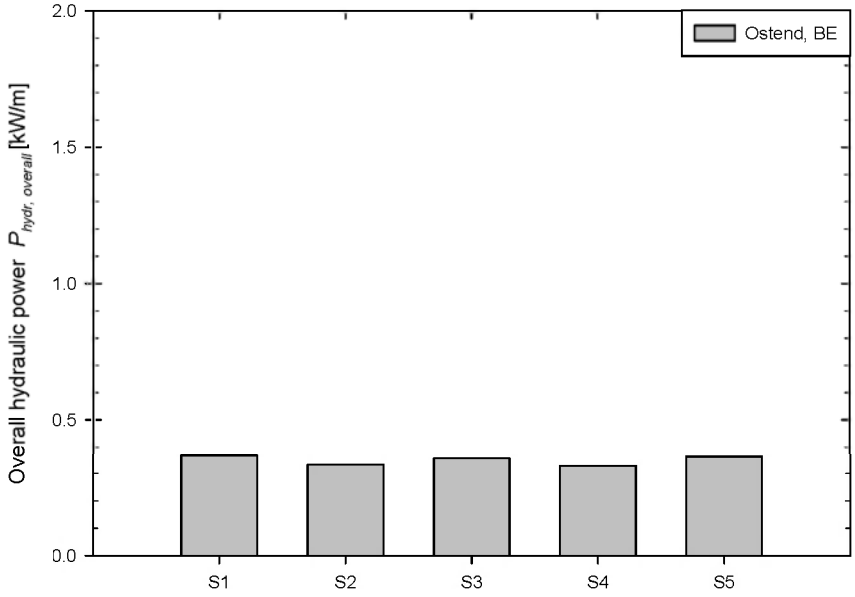

Figure 7.13: Comparison between effects of five scenarios on the overall hydraulic power for test site in Ostend, Belgian Continental Shelf.

Similar graphs have been generated for the deployment sites at MPN, NL (Fig. 7.14) and Fjaltring, DK (Fig. 7.15). The conclusions are similar to the conclusions for Ostend. Scenario 5 corresponds to an increase in mean overall hydraulic power by 10 % compared to the fixed scenario for the test locations at MPN and Fjaltring. For all three hypothetical deployment sites, the increase in power by scenario 1 is only slightly larger than the increase by scenario 5. Hence, scenario 5 (with the hinge at the bottom of the slope) is the best practically realizable scenario.

It should be noted that the increase in mean overall hydraulic power achieved by geometry control is relatively small. It is clear that adding reservoirs to the OWEC can increase the gain in power more considerably (Margeritini 2009).

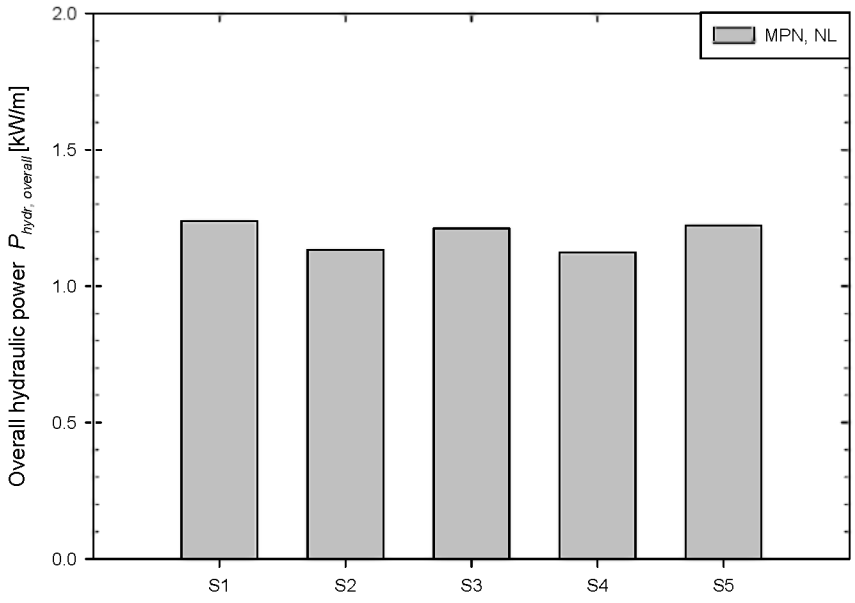

Figure 7.14: Comparison between effects of five scenarios on the overall hydraulic power for test site at MPN, Dutch Continental Shelf.

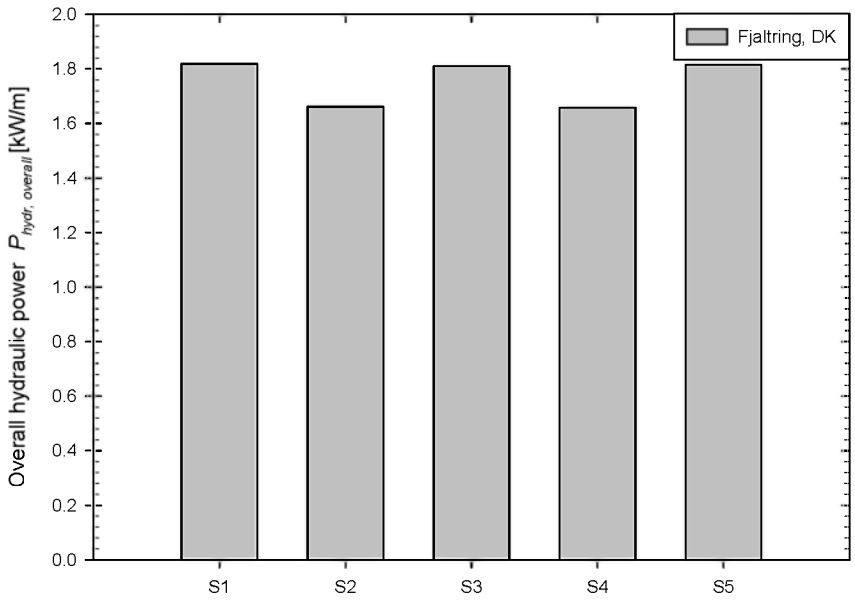

Figure 7.15: Comparison between effects of five scenarios on the overall hydraulic power for test site in Fjaltring, Danish Continental Shelf.

In order to have an idea about the obtained hydraulic power of the OWECs considered in this PhD-manuscript, the following two graphs were generated. The increase in overall hydraulic efficiency between the traditional scenario (scenario 4) and scenario 5 is shown in Fig. 7.16 for all three possible deployment sites. For example when deploying an OWEC in Fjaltring, applying scenario 5 increases the mean overall hydraulic power from 1.66 kW/m (scenario 4) to 1.81 kW/m. This means, for an OWEC with a length of 100 m (Fig. 7.17), that applying a hinge at the bottom of the slope results in an obtained power of approximately 181 kW instead of 166 kW. In Ostend, the maximum obtained hydraulic power for an OWEC with a length of 100 m is approximately 36 kW (the obtained overall hydraulic power for scenario 4 is 33 kW).

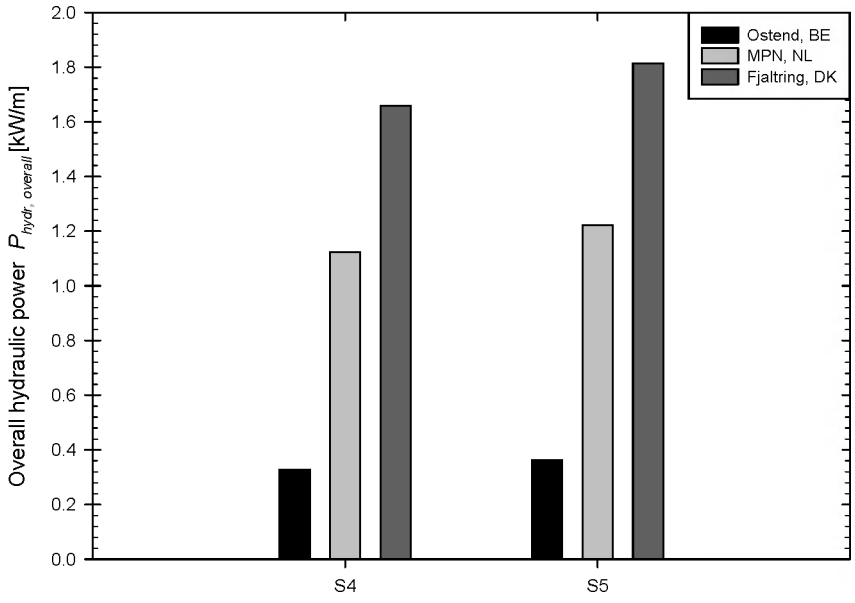

Figure 7.16: Comparison between overall hydraulic power for scenario 4 and 5 at all three test sites.

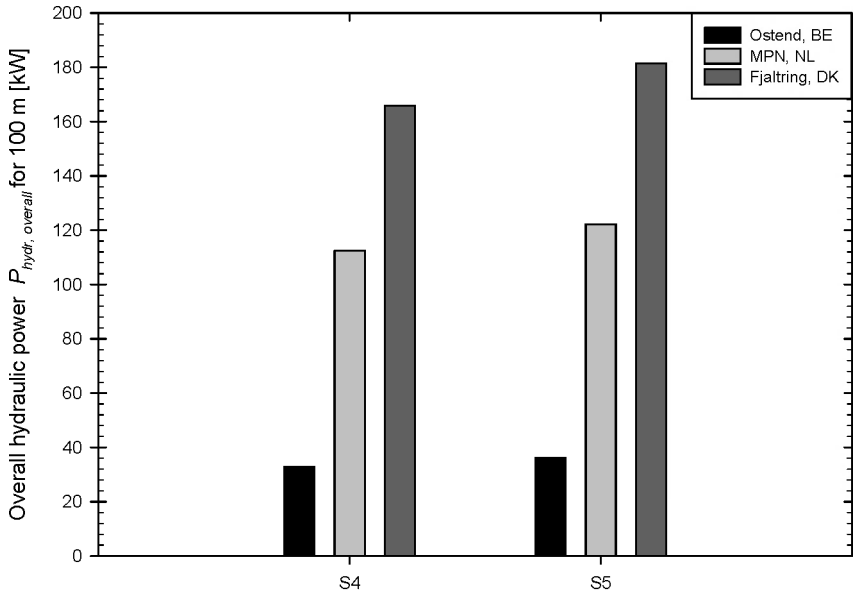

Figure 7.17: Comparison between overall hydraulic power [kW] gathered over a length of 100 m for scenario 4 and 5 at all three test sites.

7.4.5 Effect of different geometry control scenarios for reflective behaviour

In order to study the effect of the different geometry control scenarios on the reflective behaviour of OWECs, a representative overall reflection coefficient $K_{r,overall}$ needs to be chosen. By weighing the reflection coefficients for each sea state with the corresponding frequency of occurrence, Eq. (7.35), the value of $K_{r,overall}$ represents the reflection coefficients of the sea states which occur most often in time.

$$K_{r,overall} = \sum_{j=1}^{N_{ss}} K_{r,j}\, FO_j \tag{7.35}$$

This approach is used since these sea states affect most the wave field near the harbour entrance in which the OWECs are installed. A steady wave climate is very important for ships to enter the harbour safely, particularly in the less energetic but more frequent sea states.

As pointed out in section 7.2.5, the value of the reflection coefficient corresponding to scenario 1 equals 0.57. This is confirmed by Fig. 7.18, which shows the overall reflection coefficient as a function of the five scenarios for the deployment site in Ostend, BE.

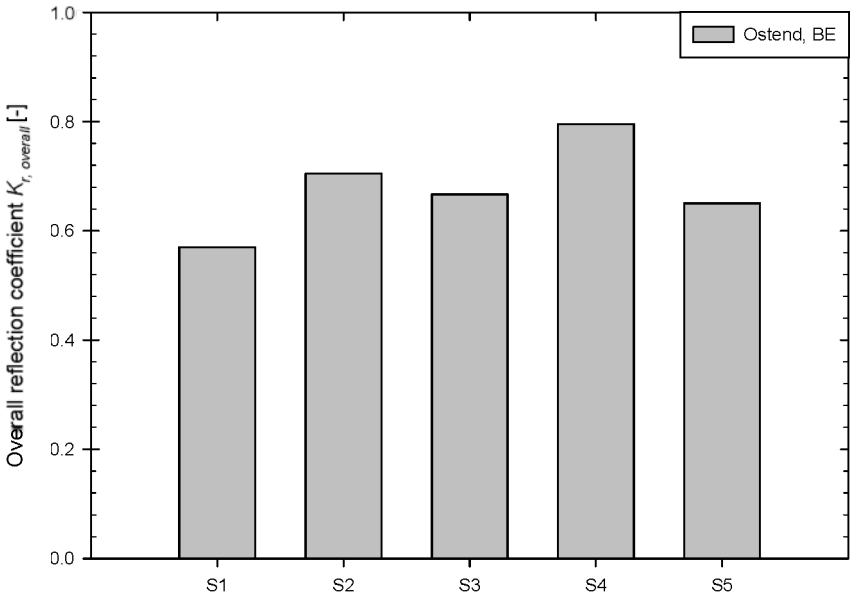

Figure 7.18: Comparison between effects of five scenarios on the overall reflection coefficient [-] for the test site in Ostend, BE.

The overall reflection coefficient for the deployment site in Ostend appears to increase for the other scenarios. Moreover, it is larger when more geometrical parameters are fixed, reaching a maximum of approx. 0.80 for scenario 4 (the fixed scenario). Correspondingly, the values of $K_{r,overall}$ for scenario 5 (which features an

adaptive crest freeboard and an accordingly variable slope angle) are only slightly larger than those for scenario 1 (approximately 0.60).

Furthermore, an adaptive crest freeboard causes a smaller increase in $K_{r,overall}$ than an adaptive slope angle. This is in accordance with the larger gain in power output when applying an adaptive crest freeboard compared to an adaptive slope angle, as discussed in section 7.4.4.

A comparison between the mean overall reflection coefficients for the three test sites is carried out in Fig. 7.19. The behaviour seen in Fig. 7.18 appears to be generally valid for all test sites. Since the overall reflection coefficients for the sea states with the largest frequencies of occurrence are still rather large for each of geometry control scenarios, a proper toe protection needs to be applied at the toe of the OWECs studied in the PhD-research.

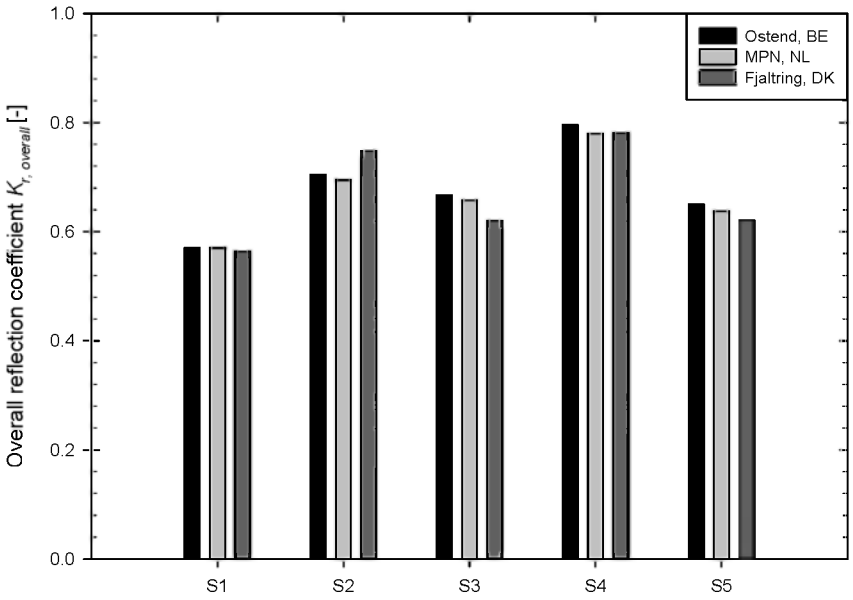

Figure 7.19: Comparison between effects of five scenarios on the overall reflection coefficient [-] for all three test sites.

7.5 Conclusions on optimal geometry of OWECs

Based on the UG10 test results, the effect of geometry control on the hydraulic efficiency, hydraulic power and reflection coefficient of OWECs deployed in wind seas (no swells) has been studied. In its strict sense, geometry control consists of adapting the slope angle and crest freeboard of the OWEC to each sea state to obtain a maximum hydraulic efficiency for each sea state and thus a maximization of the overall hydraulic efficiency. The optimal slope angle for a sea state (subscript j) is determined by the condition when: $\tan\alpha_j = 3.0\sqrt{s_{m-1,0,j}}$, while the optimal crest freeboard should fulfil $R_{c,j}/H_{m0,j} = 0.59$. The corresponding maximum hydraulic efficiency only depends on the wave steepness, while the corresponding reflection coefficient is 0.57.

Since applying such optimal geometry is not straightforward, four additional scenarios have been studied. These scenarios correspond to a more simplified control of the geometry and include the traditional fixed scenario (i.e. with a fixed slope angle and a fixed crest freeboard).

The overall hydraulic efficiency, overall hydraulic power and reflection coefficient have been calculated for each of the five scenarios for OWECs at three hypothetical deployment sites: Ostend (Belgian Continental Shelf), MPN (Dutch Continental Shelf) and Fjaltring (Danish Continental Shelf), all positioned nearshore in locations not subjected to swells.

These calculations allowed to verify whether increases in hydraulic efficiency, hydraulic power and decreases in reflection coefficient can be achieved when controlling the geometry compared to a fixed geometry. It was shown that applying an adaptive crest freeboard considerably increases the obtained overall hydraulic efficiency and power. The best practically realizable scenario corresponds to the installation of a hinge at the bottom of the slope and the application of an adaptive crest freeboard control strategy (scenario 5). Based on the calculations, the gain in overall hydraulic power for that scenario compared to a fixed geometry is approximately 10 %.

Furthermore, the overall reflection coefficient (based on the sea states with the largest frequencies of occurrence) appears to be minimal for scenario 1: $K_{r,overall} = 0.57$. When fixing the geometrical components, an increase in the overall hydraulic efficiency occurs, up to a value of approx. 0.80 for the fully fixed geometry, i.e. scenario 4. Since the reflection coefficient is still rather large for each of the scenarios, a proper toe protection should be applied for the OWECs studied in this PhD-manuscript.

8

Probability distribution of individual wave overtopping volumes for steep low-crested slopes

This chapter presents the results of a study on the probability distribution of the wave-by-wave (individual) overtopping volumes for steep low-crested slopes. This study is based on the UG10 test series, for which the individual overtopping volumes have been measured accurately (chapter 2). The governing parameters affecting the shape of the probability distribution and the probability of overtopping have been determined through a comparison of the UG10 test results with existing prediction formulae. As a result, the shortcomings of the existing prediction formulae are identified. Finally, new formulae are proposed concerning the shape of the distribution and the probability of overtopping, applicable to steep low-crested slopes, bridging the gap between mild slopes and vertical walls on relatively deep water.

8.1 Introduction

Knowledge on the probability distribution of the individual overtopping volumes of (steep) low-crested slopes is required (1) in the context of optimizing the performance of overtopping wave energy converters (OWECs), and (2) for the design of sea defence structures in severe storm conditions, when a low crest freeboard occurs.

The general concept of an OWEC is shown in Fig. 1.1. The design of the slope and crest freeboard of an OWEC is determined based on the maximization of the overall hydraulic power at the crest of the OWEC (chapter 7). When the water falls into the reservoir, part of that hydraulic power is lost. Further losses in power occur due to spill of water out of the reservoir, related to the limited size of the reservoir and to the control strategy and efficiency of the turbines (Tedd 2007). In order to

minimize these losses, knowledge on the time variation of the overtopping rate is required, i.e. on the individual overtopping volumes that enter the reservoir in time. When the distribution of those volumes is known, time series of individual overtopping waves can be simulated. These simulations enable to determine the optimal size of the reservoir and the optimal turbine strategy, leading to a maximum electrical output of the OWEC.

Attempts were made by Kofoed (2002) and Tedd and Kofoed (2009) to study the probability distribution of the wave-by-wave overtopping volumes for the floating Wave Dragon. It is unclear whether their results are applicable to the structures studied in this PhD-manuscript, which feature a slope extending to the seabed.

The reason for investigating the probability distribution of individual overtopping volumes for sea defence structures in severe storm conditions is different than for OWECs. Wave overtopping affects e.g. persons and cars behind the crest of a sea defence structure and may cause lee-side erosion of embankments leading to breaching. In this context, individual overtopping volumes and more specific the maximum individual volume V_{max} [m³/m] provide a better design measure than the average overtopping rate q [m³/s/m] (Franco et al. 1994). Accordingly, guidance on the tolerable overtopping rates has been related to V_{max} for a number of hazard situations (EurOtop 2007). The probability distribution of the individual overtopping volumes of sea defence structures has been studied extensively (Besley 1999; EurOtop 2007; Franco et al. 1994; Van der Meer and Janssen 1994). However, it is unclear whether these formulations are also applicable for very small relative crest freeboards since sea defence structures typically feature a high crest freeboard.

This PhD-research aims at improving the knowledge on the probability distribution of the wave-by-wave overtopping volumes per meter crest width V_t [m³/m] for steep low-crested slopes and tries to gain insight in the effects of the slope geometry and wave characteristics on that distribution.

In the following section 8.2, existing formulations for the probability distribution of individual overtopping volumes from literature are described. These include the formulations for traditional sea defence structures, but also for levees or dikes with a negative crest freeboard (Hughes and Nadal 2009) and for OWECs (Kofoed 2002; Tedd and Kofoed 2009). Section 8.3 discusses the applicability of the existing formulations to the steep low-crested slopes studied in this PhD-research. The probability distributions of the individual overtopping volumes measured during the UG10 test series are studied in section 8.4. Eventually, the probability of overtopping (which plays an important role in the scale of the probability distribution) for the UG10 test series is investigated in section 8.5.

8.2 Existing formulations for probability distribution of individual overtopping volumes

Similar to the prediction formulae for the average overtopping rate available in literature (chapter 4), the expressions for the probability distribution of the individual overtopping volumes (section 8.2.1) and the probability of overtopping (section 8.2.2) are mainly determined for sea defence structures. Recently, the probability distribution of the individual overtopping volumes for levees or dikes with a negative crest freeboard (section 8.2.3) and OWECs (section 8.2.4) have been studied.

8.2.1 Probability distribution of individual overtopping volumes for sea defence structures

Two of the first studies on the probability distribution of individual overtopping volumes for sea defence structures have been carried out by Van der Meer and Janssen (1994) (for sloped structures) and by Franco et al. (1994) (for vertical walls in relatively deep water). The probability $P_V = P\left[V_i \geq V\right]$ [-] of an individual overtopping volume V_i to exceed a particular volume V appears to be well fitted by a Weibull distribution for the tested sea defence structures. The values of $\hat{P}_V$ related to the number of incoming waves N_w [-] (using the Weibull plotting position formula (Goda 2000)) defined in Eq. (8.1a) are well fitted by a three-parameter Weibull distribution (Eq. 8.1b). The index i is the rank of the individual volume (ranked from large to small). The circumflex of $\hat{P}_V$ in Eq. (8.1a) means that $\hat{P}_V$ is an estimator of P_V.

$$\hat{P}_V = \frac{i}{N_w + 1} \tag{8.1a}$$

$$P_V = r \exp\left(-\left(\frac{V}{a}\right)^b\right) \tag{8.1b}$$

The coefficient b [-] determines the shape of the Weibull distribution and is therefore referred to as the *shape factor*. The coefficient a [m³/m] is the *scale factor*, while r [-] is the *set-off coefficient*. By definition, r is the probability of

overtopping P_{ow} [-], which is the ratio of the number of overtopping waves N_{ow} [-] and the number of incoming waves N_w (Eq. 8.2).

$$P_{ow} = \frac{N_{ow}}{N_w} \tag{8.2}$$

When expressing the exceedance probability as a function of the number of overtopping waves N_{ow} (Eq. 8.3a), the coefficient r equals 1.0 and the probability distribution reduces to a two-parameter Weibull distribution (Eq. 8.3b) (similar to the distribution of the individual wave heights in limited water depth given in Eq. 3.21). This expression is most commonly applied in literature (e.g. EurOtop 2007) and therefore also used further in this chapter. Note that the Weibull distribution turns into a Rayleigh distribution when the shape factor $b = 2.0$.

$$\hat{P}_V = \frac{i}{N_{ow}+1} \tag{8.3a}$$

$$P_V = \exp\left(-\left(\frac{V}{a}\right)^b\right) \tag{8.3b}$$

When the distribution of the individual overtopping volumes is accurately described by the Weibull distribution in Eq. (8.3b), the following expression is found for the individual overtopping volume:

$$V = a\left(-\ln\left(P_V\right)\right)^{\frac{1}{b}} \tag{8.4}$$

Assuming that the maximum volume corresponds to an exceedance probability P_V of $1/N_{ow}$, the expression for $V_{\max}$ is (as mentioned in EurOtop (2007)):

$$V_{\max} = a\left(-\ln\left(\frac{1}{N_{ow}}\right)\right)^{\frac{1}{b}} = a\left(\ln\left(N_{ow}\right)\right)^{\frac{1}{b}} \tag{8.5}$$

Note that the prediction of $V_{\max}$ by Eq. (8.5) is subject to quite some uncertainty, since the assumption that $V_{\max}$ corresponds to an exceedance probability of $1/N_{ow}$ is only approximate.

The scale factor a can be expressed as a function of the shape factor b [-], based on the equality of the theoretical and measured mean individual overtopping volume (Franco and Franco 1999). The measured mean individual overtopping volume is defined by:

$$\bar{V}_{meas} = \frac{V_0}{N_{ow}} = \frac{\sum V_i}{N_{ow}} \tag{8.6}$$

Given the definition of the average overtopping rate q as the ratio of the total overtopping volume V_0 [m³/m] (i.e. the sum of individual volumes V_i) and the total test duration T_0 (i.e. the sum of the wave periods of each wave in the wave train T_i), the following expression for the measured mean individual volume can be derived (T_m [s] is the mean wave period):

$$q = \frac{V_0}{T_0} = \frac{\sum V_i}{\sum T_i} = \frac{\sum V_i}{N_w T_m} \tag{8.7a}$$

$$\Rightarrow \frac{q N_w T_m}{N_{ow}} = \frac{\sum V_i}{N_{ow}} \tag{8.7b}$$

$$\Rightarrow \bar{V}_{meas} = \frac{q T_m}{P_{ow}} \tag{8.7c}$$

By definition, the theoretical mean individual overtopping volume for a two-parameter Weibull distribution is expressed by (Γ stands for the mathematical gamma function):

$$\bar{V}_{theor} = E[V]_{Weibull} = a\,\Gamma\left(1+\frac{1}{b}\right) \tag{8.8}$$

When the two-parameter Weibull distribution properly characterizes the individual overtopping volumes, the expressions for $\bar{V}_{meas}$ (Eq. 8.7c) and $\bar{V}_{theor}$ (Eq. 8.8) are equal to each other. Accordingly, the following relationship exists between a and b:

$$a = \frac{1}{\Gamma\left(1+\frac{1}{b}\right)} \frac{q T_m}{P_{ow}} \tag{8.9a}$$

The coefficient $1/\Gamma\left(1+1/b\right)$ is denoted by a' (Eq. 8.9b).

$$a' = \frac{1}{\Gamma\left(1+\frac{1}{b}\right)} \tag{8.9b}$$

As a result, the expression for a becomes:

$$\Rightarrow a = a'\frac{qT_m}{P_{ow}} = a'\overline{V}_{meas} \tag{8.9c}$$

Based on Eq. (8.9), the coefficient a is proportional to the mean individual overtopping volume, consequently scaling the individual volumes in Eq. (8.3b). This explains the name *scale factor* of the coefficient a. When the individual volumes V_i are larger on average, the scale factor a is also larger.

Values of a' for a shape factor b ranging from 0.6 to 2.0 are given in Table 8.1, using Eq. (8.9b). The value of b is expected to be within this range of b -values for structures with a positive crest freeboard (see e.g. Besley (1999)). The upper boundary (b = 2.0) corresponds to a Rayleigh distribution.

Table 8.1: Coefficient a' as a function of the shape factor b.

Shape factor *b* [-]	**Coefficient *a'***
0.60	0.66
0.75	0.84
0.90	0.95
1.05	1.02
1.20	1.06
1.35	1.09
1.50	1.11
1.65	1.12
1.80	1.12
1.95	1.13
2.00	1.13

Table 8.1 is shown graphically in Fig. 8.1. The relationship between the coefficient a' and the shape factor b is accurately expressed using a hyperbolic

tangent fit (Eq. 8.10) for the range of application of b in Table 8.1 and Fig. 8.1 (the corresponding value of the determination coefficient r^2 is 0.96).

$$a' = 1.13 \tanh\left(1.32 b\right) \tag{8.10}$$

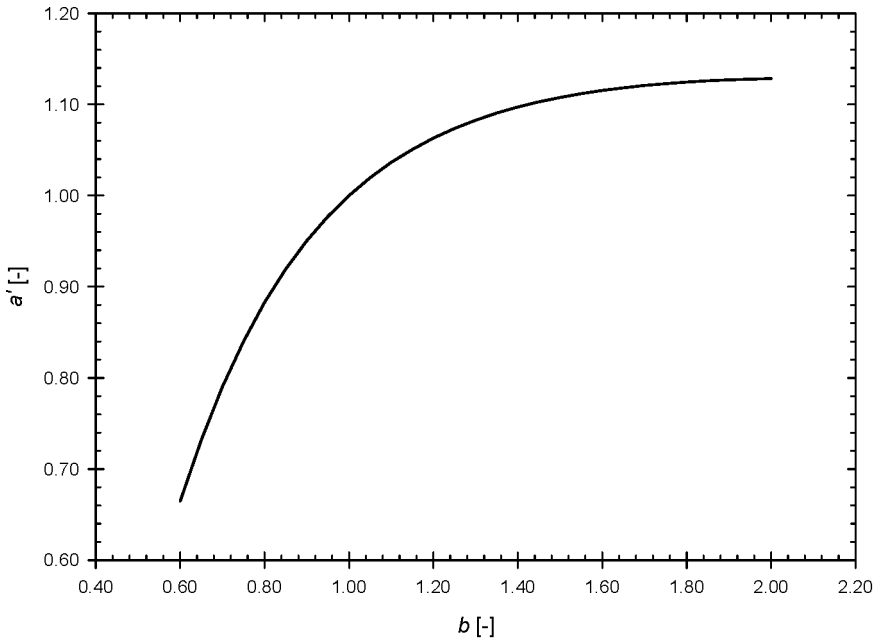

Figure 8.1: Coefficient a' as a function of the shape factor b, with $0.6 \leq b \leq 2.0$.

The shape factor b is an empirical coefficient, which depends on the structure type and the wave characteristics. Van der Meer and Janssen (1994) assigned the constant value of $b = 0.75$ to the shape factor, based on an investigation of the distribution of the individual overtopping volumes at a wide variety of sloped sea defence structures. An identical value of the shape factor has been found based on experiments on caisson breakwaters (vertical walls) in relatively deep water with non-impacting waves and normal wave attack (Franco et al. 1994).

The expression for the scale factor a_{trad} [m³/m] (*trad* refers to traditional sea defences structures) corresponding to a shape factor $b = 0.75$ (based on Table 8.1) is given in Eq. (8.11).

$$a_{trad} = 0.84 \frac{q T_m}{P_{ow}} \tag{8.11}$$

A more detailed analysis of the shape factor b has been carried out by Besley (1999) based on a number of datasets restricted to more limited types of sea defence structures. The applicability of the two-parameter Weibull distribution for sea defence structures has been confirmed for all tested structures. Furthermore, Besley (1999) did not focus on an "average" value of the shape factor b, but fitted values of b to each dataset. The shape factor appears to be dependent on the wave steepness $s_p = 2\pi H_s / \left(g T_p^2\right)$ and on the occurrence of impacting waves (Table 8.2). A dependency on the slope angle α has also been noticed by Besley (1999). However, no distinct pattern has been recognized for the effect of the slope angle on b. Hence, its effect is not present in Table 8.2. The values of the scale factor corresponding to the shape factors in Table 8.2 are calculated based on Eq. (8.9a).

Table 8.2: Shape factor b predicted by Besley (1999).

	$s_p = 0.02$	$s_p = 0.04$
Vertical wall, non-impacting waves	0.66	0.82
Vertical, impacting waves	0.85	0.85
Smooth sloping structures	0.76	0.92

The more detailed analysis by Besley (1999) results in values of the shape factor b for smooth sloping structures and vertical walls subjected to non-impacting waves that are mostly within the range $0.6 < b < 0.9$. Since the average value $b = 0.75$ of this interval is identical to the shape factor derived by Van der Meer and Janssen (1994) and Franco et al. (1994), one may question the usefulness of using different shape factors over the constant value 0.75. Therefore, a shape factor $b = 0.75$ is normally applied for smooth structures, which means that the effect of the wave steepness and the type of smooth structure (either sloping or vertical) are neglected.

Bruce et al. (2009) concluded that the effect of the wave steepness on the shape of the Weibull distribution is unclear for rubble mound breakwaters, based on a large

dataset of experiments with those structures. A detailed analysis showed that the shape factor of the distribution is most accurately represented by its average value: $b = 0.74$. Hence, the test results for rubble mound breakwaters also provided little support to change the generally applicable shape factor $b = 0.75$.

In conclusion, the average value of the shape factor b is approximately 0.75 for the different types of sea defence structures (sloped smooth, vertical and rubble mound breakwaters). The corresponding probability distribution is determined by Eq. (8.3b) and Eq. (8.11). Only the probability of overtopping P_{ow} is unknown in Eq. (8.11). A number of expressions for P_{ow} are available in literature, as discussed in the next section 8.2.2.

8.2.2 Probability of overtopping P_{ow} for sea defence structures

Wave overtopping at the steep slopes studied in this PhD-research is dominated by wave run-up. Accordingly, the number of waves that overtop the crest of the structure is determined by the number of run-ups that exceed the level of the crest. This means that the distribution of the run-up heights plays an important role in the value of the probability of overtopping P_{ow}.

When the wave heights are Rayleigh distributed, the individual run-up heights $R_{u,i}$ [m] for a non-overtopped sloped structure are also Rayleigh distributed (Allsop et al. 1985). This means that the exceedance probability of the run-up heights $P_{R_u} = P[R_{u,i} \geq R_u]$ is expressed by:

$$P_{R_u} = \exp\left(-\left(\frac{R_u}{H_{m0}}\right)^2\right) \tag{8.12}$$

Given the expression for the exceedance probability in Eq. (8.12), an expression can be derived for the run-up height $R_{u2\%}$ which is exceeded by only 2% of the run-up heights (Eq. 8.13).

$$0.02 = \exp\left(-\left(\frac{R_{u2\%}}{H_{m0}}\right)^2\right) \tag{8.13a}$$

$$\Rightarrow \frac{R_{u2\%}}{H_{m0}} = \sqrt{-\ln(0.02)} \tag{8.13b}$$

Since overtopping only occurs when $R_{u,i} > R_c$, the following definition for the overtopping probability is then valid:

$$P_{ow} = P\left[R_{u,i} \geq R_c\right] \tag{8.14a}$$

$$= \exp\left(-\left(\sqrt{-\ln(0.02)}\,\frac{R_c}{R_{u2\%}}\right)^2\right) \tag{8.14b}$$

Van der Meer and Janssen (1994) and Franco et al. (1994) assumed the run-up heights of the considered structures are Rayleigh distributed and gave the following expression for the probability of overtopping P_{ow} :

$$P_{ow} = \exp\left(-\left(\frac{1}{\chi}\frac{R_c}{H_{m0}}\right)^2\right) \tag{8.15}$$

The value of the coefficient χ in Eq. (8.15) can be determined by using an expression for the relative 2% run-up height $R_{u2\%}/H_{m0}$. By comparing Eq. (8.15) to Eq. (8.14), the expression for χ is:

$$\chi = \frac{R_{u2\%}}{H_{m0}}\frac{1}{\sqrt{-\ln(0.02)}} \approx 0.51\frac{R_{u2\%}}{H_{m0}} \tag{8.16}$$

Van der Meer and Janssen (1994) derived the following expression for the relative 2% run-up height:

$$\frac{R_{u2\%}}{H_{m0}} = 1.5\,\gamma_h\,\gamma_f\,\gamma_\beta\,\gamma_b\,\xi_p \tag{8.17a}$$

for breaking waves, with a maximum for non-breaking waves of:

$$\frac{R_{u2\%}}{H_{m0}} = 3.0\;\gamma_h\,\gamma_f\,\gamma_\beta \tag{8.17b}$$

The breaker parameter ξ_p is defined by $\tan\alpha / \sqrt{s_p}$. The corresponding expressions for the coefficient χ are:

$$\chi = 0.76\,\gamma_h\,\gamma_f\,\gamma_\beta\,\gamma_b\,\xi_p \tag{8.18a}$$

with a maximum of:

$$\chi = 1.52\,\gamma_h\,\gamma_f\,\gamma_\beta \tag{8.18b}$$

The γ -factors are influence or reduction factors which take into account the effects of a shallow foreshore (γ_h), the slope roughness (γ_f), oblique wave attack (γ_β) and a berm (γ_b). Equation (8.17) gives the mean of a stochastic parameter with variation coefficient $\sigma / \mu =$ 0.06.

Based on a larger number of experimental datasets with sloped coastal structures, TAW (2002) derived a slightly different expression for the relative 2% run-up height (also given in EurOtop 2007):

$$\frac{R_{u2\%}}{H_{m0}} = 1.65\,\gamma_f\,\gamma_\beta\,\gamma_b\,\xi_{m-1,0} \tag{8.19a}$$

with a maximum of:

$$\frac{R_{u2\%}}{H_{m0}} = 1.0\,\gamma_f\,\gamma_\beta\,\gamma_b\left(4.0 - \frac{1.5}{\sqrt{\xi_{m-1,0}}}\right) \tag{8.19b}$$

The range of application of Eq. (8.19) for $\gamma_b\,\xi_{m-1,0}$ is: $0.5 < \gamma_b\,\xi_{m-1,0} <$ 8.0 to 10.0. The reliability of Eq. (8.19) is expressed by considering Eq. (8.19) as the mean of a stochastic parameter $R_{u2\%} / H_{m0}$ with variation coefficient $\sigma / \mu =$ 0.07. In contrast to the constant maximum relative 2% run-up height for non-breaking waves in Eq. (8.17b), a continuously increasing relative 2% run-up height is predicted by Eq. (8.19b) for large values of the breaker parameter.

Ahrens et al. (1993) derived another prediction formula for the relative 2% run-up height based on test results with plane smooth impermeable non-overtopped slopes with slope angles varying between $\cot\alpha = 1.0$ and $\cot\alpha = 4.0$. The formula consists

of two parts, one for breaking waves with $\xi_p \leq 2.5$ (Eq. 8.20a), the other for non-breaking waves with $\xi_p \geq 4.0$ (Eq. 8.20b to 8.20d).

$$\frac{R_{u2\%}}{H_{m0}} = \frac{2.26\xi_p}{1+0.32\xi_p} \tag{8.20a}$$

$$\frac{R_{u2\%}}{H_{m0}} = 1.61\exp\left(2.48X_p + 0.45\cos\alpha + 0.19\Pi\right) \tag{8.20b}$$

$$X_P = h_t\frac{\cot\alpha}{L_p} - \left(h_t\frac{\cot\alpha}{L_p}\right)^2 \tag{8.20c}$$

$$\Pi = \frac{H_{m0}/L_p}{\left(\tanh\left(\frac{2\pi h_t}{L_p}\right)\right)^3} \tag{8.20d}$$

For values of the breaker parameter $2.5 < \xi_p < 4.0$, the following interpolation was suggested (Ahrens et al. 1993):

$$\left(4.0-\xi_p\right)/1.5\,Eq.(8.22a) + \left(\xi_p - 2.5\right)/1.5\,Eq.(8.22b) \tag{8.21}$$

Instead of using an expression for $R_{u2\%}/H_{m0}$ of vertical walls, Franco et al. (1994) used a best fit of their experimental test results for vertical walls in relatively deep water to Eq. (8.15), resulting in a coefficient $\chi = 0.91$.

8.2.3 Probability distribution of individual overtopping volumes for negative crest freeboards

Hughes and Nadal (2009) investigated the probability distribution of individual overtopping volumes for levees or dikes subjected to combined wave overtopping and storm surge overflow. Accordingly, the tested structures featured negative crest freeboards, with $-2.0 < R_c/H_{m0} < 0.0$. The overtopping probability P_{ow} is 1.0.

Individual overtopping volumes have been identified based on the time series of the water depth measured at a location on the crest of the tested structures. The distribution of the individual overtopping volumes still fits the two-parameter Weibull distribution (Eq. 6.3b), with values of the shape factor b ranging between

1.0 and 3.5 for the 27 tests carried out by Hughes and Nadal (2009). The values diverge strongly from the shape factor $b = 0.75$, but submerged levees or dikes are also very different from emerged dikes.

The measured average overtopping rate q_{ws} consists of both a component related to wave overtopping (q_w) and a component due to surge overflow (q_s). Hence, Eq. (8.7) is no longer valid. Furthermore, the relationship between the scale factor a and shape factor b established in Eq. (8.9a) is only valid when the scale factor is determined based on the component of the average overtopping rate due to wave overtopping q_w. However, since only the total average overtopping rate q_{ws} was measured, Eq. (8.9a) is not applicable. Instead, two independent expressions for the shape factor (Eq. 8.23) and scale factor (Eq. 8.24) were derived.

$$a = 0.79\, q_{ws}\, T_p \tag{8.23}$$

$$b = 15.7\left(\frac{q_s}{g T_p H_{m0}}\right)^{0.35} - 2.3\left(\frac{q_s}{\sqrt{g H_{m0}^3}}\right)^{0.79} \tag{8.24}$$

Note that Eq. (8.23) resembles Eq. (8.11) relatively well, taking into account the value of the overtopping probability $P_{ow} = 1.0$. Only the characteristic wave period is different. This confirmed the validity of Eq. (8.23) (Hughes and Nadal 2009).

8.2.4 Probability distribution of individual overtopping volumes for OWECs

Attempts have been made by Kofoed (2002) and Tedd and Kofoed (2009) to study the probability distribution of wave-by-wave overtopping volumes for the floating Wave Dragon (WD). Their methodology is initially based on a comparison between (1) individual overtopping volumes identified from the time series of the average overtopping rate (measured in laboratory experiments (Kofoed 2002) or at the prototype of the WD (Tedd and Kofoed 2009)) subdivided into blocks with a time interval equal to the mean period T_m and (2) the individual overtopping volumes corresponding to a theoretical probability distribution. However, due to inaccuracies in the measurement systems, unrealistic negative volumes occurred when applying this methodology. Therefore, a different approach eventually has been used. It consists of a comparison of the distributions of measured and theoretical average overtopping rates over time intervals of a number of mean periods, normalized by the

mean average overtopping rate of the total duration of the test. Hence, the applicability of the theoretical distribution of the individual volumes is only verified in an indirect way.

Using time intervals of $10\,T_m$ and assuming a coefficient $\chi = 1.21$ in Eq. (8.15), Kofoed (2002) concludes that the Weibull distribution with $b = 0.75$ and a scale factor determined by Eq. (8.11) is a good estimate for the distribution of the individual overtopping volumes of the floating WD. A similar conclusion is drawn by Tedd and Kofoed (2009), using time intervals of $5T_m$ and both $\chi = 1.21$ and $\chi =$ 1.62. The arguments for choosing one of both values of χ appear to be rather weak (Tedd and Kofoed 2009) and finally the value $\chi = 1.62$ has been suggested, since it is the most documented value (close to $\chi = 1.52$ in Eq. (8.18b) (Van der Meer and Janssen 1994)).

It is clear that the methodology applied above is rather rough (due to the limitations of the measurement system). Hence, it is not clear whether the corresponding conclusions are accurate, or if they are applicable to the steep low-crested slopes studied in this PhD-research. A discussion on the applicability of the existing formulations for the probability distribution of the individual overtopping volumes for steep low-crested slopes is given in the next section.

8.3 Applicability of existing formulations to steep low-crested slopes

8.3.1 General

Similar to the average overtopping rate (chapter 4), the existing formulations for the probability distribution of the individual overtopping volumes (section 8.2) mainly apply to the neighbouring structures (from a geometrical point of view) of the steep low-crested slopes with positive crest freeboard considered in this PhD-research. Correspondingly, these formulations allow to draw a number of conclusions concerning the probability distribution of the individual overtopping volumes of steep low-crested slopes.

First, the probability distribution is expected to be well described by a two-parameter Weibull distribution (Eq. 8.3b). Furthermore, since the structures feature positive crest freeboards, no surge overflow occurs. This means Eq. (8.9a) is still valid. The expected values for the shape factor b and for the probability of overtopping P_{ow} are discussed in section 8.3.2 and 8.3.3 respectively.

8.3.2 Shape factor *b*

Based on the existing formulations, the following conclusions are drawn concerning the value of the shape factor of the Weibull distribution for steep low-crested slopes:

- both for vertical walls and mildly sloping dikes with relatively high crest freeboards, the value of the shape factor b is approximately 0.75. Since the effect of the slope angle on b is unclear (Besley 1999), the shape factor for steep slopes with relatively high crest freeboard is expected to be $b = 0.75$ as well;

- on the other hand, since structures with negative crest freeboards correspond to values of the shape factor larger than 1.0, the shape factor for the structures with relatively low relative crest freeboards are expected to be larger than 0.75.

These conclusions point at a dependency of the shape factor on the relative crest freeboard. This contradicts the findings in section 8.2.4 for the floating WD. In order to show the effect of a shape factor larger than 0.75 on the probability distribution of the individual overtopping volumes, four examples of a theoretical two-parameter Weibull distribution are given in Fig. 8.2: with shape factor $b = 0.75$ (dash-dotted line), $b = 1.0$ (dotted line), $b = 2.0$ (short-dashed line) and $b = 3.0$ (long-dashed line).

The dotted line corresponds to the exponential curve. The short-dashed line shows the Rayleigh distribution (i.e. the distribution of the wave heights in deep water) which is a straight line in Fig. 8.2 since the horizontal axis is scaled according to a Rayleigh distribution. The theoretical distribution with $b = 3.0$ is also shown in Fig. 8.2; this is a value of the shape factor found by Hughes and Nadal (2009) for negative crest freeboards.

When $b = 0.75$, large part of the overtopping volumes are relatively small, while only a small percentage of the volumes is very large (EurOtop 2007). Such distribution is typical for sea defence structures, for which the average overtopping rate is largely determined by a small number of very large overtopping volumes (EurOtop 2007).

On the other hand, the overtopping volumes are more evenly distributed when b becomes larger: a larger percentage of overtopping volumes contributes considerably to the average overtopping rate. Since the values of the shape factor found by Hughes and Nadal (2009) are of the order of 2.0 and 3.0, a more evenly distribution of the overtopping volumes applies for structures with a negative crest freeboard.

Furthermore, a small value of the shape factor corresponds to larger maximum volumes. This means that the value of the shape factor is important for the design of sea defence structures. Applying a smaller shape factor results in a more conservative approach.

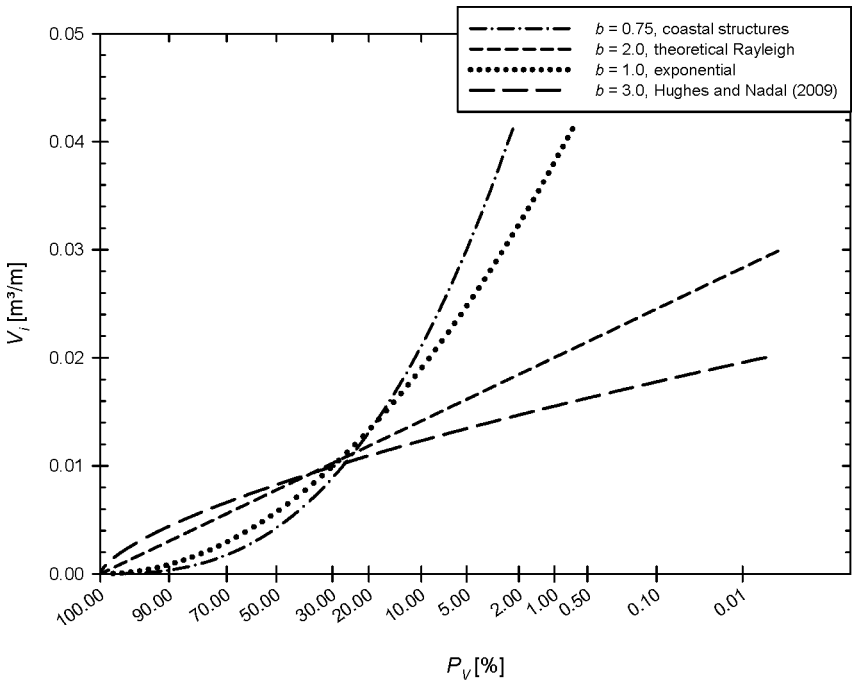

Figure 8.2: Theoretical probability distributions of individual wave overtopping volumes for $\bar{V}_{meas}$ = 0.008 m³/m with b=0.75, 1.0, 2.0 and 3.0.

8.3.3 Probability of overtopping P_{ow}

The probability of overtopping P_{ow} for sloping structures is traditionally related to the relative crest freeboard and the relative 2% run-up height, determined for non-overtopped structures (section 8.2.2).

The commonly used formula for the relative 2% run-up height $R_{u2\%}/H_{m0}$ in Eq. (8.19b) predicts a continuous increase in relative 2% run-up height for increasing value of the breaker parameter (Fig. 8.3). However, this equation has been derived based on tests of Van Gent (2001) on dikes with shallow foreshores, resulting in small values of the wave steepness and thus large breaker parameters, not on tests with steep slopes. When the large breaker parameters are due to steep slopes, the value of $R_{u2\%}/H_{m0}$ is expected to decrease towards the theoretical value for vertical walls with non-impacting waves (dotted line in Fig. 8.3) which is positioned significantly below the predictions by Eq. (8.19b). The dotted line is also positioned significantly below the prediction line of Eq. (8.17b).

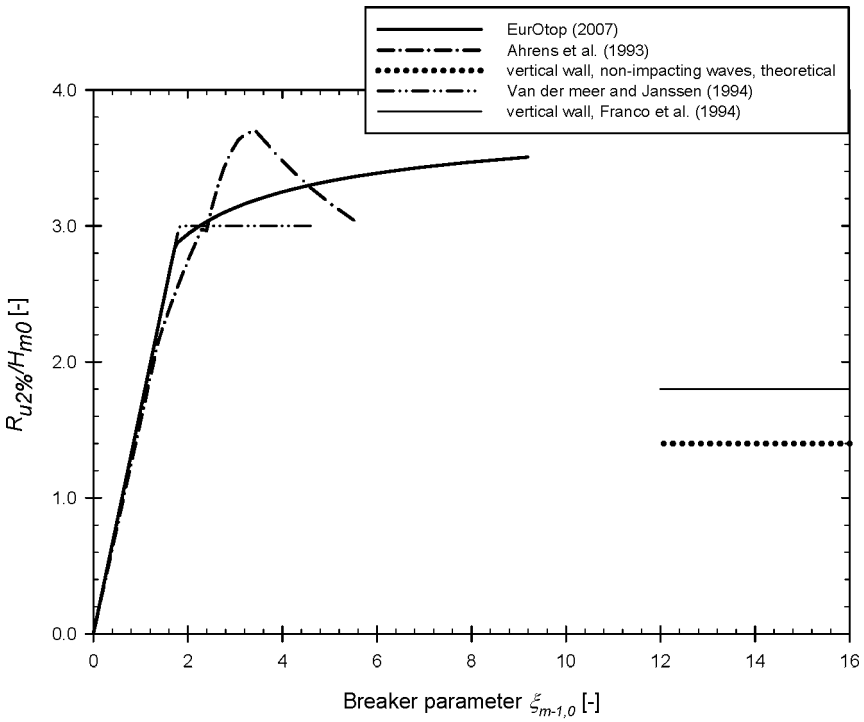

Figure 8.3: Predicted relative 2% run-up height as a function of the breaker parameter for a wave height H_{m0} = 0.10 m and a wave period T_p = 1.534 s.

The theoretical relative 2% run-up height for vertical walls with non-impacting waves in Fig. 8.3 is determined as follows. Wave reflection at these non-overtopped vertical walls is presumed to be 100%. Accordingly, the theoretical run-up height for a wave at a vertical non-overtopped wall is equal to its wave height. Hence, the run-up height distribution follows the wave height distribution. Assuming that the wave heights follow a Rayleigh distribution, a fixed relationship exists between $R_{u2\%}$ and H_{m0}:

$$\frac{R_{u2\%}}{H_{m0}} = \frac{H_{2\%}}{H_{m0}} = 1.4 \tag{8.25}$$

Based on Eq. (8.16) and the value $\chi = 0.91$ found by Franco et al. (1994) for vertical walls in relatively deep water, the relative 2% run-up height for those vertical walls is approximately 1.8. This value is slightly larger than the theoretical value in Eq. (8.25).

In conclusion, a decrease in $R_{u2\%}/H_{m0}$ is expected to occur for steep slopes towards the theoretical value for vertical walls (Eq. 8.25), similar to the average overtopping rate in chapter 5. This is confirmed by the empirical formula of Ahrens et al. (1993) (Eq. 8.20).

8.3.4 Conclusions

Based on the discussion above, both the value of the shape factor b and the expression of the probability of overtopping P_{ow} require further investigation for steep low-crested slopes. This investigation has been carried out based on the UG10 test series (chapter 2).

It should be noted that individual overtopping volumes were also determined for the AAU08 test series. However, due to the inaccuracies in the pump compensation and the lack of a return valve, those overtopping volumes were considered to be inaccurate and thus have not been analyzed.

8.4 Probability distribution of individual overtopping volumes for UG10 test series

Individual overtopping volumes have been determined accurately for each test of the UG10 test series based on the weigh cell signal (chapter 2). Successively, a Weibull plot has been generated for each test of the UG10 test series (1) in order to verify if

these volumes follow a two-parameter Weibull distribution, and (2) to determine the scale factor a and shape factor b of that Weibull distribution. This methodology was also applied when deriving the expressions of the probability distribution for the traditional sea defence structures in section 8.2.1. The principle of a Weibull plot is explained in the following section 8.4.1.

8.4.1 Weibull plots for UG10 tests

The method to generate a Weibull plot is explained hereafter. It is based on Eq. (8.4). By taking the logarithm of its both sides, Eq. (8.4) is converted into:

$$\log V = \log a + \frac{1}{b}\log\left(-\ln P_V\right) \tag{8.26}$$

The theoretical exceedance probability P_V is approximated by the empirical exceedance probability $\hat{P}_V$ (Eq. 8.3a), here denoted by y. By setting $\log a = \lambda$ and $1/b = \psi$, Eq. (8.26) can be rewritten as:

$$\begin{cases} \log V = \lambda + \psi \log\left(-\ln y\right) \\ \lambda = \log a \\ \psi = \dfrac{1}{b} \end{cases} \tag{8.27}$$

Equation (8.27) is the basic equation for the Weibull plot, which consists of a plot of $\log V$ for all measured individual overtopping volumes as a function of $\log\left(-\ln y\right)$. When the data points follow a linear trend in the Weibull plot, the distribution of the individual overtopping volumes fits a two-parameter Weibull distribution. Based on Eq. (8.27), the scale factor a is related to the intersection point of the linear trend line with the vertical axis of the Weibull plot, while the shape factor b is linked to the slope angle of that trend line.

It should be noted that this methodology is not applicable when the individual volumes are not determined accurately, for example in Kofoed (2002) and Tedd and Kofoed (2009) for the individual overtopping volumes of the WD. This is the reason why the methodology described in section 8.2.4 was applied.

An example of a Weibull plot is given in Fig. 8.4 for a test of the UG10 dataset with H_{m0} = 0.10 m, R_c = 0.02 m, T_p = 1.789 s and $\cot\alpha = 1.0$. The corresponding relative crest freeboard is R_c / H_{m0} = 0.20. The general trend described by the data points in Fig. 8.4 is linear, and the conclusion is drawn that the individual volumes fit a two-parameter Weibull distribution. The data points corresponding to the example in Fig. 8.4 are also plotted in a graph similar to Fig. 8.2 (Fig. 8.5), with a Rayleigh scale on the horizontal axis.

The small overtopping volumes deviate most significantly from the linear trend and affect the slope angle of the corresponding linear trend line to a large extent. On the other hand, Fig. 8.5 shows that the contribution of the small volumes to the probability distribution is actually rather limited. Accordingly, the characteristics of the Weibull plot have been determined without considering the small overtopping volumes.

It has been emphasized by Van der Meer and Janssen (1994) and Besley (1999) that the two-parameter Weibull distribution is particularly a good fit at higher values of the individual volumes and thus is able to accurately represent extreme values of V_i, both for sloped sea defence structures and vertical walls. Hence, the coefficients a and b are traditionally determined by only considering a particular percentage of the largest individual volumes. For example, the Weibull distribution is only fitted to individual volumes $V_i > \overline{V}_{meas}$ for smooth dikes by Van der Meer and Janssen (1994) and for vertical walls studied by Besley et al. (1998), since this gave the most reliable estimates of $V_{\max}$. An identical approach has been applied by Bruce et al. (2009) for rubble mound breakwaters.

On the other hand, when studying the distribution of individual volumes for the optimization of OWECs, all volumes should be considered since the design of the reservoir and turbines is based on realistic simulations of individual wave overtopping volumes and not on the maximum volume. However, the small volumes should also be left out of the linear regression analysis for OWECs, since these volumes distort the slope angle of the linear trend line in the Weibull plot.

Furthermore, a constraint on the possible combinations of a and b is established by the relationship between a and b in Eq. (8.7). For large values of b (but smaller than 2.0) the value of a' is approximately constant (Fig. 8.1). This means that the intersection point of the linear trend line of the data points with the vertical axis of the Weibull plot is approximately constant for large values of b of say $1.5 < b < 2.0$.

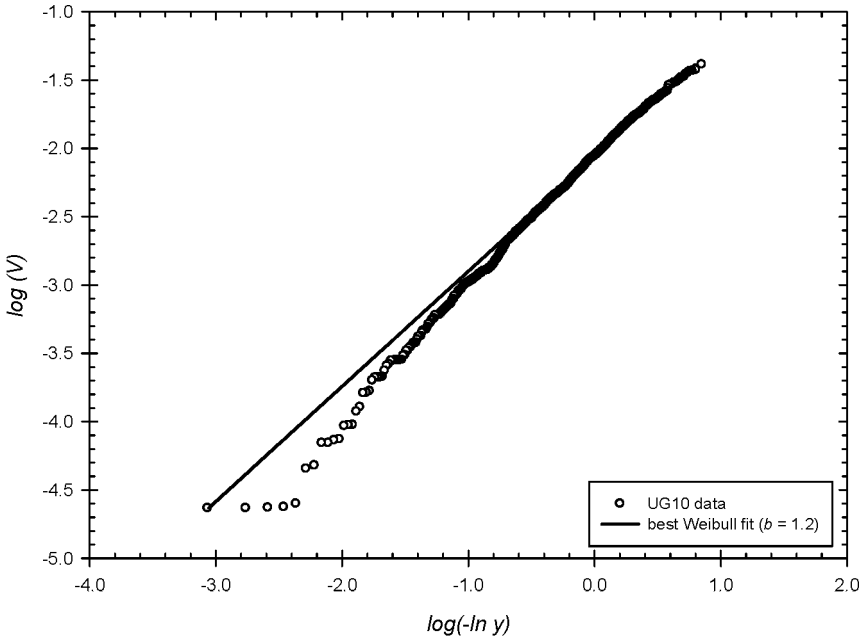

Figure 8.4: Weibull plot for UG10 test with $H_{m0} = 0.10$ m, $R_c = 0.02$ m, $T_p = 1.789$ s and $\cot\alpha = 1.0$. The corresponding relative crest freeboard is $R_c / H_{m0} = 0.20$.

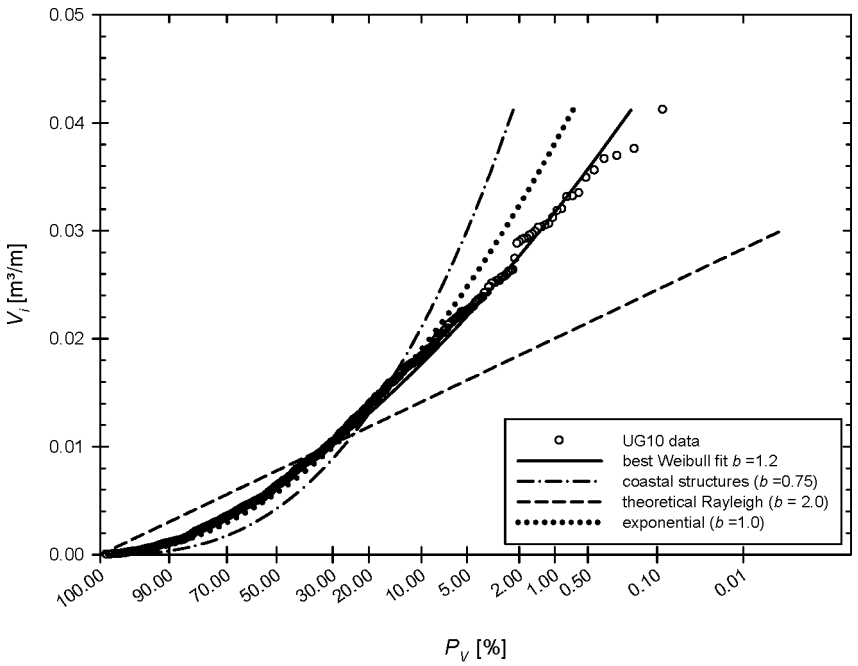

Figure 8.5: Probability distribution of individual wave overtopping volumes for UG10 test results with $H_{m0} = 0.10\,m$, $R_c = 0.02\,m$, $T_p = 1.789\,s$ *and* $\cot\alpha = 1.0$. *The corresponding relative crest freeboard is* $R_c / H_{m0} = 0.20$.

Eventually, the coefficients a and b have been determined for the tests of the UG10 test series based on a Weibull plot of the individual overtopping volumes with $V_i > \overline{V}_{meas}$. The corresponding Weibull distributions are referred to as *the best Weibull fits*. A best Weibull fit has been determined for each test of the UG10 dataset, except for the tests with less than 30 overtopping events. In total, 364 best Weibull fits have been determined.

The shape factor for the example shown in Fig. 8.4, only taking into account the individual volumes $V_i > \overline{V}_{meas}$, equals b = 1.2. The best Weibull fit for that particular example is added to Figs. 8.4 and 8.5. Based on Fig. 8.5, this fit is positioned in between the long-dashed line corresponding to the two-parameter Weibull

distribution for sea defence structures ($b = 0.75$) and the short-dashed line of the theoretical Rayleigh distribution ($b = 2.0$), since the value of the shape factor $b = 1.2$, close to an exponential distribution.

8.4.2 Effect of non-Rayleigh distributed wave heights on shape factor *b*

Among the 364 UG10 tests considered for studying the probability distribution of steep low-crested slopes, a number of tests correspond to non-Rayleigh distributed wave heights. The wave heights of the tests of the UG10 dataset with large significant wave heights H_{m0} do not fit a Rayleigh distribution, but a composite Weibull distribution (Battjes and Groenendijk 2000) (section 3.4). Although the sea state is categorized as non-breaking, depth-induced breaking of the largest waves occurs, limiting the value of the maximum individual volume. In accordance to Fig. 8.2, a decrease in the largest individual volumes corresponds to an increase in the value of the shape factor b.

The differences in the Weibull distribution between a test with Rayleigh distributed wave heights and a test with non-Rayleigh distributed wave heights are clear when comparing Fig. 8.4 and Fig. 8.6 on the one hand, and Fig. 8.5 and Fig. 8.7 on the other hand. Although both tests correspond to identical slope angles and a similar value of the relative crest freeboard, the shape factor in Figs. 8.4 and 8.5 is 1.2, while it is 1.4 for the case shown in Figs. 8.6 and 8.7. The probability distribution in Fig. 8.7 is a little flatter, due to the non-Rayleigh distribution of the wave heights. The linear trend line of the largest volumes clearly deviates from the linear trend line followed by the medium-sized overtopping volumes. Furthermore, the smallest individual volumes are not accurately described by the Weibull distribution derived based on the individual overtopping volumes V_i larger than $\overline{V}_{meas}$ (Fig. 8.7).

The example in Figs. 8.6 and 8.7 shows that when the wave heights are not Rayleigh distributed, the distribution of the individual overtopping volumes is more accurately described by using two Weibull distributions, similar to the distribution of the wave heights (Battjes and Groenendijk 2000).

The differences in the wave height distribution between the UG10 tests in Fig. 8.5 and Fig. 8.7 are explicitly shown in Figs. 8.8 and 8.9. The wave heights in Fig. 8.8 (corresponding to the example in Fig. 8.5) clearly follow the Rayleigh distribution, while the wave heights in Fig. 8.9 (corresponding to the example in Fig. 8.7) clearly deviate from the Rayleigh distribution.

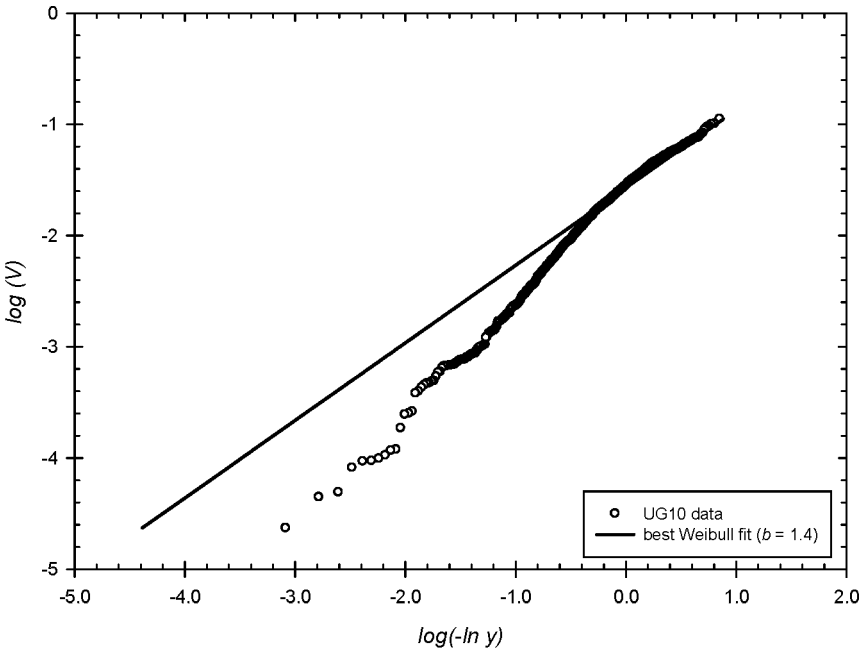

Figure 8.6: Weibull plot for UG10 test results with $H_{m0} = 0.19$ m, $R_c = 0.045$ m, $T_p = 2.045$ s and $\cot\alpha = 1.0$. The corresponding relative crest freeboard is $R_c / H_{m0} = 0.24$.

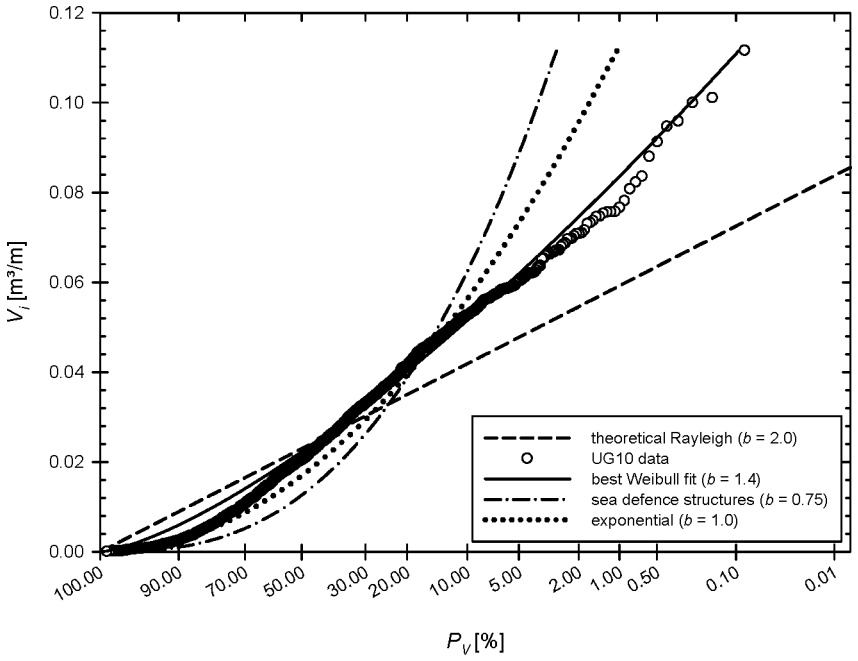

Figure 8.7: Probability distribution of individual wave overtopping volumes for UG10 test results with $H_{m0} = 0.19$ *m,* $R_c = 0.045$ *m,* $T_p = 2.045$ *s and* $\cot\alpha = 1.0$. *The corresponding relative crest freeboard is* $R_c / H_{m0} = 0.24$.

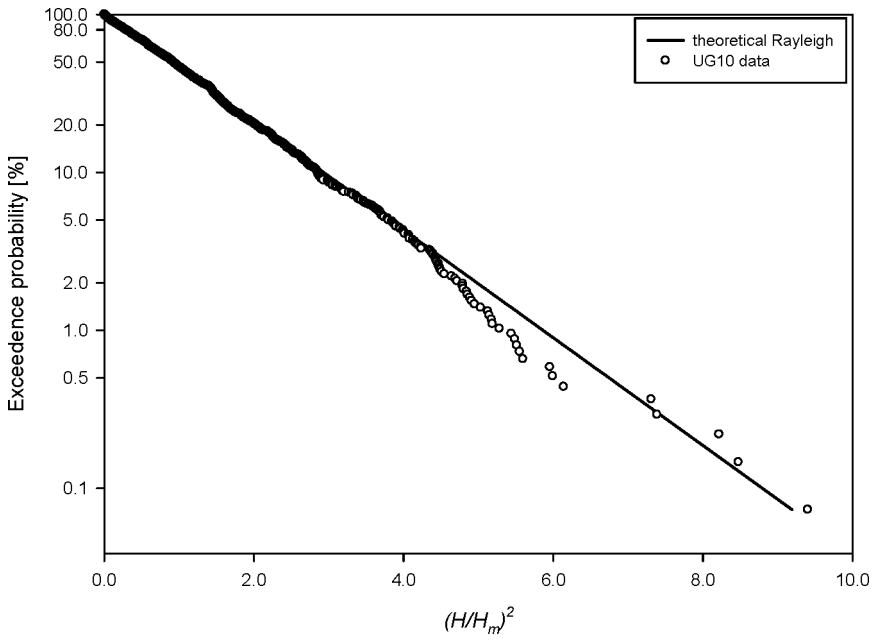

Figure 8.8: Probability distribution of individual wave heights for UG10 test with $H_{m0} = 0.10$ *m,* $R_c = 0.02$ *m,* $T_p = 1.789$ *s and* $\cot\alpha = 1.0$. *The corresponding relative crest freeboard is* $R_c / H_{m0} = 0.20$.

The observation that tests with non-Rayleigh distributed wave heights correspond to larger values of the shape factor *b* should be kept in mind when studying the effects of the slope angle, relative crest freeboard and wave steepness on the shape factor *b* of the Weibull distribution of the individual overtopping volumes for steep low-crested slopes. These effects have been studied based on the best Weibull fits for the 364 tests of the UG10 test series, as discussed in the following three sections 8.4.3 to 8.4.5.

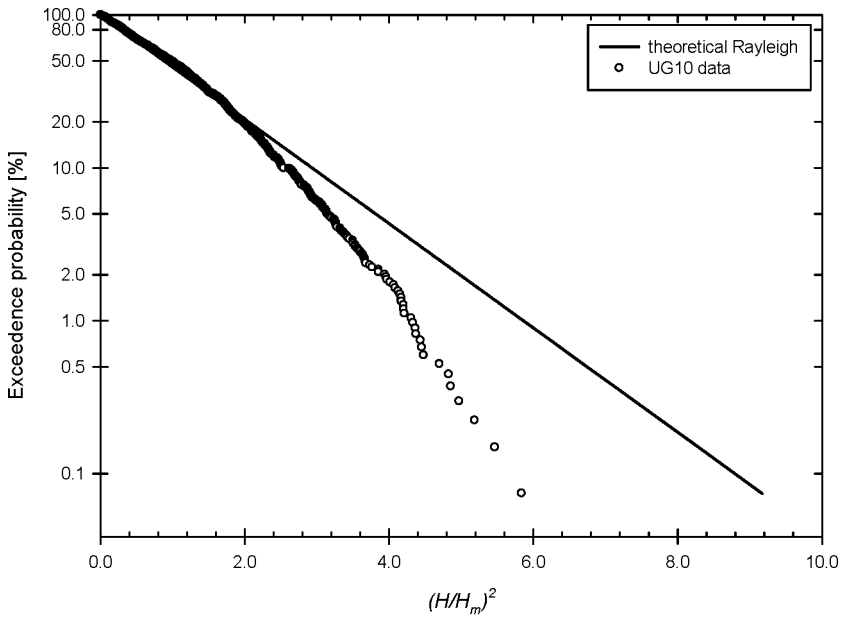

Figure 8.9: Probability distribution of individual wave heights for UG10 test results with $H_{m0} = 0.19$ *m,* $R_c = 0.045$ *m,* $T_p = 2.045$ *s and* $\cot\alpha = 1.0$*. The corresponding relative crest freeboard is* $R_c / H_{m0} = 0.24$*.*

8.4.3 Effect of slope angle on shape factor *b*

A clear effect of the slope angle on the shape factor b is distinguished for the test results of the UG10 dataset with $0.8 < R_c / H_{m0} < 1.0$ which correspond to Rayleigh distributed wave heights at the toe of the structure (Fig. 8.10). The shape factor increases from 0.8 for $\cot\alpha = 0.36$ to 1.07 for $\cot\alpha = 2.75$, approximately following a linear trend line.

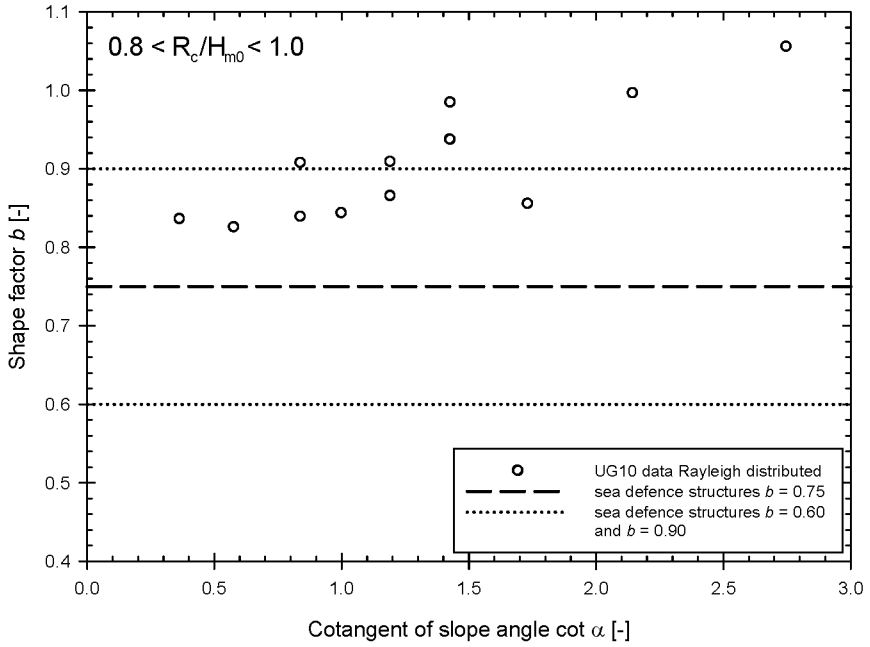

Figure 8.10: Effect of the slope angle on the shape factor b for 0.8 < R_c / H_{m0} < 1.0.

Based on similar graphs for other ranges of R_c / H_{m0} (e.g. Figs. 8.11 and 8.12), it appears that the dependency of the shape factor on the slope angle for steep low-crested slopes in general follows a linear trend line, increasing for decreasing slope angle. Figure 8.11 shows the effect of the slope angle on the shape factor of the Weibull distribution for relatively large crest freeboards. The linear increasing trend is clearly visible. This is in contrast to the findings by Besley (1999) that a clear effect of the slope angle on the shape factor *b* could not be distinguished for sea defence structures. On the other hand, the average value of the shape factor in Fig. 8.11 is still equal to 0.75, i.e. the value traditionally used for sea defence structures (section 8.2.1).

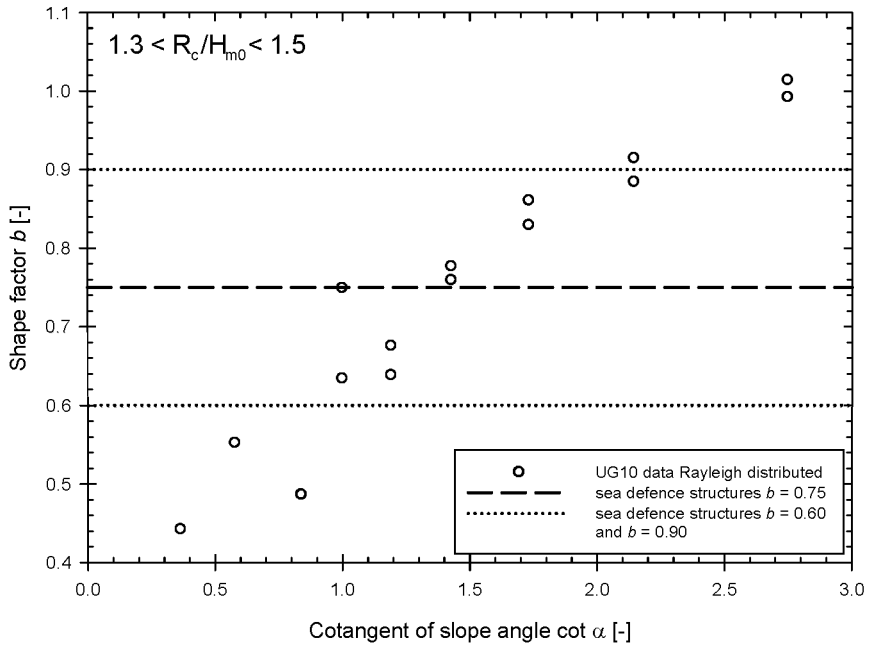

Figure 8.11: Effect of slope angle on the shape factor b for 1.3 < R_c / H_{m0} < 1.5.

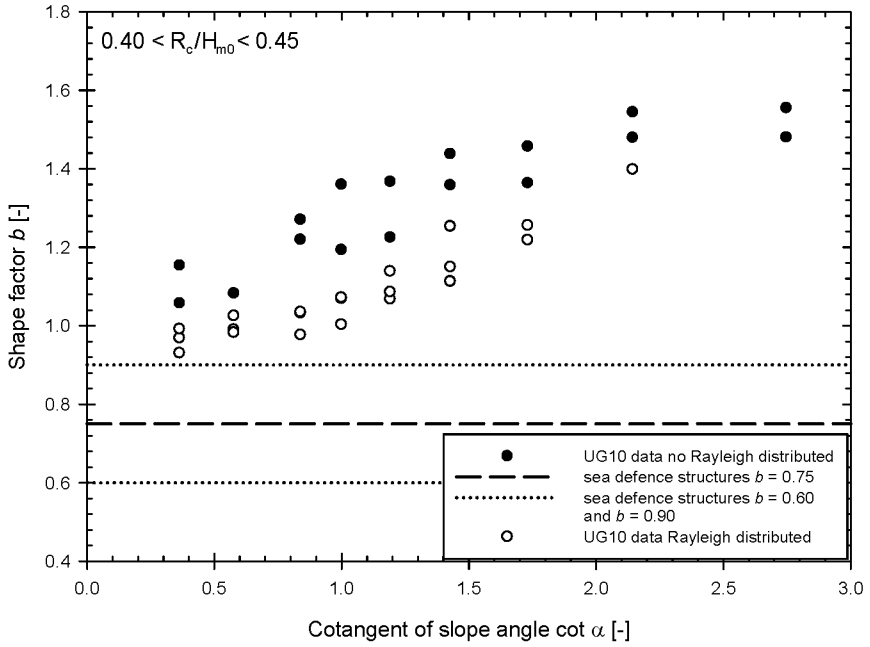

Figure 8.12: Effect of slope angle on the shape factor b for 0.40 < R_c / H_{m0} < 0.45.

The general conclusion of the linear trend line is also valid for tests of the UG10 test series with non-Rayleigh distributed wave heights (marked in black in Fig. 8.12). The corresponding shape factors are larger than the shape factors for the tests with Rayleigh distributed wave heights (see section 8.4.2).

Approximately all data points in Fig. 8.12 correspond to a shape factor larger than 1.0. This is due to the relatively small crest freeboards of those data points. The effect of the relative crest freeboard on the shape factor b is discussed in the next section 8.4.4.

8.4.4 Effect of relative crest freeboard on shape factor *b*

The effect of the relative crest freeboard on the shape factor b for the UG10 test results with Rayleigh distributed wave heights is shown in Fig. 8.13. For a particular

slope angle, an increase in relative crest freeboard causes a decrease of the shape factor b, until it approximately reaches a constant for $R_c / H_{m0} > 1.2$. The data points approximately follow a negative exponential trend line for each value of the slope angle α.

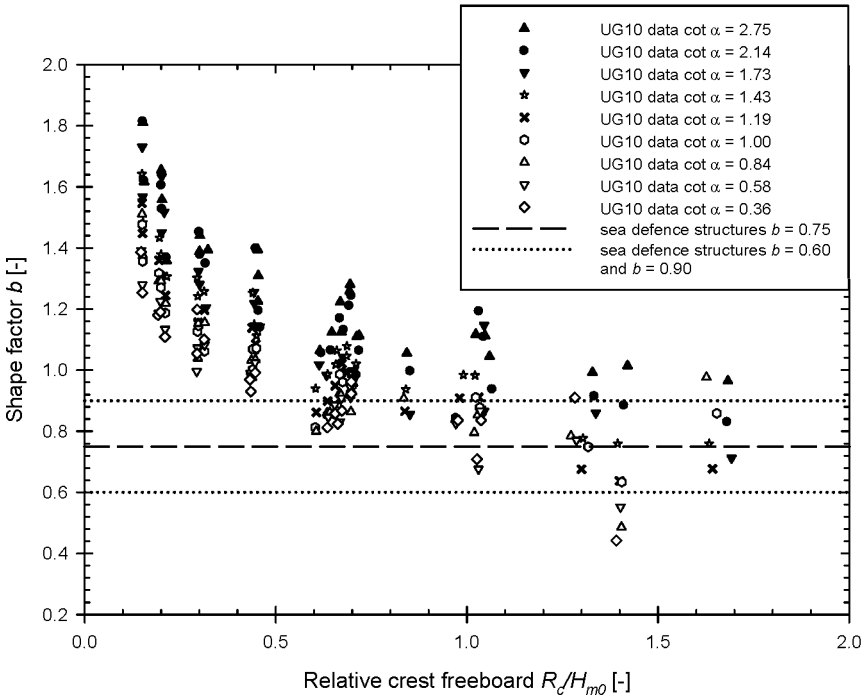

Figure 8.13: Effect of the relative crest freeboard on the shape factor b, for UG10 test results with Rayleigh distributed wave heights.

The data points corresponding to tests with $R_c / H_{m0} > 1.2$ are in general positioned around the shape factor $b = 0.75$, confirming the validity of the predicted characteristics for the Weibull distribution of sea defence structures (section 8.2.1) for steep slopes with relatively large crest freeboards (see also discussion on Fig. 8.11 in section 8.4.3).

On the other hand, the majority of the data points with $R_c / H_{m0} < 1.2$ is positioned above the horizontal line corresponding to $b = 0.75$. Furthermore, the deviation increases with a decreasing relative crest freeboard R_c / H_{m0} (Fig. 8.13) up to values of $b = 1.8$ for very low relative crest freeboards. These values are positioned in between the value of $b = 0.75$ for traditional sea defence structures and the values of b for negative crest freeboards (Hughes and Nadal 2009) as suggested in section 8.3. The different shape of the best Weibull fits of the individual overtopping volumes between small relative crest freeboards and large relative crest freeboards is illustrated by comparing Fig. 8.5 to Fig. 8.14.

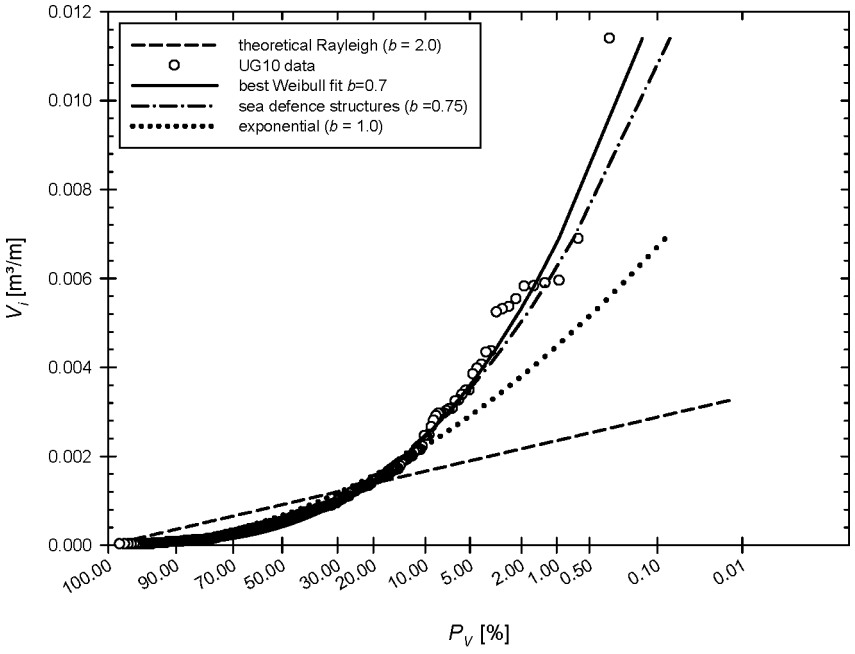

Figure 8.14: Probability distribution of individual wave overtopping volumes for UG10 test results with $H_{m0} = 0.067$ m, $R_c = 0.07$ m, $T_p = 1.28$ s and $\cot\alpha = 0.58$. The corresponding relative crest freeboard is $R_c / H_{m0} = 1.04$.

The data points in Fig. 8.14 correspond to a relative crest freeboard $R_c / H_{m0} =$ 1.04 (with $\cot\alpha = 1.0$), while the relative crest freeboard in Fig. 8.5 is only 0.20 (with $\cot\alpha = 0.58$). The solid line of the best Weibull fit in Fig. 8.14 is positioned near the dash-dotted line corresponding to $b =$ 0.75, as expected for the larger relative crest freeboard. The value of the shape factor of the best Weibull fit is $b =$ 0.7, which is much smaller than the value of 1.2 found for the example in Fig. 8.5. The shape factors of the UG10 tests with non-Rayleigh distributed wave heights are larger than for the tests with Rayleigh distributed wave heights (Fig. 8.15). Nevertheless, a similar effect of the relative crest freeboard on the shape factor b is observed.

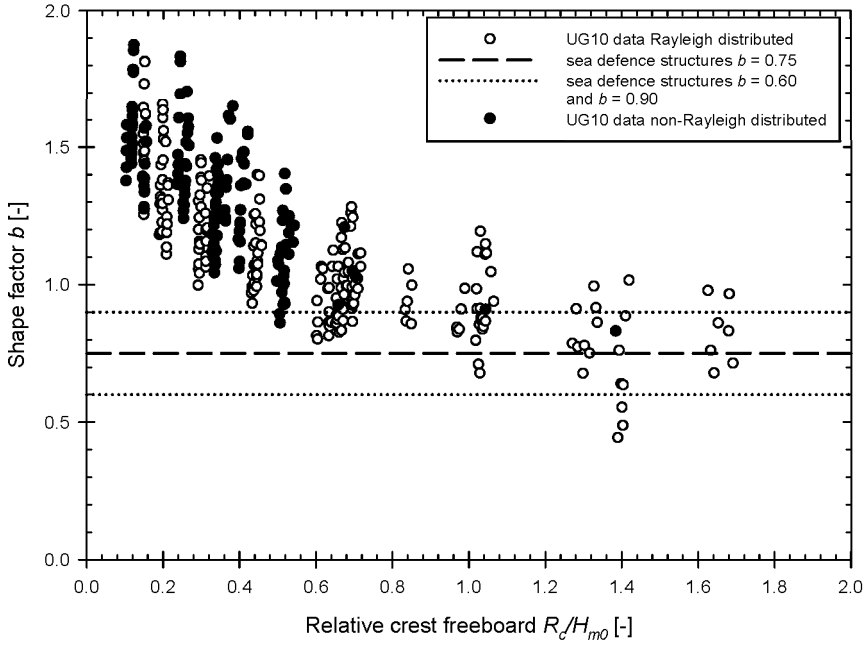

Figure 8.15: Effect of the relative crest freeboard on the shape factor b, for UG10 test results with Rayleigh distributed wave height and non-Rayleigh distributed wave heights.

8.4.5 Effect of wave steepness on shape factor *b*

When plotting the shape factor b as a function of the wave steepness $s_{m-1,0}$ for test results of the UG10 dataset with $\cot\alpha$ = 1.0, R_c = 0.045 m and Rayleigh distributed wave heights (Fig. 8.16), no clear effect of the wave steepness on the shape factor of the Weibull distribution can be distinguished.

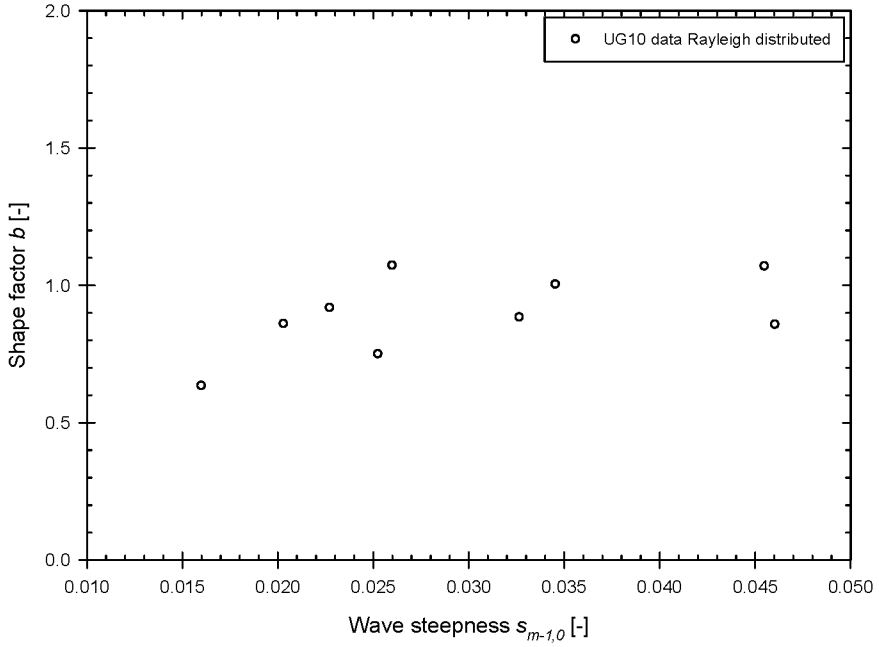

Figure 8.16: Effect of the wave steepness on the shape factor b, for UG10 test results with $\cot\alpha$ = *1.0 and* R_c = *0.045 m - Rayleigh distributed wave heights.*

Based on similar graphs for other sets of slope angle and crest freeboard, the general conclusion is drawn that the effect of the wave steepness on the shape of the Weibull distribution of the individual volumes for steep low-crested slopes is negligible compared to the effects of the slope angle (section 8.4.3) and the relative crest freeboard (section 8.4.4). This is in contrast to the findings by Besley (1999)

that an increase in the value of the shape factor occurs for increasing wave steepness (Table 8.2).

Note that the effect of the wave steepness on the shape of the Weibull distribution for rubble mound breakwaters has also been neglected (Bruce et al. 2009).

8.4.6 Prediction formula for shape factor *b* of Weibull distribution for steep low-crested slopes

Based on sections 8.4.3 to 8.4.5, the shape factor b of the two-parameter Weibull distribution of the individual overtopping volumes for steep low-crested slopes appears to be a function of the slope angle and the relative crest freeboard. The effect of the wave steepness on b is negligible.

The shape factor b describes a decreasing exponential trend for increasing relative crest freeboard that is quasi-parallel for each value of the slope angle (Fig. 8.15). The exponential trend lines become horizontal for relatively large crest freeboards; the corresponding values of the shape factor decrease for increasing slope angle (Fig. 8.11). Accordingly, the following expression is valid for the shape factor b (f_1 and f_2 are random functions here):

$$\begin{cases} b = \exp\left(-C1\dfrac{R_c}{H_{m0}}\right) + C2 \\ C1 = f_1\left(\cot\alpha\right) \\ C2 = f_2\left(\cot\alpha\right) \end{cases} \tag{8.28}$$

Since the trend lines for each slope angle in Fig. 8.15 are quasi-parallel, the dependency of $C1$ on the slope angle is expected to be rather weak. Based on section 8.4.3, f_2 is expected to be a linear function of $\cot\alpha$, increasing for an increasing value of $\cot\alpha$.

Values of $C1$ and $C2$ have been determined based on a non-linear regression analysis of the shape factors of the UG10 test results, for each category of the slope angle, containing both tests with Rayleigh and non-Rayleigh distributed wave heights. The corresponding values are given in Table 8.3 and visually shown in Figs. 8.17 and 8.18.

Table 8.3: Values of C1 and C2 (Eq. 8.28) for UG10 test results.

cot α	***C1***	***C2***
2.75	1.92	0.93
2.14	2.07	0.91
1.73	1.90	0.83
1.43	1.79	0.76
1.19	1.97	0.71
1.00	2.55	0.75
0.84	2.64	0.74
0.58	1.90	0.60
0.36	1.91	0.59

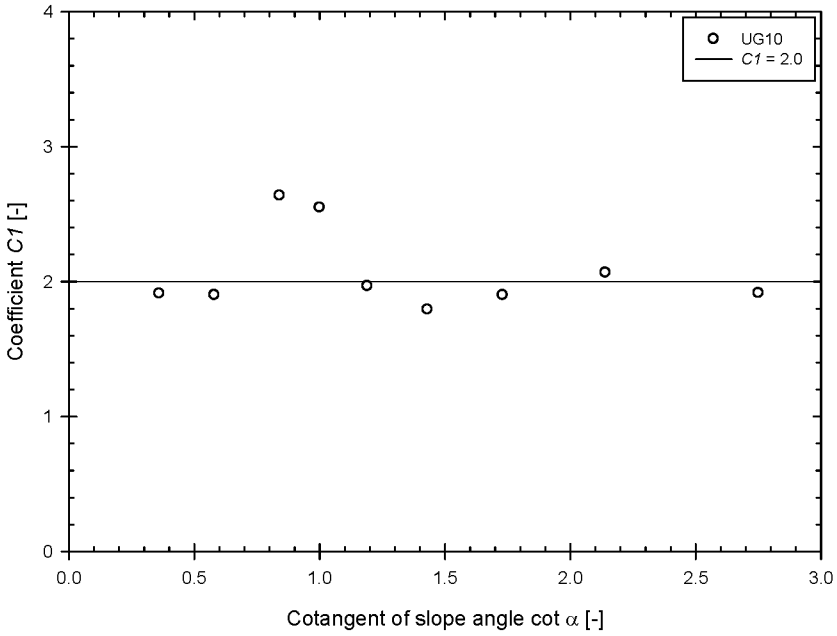

Figure 8.17: Effect of slope angle on the coefficient C1 of Eq. (8.28).

Table 8.3 confirms that the dependency of the coefficient *C1* on the slope angle is relatively weak. It approximates the constant value of 2.0 (Fig. 8.17). Furthermore, the coefficient *C2* increases linearly for increasing value of $\cot\alpha$ (Fig. 8.18).

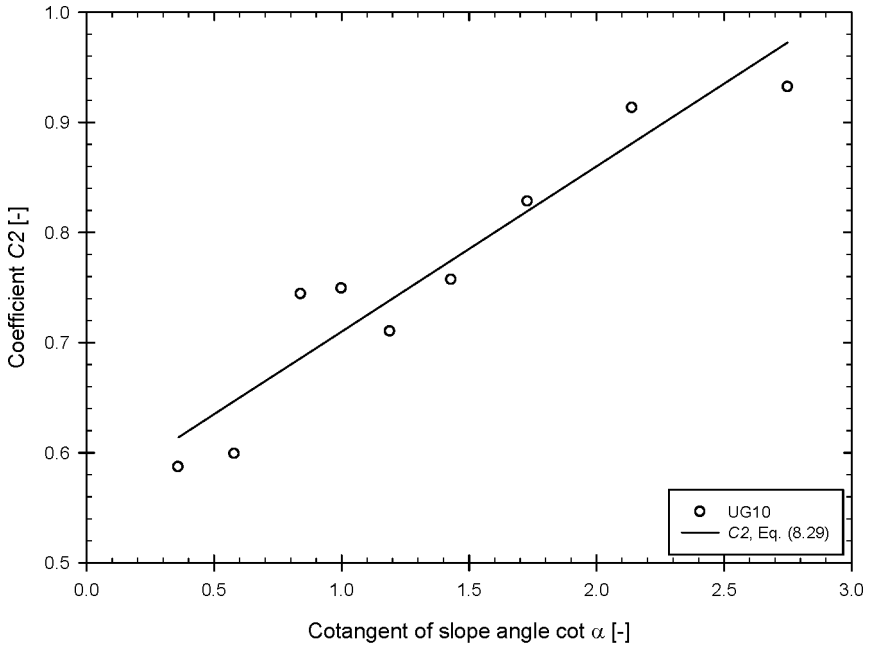

Figure 8.18: Effect of slope angle on the coefficient C2 of Eq. (8.28).

Eventually, the following prediction formula for the shape factor *b* for steep low-crested slopes has been found based on the UG10 test results:

$$b = \exp\left(-2.0\frac{R_c}{H_{m0}}\right) + \left(0.56 + 0.15\cot\alpha\right) \tag{8.29}$$

Measured and predicted values of the shape factor are shown in Fig. 8.19. The reliability of Eq. (8.29) is expressed by applying an *rmse* value of 0.10. Accordingly, the 90% prediction interval is determined by $b \pm 1.645\,rmse$; this interval is added to Fig. 8.19. The shape factor corresponding to the horizontal part of the exponential

function in Eq. (8.29) for $\cot\alpha = 0.0$ and for relatively large crest freeboards equals 0.56. This value is closer to the value of 0.66 suggested by Besley (1999) for vertical walls under non-impulsive wave attack (Table 8.2) than to the value of 0.75 suggested by Franco et al. (1994) for vertical walls with a large relative crest freeboard in relatively deep water.

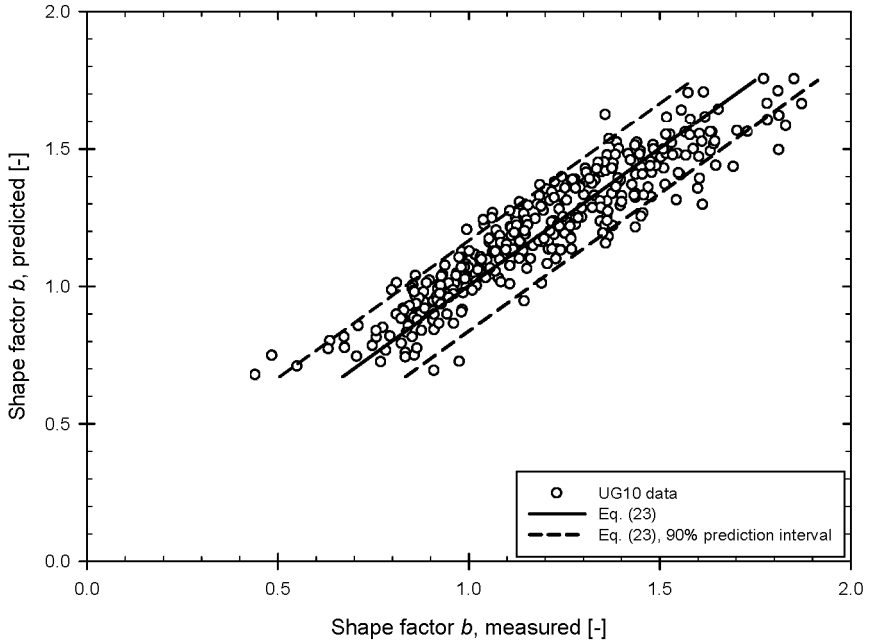

Figure 8.19: Comparison between measured and predicted (Eq. 8.29) shape factors.

The validity of Eq. (8.29) is confirmed when plotting experimentally determined shape factors and predicted values of Eq. (8.29) as a function of the relative crest freeboard for $\cot\alpha = 2.75$ (Fig. 8.20) and $\cot\alpha = 0.36$ (Fig. 8.21).

Since the coefficients *C1* and *C2* are based on all UG10 test results, the effect of the distribution of the wave heights (Rayleigh or non-Rayleigh) is included in the scatter of the shape factor of the Weibull distribution for the individual overtopping volumes of steep low-crested slopes.

The shape of the Weibull distribution of the individual overtopping volumes for steep low-crested structures is determined based on Eq. (8.29). In order to determine the scale factor a (Eq. 8.9a), knowledge on the probability of overtopping P_{ow} of steep low-crested slopes is required. This is the subject of the next section 8.5.

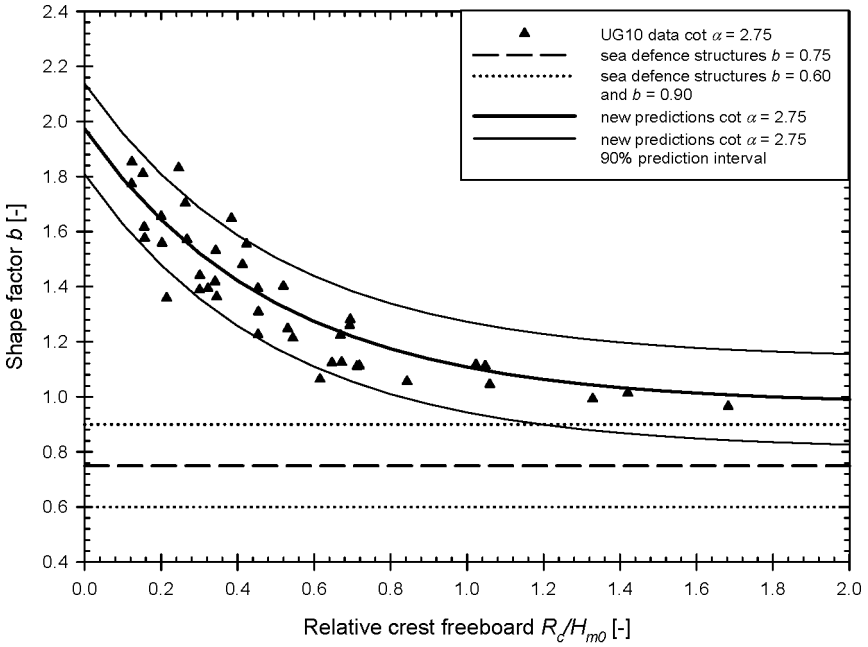

Figure 8.20: Effect of the relative crest freeboard on the shape factor b (measured and predicted by Eq. (8.29)) for UG10 test results with $\cot\alpha = 2.75$.

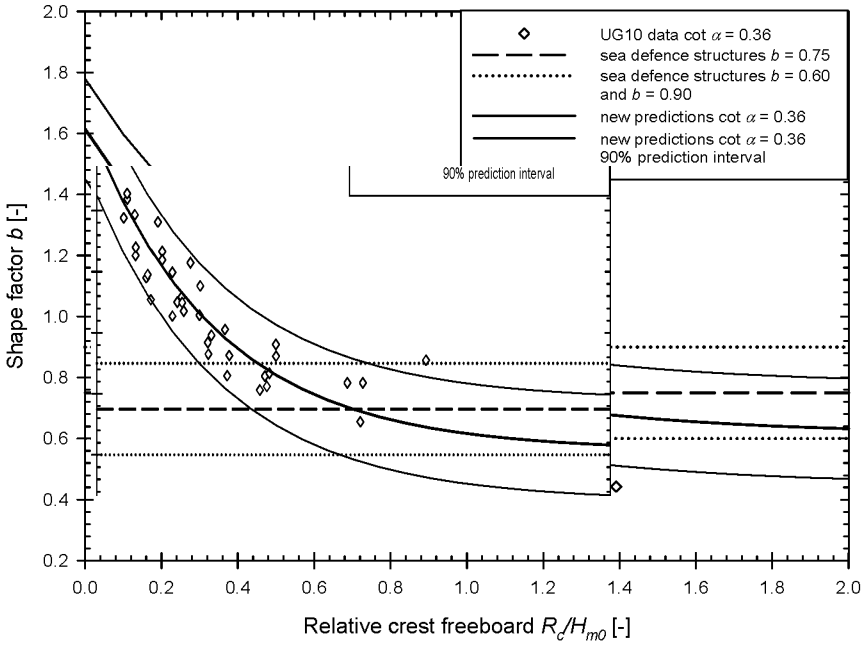

Figure 8.21: Effect of the relative crest freeboard on the shape factor b (measured and predicted by Eq. (8.29)) for UG10 test results with $\cot\alpha = 0.36$.

8.5 Overtopping probability for test results of the UG10 dataset

The expressions for the probability of overtopping P_{ow} in section 8.2.2 are based on a Rayleigh distribution of the run-up heights, requiring the wave heights to be Rayleigh distributed as well. It is unclear if the run-up heights are Rayleigh distributed when the wave heights are not Rayleigh distributed. Since the structures studied in this PhD-research feature relatively low crest freeboards, the effect of non-Rayleigh distributed wave heights on P_{ow} is expected to be relatively small.

The effects of the slope angle, relative crest freeboard and wave steepness on the probability of overtopping for the UG10 test results are discussed in the following three sections 8.5.1 to 8.5.3.

8.5.1 Effect of slope angle on P_{ow}

Translating the relative 2% run-up height in Fig. 8.3 to probabilities of overtopping using Eqs. (8.15) and (8.16) results in Fig. 8.22, to which specific measured values of P_{ow} for the UG10 dataset are added for a given relative crest height of $R_c / H_{m0} = 0.45$. The effect of the slope angle on the probability of overtopping for steep slopes is clearly visible. A significant decrease in P_{ow} occurs for increasing slope angle from the values predicted by Eqs. (8.17) and (8.19) towards the theoretical value for vertical walls. This trend also occurs for tests of the UG10 test series with non-Rayleigh distributed wave heights (Fig. 8.23).

Based on Fig. 8.22, it is clear that when the breaker parameter increases due to a decrease in the wave steepness (heavily breaking waves on very depth limited foreshores, see Van Gent 2001), an increase in the probability of overtopping occurs. On the other hand, when an increase in breaker parameter occurs due to an increase in the slope angle, a decrease in the probability of overtopping is to be expected.

The value of P_{ow} for vertical walls is related to the theoretical value of the relative 2% run-up height given in Eq. (8.25). Based on Eqs. (8.15) and (8.16), the corresponding expression for the probability of overtopping for vertical walls is found:

$$\chi = 0.51 \cdot 1.4 = 0.71 \qquad (8.30a)$$

$$\Rightarrow P_{ow} = \exp\left(-\left(1.4\frac{R_c}{H_{m0}}\right)^2\right) \tag{8.30b}$$

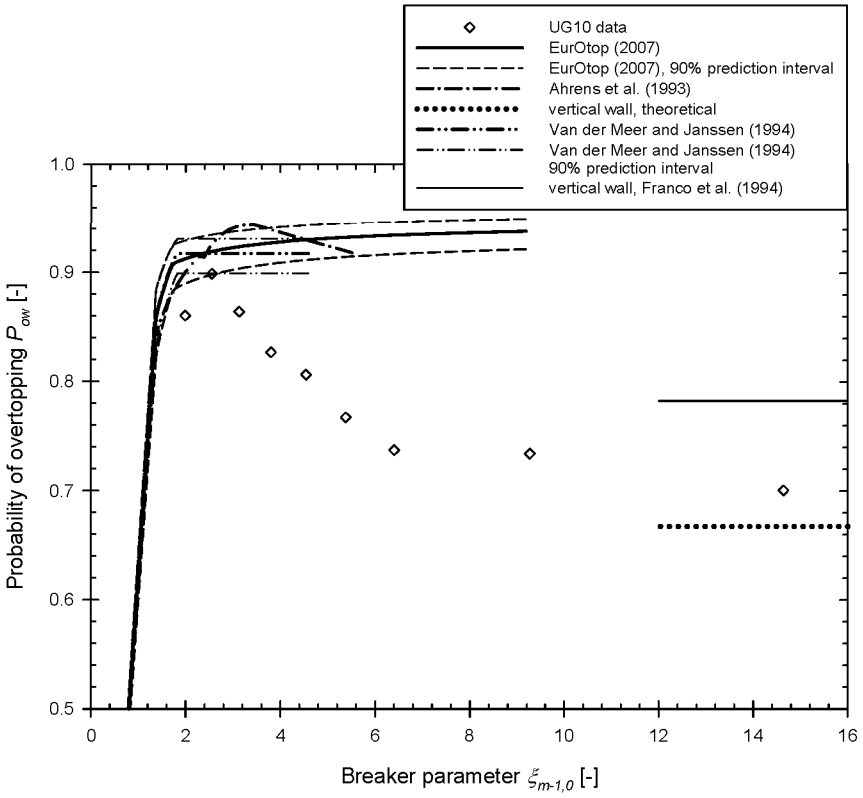

Figure 8.22: Measured and predicted probabilities of overtopping for UG10 test results with H_{m0} = 0.100 m, R_c = 0.045 m and T_p = 1.534 s versus the breaker parameter – Rayleigh distributed wave heights.

Note that Franco et al. (1994) found a value of $\chi = 0.91$ for vertical walls in relatively deep water, resulting in a probability of overtopping that is larger than calculated by Eq. (8.30b):

$$P_{ow} = \exp\left(-\left(1.1\frac{R_c}{H_{m0}}\right)^2\right) \tag{8.30c}$$

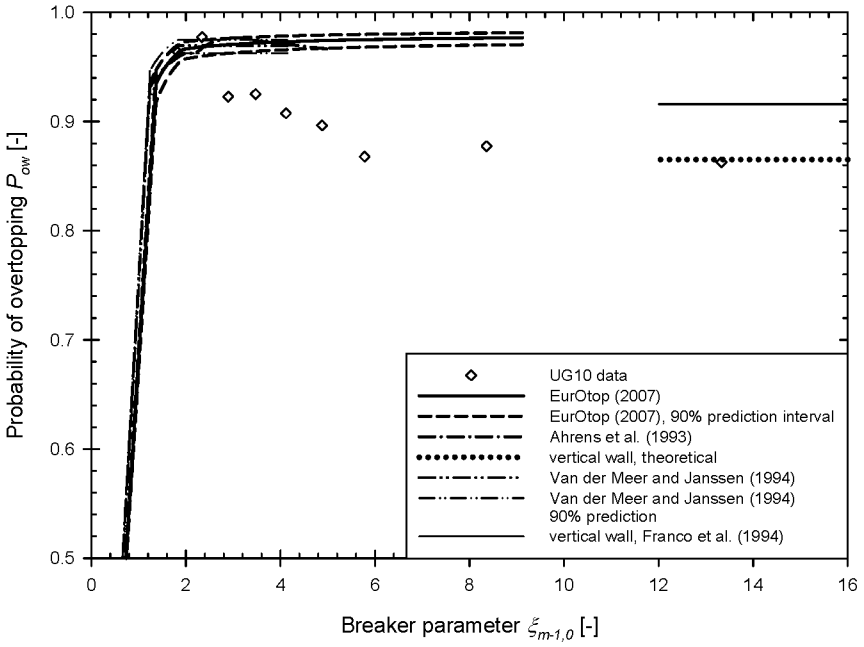

Figure 8.23: Measured and predicted probabilities of overtopping for UG10 test results with H_{m0} = 0.167 m, R_c = 0.045 m and T_p = 1.789 s versus the breaker parameter – non-Rayleigh distributed.

Equations (8.30b) and (8.30c) show that the effect of the relative crest freeboard on the probability of overtopping is according to a Rayleigh distribution. The effect of the relative crest freeboard on P_{ow} is studied in section 8.5.2.

8.5.2 Effect of relative crest freeboard on P_{ow}

A decrease in the relative crest freeboard R_c / H_{m0} causes an increase in P_{ow} for a specific slope angle (Fig. 8.24). This is valid for all UG10 tests, including tests with Rayleigh and non-Rayleigh distributed wave heights (Fig. 8.25).

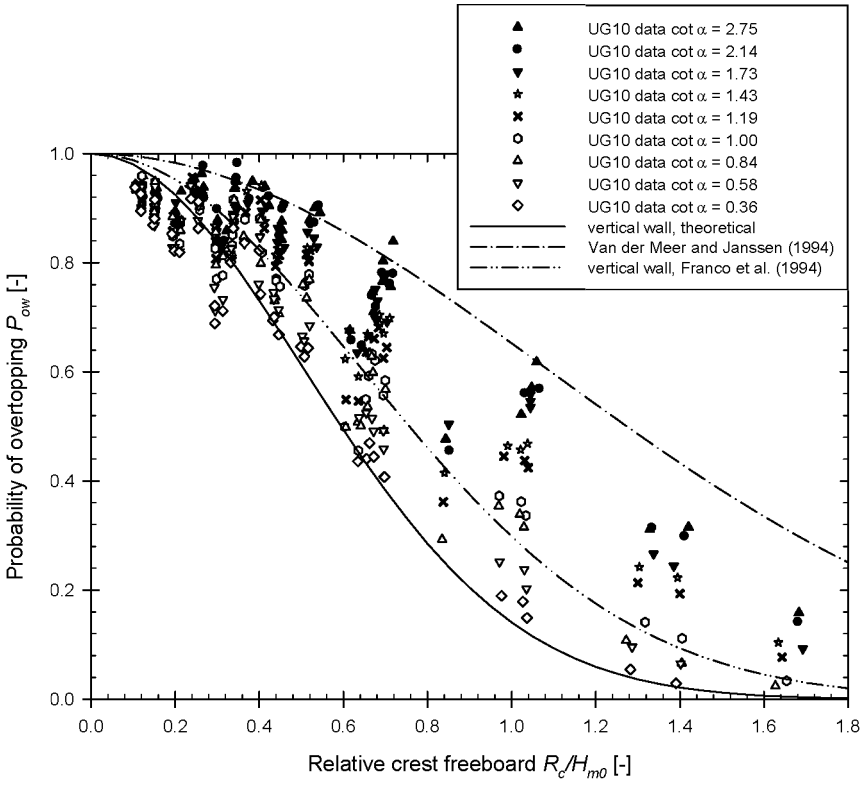

Figure 8.24: Effect of relative crest freeboard on probability of overtopping for UG10 test results, categorized by the slope angle.

The probabilities of overtopping for tests of the UG10 test series with non-Rayleigh distributed wave heights are positioned among the values of P_{ow} for the tests with Rayleigh distributed wave heights. This confirms that the effect of the wave height distribution on P_{ow} is small for relatively small crest freeboards.

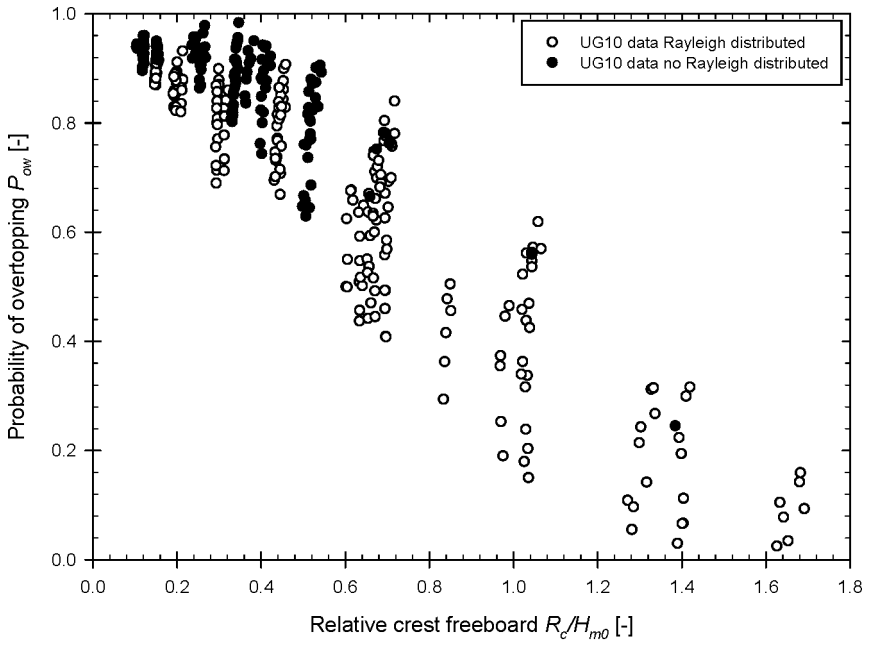

Figure 8.25: Effect of relative crest freeboard on probability of overtopping for UG10 test results – Rayleigh distributed versus non-Rayleigh distributed wave heights.

There are two physical bounds for P_{ow} that are clearly visible in Figs. 8.24 and 8.25: P_{ow} becomes 1.0 for a zero relative crest freeboard (all waves overtop the crest of the structure) and 0.0 for very large relative crest freeboards (no waves overtop the structure), the last dependent of the slope angle.

The predicted effect of the relative crest freeboard on the probability of overtopping is shown in Fig. 8.24 for the theoretical value of P_{ow} for vertical walls (Eqs. 8.30b and 8.30c) and for the probability of overtopping related to the relative 2% run-up height predicted by Van der Meer and Janssen (1994) (Eq. 8.31).

$$\chi = 0.51 \cdot 3.0 = 1.53 \tag{8.31a}$$

$$\Rightarrow P_{ow} = \exp\left(-\left(0.65\frac{R_c}{H_{m0}}\right)^2\right) \tag{8.31b}$$

The UG10 data points are largely positioned in between the prediction lines corresponding to Eqs. (8.30b) and (8.31b).

8.5.3 Effect of wave steepness on P_{ow}

The effect of the wave steepness $s_{m-1,0}$ on the probability of overtopping P_{ow} is shown in Fig. 8.26 for the tests of the UG10 dataset with $\cot\alpha$ = 1.0, R_c = 0.045 m and H_{m0} = 0.067 m, 0.100 m and 0.133 m.

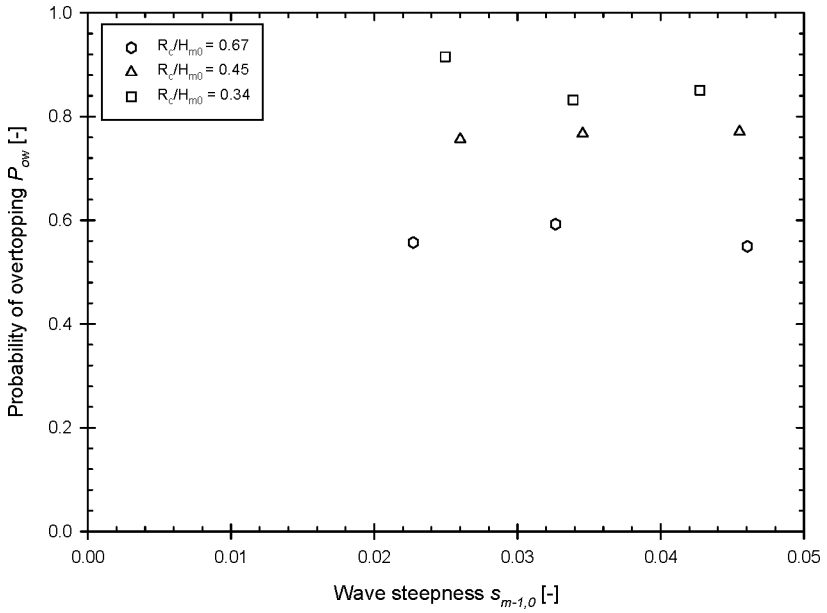

Figure 8.26: Effect of wave steepness on probability of overtopping for UG10 test results with $\cot\alpha$ *=1.00,* R_c *= 0.045 m and* H_{m0} *= 0.067 m, 0.100 m and 0.133 m. Data categorized by the relative crest freeboard.*

The data points are categorized by the wave height. Based on Fig. 8.26, the effect of the wave period on P_{ow} is considered to be negligible compared to the effects of the slope angle (section 8.5.1) and the relative crest freeboard (section 8.5.2). Similar graphs for other sets of $\cot\alpha$ and R_c/H_{m0} confirm this conclusion.

8.5.4 Prediction formula for probability of overtopping P_{ow} for steep low-crested slopes

Based on Fig. 8.24, the increase in P_{ow} with a decrease in relative crest freeboard R_c/H_{m0} for a particular slope angle is assumed to be well described by a Rayleigh distribution using the relative crest freeboard:

$$P_{ow} = \exp\left(-\left(C3\frac{R_c}{H_{m0}}\right)^2\right) \tag{8.32}$$

The expression in Eq. (8.32) is similar to Eq. (8.15), with $\chi = 1/C3$. It takes into account the two physical bounds given in section 8.5.2. Due to the negligible effect of the wave steepness on the probability of overtopping, *C3* is not a function of the wave steepness. Since Eq. (8.32) contains the relative crest freeboard, *C3* is expected to be only a function of the slope angle. Indeed, the values of P_{ow} of the UG10 test results are accurately described by a Rayleigh distribution for each category of the slope angle. However, when plotting the values of *C3* obtained by $C3 = \sqrt{-\left(\ln\left(P_{ow}\right)\right)}/\left(R_c/H_{m0}\right)$ against the relative crest freeboard (Fig. 8.27), one may conclude that *C3* is still a function of the relative crest freeboard. The values of *C3* are approximately independent of the relative crest freeboard for $R_c/H_{m0} > 0.4$, but increase considerably when the relative crest freeboard decreases to very low values.

On the other hand, the probability of overtopping P_{ow} is expected to be approximately equal to 1.0 for very small relative crest freeboards. This means that the large values of *C3* in Fig. 8.27 are introduced by the small relative crest freeboards R_c/H_{m0} in the expression $C3 = \sqrt{-\left(\ln\left(P_{ow}\right)\right)}/\left(R_c/H_{m0}\right)$.

Hence, the coefficient *C3* is assumed to be independent of the relative crest freeboard, determined by the values of *C3* with $R_c/H_{m0} > 0.4$ (Fig. 8.27). The corresponding values of *C3* are given in Table 8.4 for each category of the slope

angle (shown in Fig. 8.28) and are valid for tests both with and without Rayleigh distributed wave heights (part of the scatter).

Based on Fig. 8.28, the values of *C3* appear to be accurately described by a linear function of the cotangent of the slope angle (Eq. 8.33).

$$C3 = 1.4 - 0.30\cot\alpha \qquad (C3 > 0.65) \qquad (8.33)$$

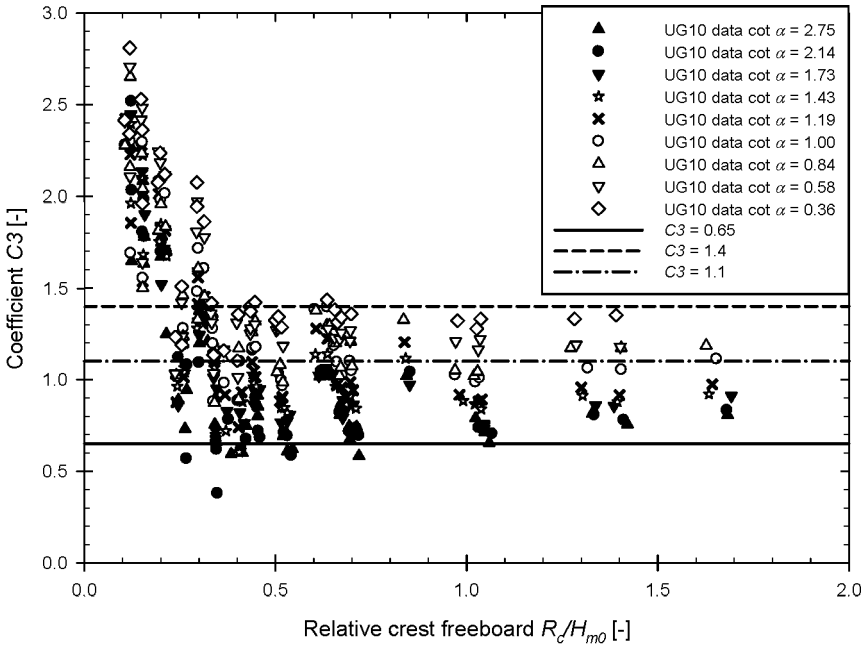

Figure 8.27: Effect of the relative crest freeboard on the coefficient C3 of Eq. (8.32).

Table 8.4: Values of C3 for UG10 test results.

cot α	***C3***
2.75	0.79
2.14	0.80
1.73	0.86
1.43	0.96
1.19	0.96
1.00	1.08
0.84	1.16
0.58	1.20
0.36	1.34

The reliability of Eq. (8.33) is expressed by applying an *rmse* value of 0.13 ($R_c / H_{m0} > 0.4$). The corresponding 90% prediction interval is added to Fig. 8.28.

Note that Eq. (8.33) takes the theoretical value of 1.4 for vertical walls (Eq. 8.30b) ($\cot\alpha = 0.0$). Furthermore, Eq. (8.33) becomes equal to 0.65 (i.e. the value of *C3* for milder slopes with non-breaking waves predicted by Van der Meer and Janssen (1994) (Eq. 8.31b)) for $\cot\alpha = 2.5$. For slopes milder than that value, P_{ow} should be predicted based on the existing formulations for P_{ow} of Van der Meer and Janssen (1994). Accordingly, the restriction $C3 > 0.65$ is added to Eq. (8.33).

The corresponding expression for the probability of overtopping is:

$$P_{ow} = \exp\left[-\left((1.4 - 0.30\cot\alpha)\frac{R_c}{H_{m0}}\right)^2\right] \quad (0.0 \le \cot\alpha \le 2.5) \qquad (8.34)$$

The *rmse* value based on the measured and predicted values of P_{ow} equals only 0.073, which shows that the predictions agree well with the measurements. This is also illustrated by the two graphs below (Figs. 8.29 and 8.30). Figure 8.29 is similar to Fig. 8.20 (relative crest freeboard $R_c / H_{m0} = 0.45$) to which the predicted values by Eq. (8.34) (together with its 90% prediction interval) have been added.

Figure 8.30 shows a similar graph for a larger relative crest freeboard: $R_c / H_{m0} = 1.04$. In both figures, the predicted probabilities of overtopping of Eq. (8.34) approach the data points of the UG10 test results quite accurately. Furthermore, the predictions tend towards the theoretical probability of overtopping for very large values of the breaker parameter (i.e. the asymptotic case of a vertical

wall) and intersect the prediction line by Van der Meer and Janssen (1994) approximately at $\xi_{m-1,0} = 3.0$.

Both figures illustrate the validity of Eq. (8.34) within the ranges of application of the UG10 test series.

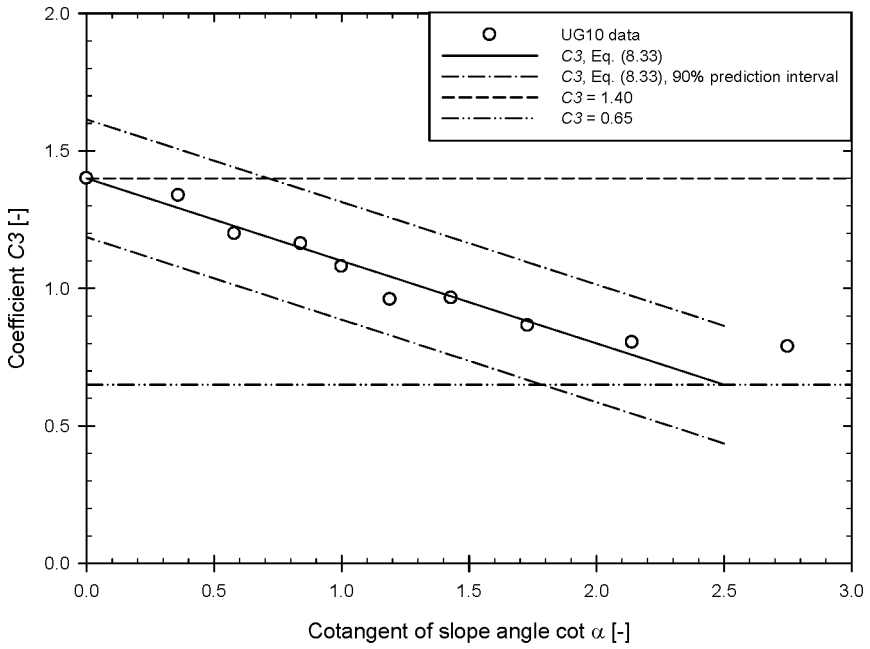

Figure 8.28: Effect of the slope angle on the coefficient C3 of Eq. (8.32).

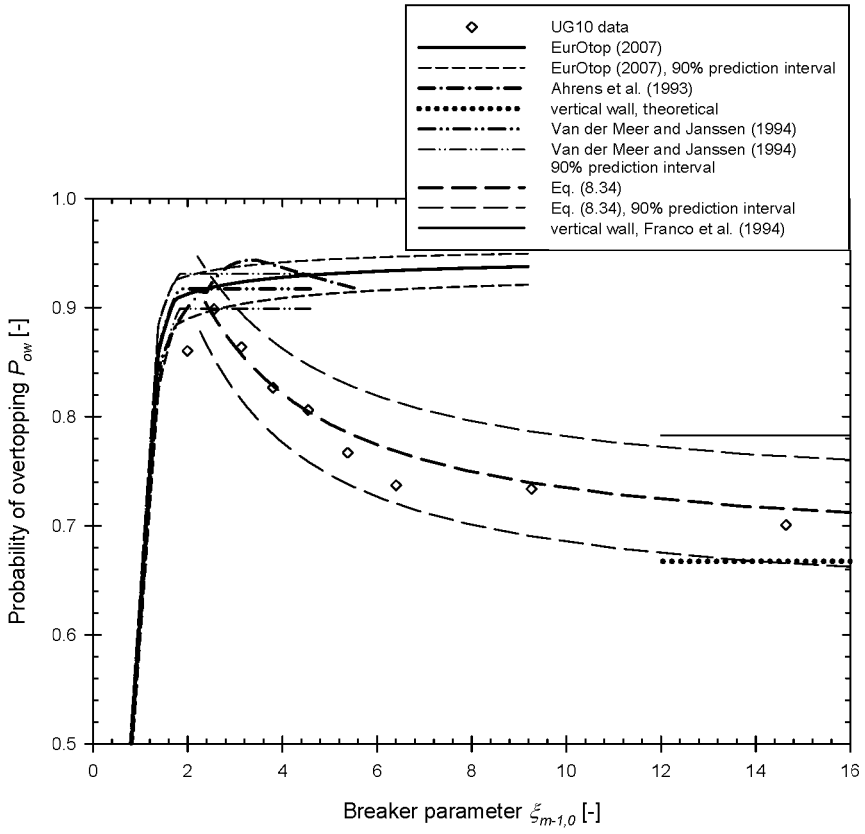

Figure 8.29: Measured and predicted probabilities of overtopping for UG10 test results with H_{m0} = 0.100 m, T_p = 1.534 s and R_c = 0.045 m versus the breaker parameter.

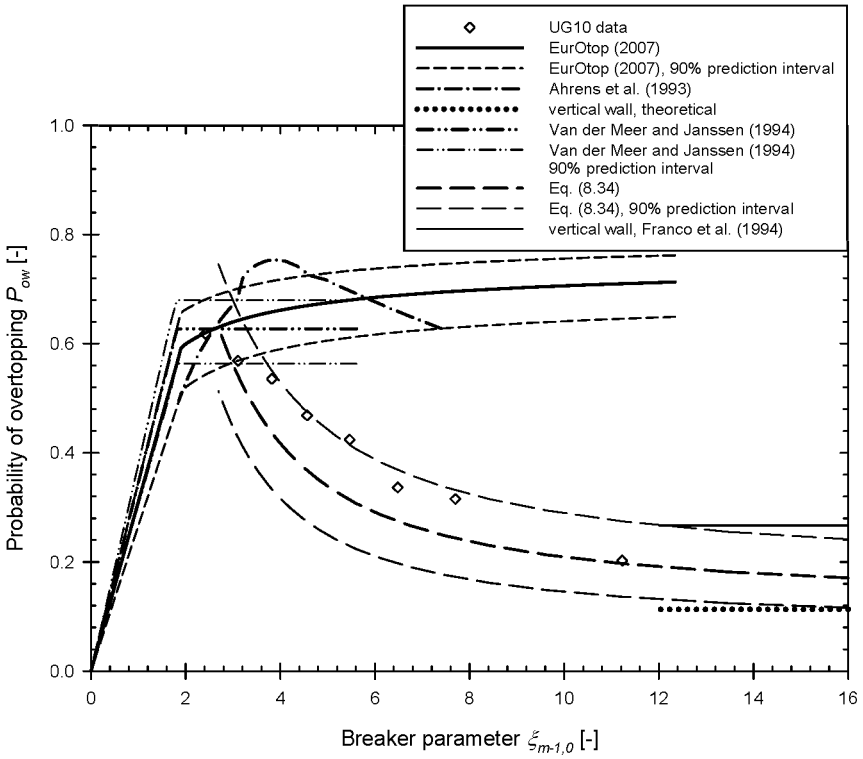

Figure 8.30: Measured and predicted probabilities of overtopping for UG10 test results with $H_{m0} = 0.067$ m, $T_p = 1.534$ s and $R_c = 0.07$ m versus the breaker parameter.

8.5.5 Prediction formula for relative 2% run-up height $R_{u2\%}/H_{m0}$ for steep low-crested slopes

Based on the expression for *C3* in Eq. (8.33), Eq. (8.16) and taking into account $\chi = 1/C3$, the following expression for the relative 2% run-up height has been derived for steep low-crested slopes in relatively deep water:

$$\frac{R_{u2\%}}{H_{m0}} = \frac{1}{0.71 - 0.15\cot\alpha} \tag{8.35}$$

It is important to note that the relationship between $R_{u2\%}/H_{m0}$ and P_{ow} established by Eqs. (8.15) and (8.16) is based on knowledge concerning $R_{u2\%}/H_{m0}$ (non-overtopped structures) applied to structures with a limited amount of wave overtopping (Franco et al. 1994; Van der Meer and Janssen 1994). This means that deriving an expression for $R_{u2\%}/H_{m0}$ based on measurements of P_{ow} is only valid for sloped structures with relatively large crest freeboards. When the relative crest freeboards are smaller, the expression derived for $R_{u2\%}/H_{m0}$ is only approximate. Since the UG10 test results feature steep low-crested slopes, the expression for the relative 2% run-up height in Eq. (8.35) only approximates the values of $R_{u2\%}/H_{m0}$ for non-overtopped steep slopes in relatively deep water. Due to the fact that the coefficients *C3* (section 8.5.4) are determined for the UG10 test results with $R_c/H_{m0} > 0.4$ that are quasi-independent of the relative crest freeboard (Fig. 8.27), the deviations between the real values of $R_{u2\%}/H_{m0}$ for steep slopes in relatively deep water and their predictions by Eq. (8.35) are expected to be relatively small.

A figure similar to Fig. 8.3 is shown in Fig. 8.31, to which the predictions by Eq. (8.35) have been added. The new prediction formula clearly confirms the expected decreasing trend of the relative 2% run-up heights for steeper slopes with increasing slope angle in relatively deep water (section 8.3.3).

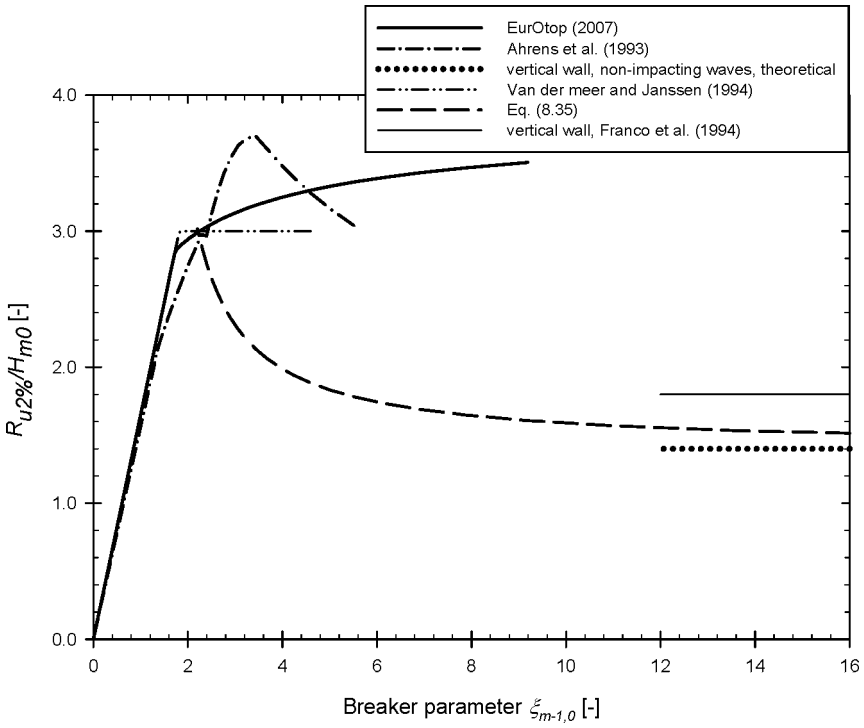

Figure 8.31: Predicted relative 2% run-up heights with $H_{m0} = 0.100$ m, $T_p = 1.534$ s and $R_c = 0.045$ m versus the breaker parameter.

8.6 Conclusions

The probability distribution of the individual overtopping volumes of steep low-crested slopes has been investigated based on the UG10 test results and through a comparison with existing formulations from literature.

Similar to traditional sea defence structures, the individual overtopping volumes appear to follow a two-parameter Weibull probability distribution, characterized by a scale factor a and a shape factor b. The scale factor a of the Weibull distribution is closely related to the probability of overtopping P_{ow}, which has also been studied based on the UG10 test results.

Both the shape factor b and the probability of overtopping P_{ow} appear to depend on the slope angle and relative crest freeboard. The effect of the wave steepness is negligible.

The effect of the relative crest freeboard on the shape factor of the Weibull distribution is described by a negative exponential function. When $R_c / H_{m0} < 1.2$, values of the shape factor $b > 0.75$ (typical value for traditional sea defence structures) have been found for the UG10 test results (up to $b = 1.8$), both for milder and steeper slopes. Accordingly, a smaller maximum volume $V_{\max}$ and a larger percentage of medium-sized overtopping volumes occur for low-crested structures compared to structures with a relatively large crest freeboard. This means that the design of traditional structures with small relative crest freeboards is conservative when applying the value of the shape factor for traditional sea defence structures $b = 0.75$. Furthermore, b follows a linear increasing trend for a decreasing slope angle, even for relatively large crest freeboards. A prediction formula (Eq. 8.29) has been derived based on the UG10 test results, which takes into account these effects.

The values of the overtopping probability P_{ow} determined for the UG10 test results with steep slopes appear to be overpredicted by the commonly used empirical prediction formulae from literature. This is due to the fact that the existing prediction formulae of P_{ow} for larger breaker parameters are based on tests with small values of the wave steepness induced by heavily breaking waves on very depth limited situations. For deeper water and $\xi_{m-1,0} \approx 3.0$, P_{ow} is more or less constant. When larger breaker parameters of $\xi_{m-1,0} > \approx 3.0$ are caused by larger slope angles, a decrease in probability of overtopping occurs which is described by a linear function of the cotangent of the slope angle. Furthermore, the effect of the relative crest freeboard on P_{ow} is described by a Rayleigh distribution of R_c / H_{m0}, decreasing

from P_{ow} = 1.0 for a zero crest freeboard (all waves overtop the structure) to P_{ow} = 0.0 for large relative crest freeboards (no waves overtop the structure). Similar to *b*, a prediction formula has been derived that takes into account these effects. Based on this prediction formula and the relationship between the relative 2% run-up height $R_{u2\%}/H_{m0}$ and P_{ow} established in literature for sloped structures with limited wave overtopping, a new prediction formula has been proposed for $R_{u2\%}/H_{m0}$ at steep slopes in relatively deep water. Since this formula is based on the UG10 test results that feature relatively small crest freeboards, the new predictions of $R_{u2\%}/H_{m0}$ are only approximate. Nevertheless, these predictions indicate that a decrease in the relative 2% run-up height should occur for steep slopes in relatively deep water with increasing slope angle.

The importance of the distribution of the incident wave heights has been investigated, both for the shape factor *b* and for the probability of overtopping P_{ow}. When the wave heights are not Rayleigh distributed, slightly larger values of the shape factor are found, while the effect of the wave height distribution on the probability of overtopping appears to be relatively small. The effect of the distribution of the wave heights is part of the scatter on the new prediction formulae for *b* and P_{ow} based on the UG10 test results.

The improved knowledge on the probability distribution of low-crested structures achieved in this chapter allows to carry out more realistic simulations of wave-by-wave overtopping volumes in order to optimize the design of the reservoir and the turbine control strategy of OWECs.

Moreover, this knowledge is applicable to sea defence structures in severe storm conditions, when a low crest freeboard occurs. Applying a shape factor $b > 0.75$ results in more realistic (lower) maximum overtopping volumes than when applying the shape factor $b = 0.75$ for traditional sea defence structures with relatively large crest freeboards.

9

Conclusions and recommendations for further work

9.1 General conclusions

This PhD-research fits within the search for economically viable sources of renewable energy. Wave energy, i.e. energy from ocean waves, is a promising renewable energy source, but its possibilities are not yet fully explored. The optimization of a particular type of wave energy converter has been studied in this PhD-research: overtopping wave energy converter (OWEC). The working principle of an OWEC is based on waves running up a slope and overtopping into a reservoir, which is emptied into the ocean through a set of low-head turbines (chapter 1). Until present, rather complex OWECs have been studied in literature. In order to further optimize the performance of OWECs, a fundamental study on the relationship between the geometry, wave characteristics and power output has been carried out in this PhD-research, for a simplified geometry, i.e. single reservoir OWECs with a uniform slope extending to the seabed. In particular, two aspects have been studied in detail:

- the optimal (adaptive) geometry for these OWECs in relation to the wave characteristics that results in a maximum power output; and the corresponding reflection coefficient

- the probability distribution of the individual overtopping volumes of these OWECs. When this probability distribution is known a priori, simulations can be carried out of series of incoming overtopping volumes, enabling to

optimize the turbine control strategy and the size of the reservoir of the OWEC.

Hence, this PhD-manuscript summarizes the results of a fundamental study on the relationship between the geometry of a simplified OWEC and (1) the average overtopping rate, (2) the reflection coefficient and (3) the probability distribution of the individual overtopping volumes.

Since the obtained power needs to be maximized, it is clear that the OWECs feature a particular geometry: a uniform smooth impermeable steep slope with a low crest freeboard (chapter 1). The number of test results on steep-low crested slopes available in literature appeared to be very limited. Therefore, experimental tests have been carried out during this PhD-research, which enable to study each of the three relationships above.

Correspondingly, the methodology is based on an experimental study (chapters 2 and 3). Two laboratory test set-ups have been developed during this PhD-research which enable to measure large wave-by-wave overtopping volumes accurately: AAU08 test series (207 tests) and the more accurate UG10 test series (366 tests). Both test set-ups are based on the weigh cell technique, which is traditionally used for measuring small wave overtopping masses at scale models of sea defence structures. A number of adaptations have been carried out to the traditional weigh cell technique. The adaptations for the most accurate UG10 test set-up consist of structural adjustments and measures taken in the data acquisition system (a small sampling frequency for the weigh cell, a binary signal) and during the analysis of the output signals. The structural adjustments incorporate a decrease of the length of the chute (installation of the weigh cell inside the wave flume), the installation of a proper overtopping detection system, the application of a pump with a return valve to pump water from the reservoir to the wave flume (with accurate calibration curve and pump compensation), allowing wave overtopping over the whole width of the flume, guiding the outflow of the pump to the front of the wave flume below the structure and limiting the oscillations of the water inside the reservoir. A methodology has been developed to determine the average overtopping rates and large wave-by-wave overtopping volumes accurately for the adjusted test set-ups and has been programmed in a Matlab®-script. This script appeared to be very effective to determine the average overtopping rates and individual overtopping masses, in particular for the more accurate UG10 test set-up.

Broad ranges of slope angle, crest freeboard, wave characteristics have been applied. This means that the acquired knowledge in this PhD-research is not only applicable to OWECs, but also to sea defence structures in severe storm conditions, i.e. when low crest freeboards occur. Hence, the structures studied in this PhD-

research have been referred to as *steep low-crested slopes* throughout this PhD-manuscript.

Consequently, two deliverables of this PhD-research are:

- an extensive database, containing the average overtopping rates, reflection coefficients and individual overtopping volumes of experimental tests on steep low-crested slopes with broad ranges of application for the slope angle, relative crest freeboard and wave steepness. This database will be freely accessible and can be used for comparison with other measurements or for further training of the DHNN tool;

- a test set-up (UG10) and corresponding data analysis methodology, which enable to measure both (large) average overtopping rates and (large) wave-by-wave overtopping volumes accurately. The developed test set-up and measurement technique could be used as a reference for carrying out accurate overtopping measurements.

The deliverables for each of the four objectives for this PhD-research (chapter 1) in particular (which have been met based on the experimental study) are given below (section 9.2).

9.2 Conclusions and results for each objective

1. *Detailed study of relationship between OWEC geometry, wave characteristics and wave overtopping*

First, an overview of the existing knowledge on the average overtopping rates of steep low-crested slopes has been given (chapter 4). A number of commonly used prediction models (originally developed for sea defence structures) appear to be valid within the ranges of application of steep low-crested slopes. The ranges of application and reliability of these models have been described. Furthermore, prediction models for the overtopping behaviour of vertical walls under non-impulsive wave attack and of structures with zero crest freeboard have been given, since these structures determine the asymptotic (from a geometrical point of view) overtopping behaviour for steep low-crested slopes.

In a next step, a comparison between the predicted and measured average overtopping rates for the AAU08 and UG10 test series (chapter 5) has been carried out. This allowed to study the independent effects of the slope angle, relative crest

freeboard and wave period on the average overtopping rates of steep low-crested slopes, and their interactions.

Two zones of different overtopping behaviour have been identified for the slope angle, separated by $\cot\alpha = 1.5$. Slopes with $1.5 < \cot\alpha < 3.0$ correspond to the largest average overtopping rates, for which a weak dependency of the dimensionless average overtopping rate on the slope angle occurs. When assuming that this dependency is significant, a maximum average overtopping rate occurs for $\xi_{m-1,0} = 3.0$. When $\cot\alpha < 1.5$, a sharp decrease in average overtopping rate occurs for increasing slope angle towards the predicted rate for vertical walls under non-impulsive wave attack.

Furthermore, two zones of different overtopping behaviour have been identified for the relative crest freeboard, separated by $R_c / H_{m0} = 0.80$. The slope of the decreasing linear trend line of the data points with $R_c / H_{m0} < 0.80$ in a log-linear graph of the dimensionless average overtopping rate as a function of the relative crest freeboard is milder than the slope of the decreasing linear trend line of the data points with $R_c / H_{m0} > 0.80$.

The interaction between the effect of the slope angle and the effect of the relative crest freeboard appears to be expressed by an increased effect of the slope angle for larger relative crest freeboards. When the relative crest freeboard becomes very small, the effect of the slope angle becomes negligible.

Eventually, combining the zones of different overtopping behaviour for the slope angle and relative crest freeboards, four zones have been identified:

- zone Z1: $0.0 \le \cot\alpha \le 1.43$ and $0.0 \le R_c / H_{m0} \le 0.8$
- zone Z2: $0.0 \le \cot\alpha \le 1.43$ and $0.8 \le R_c / H_{m0} \le 2.0$
- zone Z3: $1.73 \le \cot\alpha \le 2.75$ and $0.0 \le R_c / H_{m0} \le 0.8$
- zone Z4: $1.73 \le \cot\alpha \le 2.75$ and $0.8 \le R_c / H_{m0} \le 2.0$

None of the prediction models described in chapter 4 appeared to be able to predict the average overtopping rates accurately for all zones Z1 to Z4. The DHNN tool (neural network tool) is the most accurate prediction model, but it tends to overpredict the average overtopping rates in zone Z2. Furthermore, it has wide 90% prediction intervals due to its wide ranges of application. Enhanced by the ability to incorporate physical insights in an empirical formula, a set of new prediction formulae (the UG10 formulae) has been derived based on the UG10 test results, in order to predict the average overtopping rates accurately for each of the zones Z1 to Z4. For the zones Z3 and Z4, two expressions have been derived, incorporating or neglecting the effect of the slope angle. The differences between the average

overtopping rates determined by both expressions are small, but predictions appeared to be more accurate when incorporating the effect of the slope angle. The ability of the UG10 formulae to predict the independent effects of the slope angle and the crest freeboard (and their interactions) accurately for steep low-crested slopes has been illustrated in a number of graphs.

2. *Detailed study of the relationship between OWEC geometry, wave characteristics and wave reflection*

The reflection coefficients measured during the UG10 test series have been used to study the reflective behaviour of steep low-crested structures (chapter 6). The approach suggested in literature to predict the reflection coefficient of low-crested rock slopes consists of applying a reduction factor for smaller relative crest freeboards to a prediction formula for non-overtopped rock slopes. This approach has not yet been applied to smooth impermeable structures with small relative crest freeboards. Based on the reflection coefficients measured during the UG10 test series, this methodology appeared to be applicable to steep low-crested slopes. The new prediction formula for the reflection coefficient of steep low-crested slopes combines a prediction formula for larger relative crest freeboards and a reduction factor, both from literature.

Furthermore, a relationship between the average overtopping rate and the reflection coefficient has been established, based on the energy balance equation. It appears that an increase in the dimensionless average overtopping rate causes a decrease in the reflection coefficient for non-breaking waves. An identical conclusion is valid for structures with a relatively small crest freeboard subjected to breaking waves, when the increase in average overtopping rate is determined by a decrease in relative crest freeboard.

3. *Case study on "adaptive geometry" for OWECs*

The optimal geometry of an OWEC is based on a maximization of the overall hydraulic efficiency, which is the ratio of the overall (hydraulic) power of the water at the crest of the slope to the overall wave power (overall means summed over all characteristic sea states at a particular deployment site). Traditionally, the overall hydraulic efficiency is maximized for a fixed geometry. Geometry control (adaptive geometry) consists of adapting the slope angle and crest freeboard of the OWEC to each sea state to obtain a maximum hydraulic efficiency for each sea state and thus a larger overall hydraulic power and efficiency. The optimal slope angle for a sea state (subscript *j*) is determined by the condition when: $\tan\alpha_j = 3.0\sqrt{s_{m-1,0,j}}$ (chapter 5), while the optimal crest freeboard should fulfil $R_{c,j}/H_{m0,j} = 0.59$. The corresponding

maximum hydraulic efficiency is only dependent on the wave steepness, while the corresponding reflection coefficient is 0.57 (chapter 6).

Since applying such optimal geometry is not straightforward, four additional scenarios have been studied (chapter 7), which correspond to a more simplified control of the geometry. These scenarios include the traditional fixed scenario, i.e. with a fixed slope angle and a fixed crest freeboard. The overall hydraulic efficiency, overall hydraulic power and reflection coefficient have been calculated for each of the five scenarios for OWECs at three hypothetical deployment sites: Ostend (Belgian Continental Shelf), MPN (Dutch Continental Shelf) and Fjaltring (Danish Continental Shelf), i.e. nearshore locations not subjected to swells (fulfilling the ranges of application of the UG10 test series). It appeared that applying an adaptive crest freeboard considerably increases the obtained overall hydraulic efficiency and power. The effect of an adaptive slope angle is relatively small. The best practically realizable scenario features a hinge installed at the bottom of the slope, combined with an adaptive crest freeboard control strategy. Based on the calculations, the gain in mean overall hydraulic power for that scenario compared to a fixed geometry is approximately 10%.

Furthermore, the overall reflection coefficient (based on the sea states with the largest frequencies of occurrence) appears to be minimal for scenario 1: $K_{r,overall}$ = 0.57. When fixing the geometrical components, an increase in the overall hydraulic efficiency occurs, up to a value of approx. 0.80 for the fully fixed geometry, i.e. scenario 4. Since the reflection coefficient is still rather large for each of the scenarios, a proper toe protection should be applied for the OWECs studied in this PhD-manuscript.

4. Detailed study on the distribution of the wave-by-wave overtopping volumes for OWECs

The probability distribution of the individual overtopping volumes of steep low-crested slopes has been studied based on the UG10 test results (chapter 8). It is accurately described by a two-parameter Weibull probability distribution, similar to traditional sea defence structures.

However, the shape factor of the Weibull distribution is considerably larger (up to b = 1.8) than the value of b = 0.75 (typical for traditional sea defence structures) for relatively small crest freeboards, both for milder and steeper slopes. This means that a smaller maximum volume V_{max} and larger percentage of medium-sized overtopping volumes occur for low-crested structures compared to structures with a relatively large crest freeboard. Hence, applying a shape factor b = 0.75 results in a conservative approach in the design of traditional structures with small relative crest freeboards. The shape factor appears to be related to the relative crest freeboard

through a negative exponential function. Furthermore, it is a linear function of the cotangent of the slope angle, increasing for decreasing slope angle.

The probability of overtopping P_{ow} (which is related to the scale factor a of the Weibull distribution) decreases for increasing relative crest freeboard according to a Rayleigh distribution. The effect of the slope angle on the probability of overtopping, i.e. decreasing for increasing slope angle, is expressed by a linear function of the cotangent of the slope angle.

Two new prediction formulae for b and P_{ow} have been derived (based on the UG10 test results), which take into account the observed effects of the slope angle and relative crest freeboard.

The improved knowledge on the probability distribution of low-crested structures allows to carry out more realistic simulations of wave-by-wave overtopping volumes in order to optimize the design of the reservoir and the turbine control strategy of OWECs. Furthermore, this knowledge can be used to predict the overtopping volumes for sea defence structures with a low crest freeboard in severe storm conditions.

9.3 Recommendations for further research

Although the objectives for this PhD-research have been met (section 9.2), a number of aspects are worth further investigating. An overview of these aspects is given below.

A set of new prediction formulae has been derived in chapter 5 for the average overtopping rate of steep low-crested slopes, enhanced by the physical insights offered by an empirical formula. However, the predictions by the DHNN tool may achieve similar accuracy (but with wider prediction intervals) when adding the AAU08 and UG10 test results to the CLASH database and when training the **DHNN tool** using the extended CLASH database. This should be investigated in the near future.

For **zero crest freeboards**, the set of new prediction formulae has been aligned with the test results of Smid et al. (2001). As mentioned in section 4.4.2, these test results are considered to be unreliable in the CLASH database.

On the other hand, the predictions by Schüttrumpf (2001) for slopes of 1:3 to 1:6 with a zero crest freeboard are believed to be more reliable. However, they are only valid for breaking or broken waves (large value of the breaker parameter due to small wave steepness).

Consequently, there is a lack of reliable test results for structures with steep slopes and zero crest freeboards, subjected to non-breaking waves. Although generating such test results is not straightforward (very large overtopping rates need to be measured accurately), the corresponding dataset is really valuable to improve our understanding of wave overtopping.

The set of new prediction formulae for the average overtopping rate is closely aligned with the prediction formula of Franco et al. (1994) (Eq. 4.15) for the overtopping behaviour at **vertical walls** with relatively large crest freeboards. This is in contrast to the more recently derived formula in EurOtop (2007) (Eq. 4.16). A large spreading occurs in the average overtopping rate for these structures. Hence, a more detailed study on the average overtopping rates of vertical walls with relatively large crest freeboards is required.

Furthermore, the interaction between the wave period and the effect of the slope angle is expressed by a larger effect of the slope angle for milder and steeper slopes (Fig. 5.26). Hence, it is interesting to have a look at the effect of the wave period on the average overtopping rate of vertical walls, to verify whether a decrease in wave period also results in an increase in the average overtopping rate. Traditionally, this effect is part of the spreading on the average overtopping rate of vertical walls, which is rather wide.

The shape factor of the Weibull distribution of the wave-by-wave overtopping volumes appears to be a linear function of the cotangent of the slope angle (section 8.4.6), reaching a value of approximately 0.56 for vertical walls ($\cot \alpha = 0.0$) with relatively large crest freeboards. This is in contrast with the shape factor of 0.75 mentioned by Franco et al. (1994) based on tests with vertical walls in relatively deep water with relative large crest freeboards. On the other hand, Besley (1999) predicts a shape factor of 0.66. The discrepancy between these three values of the shape factor is subject to further research.

The relatively simple geometry of the steep low-crested slopes considered in this PhD-research is ideal in the context of **numerical simulations**. The accurate test results gathered in this PhD-work can be applied to validate numerical models (for example NS-VOF (Navier Stokes Volume of Fluid) codes or SPH codes (Smooth Particle Hydrodynamics) for their ability to model the wave overtopping process accurately. A challenging aspect is the exact reproduction of the time series of wave elevation at the toe of the structure, in order to compare the individual overtopping volumes both determined numerically and measured at the test set-up.

Furthermore, once the numerical model is validated, it could be applied to simple slopes with broader ranges of application of the slope angle (e.g. vertical walls),

relative crest freeboard (e.g. zero crest freeboard) and wave steepness, but also to more complex geometries.

The case study on the effect of geometry control on the power output discussed in chapter 7 is based on a limited number of sea states (i.e. the characteristic sea states). More accurate conclusions could be drawn when taking into account all sea states in the scatter diagram for a particular deployment site. These calculations should be relatively straightforward.

Although this PhD-research contributes to the optimization of OWECs, further research on a number of aspects could **further improve the performance of OWECs**. Based on the probability distribution of the individual overtopping volumes, an optimal control strategy for the turbines and the size of the reservoir should be determined.

Furthermore, since this strategy needs to be applied in real time, a priori knowledge on the overtopping volumes is required. Hence, it is interesting to investigate the relationship between the incident wave characteristics and the overtopping volumes on a wave-by-wave basis. The UG10 test results should deliver the required input for setting up such relationship. Linking the height of the peaks of the overtopping detection system and the size of the overtopping volumes may contribute to this relationship.

The OWECs studied in this PhD-work are assumed to be fixed nearshore. Applying geometry control significantly increases the obtained hydraulic power for these OWECs. Similar conclusions are expected to be valid for floating OWECs with a limited draft. This should be further investigated.

The tests carried out during this PhD-work are limited to fetch-limited sea conditions. It could be interesting to carry out tests with steep low-crested slopes in swells, in order to verify the optimal geometry and performance of OWECs in swells. Swell seas are more energetic and a larger energy output of OWECs deployed in swells is expected, which could convince investors to invest in the OWEC technology.

References

Ahrens, J.P., 1977. Prediction of irregular wave overtopping, U.S. Army Corps of Engineers, CETA 77-7, Coastal Engineering Research Center, Department of the Army, Fort Belvoir, Virginia, USA.

Ahrens, J.P., 1980. Unpublished irregular wave reflection data. U.S. Army Corps of Engineers, Coastal Engineering Research Center, Fort Belvoir, Virginia.

Ahrens, J.P., 1992. Overtopping rates for seawalls. Miscellaneous paper CERC-92-3, Coastal Engineering Research Center, Department of the Army, USA.

Ahrens, J.P., Seelig, W.N., Ward, D.L. and Allsop, N.W.H., 1993. Wave Runup on and Wave Reflection from Coastal Structures. In Proc. Ocean Wave Measurement & Analysis - Waves 93, New Orleans, Louisiana, ASCE, pp. 489-502.

Allsop, N.W.H., Hawkes, P.J., Jackson, F.A. and Franco, L., 1985. Wave run-up on steep slopes - Model tests under random waves. Report SR2, Hydraulics Research Limited, Wallingford.

Allsop, N.W.H., Besley, P. and Madurini, L., 1995. Overtopping performance of vertical and composite breakwaters, seawalls and low reflection alternatives. Paper 4.7 in MCS Project. (Final Report, University of Hannover).

Allsop, N.W.H., Bruce, T. and Pearson, J., 2000. Violent Overtopping of Waves at Seawalls (VOWS) - Physical Model Study. In Proc. Coastal Engineering 2000, Sydney, Australia, Poster.

Battjes, J.A., 1974. Computation of set-up, longshore currents, run-up and overtopping due to wind-generated waves. Ph.D. Thesis, Technical University Delft, Delft.

Battjes, J.A. and Groenendijk, H.W., 2000. Wave height distributions on shallow foreshores. Coastal Engineering, 40(3): pp. 161-182.

Besley, P., Stewart, T. and Allsop, N.W.H., 1998. Overtopping of vertical structures: new prediction methods to account for shallow water conditions. In Proc. Coastlines, structures and Breakwaters, London, UK, pp. 46-57.

Besley, P., 1999. Overtopping of seawalls - design and assessment manual, R&D Technical Report W178, Environment Agency, Bristol, UK.

Bradbury, A.P., Allsop, N.W.H. and Stephens, R.V., 1988. Hydraulic performance of breakwater crown walls, Hydraulic Research Institute Wallingford, Report SR146.

Bruce, T., van der Meer, J.W., Franco, L. and Pearson, J.M., 2009. Overtopping performance of different armour units for rubble mound breakwaters. Coastal Engineering, In Press, Corrected Proof.

Brooke, J., 2003. Wave energy conversion. Elsevier Ocean Engineering Book Series, Vol. 6. Eds. R. Bhattacharyya, M.E. McCormick. . Elsevier, Amsterdam.

Coates, T.T., Jones, R.J. and Bona, P.F.D., 1997. Wind/swell seas and steep approach slopes, Hydraulic Research Institute Wallingford, Technical Report on wave flume studies, TR24.

COM, 2007. Communication from the Commision to the European Council and the European Parliament - An energy policy for Europe

CUR/CIRIA, 1991. Rock Manual. Manual on the use of rock in coastal and shoreline engineering. CUR Report 154, the Netherlands; CIRIA Special Publication 83, UK.

Cruz, J., 2008. Chapter 1: Introduction. In: J. Cruz (Editor), Ocean Wave Energy, Current Status and Perspectives. Springer, pp. 1-6.

Daemrich, K.-F., Meyering, J., Ohle, N. and Zimmermann, C., 2006. Irregular wave overtopping at vertical walls - learning from regular wave tests. In Proc. Coastal Engineering.

Dean, R.G. and Dalrymple, R.A., 1991. Water wave mechanics for engineers and scientists. Advanced series on ocean engineering, Volume 2. World Scientific Publishing Co. Pte. Ltd., Singapore.

De Rouck, J., Geeraerts, J., Troch, P., Kortenhaus, A., Pullen, T. and Franco, L., 2005. New Results on Scale Effects for Wave Overtopping at Coastal Structures, International Conference on Coastlines, Structures and Breakwaters 2005, ICE Thomas Telford London, pp. 29–43.

De Rouck, J., Verhaeghe, H. and Geeraerts, J., 2009. Crest level assessment of coastal structures -- General overview. Coastal Engineering, 56(2): pp. 99-107.

EC, 2011. European Commission - Renewables make the difference. Publications Office of the European Union, Luxemburg.

EEP, 2011. Europe's Energy Portal - www.energy.eu. Accessed August 2011.

EurOtop, 2007. EurOtop. Wave Overtopping of Sea Defences and Related Structures: Assessment Manual, Environment Agency, UK/ENW Expertise Netwerk Waterkeren, NL/KFKI Kuratorium für Forschung im Küsteningenieurwesen, DE, Pullen, T., Allsop, N.W.H., Bruce, T., Kortenhaus, A., Schüttrumpf, H. and van der Meer, J.W. http://www.overtopping-manual.com.

Franco, L., de Gerloni, M. and van der Meer, J., 1994. Wave overtopping on vertical and composite breakwaters. In Proc. 24th International Conference on Coastal Engineering, New York, ASCE, pp. 1030–1044.

Franco, C. and Franco, L., 1999. Overtopping formulas for caisson breakwaters with nonbreaking 3D waves. Journal of Waterway Port Coastal and Ocean Engineering-Asce, 125(2): pp. 98-108.

Franco, L., Geeraerts, J., Briganti, R., Willems, M., Bellotti, G. and De Rouck, J., 2009. Prototype measurements and small-scale model tests of wave overtopping at shallow rubble-mound breakwaters: the Ostia-Rome yacht harbour case. Coastal Engineering, 56(2): pp. 154-165.

Frigaard, P. and Brorsen, M., 1995. A time-domain method for separating incident and reflected irregular waves. Coastal Engineering, 24(3-4): pp. 205-215.

Friis-Madsen, E., 2011. http://www.wavedragon.net, accessed in June 2011.

Goda, Y., 2000. Random seas and design of maritime structures (2nd Edition). Advanced Series on Ocean Engineering - Volume 15. World Scientific Publishing Co. Pte. Ltd., Singapore.

Goda, Y., 2009. Derivation of unified wave overtopping formulas for seawalls with smooth, impermeable surfaces based on selected CLASH datasets. Coastal Engineering, 56(4): pp. 385-399.

Graw, K.-U., 1996. Wave energy breakwaters - a device comparison. In Proc. Conference in Ocean Engineering, Madras, INDIA.

Hasselmann, K. et al., 1973. Measurements of wind-wave growth and swell decay during the Joint North Sea Wave Project (JONSWAP), Deutsche Hydr. Zeit Reihe A (8°) 12.

Hawkes, P.J., 1999. Mean overtopping rate in swell and bimodal seas. Proceedings of the Institution of Civil Engineers-Water Maritime and Energy, 136(4): pp. 235-238.

Hedges, T.S. and Reis, M.T., 1998. Random wave overtopping of simple sea walls: A new regression model. Proceedings of the Institution of Civil Engineers-Water Maritime and Energy, 130(1): pp. 1-10.

Hordijk, D., 2003. Report on field measurements, Petten Sea defence Stormseason 2002-2003. Report RIKZ/OS_2003.135X by Rijkswaterstaat - RIKZ. July 2003.

Hu, K., Mingham, C.G. and Causon, D.M., 2000. Numerical simulation of wave overtopping of coastal structures using the non-linear shallow water equations. Coastal Engineering, 41(4): pp. 433-465.

Hughes, S.A. and Nadal, N.C., 2009. Laboratory study of combined wave overtopping and storm surge overflow of a levee. Coastal Engineering, 56(3): pp. 244-259.

Ingram, D., 2005. Guidance on the use of Numerical Models of Wave Overtopping, CLASH internal report, Manchester Metropolitan University, United Kingdom.

IBM®, 2010. SPSS® Statistics 17.

IPCC, 2007. Climate change 2007: Synthesis Report, An assessment of the Intergovernmental Panel on Climate Change.

Jensen, O.J. and Sorensen, T., 1979. Overspilling/Overtopping of Rubble Mound Breakwaters, Results of Studies, Useful in Design Procedures. Coastal Engineering, Vol. 3: pp. pp. 51-65.

Kikkawa, H., Shi-igai, H. and Kono, T., 1968. Fundamental study of wave overtopping on levees. Coastal Engineering in Japan, Vol. 11: pp. pp. 107-115.

Kofoed, J.P., Frigaard, P., Sorensen, H.C. and Friis-Madsen, E., 2000. Development of the Wave Energy Converter - Wave Dragon. In Proc. Tenth (2000) International Offshore and Polar Engineering Conference, Seattle, USA, The International Society of Offshore and Polar Engineers.

Kofoed, J.P., 2002. Wave overtopping of Marine Structures - Utilization of Wave Energy. PhD Thesis, Aalborg University, Aalborg, DK.

Kofoed, J.P., Hald, T. and Frigaard, P., 2002. Experimental study of a multi level overtopping wave power device. In Proc. The Tenth Congress of International Maritime Association of the Mediterranean (IMAM 2002).

Kortenhaus, A., Oumeraci, H., Geeraerts, J., De Rouck, J., Medina, J.R. and Gonzalez-Escriva, J.A., 2004. 'Laboratory effects and other uncertainties in wave overtopping measurements'. In Proc. 29th International Conference on Coastal Engineering, Lisbon, P.

Li, T.Q., Troch, P. and De Rouck, J., 2004. Wave overtopping over a sea dike. Journal of Computational Physics, 198(2): pp. 686-726.

Longuet-Higgins, M.S., 1952. On the statistical distributions of heights of sea waves. . J. Mar. Res., 11: pp. 245–266.

Losada, I.J., Lara, J.L., Guanche, R. and Gonzalez-Ondina, J.M., 2008. Numerical analysis of wave overtopping of rubble mound breakwaters. Coastal Engineering, 55(1): pp. 47-62.

Lykke Andersen, T. and Frigaard, P., 2008. Lecture notes for the course in water wave mechanics. Lecture notes No. 16. Department of Civil Engineering, Aalborg University, Denmark.

Lykke Andersen, T. and Burcharth, H.F., 2009. Three-dimensional investigations of wave overtopping on rubble mound structures. Coastal Engineering, 56(2): pp. 180-189.

Mansard, E.P.D. and Funke, E.R., 1980. The measurement of incident and reflected spectra using a least squares method. . In Proc. National Conference Publication - Institution of Engineers, Australia, ASCE, n.80/1, pp. 95-96.

Margheritini, L., 2009. R&D towards commercialization of the Sea wave Slot cone Generator (SSG) overtopping wave energy converter, Aalborg University, Aalborg.

Margheritini, L., Vicinanza, D. and Frigaard, P., 2009a. SSG wave energy converter: Design, reliability and hydraulic performance of an innovative overtopping device. Renewable Energy, 34(5): pp. 1371-1380.

Margheritini, L., Victor, L., Kofoed, J.P. and Troch, P., 2009b. Geometrical Optimization for Improved Power Capture of Multi-Level Overtopping Based Wave Energy Converters. In Proc. Nineteenth (2009) International Offshore and Polar Engineering Conference (ISOPE), Osaka, Japan, International Society of Offshore & Polar Engineers, 19, pp. 339-344.

Meyer, N.I., 2002. Bolgekraftprogram. Technical report, Bolgekraftudvalgets Sekretariat RAMBOLL, 2002.

Nelson, R.C., 1994. Depth limited design wave heights in very flat regions. Coastal Engineering, 23(1-2): pp. 43-59.

Owen, M.W., 1980. Design of sea walls allowing for wave overtopping. Report EX 924, Hydraulics Research, Wallingford, UK (1980).

Paape, A., 1960. Experimental data on the overtopping of seawalls by waves. .

Pearson, J., Bruce, T. and Allsop, N.W.H., 2002. Violent wave overtopping: measurements at large and small scale. In Proc. Int. Conf. Coastal Engineering (ICCE 2002), Cardiff, ASCE, pp. 2227-2238.

Perdijk, H.W.R., 1987. Golfoverslag bij dijken, Waterloopkundig Laboratorium, Verslag modelonderzoek H181/M1256.

Pontes, M.T., Athanassoulis, G.A., Bartsow, S., Bertotti, L., Cavaleri, L. and Holmes, B., 1998. The European Wave Energy Resource. , 3rd European Wave Energy Conference (EWEC), Patras, Greece.

Postma, G.M., 1989. Wave reflection from rock slopes under random wave attacks. PhD Thesis, Delft University of Technology.

Pullen, T., Allsop, N.W.H. and Bruce, T., 2006. Wave overtopping at vertical seawalls: field and laboratory measurements of spatial distributions. In Proc. Coastal Engineering.

Pullen, T., Allsop, W., Bruce, T. and Pearson, J., 2009. Field and laboratory measurements of mean overtopping discharges and spatial distributions at vertical seawalls. Coastal Engineering, 56(2): pp. 121-140.

RAMBØLL, Dansk Hydraulisk Institut and Danmarks Meteorologisk Institut, 1999. Kortlaegning af bolgeenergiforhold i den Danske del af Nordsoen.

Reeve, D.E., Soliman, A. and Lin, P.Z., 2008. Numerical study of combined overflow and wave overtopping over a smooth impermeable seawall. Coastal Engineering, 55(2): pp. 155-166.

Rijkswaterstaat, 2010. Golfklimaat. http://www.golfklimaat.nl. National Institute for Coastal and Marine Management (Rijkswaterstaat), The Netherlands. Accessed July 2010. .

Saville, T., 1955. Laboratory data on wave run-up and overtopping on shore structures. TM-64, Beach Erosion Board, US Army Corps of Engineers, USA.

Schüttrumpf, H., 2001. Wellenüberlaufströmung bei Seedeichen - Experimentelle und theoretische Untersuchungen. Phd Thesis, Technischen Universität Carolo-Wilhelmina, Braunschweig, DE.

Seelig, W.N. and Ahrens, J.P., 1981. Estimation of wave reflection and energy dissipation coefficients for beaches, revetments and breakwaters. CERC Technical paper 81-1, Fort Belvoir, U.S.A.C.E. MS, Vicksburg.

Sibul, O.J. and Tickner, E.G., 1956. Model study of overtopping of wind generated waves on levees with slopes of 1:3 and 1:6, Beach Erosion Board, Tech. Memo., No. 80.

Smid, R., Schüttrumpf, H. and Möller, J., 2001. Untersuchungen zur Ermittlung der mittleren Wellenüberlaufrate an einer senkrechten Wand und einer 1:1,5 geneigten Böschung für Versuche mit und ohne Freibord (Report on small scale tests, in German), Leichtweiβ Institute for Hydraulics, Technical University of Braunschweig, Germany.

Steendam, G.J., van der Meer, J., Verhaeghe, H., Besley, P., Franco, L. and van Gent, M.R.A., 2004. The international database on wave overtopping. In Proc. 29th International Conference on Coastal Engineering, Singapore, ASCE, World Scientific, pp. 4301-4313.

TAW, 2002. Technical Report Wave Run-up and Wave Overtopping at Dikes, Technische Adviescommissie voor de Waterkeringen, Delft.

Tedd, J., 2007. Testing, Analysis and Control of the Wave Dragon Wave Energy Converter, PhD Thesis. Aalborg University, Aalborg.

Tedd, J. and Kofoed, J.P., 2009. Measurements of overtopping flow time series on the Wave Dragon, wave energy converter. Renewable Energy, 34(3): pp. 711-717.

Troch, P., 2000. Experimentele studie en numerieke modellering van golfinteractie met stortsteengolfbrekers. PhD Thesis, Ghent University, Ghent

Troch, P., Geeraerts, J., Van de Walle, B., De Rouck, J., Van Damme, L., Allsop, W. and Franco, L., 2004. Full-scale wave overtopping measurements on the Zeebrugge rubble mound breakwater. Coastal Engineering, 51(7): pp. 609-628.

van der Meer, J.W. and Janssen, J.P.F.M., 1994. Wave run-up and wave overtopping at dikes and revetments, Delft Hydraulics.

van der Meer, J.W., Verhaeghe, H. and Steendam, G.J., 2005a. Database on wave overtopping at coastal structures, CLASH WP2 database, Inframm, Marknesse, NL.

van der Meer, J.W., Briganti, R., Zanuttigh, B. and Wang, B., 2005b. Wave transmission and reflection at low-crested structures: Design formulae, oblique wave attack and spectral change. Coastal Engineering, 52(10-11): pp. 915-929.

van Gent, M.R.A., 2001. Wave runup on dikes with shallow foreshores. Journal of Waterway Port Coastal and Ocean Engineering-Asce, 127(5): pp. 254-262.

van Gent, M.R.A., Van den Boogaard, H.F.P., Pozueta, B. and Medina, J.R., 2007. Neural network modelling of wave overtopping at coastal structures. Coastal Engineering, 54(8): pp. 586-593.

Verhaeghe, H., De Rouck, J. and van der Meer, J., 2008. Combined classifier-quantifier model: A 2-phases neural model for prediction of wave overtopping at coastal structures. Coastal Engineering, 55(5): pp. 357-374.

Waveplam, 2009. A Cautiously Optimistic Review of the Technical Status of Wave Energy Technology, Hydraulics and Maritime Research Centre, IRL.

Young, D.M. and Testik, F.Y., 2011. Wave reflection by submerged vertical and semicircular breakwaters. Ocean Engineering, 38(10): pp. 1269-1276.

Zanuttigh, B. and Van der Meer, J., 2006. Wave reflection from coastal structures. In Proc. ICCE, San Diego.

Zanuttigh, B. and Van der Meer, J.W., 2008. Wave reflection from coastal structures in design conditions. Coastal Engineering, 55(10): pp. 771-779.

Zanuttigh, B., Margheritini, L., Gambles, L. and Martinelli, L., 2009. Analysis of wave reflection from wave energy converters installed as breakwaters in harbour, 8th European Wave and Tidal Energy Conference, Uppsala, Sweden.

A

Appendix A: Technical drawings

A.1 AAU08 test set-up

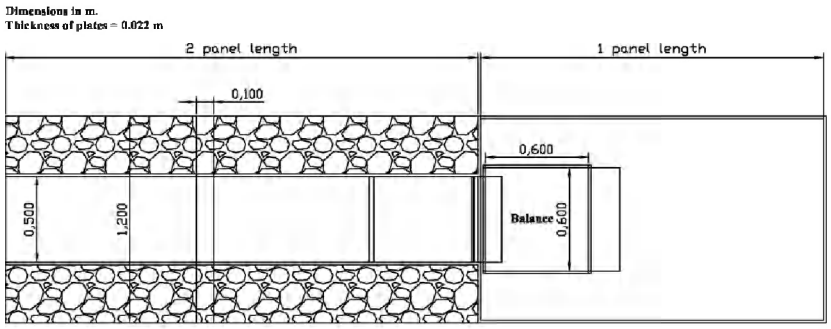

Figure A.1: Top view of experimental set-up AAU08.

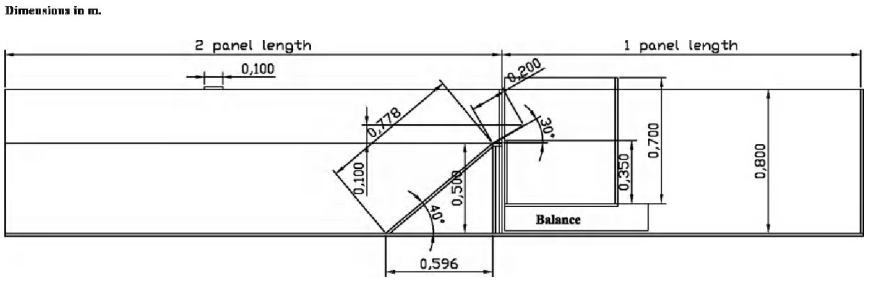

Figure A.2: Side view of experimental set-up AAU08.

A.2 UG10 test set-up

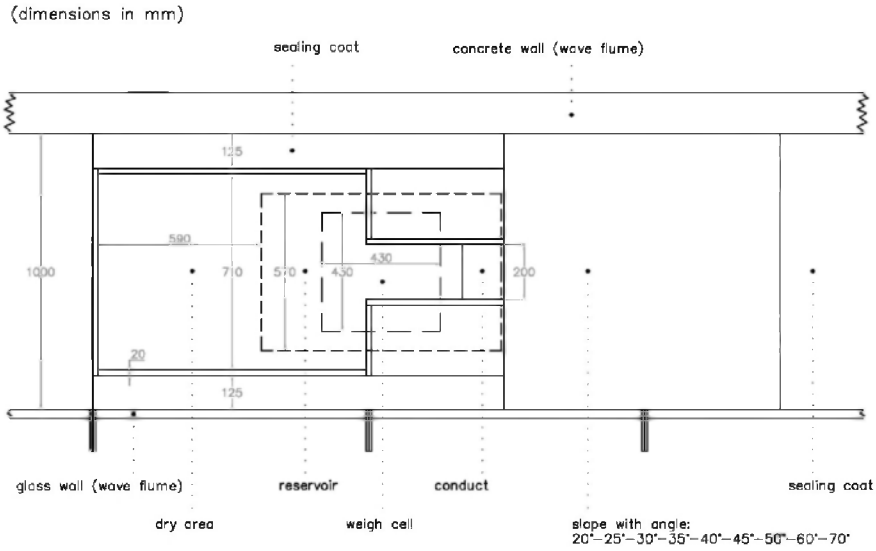

Figure A.3: Top view of experimental set-up UG10.

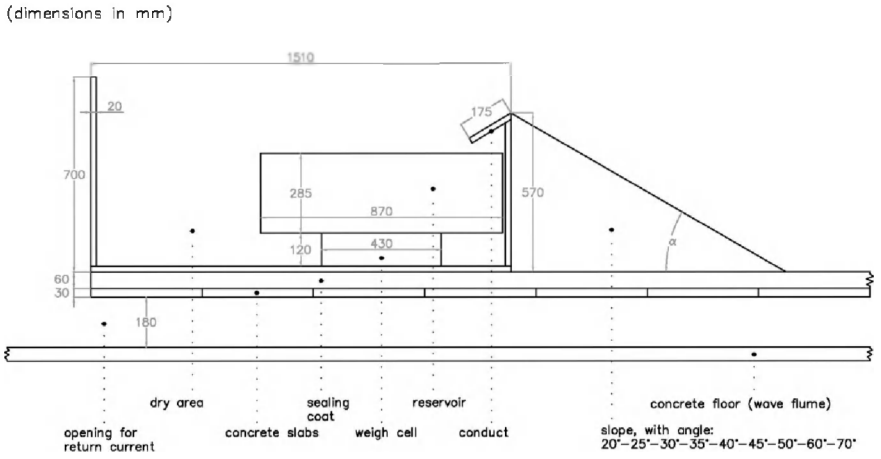

Figure A.4: Side view of experimental set-up UG10.

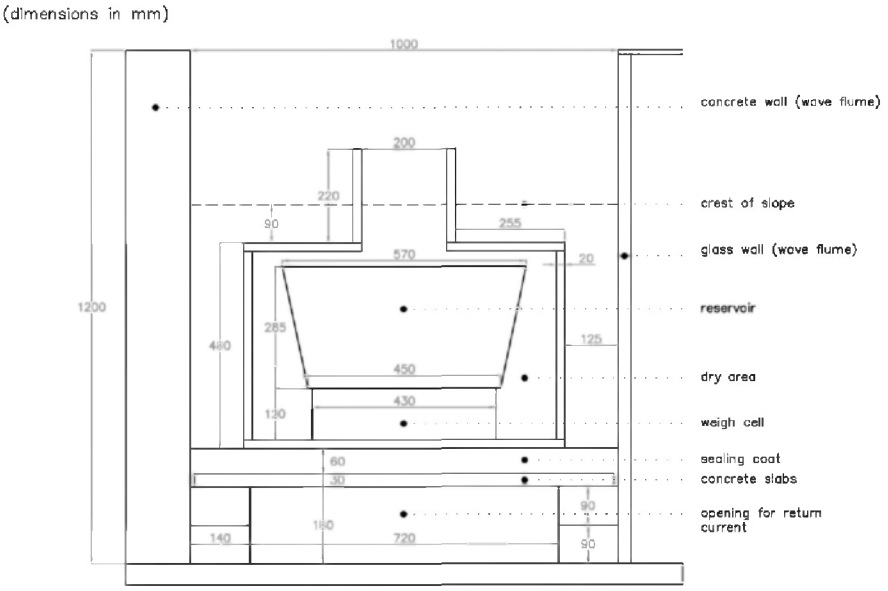

Figure A.5: Rear view of experimental set-up UG10.

B

Appendix B: Matlab® script

This appendix gives the code of the Matlab® script and explains how to use this code.

B.1 Preparation

Put the following documents in one folder:

- file with characteristic pump curve
- file with the calibration curve of the reservoir
- Matlab® script (see section B.3)
- xlsread2007.m (enables to get data and text from a spreadsheet in an MS Excel workbook) and xlswrite2007.m (enables to write data and text to a spreadsheet in an MS Excel workbook).
- Input file.xlsx (contains input data of the tests)
- Output file.xlsx (contains the template of the output file)
- a folder: Data files, which contains the signals of the wave gauges (.ghm) and weigh cell (.bal) of all tests.

Then open the .m-file containing the script and press the button "Evaluate Entire File".

B.2 What happens in the code?

General:

1. Read in file with calibration curve of reservoir: Calibration reservoir.bal

2. Read in file with average pump curve with fixed sample frequency and limited length and convert it to absolute masses (on a two-by-two basis, not using general interpolation): Average pump curve.bal

For every test one after the other:

3. Read in name of the test, relative crest freeboard R_c, wave power P_{wave}, skip end and begin time (i.e. the horizontal parts at the start and end of each test, e.g. Fig. 2.3), value begin & value end overtopping (i.e. the thresholds for the overtopping detection signal) through a file: Input.xlsx.

4. Read in the weigh cell signal (.bal) and the wave gauge signals (.ghm) based on the name of the test. The weigh cell signal has no fixed frequency for the UG10 test series, the .ghm files have a sampling frequency of 40 Hz. Only the last column of the .ghm file is of interest here, as it contains the overtopping detection signal at the crest.

5. Determine the start and stop positions of pumping, based on reaching a relative mass of 70 kg and the duration of pumping.

6. Due to difference in time axis between pump curve and weigh cell signal, determine "new" interpolated absolute characteristic pump curves and connect them together in a curve "to be added" to the weigh cell signal to compensate for pumping. This is the curve of pumped mass, which then has the same time axis as the weigh cell signal.

7. Convert weigh cell signal to absolute masses (on a two-by-two basis, not using general interpolation). Add the curve of pumped mass to it, to achieve the curve of cumulative absolute mass. It still has the same time axis as the original weigh cell signal.

8. Determine the start times of wave overtopping based on the measured peaks of the overtopping detection signal.

9. Convert the start times of wave overtopping from the time axis of the overtopping detection signal to the time axis of the cumulative absolute weigh cell signal and determine the new time of overtopping on that axis based on the most horizontal part.

10. Read the values of the cumulative curve for the new times of overtopping.

11. The individual overtopping volumes are derived as the differences between those values of the cumulative curve for two consecutive times of overtopping.

12. Limit the individual volumes and time intervals to the regime situation (i.e. the total duration of the test without the end and begin time) and calculate average, minimum, maximum and standard deviations of the individual volumes.

13. Write out all data, in the Output.xlsx file and in Matlab figure files.

B.3 The code

```
%% Post Processing of overtopping tests UG10

%% Loading the calibration curve of the reservoir and the
average pump curve and the conversion to absolute masses
for the pump curve

clear all;

fileToRead1 = 'Calibration reservoir.BAL';

%The .bal extension is misleading. This file only
contains 2 columns: relative masses versus absolute
masses. It is not the weigh cell signal of a test.

Data1 = load(fileToRead1);

absmass = Data1(:,1);
relmass = Data1(:,2);
```

```
fileToRead2 = 'Average pump curve.BAL';

% This is the signal of characteristic pump curve as
calibrated for non-dynamic circumstances in relative
masses. It decreases from 70 kg until it reaches a
constant value.

Data2 = load(fileToRead2);

signaltimepump = Data2(:,1);
pumpchar = Data2(:,2);

dim1 = length(pumpchar);
%Interpolation to change to absolute masses.

for i = 1:dim1
    for j = 1:length(relmass)-1
        if    (pumpchar(i,1)    >=    relmass(j,1))    &&
(pumpchar(i,1) <= relmass(j+1,1))
            masspump(i,1) = absmass(j,1) + (pumpchar(i,1)
-  relmass(j,1))  *  (absmass(j+1,1)  -  absmass(j,1))  /
(relmass(j+1,1) - relmass(j,1));
        end;
    end;
end;

%% Reading the input

Excel = actxserver('Excel.Application');
File = '…\Input file irregular waves.xlsx';  %Make sure
you put the whole path.
ExcelWorkbook = Excel.Workbooks.Open(File);

[Inputnum, Inputtxt] = xlsread2007(File,'Sheet'); %Puts
the numerical cells in Inputnum and the textual cells in
Inputtxt.
%This means Rc will come at the first column of Inputnum.
numbertests = size(Inputnum);
```

```
ExcelWorkbook.Close;

for test = 1:numbertests(1,1) %The corresponding end is
at the end of this script. This is the for-loop that runs
over all tests.

nametest = Inputtxt{test+1,1}; % Name of the test.
Rc = Inputnum(test,1); % Rc in m.
Pwave = Inputnum(test,2); % Pwave in W/m.
skipbegintime = Inputnum(test,3); % This is the number of
seconds for the build up.
skipendtime = Inputnum(test,4); % This is the number of
seconds for the tapering off.
% Inputnum(test,5 & 6) are skip end & skip begin
expressed as datapoints, not in seconds.
valueforbeginovertopping = Inputnum(test,7); % This is
the value of the overtopping detection signal for the
start of an overtopping.
%This value is chosen so that even the smallest
overtopping masses are detected.
valueforendovertopping = Inputnum(test,8); % This is the
value of the overtopping detection signal for the end of
an overtopping.

%% These are the input data from the test

File = '…\Output file.xlsx';  % Make sure you put the
whole path.
ExcelWorkbook = Excel.Workbooks.Open(File);
%By opening this file, you open the form that needs to be
filled in with data and headers. The name of the output
file is given at the end of this code.

mkdir(strcat('Output\',nametest));%This opens a folder
with the name of the test in the folder with the name
Output.

% Import the file
fileToRead3 = strcat('Data files\',nametest,'.BAL'); %
Relative masses!
```

```
Data3 = load(fileToRead3);

% First the time signal is isolated as the signal of the
weigh cell doesn't have a fixed sample frequency.
signaltime = Data3(:,1);

% Then the column for the weigh cell signal is isolated.
This is the continuous measured signal of the balance.
signalscale = Data3(:,2);

dim = length(signalscale);

samplefreq = (dim - 1) / signaltime(dim); % This is the
average sample frequency used during the test.

% The signal of the weigh cell gives sometimes a zero
when the maximal mass is approached, this happens almost
only in horizontal parts of the signal. Solution: the
zero is replaced by the previous value of the signal.

for i = 1:dim
    if signalscale(i,1) == 0
        if i == 1
            signalscale(i,1) = signalscale(i+1,1);
        else
            signalscale(i,1) = signalscale(i-1,1);
        end;
    end;
end;

% Then the signal from the overtopping detection system
is isolated.
fileToRead4 = strcat('Data files\',nametest,'.GHM');

Data4 = load(fileToRead4);

signalovertdet = Data4(:,8);

dimdetection = length(signalovertdet) - 1;
```

```
signalovertdetection = [];

for i = 1:dimdetection
    signalovertdetection(i,1) = signalovertdet(i+1,1);
end;

samplefreqdetection = signalovertdet(1,1);

signalovertdetnew = [];

for i = 1:dimdetection
    signalovertdetnew(i,1)        =        10000        *
signalovertdetection(i,1); % This is only for graphical
purposes.
end;

sampleintdetection = 1 / samplefreqdetection;
endtimedetection     =     (dimdetection     -     1)     *
sampleintdetection;
timedetectioninv                                          =
(0:sampleintdetection:endtimedetection);
timedetection = timedetectioninv.';

% Determining the skip begin and skip end in number of
data points. This is to leave out the build up and
tapering off periods when calculating the average
overtopping rate.

for i = 2:dim
    if    (signaltime(i,1)    >=    skipbegintime)    &&
(signaltime(i-1,1) < skipbegintime)
        skipbegin = i - 1;
    end;
    if (signaltime(i,1) >= endtimedetection - skipendtime)
&& (signaltime(i-1,1) < endtimedetection - skipendtime)
        skipend = dim - (i - 1);
    end;
end;
```

```
if skipbegintime == 0
    skipbegin = 0;
end;

if skipendtime == 0
    skipend = 0;
end;

%% Conversion to absolute masses of the weigh cell signal
by using the calibration curve of the reservoir.


massres = [];

for i = 1:dim
    for j = 1:length(relmass)-1
        if  ((signalscale(i,1)  >=  (relmass(j,1)))  &&
(signalscale(i,1) <= (relmass(j+1,1))))
            massres(i,1)      =      absmass(j,1)      +
(signalscale(i,1)  -  relmass(j,1))  *  (absmass(j+1,1)  -
absmass(j,1)) / (relmass(j+1,1) - relmass(j,1));
        end;
    end;
end;

plot(signaltime,massres);
xlabel('Time [s]')
ylabel('Absolute mass in reservoir [kg]')
title('Absolute mass in reservoir')
grid
saveas(gcf,strcat('Output\',nametest,'\Absmassreservoir.f
ig'));

plot(signaltime,massres,'*');
xlabel('Time [s]')
hold on
plot(timedetection,signalovertdetnew,'*k');
legend('Absolute       mass    in    reservoir    [kg]',
'Overtoppingdetectionsignal')
```

```
title('Absolute mass in reservoir with
overtoppingdetectionsignal')
grid
saveas(gcf,strcat('Output\',nametest,'\Overtoppingdetecti
onsignal_with_absmassreservoir.fig'));
hold off

%% Determining start- and stoppositions of pumping. This
is the preparation for composing the curve of pumped mass.
%  First, a dynamic list of all the start- and
stoppositions of the pump is made. Imagine a continuous
time line. We only get to see a sampled version, but the
system reasons as if the time axis is not discrete.

startpos = [];
startpostime = [];
stoppos = [];
stoppostime = [];

a = 0;
t1 = 0;
i=0;

while (a==0) && (i<dim)
    i=i+1;
    if signalscale(i,1)>=70
        a=a+1;
        t1=t1+1;
        startpostime(t1,1)=signaltime(i,1);
        startpos(t1,1)=i;
    end;
end;


while i<dim-1
b=0;
tijd=startpostime(t1,1)+4.6;
while (b==0) && (i<dim-1)
     if
((signaltime(i+1,1)>=tijd)&&(signaltime(i,1)<tijd))
          b=b+1;
```

```
          low=i;
          high=i+1;
          signalscaleinterp=((tijd-
signaltime(low,1))/(signaltime(high,1)-
signaltime(low,1)))*(signalscale(high,1)-
signalscale(low,1))+signalscale(low,1);
     end;
  i=i+1;
end;

if signalscaleinterp >=70
     t1=t1+1;
     startpostime(t1,1)=tijd;
     startpos(t1,1)=high;
    stoppos(t1-1,1)=startpos(t1,1)+6;
    stoppostime(t1-1,1)=signaltime(stoppos(t1-1,1),1);
end;


if signalscaleinterp < 70
   c=0;
   while (c==0) && (i<dim-1)
     if signalscale(i,1)>=70
        c=c+1;
        t1=t1+1;
        startpostime(t1,1)=signaltime(i,1);
        startpos(t1,1)=i;
        stoppos(t1-1,1)=startpos(t1,1)+6;
        stoppostime(t1-1,1)=signaltime(stoppos(t1-1,1),1);
        if stoppos(t1-1,1)>startpos(t1-1,1)+37
           stoppos(t1-1,1)=startpos(t1-1,1)+37;
           stoppostime(t1-1,1)=signaltime(stoppos(t1-
1,1),1);
        end;
     end;
    i=i+1;
   end;
   stoppos(t1,1)=startpos(t1,1)+37;
   stoppostime(t1,1)=signaltime(stoppos(t1,1),1);
end;
end;
```

```
numpumpturns = t1; % The total number of pumping events
is then equal to the final value of t1.

%% Create the cumulative pumping curve including all pump
masses. The curve of pumped mass is added to the curve of
the reservoir to get the cumulative curve. It should be
noted that the average pump curve is given at a fixed
sample frequency while the signal of the weigh cell
doesn't have a fixed sample frequency. Therefore, the
average pump curve is interpolated at the required
moments determined by the time signal of the weigh cell.

masspump_int = [];

for i = 1:t1
    for j = startpos(i,1):stoppos(i,1)-1
        d = signaltime(j,1) - signaltime(startpos(i,1),1);
        for k = 1:dim1-1
            if (d >= signaltimepump(k,1)) && (d <=
signaltimepump(k+1,1))
                masspump_int(j-startpos(i,1)+1,i)       =
masspump(k,1)    +    (d    -    signaltimepump(k,1))    *
(masspump(k+1,1) - masspump(k,1)) / (signaltimepump(k+1,1)
- signaltimepump(k,1));
            end;
        end;
    end;
    masspump_int(stoppos(i,1)-startpos(i,1)+1,i)        =
masspump(dim1,1);
end;

matrix = [startpos startpostime stoppos stoppostime];

columnHeader = {'Startposition of pumping event',
'Starttime of pumping event [s]', 'Stopposition of
pumping event', 'Stoptime of pumping event [s]'};
numericalData = num2cell(matrix);
allData = [columnHeader; numericalData];

xlswrite2007(File, allData, 'All pumping events');
```

```
% Determine the curve of pumped mass. This is a
cumulative function of the pump curves.

pumping = [];

for i = 1:dim
    pumping(i,1) = 0;
end;

if t1 ~= 0
    for i = 1:t1-1
       for j = startpos(i,1):dim
            if (j <= stoppos(i,1)) && (j <=
startpos(i+1,1)+6) % The value +6 is determined after
comparing the analyses of different regular wave tests
                f = j - startpos(i,1) + 1;
                pumping(j,1)     =     pumping(j,1)     +
masspump_int(1,1) - masspump_int(f,1);
            else
                pumping(j,1)     =     pumping(j,1)     +
masspump_int(1,1) - masspump_int(f,1);
            end;
        end;
    end;
end;

if t1 ~= 0
    for i = t1:t1
       for j = startpos(i,1):dim
            if j <= stoppos(i,1)
                g = j - startpos(i,1) + 1;
                pumping(j,1)     =     pumping(j,1)     +
masspump_int(1,1) - masspump_int(g,1);
            else
                pumping(j,1)     =     pumping(j,1)     +
masspump_int(1,1) - masspump_int(g,1);
            end;
        end;
    end;
end;
```

```
plot(signaltime,pumping);
xlabel('Time [s]')
ylabel('Pumped absolute mass [kg]')
title('Pumped absolute mass')
grid
saveas(gcf,strcat('Output\',nametest,'\Pumpedmass.fig'));

%% The cumulative mass curve for the reservoir
% The curve of pumped mass is added to the curve of the
reservoir to get the cumulative curve.

massrescumul = [];

for i = 1:dim
    massrescumul(i,1) = massres(i,1) + pumping(i,1);
end;

matrix = [signaltime massres pumping massrescumul];

columnHeader = {'Time [s]', 'Absolute mass in reservoir
[kg]', ' Pumped absolute mass [kg]', 'Cumulative absolute
mass in reservoir [kg]'};
numericalData = num2cell(matrix);
allData = [columnHeader; numericalData];

xlswrite2007(File, allData, 'Absolute, pumped and
cumulative mass');

plot(signaltime,massrescumul);
xlabel('Time [s]')
ylabel('Cumulative absolute mass in reservoir [kg]')
title('Cumulative absolute mass in reservoir')
grid
saveas(gcf,strcat('Output\',nametest,'\Cummassreservoir.f
ig'));

% The resulting massrescumul(:,1) array should contain
the cumulative mass function in time. However, it is seen
that when only this standard method is applied, negative
```

```
peaks occur in the time-differentiated signal of the
cumulative curve. This shows that there are descending
parts in the cumulative curve. They are seen to occur
where:
% 1. Impact overtopping events occur: there is a small
overestimation by the weigh cell when the overtopping
mass enters the reservoir.
% 2. Inaccuracies in compensation for pumping. This is a
problem due to the fact that the pump curve differs a
little every time pumping occurs.

% The first small peaks are eliminated by using a value
of the weigh cell signal in the horizontal part.
% The second ones are less easy to solve. As the real
pump curve deviates little from the calibrated pump curve,
a new pump curve should be assembled for each pump event,
which is impossible to do.

%% Determining the overtopping positions

% Sometimes one overtopping causes two peaks in the
overtopping detection signal. Therefore it is required
that the detection signal has to reach a certain minimum
value before the next overtopping is searched for.

overtposdetection = [];
overttimedetection = [];

h = 0;
lookingfornextovertopping = 1;
duringovertopping = 0;
for i = 2:length(signalovertdetnew)
    if (duringovertopping == 1) && (signalovertdetnew(i,1)
<= valueforendovertopping)
        lookingfornextovertopping = 1;
        duringovertopping = 0;


    end;
```

```
    if     (lookingfornextovertopping     ==     1)     &&
(signalovertdetnew(i,1)  >=  valueforbeginovertopping)  &&
(signalovertdetnew(i-1,1) < valueforbeginovertopping)
        h = h + 1;
        overtposdetection(h,1)  =  i;  % The  overtopping
position and time are determined according to the time
axis of the overtopping detection system.
        overttimedetection(h,1)    =    (i    -    1)    *
sampleintdetection;
        duringovertopping = 1;
        lookingfornextovertopping = 0;
    end;
end;

dim2 = length(overtposdetection);

if dim2 ~=0

overtpos = [];
overttime = [];

z = 2;
for i = 1:dim2
    for j = z:dim
        if  (signaltime(j,1)  >=  overttimedetection(i,1))
&& (signaltime(j-1,1) < overttimedetection(i,1))
        z = j;
        overtpos(i,1) = j; % The overtopping position and
time  are  determined  according  to  the  time  axis  of  the
weigh cell signal.
        overttime(i,1) = signaltime(j,1);
        end;
    end;
end;

%% Relation between the detection of a overtopping and
the increase in the signal of the weigh cell. We are
looking for the most horizontal part in the cumulative
curve before each overtopping occurs so that the increase
in the weigh cell signal due to the overtopping can be
determined.
```

```
massrescumul_overt = [];
overtposscale = [];
signaltime_overt = [];

for i = 1:dim2 % This method of determining the most
horizontal part is chosen after comparing different
overtopping events with the resulting increase in the
weigh cell signal.
    w      =      massrescumul(overtpos(i,1)+1,1)      -
massrescumul(overtpos(i,1),1);
    x      =      massrescumul(overtpos(i,1)+2,1)      -
massrescumul(overtpos(i,1)+1,1);
    y      =      massrescumul(overtpos(i,1)+3,1)      -
massrescumul(overtpos(i,1)+2,1);
    if w < 0
       m       =       [massrescumul(overtpos(i,1)+1,1);
massrescumul(overtpos(i,1)+2,1);
massrescumul(overtpos(i,1)+3,1)];
       [massrescumul_overt(i,1),minposition]           =
min(m); %This commando gives the minimum, but also the
position of the minimum.
    elseif x < 0
        m       =       [massrescumul(overtpos(i,1)+2,1);
massrescumul(overtpos(i,1)+3,1)];
        [massrescumul_overt(i,1),minposition] = min(m);
        minposition = minposition + 1;
    elseif y < 0
        massrescumul_overt(i,1)                         =
massrescumul(overtpos(i,1)+3,1);
        minposition = 3;
    else
        m = [w; x; y];
        [minimaldifference,minpositiondifference]       =
min(m);
        if minpositiondifference < 3
            massrescumul_overt(i,1)                     =
massrescumul(overtpos(i,1)+1,1); %The corresponding value
is saved, as it is important for the individual
overtopping volumes.
```

```
            minposition = 1; %The most horizontal one is
then the previous one.
        else
            massrescumul_overt(i,1)                     =
massrescumul(overtpos(i,1)+2,1);
            minposition = 2;
        end;
    end;
    overtposscale(i,1) = overtpos(i,1) + minposition;
    signaltime_overt(i,1)                               =
signaltime(overtposscale(i,1),1);
end;

massrescumul_overtreal = [];
signaltime_overtreall = [];
overtposreall = [];
overttimereall = [];

massrescumul_overtreal(1,1)                             =
massrescumul_overt(1,1); %Consists of list of cumulative
individual overtopping volumes.
signaltime_overtreall(1,1) = signaltime_overt(1,1);
overtposreall(1,1) = overtpos(1,1);
overttimereall(1,1) = overttime(1,1);

v = 1;

for i = 2:dim2
    if (overtposscale(i,1) - overtposscale(i-1,1) > 1) &&
(massrescumul_overt(i,1)-massrescumul_overt(i-1,1)>0)   %
Sometimes one overtopping causes two peaks in the
overtopping detection signal. Therefore, the requirement
that there is at least one data point between two
overtopping positions in the weigh cell signal has been
imposed. If this is not the case, the two overtopping
peaks will be taken as one overtopping.

        v = v+1;
        massrescumul_overtreal(v,1)                     =
massrescumul_overt(i,1);
```

```
        signaltime_overtreall(v,1)                          =
signaltime_overt(i,1);
        overtposreall(v,1) = overtpos(i,1);
        overttimereall(v,1) = overttime(i,1);
    end;
end;

dim3 = length(massrescumul_overtreal);

plot(signaltime,massrescumul,'*');
xlabel('Tijd [s]')
hold on
plot(timedetection,signalovertdetnew + 85,'*k'); % For
graphical purposes.
plot(signaltime_overtreall,massrescumul_overtreal,'*g');
%Plots the dots green on the massrescumul curve.
legend('Cumulative absolute mass in reservoir [kg]',
'Overtoppingdetectionsignal','Value of weigh cell signal
used for determing the overtopping mass')
title('Cumulative absolute mass in reservoir with
overtoppingdetectionsignal')
grid
saveas(gcf,strcat('Output\',nametest,'\Overtoppingdetecti
onsignal_with_cummassreservoir.fig'));
hold off

%% Calculation of all individual overtopping masses based
on cumulative curve

indivmass_all = [];
signaltime_overtreal = [];
overtposreal = [];
overttimereal = [];

teller=0;
for i = 1:(dim3-1)
     if         ((massrescumul_overtreal(i+1,1)         -
massrescumul_overtreal(i,1))>0)
          teller=teller+1;
```

```
          indivmass_all(teller,1)                          =
massrescumul_overtreal(i+1,1)                              -
massrescumul_overtreal(i,1);
          signaltime_overtreal(teller,1)                   =
signaltime_overtreall(i,1);
          overtposreal(teller,1) = overtposreall(i,1);
          overttimereal(teller,1) = overttimereall(i,1);
     end;
end;
if                  (massrescumul(dim,1)                   -
massrescumul_overtreal(dim3,1)>0)
    indivmass_all(teller+1,1)   =   massrescumul(dim,1)    -
massrescumul_overtreal(dim3,1);
    signaltime_overtreal(teller+1,1)                       =
signaltime_overtreall(dim3,1);
    overtposreal(teller+1,1) = overtposreall(dim3,1);
    overttimereal(teller+1,1) = overttimereall(dim3,1);
 end;

dim5=length(indivmass_all);

indivmass_all_meter = [];

for i = 1:dim5
    indivmass_all_meter(i,1)   =   indivmass_all(i,1)   /
0.2; %Until now: only over 20 cm of the test set-up.
Better in meter.
end;

overtinterval_all = [];

for i = 2:dim5
    overtinterval_all(i-1,1)   =   overttimereal(i,1)   -
overttimereal(i-1,1);
end;

overtinterval_all_last = NaN; % This last element of the
matrix is not included in overtinterval_all so that the
mean value of overtinterval_all can be calculated.
overtinterval_allmatr                                      =
[overtinterval_all;overtinterval_all_last];
```

```
overtposreal_allmatrix = num2cell(overtposreal);
overttimereal_allmatrix = num2cell(overttimereal);
overtinterval_allmatrix = num2cell(overtinterval_allmatr);
indivmass_allmatrix = num2cell(indivmass_all);
indivmass_all_metermatrix = num2cell(indivmass_all_meter);

matrix = [overtposreal_allmatrix overttimereal_allmatrix
overtinterval_allmatrix              indivmass_allmatrix
indivmass_all_metermatrix];

columnHeader = {'Overtopping position', 'Overtopping Time
[s]', 'Overtopping time interval [s]', 'Overtopping mass
[kg]','Overtopping mass per meter crest width [kg/m]'};
allData = [columnHeader; matrix];

xlswrite2007(File, allData, 'All overtopping events');

plot(overttimereal,indivmass_all,':*');
xlabel('Time [s]')
ylabel('Overtopping mass [kg]')
hold on
title('Overtopping mass')
grid
saveas(gcf,strcat('Output\',nametest,'\Overtoppingmass_al
l.fig'));
plot(signaltime,pumping / 100,'k');
legend('Overtopping mass [kg]', 'Pumped absolute mass
[kg]')
title('Overtopping mass with pumped absolute mass')
saveas(gcf,strcat('Output\',nametest,'\Overtoppingmass_al
lwithpumpedmass.fig'));
hold off


%% Calculation of individual overtopping masses based on
cumulative curve between build up and tapering off

overtposreal_skip = [];
overttimereal_skip = [];
```

```
indivmass_skip = [];
indivmass_skip_meter = [];
indivmass_skip_cub_meter = [];
overtinterval_skip = [];

s = 0;
t = 0;
overtinterval_all(dim5,1) = 0;


for i = 1:dim5
    if    ((overtposreal(i,1)    >=    skipbegin+1)    &&
(overtposreal(i,1) <= dim - skipend))
        s = s + 1;
        overtposreal_skip(s,1) = overtposreal(i,1);
        overttimereal_skip(s,1) = overttimereal(i,1);
        indivmass_skip(s,1) = indivmass_all(i,1);
        t = t + indivmass_skip(s,1);
        indivmass_skip_meter(s,1)                        =
indivmass_all_meter(i,1);

indivmass_skip_cub_meter(s,1)=indivmass_all_meter(i,1)/10
00;
        overtinterval_skip(s,1) = overtinterval_all(i,1);
    end;
end;


dim4 = s;

minindivmassskip = min(indivmass_skip_cub_meter);
maxindivmassskip = max(indivmass_skip_cub_meter);
spread = (maxindivmassskip - minindivmassskip);
intlength = spread/10;

% Calculate the average discharge for reservoir
avgq   =   t   /   1000   /   (signaltime(dim-skipend)   -
signaltime(skipbegin+1)); % in m³/s.
qavg = avgq / 0.2; % in m³/s/m; width of the model is 0.2
m.
```

```
% Calculate hydraulic efficiency for reservoir
grav = 9.81;
Pres = Rc * grav * qavg * 1000;
effres = Pres / Pwave;

else
numberovertoppings=0;
totalmass=0;
indivmass_avg=0;
indivmass_std=0;
indivmass_min=0;
indivmass_max=0;
totalmass_meter=0;
indivmass_avg_meter=0;
indivmass_std_meter=0;
indivmass_min_meter=0;
indivmass_max_meter=0;
overtinterval_avg=0;
overtinterval_std=0;
overtinterval_min=0;
overtinterval_max=0;
qavg=0;
effres=0;
end;

%% All input and output

Itext = {'Name test' 'Rc [m]' 'Skip time at start of test
[s]' 'Skip time at end of test [s]' 'Pwave [W/m]'};

Input(1,1) = Rc;
Input(1,2) = skipbegintime;
Input(1,3) = skipendtime;
Input(1,4) = Pwave;
I = num2cell(Input);

m1 = [Itext; nametest I];
```

```
O1text = {'Test duration [s]' 'Start time [s]' 'End time
[s]' 'Number of data points skipped at start of test'
'Number of data points skipped at end of test' 'Average
sampling frequency weigh cell signal [Hz]' 'Number of
pumping events'};

Output1(1,1) = endtimedetection;
Output1(1,2) = signaltime(skipbegin+1);
Output1(1,3) = signaltime(dim-skipend);
Output1(1,4) = skipbegin;
Output1(1,5) = skipend;
Output1(1,6) = samplefreq;
Output1(1,7) = numpumpturns;
O1 = num2cell(Output1);

m2 = [O1text; O1];

O2text = {'Number of overtopping events' 'Total mass of
overtopping [kg]' 'Average mass of overtopping [kg]'
'Standard deviation on mass of overtopping [kg]' 'Minimum
mass of overtopping [kg]' 'Maximum mass of overtopping
[kg]' 'Total mass of overtopping per meter crest width
[kg/m]' 'Average mass of overtopping per meter crest
width [kg/m]' 'Standard deviation on mass of overtopping
per meter crest width [kg/m]' 'Minimum mass of
overtopping per meter crest width [kg/m]' 'Maximum mass
of overtopping per meter crest width [kg/m]' 'Average
time interval between overtopping events [s]' 'Standard
deviation on time interval of overtopping [s]' 'Minimum
time interval between overtopping events [s]' 'Maximum
time interval between overtopping events [s]' 'Average
overtopping rate [m³/s/m]' 'Hydraulic efficiency'};

Output2(1,1) = numberovertoppings;
Output2(1,2) = totalmass;
Output2(1,3) = indivmass_avg;
Output2(1,4) = indivmass_std;
Output2(1,5) = indivmass_min;
Output2(1,6) = indivmass_max;
Output2(1,7) = totalmass_meter;
Output2(1,8) = indivmass_avg_meter;
```

```
Output2(1,9) = indivmass_std_meter;
Output2(1,10) = indivmass_min_meter;
Output2(1,11) = indivmass_max_meter;
Output2(1,12) = overtinterval_avg;
Output2(1,13) = overtinterval_std;
Output2(1,14) = overtinterval_min;
Output2(1,15) = overtinterval_max;
Output2(1,16) = qavg;
Output2(1,17) = effres;
O2 = num2cell(Output2);

m3 = [O2text; O2];

% columnHeader1 = {'Input', ''};
% columnHeader2 = {'Intermediate results', ''};
%  columnHeader3  =  {'Final  results  through  cumulative
weigh cell signal between start skip and end skip', ''};

allData = [m1 m2 m3];

xlswrite2007(File, allData, 'Input and results');

ExcelWorkbook.SaveAs(fullfile('…\Output',       nametest,
strcat(nametest,'.xlsx')));
ExcelWorkbook.Close;

%% Differentiation for reservoir

if dim2 ~=0

diffmassrescumul = [];

diffmassrescumul(1,1) = 0;
for i = 2:dim
    diffmassrescumul(i,1)      =      (massrescumul(i,1)-
massrescumul(i-1,1))   /   (signaltime(i,1)-signaltime(i-
1,1));
end;

plot(signaltime,diffmassrescumul);
```

```
xlabel('Time [s]')
ylabel('Time-differentiated cumulative absolute mass in
reservoir [kg/s]')
title('Time-differentiated cumulative absolute mass in
reservoir')
grid
saveas(gcf,strcat('Output\',nametest,'\Differntiatedcumma
ssreservoir.fig'));

end;
end;

%% Closing of Excel

Excel.Quit;
Excel.delete;

%-----------------------------------------------------------
------------------
%END OF M FILE
```

C

Appendix C: Calculation of characteristic slope angle for AAU08 test series

The calculation of the characteristic slope angle α for the AAU08 test series is based on the definition of slope angle α_{incl} in the CLASH database: i.e. the mean slope angle that the structure makes with a horizontal, where the berm is included in this mean value. The fractioned slopes in the AAU08 test series feature a berm with a zero width. The slope angle α_{incl} is defined as the slope angle of the straight line connecting the intersection points of the slope with the horizontal lines defined by $\pm 1.5 H_{m0}$ compared to the still water level (abbreviated SWL). If the horizontal line corresponding with SWL $+1.5 H_{m0}$ exceeds the crest of the slope, the crest level should be taken instead. Due to the different values for SWL and the different geometries, each of the tests with composite slopes corresponds to a different characteristic slope angle.

Four situations occurred during the AAU08 test series. These are shown in Figs. C.1 to C.4. Based on these figures, a single expression is found for α. The tangent of the characteristic slope angle is defined by:

$$\tan\alpha = \frac{V}{H} \tag{C.1}$$

in which:

$$V = \min\left(v_u, h_t - v_d + 1.5 H_{m0}\right) + \left(v_d - h_t + 1.5 H_{m0}\right) \tag{C.2}$$

$$H = \frac{\min\left(v_u, h_t - v_d + 1.5 H_{m0}\right)}{\tan\alpha_u} + \frac{\left(v_d - h_t + 1.5 H_{m0}\right)}{\tan\alpha_d} \tag{C.3}$$

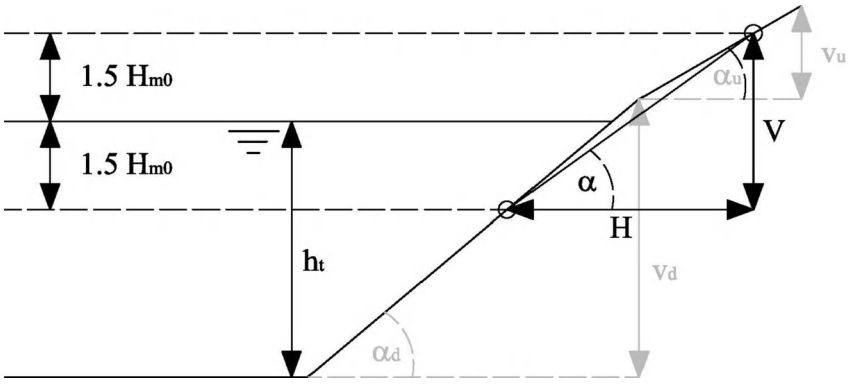

Figure C.1: Situation 1.

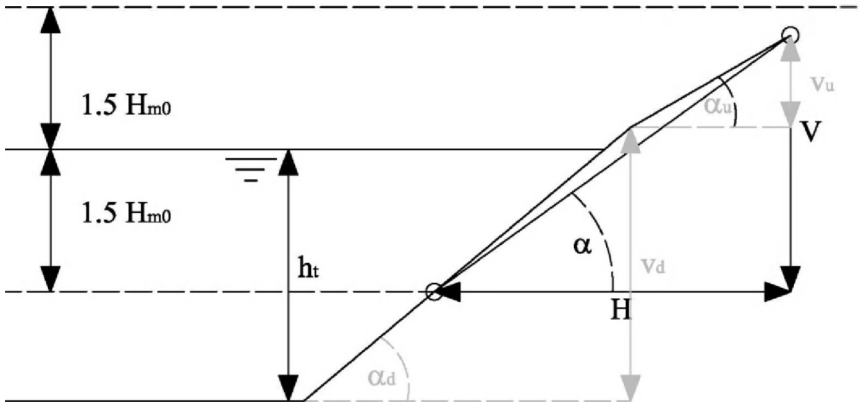

Figure C.2: Situation 2.

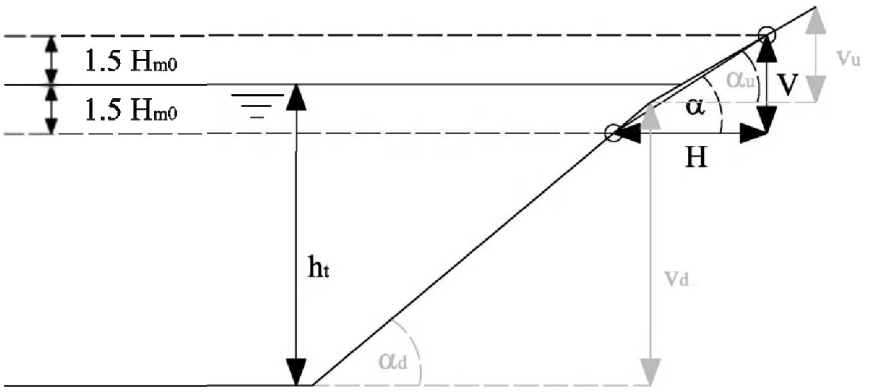

Figure C.3: Situation 3.

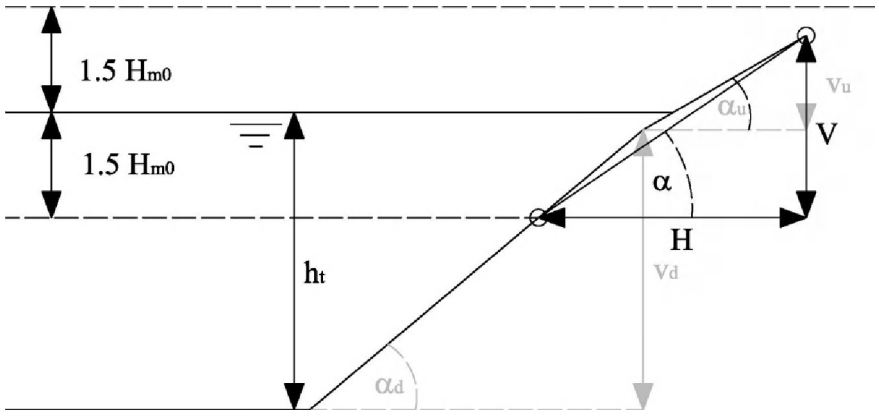

Figure C.4: Situation 4.

D

Appendix D: Derivation of expression for shoaling coefficient

The shoaling coefficient is defined by:

$$K_S = \sqrt{\frac{c_{g,deep}}{c_g}} \tag{D.1}$$

The group velocity in deep water is defined by $c_{g,deep} = 1/2\, c_{deep}$, while the denominator is defined in Eq. (3.11). Hence, Eq. (D.1) can be rewritten as:

$$K_S = \sqrt{\frac{\frac{c_{deep}}{2}}{c\left(\frac{1}{2} + \frac{kh}{\sinh(2kh)}\right)}} \tag{D.2}$$

Based on the dispersion relationship (Eq. 3.13) and the definition of the propagation velocity of a wave (Eq. 3.12), Eq. (D.2) becomes:

$$K_S = \sqrt{\frac{\frac{1}{2}\frac{gT}{2\pi}}{\frac{gT}{2\pi}\tanh(kh)\left(\frac{1}{2} + \frac{kh}{\sinh(2kh)}\right)}} \tag{D.3}$$

$$\Rightarrow K_S = \sqrt{\frac{\frac{1}{2}}{\tanh(kh)\left(\frac{1}{2}+\frac{kh}{\sinh(2kh)}\right)}} \tag{D.4}$$

Since we want to express kh and K_s as a function of $k_{deep}h$, this last factor needs to be introduced in the equations above. By definition:

$$L = L_{deep}\tanh(kh) \tag{D.5}$$

which means that:

$$\tanh(kh) = \frac{L}{L_{deep}} = \frac{k_{deep}}{k} = \frac{k_{deep}h}{kh} \tag{D.6}$$

and, based on Eq. (D.4):

$$K_S = \sqrt{\frac{\frac{1}{2}\frac{kh}{k_{deep}h}}{\left(\frac{1}{2}+\frac{kh}{\sinh(2kh)}\right)}} \tag{D.7}$$

E

List of publications

E.1 International journal publications

- L. Victor, P. Troch and J.P. Kofoed. *On the Effects of Geometry Control on the Performance of Overtopping Wave Energy Converters*. Energies, 4(10): 1574-1600, 2011 (doi: 10.3390/en4101574).

- L. Victor and P. Troch. *Wave overtopping at smooth impermeable steep slopes with low crest freeboards*. Accepted for publication in Journal of Waterway, Port, Coastal, and Ocean Engineering, 2011.

- L. Victor, J.W. van der Meer and P. Troch. *Probability distribution of individual overtopping volumes for smooth impermeable steep slopes with low crest freeboards*. Submitted for publication in Coastal Engineering, 2011.

E.2 National journal publications

- G. De Backer, C. Beels, T. Mertens and L. Victor. *Golfenergie: groene stroom uit de zeegolven*. De Grote Rede, 22: 2-8, 2008.

E.3 International conference publications

- L. Victor. *Experimental and numerical study of the hydrodynamic behavior and structural response of wave energy converters based on wave*

overtopping. In Proceedings of the 2nd International PhD Symposium on Offshore Renewable Energy (INORE 2008), Comrie (Scotland), UK, 43, 2008.

- L. Victor and D. Vanneste. *A numerical wave flume in FLOW-3D®*. In Proceedings of the 8th European FLOW-3D® Users meeting, Tübingen, Germany, CD-ROM, 2008.

- C. Beels, P. Mathys, V. Meirschaert, I. Ydens, J. De Rouck, G. De Backer and L. Victor. *The impact of several criteria on site selection for wave energy conversion in the North Sea*. In Proceedings of the 2nd International Conference on Ocean Energy (ICOE 2008), Brest, France, CD-ROM Institut Français de Recherche pour l'Exploitation de la Mer (IFREMER), 2008.

- L. Victor, P. Troch and D. Vanneste. *Experimental and numerical study of the hydrodynamic behavior of wave energy converters based on wave overtopping*. In Proceedings of the 2nd International Conference on Ocean Energy (ICOE 2008), Brest, France, CD-ROM Institut Français de Recherche pour l'Exploitation de la Mer (IFREMER), 2008.

- L. Victor. *Validation of a numerical tool to predict the individual wave overtopping volumes of a wave energy converter*. In Proceedings of the 3rd International PhD Symposium on Offshore Renewable Energy (INORE 2009), Ghent, Belgium, 35, 2009.

- L. Margheritini, L. Victor, J.P. Kofoed and P. Troch. *Geometrical Optimization for Improved Power Capture of Multi-level Overtopping Based Wave Energy Converters*. In Proceedings of the 19th International Offshore (Ocean) and Polar Engineering (ISOPE 2009), Osaka, Japan, 1: 339-344, 2009.

- L. Victor, P. Troch and J.P. Kofoed. *Prediction of the individual wave overtopping volumes of a wave energy converter using experimental testing and first numerical model results*. In Proceedings of the European Wave and Tidal Energy Conference (EWTEC 2009), Uppsala, Sweden, 1: 999-1008, 2009.

- L. Victor and P. Troch. *Numerical study of wave overtopping using FLOW-3D®*. In Proceedings of the 4th International PhD Symposium on Offshore Renewable Energy (INORE 2010), Dartmouth, UK, online, 2010.

- L. Victor and D. Vanneste. *Modelling coastal structures in FLOW-3D®*. In Proceedings of the 10th European FLOW-3D® Users meeting, Reims, France, CD-ROM, 2010.

- L. Victor, J.P. Kofoed and P. Troch. *Hydrodynamic behavior of overtopping wave energy converters built in sea defense structures*. In Proceedings of the 29th International Conference on Ocean, Offshore and Arctic Engineering (OMAE 2010), Shanghai, China, paper nr. OMAE2010-20372, 2010.

- L. Victor and P. Troch. *Development of a test set-up to measure wave-by-wave overtopping volumes*. In Proceedings of the 3rd International Conference on the Application of Physical Modelling to Port and Coastal Protection (Coastlab10), Barcelona, Spain, paper nr. 53, 2010.

- L. Victor, P. Troch and J.P. Kofoed. *Optimization of the performance of overtopping wave energy converters with a simple slope built in sea defence structures by geometry control*. In Proceedings of the 21st International Offshore (Ocean) and Polar Engineering (ISOPE 2011), Maui (Hawaii), USA, 1: 606-613, 2011.

E.4 National conference publications

- L. Victor, P. Troch and J.P. Kofoed. *Electric power from ocean waves – improving the performance of overtopping devices*. In Book of Abstracts of the 10th VLIZ Young Scientists' Day, Ostend, Belgium, VLIZ Special Publications 43: 167, 2009.

- L. Victor and P. Troch. *Electric power from ocean waves – improving the performance of overtopping devices*. In Proceedings of the 10th FirW PhD Symposium, Ghent, Belgium, 182-183, 2009.

- L. Victor and P. Troch. *Development of a test set-up to measure large wave-by-wave overtopping masses*. In Proceedings of the 11th FirW PhD Symposium, Ghent, Belgium, 48, 2010.